



Call: H2020-ICT-2020-2

Project reference: 101015956

Project Name:

A flagship for B5G/6G vision and intelligent fabric of technology enablers connecting human, physical, and digital worlds

Hexa-X

Deliverable D2.2

Initial radio models and analysis towards ultra-high data rate links in 6G

Date of delivery: 31/12/2021 Version: 1.0
 Start date of project: 01/01/2021 Duration: 30 months

Document properties:

Document Number:	D2.2
Document Title:	Initial radio models and analysis towards ultra-high data rate links in 6G
Editor(s):	Marko E. Leinonen (OUL)
Authors:	Marko E. Leinonen (OUL), Muris Sarajlic (EAB), Ahmad Nimir (TUD), Tommy Svensson (CHA), Katsuyuki Haneda (AAU), Andreas Wolfgang (QRT), Charitha Madapatha (CHA), Chao Fang (CHA), Behrooz Makki (EAB), Yinggang Li (EAB), Kilian Roth (INT), Leonardo Gomes Baltar (INT), Hardy Halbauer (NOG), Le Hang Nguyen (NOG), Mohamed Aliouane (ORA), Jean-Marc Conrat (ORA), Pekka Kyösti (OUL), Nuutti Tervo (OUL), Aarno Pärssinen (OUL), Xinxin Yang (QRT), Roberto Bomfin (TUD), Meik Dörpinghaus (TUD), Stephan Zeitz (TUD)
Contractual Date of Delivery:	31/12/2021
Dissemination level:	PU ¹ /
Status:	Final
Version:	1.0
File Name:	Hexa-X D2.2_v1.0

Revision History

Revision	Date	Issued by	Description
v0.1	27.9.2021	Marko E. Leinonen	Initial Version
v0.2	15.10.2021	Marko E. Leinonen	Table of Content for the document
v0.3	8.11.2021	Marko E. Leinonen	V0.3 from V0.2 during document writing
v0.4	10.11.2021	Marko E. Leinonen	V0.4 for internal review
v0.5	26.11.2021	Marko E. Leinonen	V0.5 for external review
v1.0	20.12.2021	Marko E. Leinonen	Release version

¹ CO = Confidential, only members of the consortium (including the Commission Services)

PU = Public

Abstract

This report provides analysis of various simulation models for future 6G radio system based on Hexa-X work package 2: “Novel radio access technologies towards 6G”. The analysis is performed from multiple viewpoints including radio system level studies, modelling of most significant non-idealities of radio parameters, signal waveform analyses with modelled radio impairments, modulation and beam forming studies and radio channel models based on measurements. A 6G simulation framework with its input parameters is presented in the report, which summarises various aspects of the report into one simulation platform.

Keywords

100 – 300 GHz, hardware model, beamforming, channel measurements, distributed MIMO, physical layer, radio model, simulation model

Disclaimer

The information and views set out in this deliverable are those of the author(s) and do not necessarily reflect views of the whole Hexa-X Consortium, nor the official opinion of the European Union. Neither the European Union institutions and bodies nor any person acting on their behalf may be held responsible for the use which may be made of the information contained therein



This project has received funding from the European Union’s Horizon 2020 research and innovation programme under grant agreement No 101015956.

Executive Summary

The main target of the document is present first simulation models and analyses of the 6G radio and physical signal layer which will be used as a basis simulation framework for further studies during the Hexa-X project. It is discussed in the report, that multiple level mathematical and simulation models are needed for performance analysis of the 6G wireless system.

Performed radio frequency (RF) system level analysis indicates that in order to achieve 100 Gbps data rate link with a present day high performance analog to digital converter (ADC) technology at least nine base band data streams are required. The power consumption of the ADC increases significantly with signal bandwidth, and thus ADC is one the main contributor for the power consumption in 6G radio.

The frequency synthesis of the radio transceiver will face new challenges, and especially the phase noise of the local oscillator (LO) will limit the RF performance. Several simulation models for phase noise analysis based on measurement data have been proposed. Similarly, simulation models for other main RF transceiver blocks, including power amplifiers (PAs), low noise amplifiers, ADC and digital to analog converters, are described in the report.

Digital modulation methods for 6G purposes are analysed based on simulations in details in the report. The OFDM like modulations (as in 5G) are compared with single carrier (SC) modulations. Results indicate that the SC modulation with frequency domain equalisation and OFDM with appropriate symbol mapping are more tolerant to PA nonidealities and phase noise than legacy OFDM. Moreover, use of DFTS-OFDM results in an extension of maximum propagation distance, compared with OFDM. Performance-complexity tradeoff is analyzed for an iterative receiver for DFTS-OFDM, and an improvement of performance is possible with only a few iterations.

Hybrid beam forming simulations combine several RF simulation models into a combined simulation frame-work. The frame-work enables radio performance simulations in three dimensional (3D)-manner including radio channel and antenna performances, as well. The beam forming simulations can include multipath and scattering effects from objects which are at non-line of sight.

The trend of wireless network densification will continue in the 6G, and it is the key enabler to meet coverage and reliability targets at the higher frequency bands. Based on analysis, low-cost solutions are more important than maximum spectral efficiency at high mmW bands (at least in the early roll-out phases) favouring for decentralized solutions, whereas in the lower mmW bands the need for higher spectral efficiency calls for digital less distributed approaches.

Based on radio wave and material interaction measurement ranging from 2 GHz to 170 GHz, it can be concluded that transmission losses through our living space materials have increasing trend. The radio channel measurements performed at 140 GHz revealed that there are a few independent radio paths at indoors, while the number of paths decreases at outdoors. These results confirm possible availability of link diversity at upper mmW frequencies.

Coming proof-of-concept demonstrations in the later phase of the project are described briefly at the end of the document.

Table of Contents

List of Figures	8
List of Tables	13
List of Acronyms, Abbreviations and Mathematical Notations	14
1 Introduction	18
1.1 Objective of the document.....	18
1.2 Structure of the document	18
2 Main requirements for the 6G radio system studies	19
3 RF system level analyses and simulations of initial 6G radio	20
3.1 Initial 6G radio architecture for simulation purposes	20
3.2 Simulation and modelling framework for RF impairments.....	21
3.2.1 Link level impacts of different RF impairments	21
3.2.2 Abstractions for modelling RF impairments for 6G Radio	21
3.3 RF system calculations of the RF reference architecture	23
3.3.1 High performance analog to digital converter analysis and modelling	23
3.3.2 Illustrative system level calculation for 100 Gbps RF architecture.....	24
3.4 Initial RF models and simulation examples	26
3.4.1 Waveform assumptions, digital transceiver, and signal model	27
3.4.2 Reference transceiver and receiver overview	28
3.5 Modelling energy efficiency/power consumption.....	29
3.6 Preliminary models for transceiver building blocks.....	31
3.6.1 Behavioural ADC/DAC models	31
3.6.2 Power amplifier	32
3.6.3 Noise figure model of analog Rx front-end.....	34
3.6.3.1 LNA noise figure.....	35
3.6.3.2 Loss of Rx front-end passives	37
3.6.4 Analog beamforming nonlinearities	38
3.6.5 Frequency synthesis considerations and phase noise	39
3.6.6 Review of current 3GPP models used for preliminary waveform studies.....	42
3.6.6.1 3GPP power amplifier models	42
3.6.6.2 3GPP phase noise models	42
3.6.6.3 Discussion on shortcomings of simplified RF impairment modelling.....	43
4 Waveform candidates for 6G: impact of hardware impairments and complexity-performance trade-offs	45
4.1 Short description of studied waveforms	45
4.1.1 OFDM-like waveforms	45
4.1.2 Single-carrier	45
4.1.3 Constrained Envelope Continuous Phase Modulation (ceCPM).....	46
4.1.4 Zero-crossing modulation (ZXM)	46
4.2 Complexity-performance trade-off for DFTS-OFDM with an iterative receiver design	47
4.2.1 Empirical sub-THz Channel Model.....	47
4.2.2 Results	48
4.2.2.1 Performance Analysis	49
4.2.2.2 Complexity Analysis	51
4.2.3 Conclusions	52
4.3 Impact of RF impairments on the performance of CP-OFDM, DFTS-OFDM and SC-FDE	52
4.3.1 Impact of phase noise	52
4.3.2 Impact of PA nonlinearity and effects on the link budget	54

4.3.2.1	PAPR Results	54
4.3.2.2	PA output backoff and link budget comparison of OFDM and DFTS-OFDM..	55
4.3.3	DFTS-OFDM under joint impact of PN and PA nonlinearity.....	60
4.4	Performance of zero-crossing modulation under the influence of phase noise	61
4.5	End-to-end performance analysis of constrained-envelope modulation under PA nonlinearity.....	63
4.6	Concluding remarks.....	65
5	Hybrid beam forming analyses	66
5.1	Hybrid beamforming architecture	66
5.1.1	Signal model under ideal hardware	66
5.1.1.1	Ideal transmitted signal	66
5.1.1.2	Planar array	67
5.1.1.3	Ideal received signal.....	68
5.1.1.4	Received signal in multipath channel.....	69
5.2	Theoretical limitations under ideal assumptions	71
5.2.1	MIMO consideration	71
5.2.2	LoS scenario limitations	72
5.2.3	Wideband consideration	73
5.3	HW design constraints and effects on the performance	73
5.4	Impact of HW limitations on Beam training strategies and initial access	74
5.5	Beam tracking and management.....	75
5.5.1	Beam Training Time Interval	75
5.5.1.1	LOS Based Model	75
5.5.1.2	Spatial Coherence Based Model	77
5.6	Simulation framework	79
5.6.1	Structure	79
5.6.2	Beamforming initial simulation module.....	81
6	D-MIMO radio architecture studies.....	83
6.1	Introduction and motivation to D-MIMO.....	83
6.1.1	What is D-MIMO for 6G?.....	83
6.1.2	Potential.....	84
6.1.3	Roll-out considerations.....	85
6.2	Transceiver and radio access/fronthaul/backhaul architecture considerations	87
6.2.1	Hardware constraints.....	87
6.2.2	Architectural considerations.....	88
6.3	Towards a common architecture.....	89
6.3.1	Analog centralized beamforming	89
6.3.2	Distributed digital beamforming	90
6.3.2.1	Beamforming Computations and Weight Distribution	90
6.3.2.2	Hybrid Precoding in Cooperative Millimeter Wave Networks	94
6.3.3	Integrated access and backhauling	96
6.4	Conclusions	101
7	Understanding the above-100 GHz wave-material interaction and wave propagation through measurements.....	102
7.1	Wave-material interaction analysis	102
7.2	Multipath Channel Measurements.....	105
7.2.1	Channel Sounder Architecture	105
7.2.2	Measurement Steps.....	106
7.2.3	Uncertainties.....	106
7.2.4	Data Post-Processing.....	107
7.2.4.1	Back-to-back Calibration	107
7.2.4.2	Path Detection	107
7.2.5	Indoor Channel Sounding and Initial Observations	108

7.2.5.1	Entrance Hall Measurements	108
7.2.5.2	Observations on Power Angular Delay Profiles.....	109
7.2.6	Outdoor Measurements	110
7.2.6.1	Campus Measurements	110
7.2.6.2	Observations of Power Angular Delay Profiles Obtained in the Campus Measurements	112
7.2.6.3	Residential Measurements.....	113
7.2.6.4	Observations of Power Angular Delay Profiles Obtained in the Campus Measurements	113
7.2.6.5	City Center Measurements.....	114
7.2.6.6	Observations of Power Angular Delay Profiles Obtained in the City Center Measurements	115
7.3	Measurement-based analysis of 140 GHz multipath channels	116
7.3.1	The number of independent beams.....	116
7.3.1.1	Methods for evaluating the beam number	116
7.3.1.2	Resulting beam counts	119
7.3.2	Wave scatterer identification.....	119
7.3.2.1	Measurement-Based Ray Tracer	120
7.3.2.2	Most Probable Ray-Traced Path	121
7.3.2.3	Scatterer Identification Results	122
8	Proof-of-concepts for communications.....	124
8.1.1	Digital Architecture and Waveforms.....	124
8.1.2	High-bandwidth communication at upper mmW using different waveforms:	124
8.1.3	Common hardware for communication, localization, and sensing.....	125
	Conclusions.....	126
	References.....	128
	Annex A	137

List of Figures

Figure 3-1: Potential one frequency conversion 6G transceiver architecture [HEX21-D21].	20
Figure 3-2: An example how RF parameters such as noise figure (NF), transmission power (TX), over the air (OTA) distance affect receiver EVM performance [PLT21].	21
Figure 3-3: Different component simulation models can be mixed on a need basis to answer the research question.	23
Figure 3-4: SNDR and power consumption of ADCs as a function of bandwidth based on data from [MUR21] and commercial data sheets.	24
Figure 3-5: Analysis of number of needed ADCs and their power consumption a 6G receiver to support 100 Gbps.	26
Figure 3-6: Overall signal flow of the whole link with the required reference digital transmitter and receiver. The digital blocks are required to generate and analyse the waveform and can be replaced by different 6G waveform candidates. The digital blocks may also include potential calibration and compensation routines for mitigating different RF impairments.	28
Figure 3-7: Functional RF blocks of a single phased array transmitter.	29
Figure 3-8: Functional RF blocks for a single phased array receiver.	29
Figure 3-9: Total power consumption of TX and RX part (analog, hybrid and digital architecture, 90 – 230 GHz carrier frequency with 90, 168 and 452 array elements, respectively). Labels indicating power consumption in Watt.	31
Figure 3-10: DAC modelling principle is similar with the ADC modelling, if the impact of the reconstruction filter is neglected, since DAC model requires first to quantize the input signal for DAC quantization levels.	32
Figure 3-11: Two different generic ADC modelling principles are (1) quantize the signal and (2) add normal-distributed quantization noise. Both approaches may be used in different simulation scenarios, depending on the assumptions.	32
Figure 3-12: PA saturated output power versus frequency [WHM+21].	33
Figure 3-13: Structure for PA modelling.	33
Figure 3-14: Input and output signals to the GaN PA in frequency domain (left) and time domain (right).	34
Figure 3-15: Measured and modelled AM-AM (left) and AM-PM (right) results of the GaN.	34
Figure 3-16 Noise figure of SiGe LNA MMICs over 30- 300 GHz: measured (circle), simulated (cross), extracted from Rx module (triangle), and exponential fitting of the minimum NF over the whole mmW range (solid line).	35
Figure 3-17: NF data of LNA ICs in CMOS (green circle), SiGe (orange circle), GaAs (red triangle) and InP (black square). The lines are exponentially fitted to the best NF of the respective technologies.	36
Figure 3-18 A conceptual drawing of basic AiP build up (the thick orange line is the RF routing path)	37
Figure 3-19: Analog phase shifter models (a) active model, where noise is added before amplitude and phase controls, and (b) passive model, where noise is added after amplitude and phase controls.	39
Figure 3-20: Example local oscillator generation architecture to support 150 GHz frequency.	39
Figure 3-21: Example phase noise spectra with parametrization taken from 3GPP [38.808, Section 4.2.3.1]	40

Figure 3-22: Normally distributed white noise is filtered with a phase noise spectrum frequency response to generate the phase noise model.....	41
Figure 3-23: Building blocks of RF transceiver for upper mmW band (one signal path).	41
Figure 3-24: AM/AM and AM/PM characteristics of PA model I.....	42
Figure 3-25: PSD of the phase noise model II at both transmit and received side, scaled up to 120 GHz carrier frequency	43
Figure 3-26: Illustration of the transmitter and receiver front-end aspects that has the main influence on waveform performance.	43
Figure 3-27: Illustration of the transmitter and receiver front-end model used for the preliminary waveform investigation.....	44
Figure 4-1: diagram of Tx digital baseband for OFDM-like waveforms.....	45
Figure 4-2: diagram of Tx digital baseband for SC-FDE	46
Figure 4-3: Block diagram of the transmitter for ZXMs systems, taken from [NDH+20b].....	46
Figure 4-4 PADP of the used channels (left), and overlaid channel power (right).	48
Figure 4-5: FER with convolutional encoder for maximum iterations of 0, 2 and 4.	49
Figure 4-6: FER with LDPC encoder for maximum iterations of 0, 2 and 4.....	50
Figure 4-7: FER comparison between convolutional and LDPC encoders for a maximum of 4 equalization iterations.	51
Figure 4-8: BLER performance for different modulation orders and waveforms. Phase noise is compensated applying the described algorithms.....	53
Figure 4-9: PAPR characteristics of CP-OFDM, DFT-S-OFDM and SC-FDE with 0.3 and 0.5 rolloff	54
Figure 4-10: illustration of terms essential for ACLR calculation as per 3GPP specification.....	56
Figure 4-11: EVM and ACLR as function of OBO for 60 GHz memoryless GaN PA	57
Figure 4-12: Minimum OBO needed for satisfying EVM and ACLR constraints	57
Figure 4-13: selection of BLER simulation results, OFDM	58
Figure 4-14: selection of BLER simulation results, DFTS-OFDM	58
Figure 4-15: Throughput as function of RMCL for OFDM and DFTS-OFDM	59
Figure 4-16: Difference in RMCL between DFTS-OFDM and OFDM as a function of throughput ...	60
Figure 4-17: DFT-s-OFDM performance with RF impairments.	61
Figure 4-18: Baseband system model.	62
Figure 4-19: Performance comparison in terms of BER for different FTN signaling factors M_{TX} , $M = 3$	63
Figure 4-20. Maximum overall HPA efficiency versus mean PAPR and RCM of various modulated signals with 1% and 0.1% clipping level [SE10].....	64
Figure 4-21. CPM-DFTS-OFDM precoder	65
Figure 5-1 Generic hybrid beamforming architecture.	66
Figure 5-2 General planar array.	68
Figure 5-3 Array steering vectors for generic TX and RX planar arrays.....	70
Figure 5-4: Beam shapes for initial access.....	74

Figure 5-5: Absolute values of beam weights for widened beams according to equation (5-43), normalized to maximum allowed power per element of $1/64$	75
Figure 5-6: Illustration of the transition of devices at positions P1 at x_1, y_1 to P3 x_3, y_3 from the region covered by one beam to other regions, given a movement radius defined by the maximum speed and beam training time interval. The faded colours show the regions covered by beams 1 to 6 denoted as A_1 to A_6 . The other colors show the intersection of the movement at each the example device positions $A(x_i, y_i, r_m)$ with the beam coverage, resulting in the areas $A_{j_i}(x_i, y_i, r_m)$	76
Figure 5-7: Probability P_l of devices leaving a given coherence area given different beam training intervals $\tau_B \in \{10 \text{ ms}, 20 \text{ ms}, 50 \text{ ms}, 100 \text{ ms}, 200 \text{ ms}, 500 \text{ ms}, 1 \text{ s}\}$ and number of beams (a) $N_b = 8$ and (b) $N_b = 16$ for cell radius $r_{AP} = 50 \text{ m}$	77
Figure 5-8: Illustration of the area in which the one beam is optimal including two device positions (P1 and P2) and the respective areas for staying inside the area of this beam or transitioning to another one.	78
Figure 5-9: Probability P_l of devices leaving a given coherence area given different beam training intervals $\tau_B \in \{10 \text{ ms}, 20 \text{ ms}, 50 \text{ ms}, 100 \text{ ms}, 200 \text{ ms}, 500 \text{ ms}, 1 \text{ s}\}$ and coherence radius (a) $r_c = 5 \text{ m}$, and (b) $r_c = 2.5 \text{ m}$	78
Figure 5-10 Simulator framework architecture.....	79
Figure 6-1: Illustration of distributed MIMO.	84
Figure 6-2: D-MIMO need to fulfil seemingly conflicting requirements on functional complexity and deployment costs.....	85
Figure 6-3: D-MIMO installation can be simplified if many distributed access points can be rolled out at once, which is the main purpose of a radio stripe (left). There is also need for both serialized (or cascaded) fronthaul connections as well as parallel (or meshed) fronthaul connections (right). The fronthaul segments may be wired or wireless.	86
Figure 6-4: Outdoor D-MIMO is well suited for dense urban areas where it can provide invisible and high-capacity deployments.	87
Figure 6-5: In indoor deployments, such as in a factory, D-MIMO can provide extremely reliable services with high capacity.	87
Figure 6-6: A wide bandwidth D-MIMO system can be implemented using ARoF and WDM.	90
Figure 6-7: SE performance comparison of IADZF and CZF for different cluster sizes for 20 UEs operating at 28 and 100 GHz.	92
Figure 6-8: SE Performance comparison of IADZF and interference unaware TDZF for different cluster sizes for 20 UEs operating at 28 GHz.....	92
Figure 6-9: SINR performance for IADZF for $N = 49$ APs and $K = 20$ UEs evaluated at (a) 28 GHz and (b) 100 GHz.	93
Figure 6-10: Performance comparison for collocated ($L = 1$), partially ($L = \{4, 16\}$) and fully distributed ($L = 64$) deployments for different operating frequencies for $N_k = \{1, 4, 64\}$	94
Figure 6-11: A mmW network where BSs jointly transmit to the users with beamforming.	94
Figure 6-12 (a) Sum RF transmit power and (b) sum power consumption versus the number of BSs. For each architecture, simulation results based on all BSs being active are compared to the optimal case when the silent mode is enabled. Network parameters: number of antennas $N_m = 64$, number of users $K = 4$, number of RF chains $L_m = 4$ per BS, PS power consumption $P_{PS} = 40 \text{ mW}$, DAC power consumption $P_{DAC} = 200 \text{ mW}$, RF chain power consumption $P_{RF} = 40 \text{ mW}$, $\Delta_m = 0.15$ and target spectral efficiency $\tau_k = 4 \text{ bit/s/Hz}$ per user.	95
Figure 6-13 Basic network to illustrate scheduling and routing problem	96

Figure 6-14: UE and BS/AP grouping in odd and even time-slots, prior to routing optimization.....	97
Figure 6-15: Network of 50 UEs and 10 BS/APs	98
Figure 6-16: Assigned network after cost-optimization (number of hops for all links).....	98
Figure 6-17: Illustration of IAB.	99
Figure 6-18: (left) fibre-backhauled networks. (right) Service coverage probability as a function of percentage of fibre-backhauled SBSs.	100
Figure 6-19: (left) Service coverage probability of the IAB network as a function of the blocking density with MBS, SBS and UE transmit powers $P_m, P_s, P_u = (40, 24, 0)$ dBm. (right) Service coverage probability of the IAB network as a function of tree density with $P_m, P_s, P_u = (40, 33, 0)$ dBm.	101
Figure 7-1: Measurement set up.....	103
Figure 7-2: Measurement and positioning system	103
Figure 7-3: Transmission losses of some measured materials	104
Figure 7-4: Transmission losses of some measured materials	105
Figure 7-5: Channel sounder for D-band (110 to 170 GHz).....	105
Figure 7-6: Entrance hall surroundings.....	109
Figure 7-7: Entrance hall (December 2020) antenna locations.....	109
Figure 7-8: Entrance hall (May 2021) antenna locations.....	109
Figure 7-9: Power Angular Delay Profile of an LOS Tx25-Rx1 link in the second entrance hall measurements.....	110
Figure 7-10: Power Angular Delay Profile of an NLOS Tx7-Rx1 link in the second entrance hall measurements.....	110
Figure 7-11: Campus surroundings.....	111
Figure 7-12: Campus antenna locations for Rx1 links.....	111
Figure 7-13: Campus antenna locations for Rx2 links.....	111
Figure 7-14: Power Angular Delay Profile of LOS Tx18-Rx1 link in the campus measurements.....	112
Figure 7-15: Power Angular Delay Profile of LOS Tx5-Rx1 link in the campus measurements.....	112
Figure 7-16: Metallic structure in the campus environment.	112
Figure 7-17: Residential surroundings.....	113
Figure 7-18: Residential antenna locations.....	113
Figure 7-19: Power Angular Delay Profile of Tx19-Rx1 link in the residential measurements.....	114
Figure 7-20: Power Angular Delay Profile of Tx7-Rx1 link in the residential measurements.....	114
Figure 7-21: City center surroundings.	115
Figure 7-22: City center antenna locations	115
Figure 7-23: Power Angular Delay Profile of Tx32-Rx1 link in the city center measurements.....	115
Figure 7-24: Power Angular Delay Profile of Tx39-Rx1 link in the city center measurements.....	116
Figure 7-25: 3GPP beam shape with 10° HPBW used in beam number evaluation (half power, i.e., -3 dB point is at 5°).	117
Figure 7-26: Measured path powers, the beam power and the independent beam directions found by using different methods in an example link. [KGH+21].....	117

Figure 7-27: Measured path powers, the beam power and the independent beam directions found by using different methods in an example link. [KGH+21].	118
Figure 7-28: Measured path powers, the beam power and found independent beam directions using different methods in an example link. [KGH+21].	119
Figure 7-29: (a) Number of beams in 55 independent links as determined using three methods and two dynamic range values. (b) Cumulative distribution functions of beam numbers in 55 links using three methods and two dynamic range values. [KGH+21].	119
Figure 7-30: Single-directional propagation measurements	120
Figure 7-31: Measurement-based ray tracer.	121
Figure 7-32: Entrance Hall point cloud data.	121
Figure 7-33: AoD estimates for Tx14-Rx2 link ($k = 38$) and path $n = 11$.	122
Figure 7-34: Linear piecewise function as weighting to derive the cost function in DBSCAN clustering.	122
Figure 7-35: Scatterers identified for path 1 of Tx14-Rx2 link of the second entrance hall measurements.	123
Figure 7-36: (a) Angle-of-departure estimates and (b) Angle-of-arrival estimates for Tx14-Rx2 link of the second entrance hall measurements.	123
Figure 8-1: Basic system partitioning, where N is the number of digital Tx streams, Y is the number of parallel DA/AD channels, M is the number of Tx and Rx antenna elements and X is the number of parallel RF channels used.	124
Figure 8-2: Digital architecture demonstration, implementing selected base-band algorithms in real-time, while the analogue system components are simulated.	124
Figure 8-3: Demonstration setup for demonstration of high bandwidth communication. IQ samples are generated and analysed offline, but real RF hardware and an over the air channel is used during the transmission.	125
Figure 8-4: Demonstration setup for joint localization, sensing and communication.	125

List of Tables

Table 2-1: Definition of frequency bands in the context of Hexa-X WP2 [HEX21-D21].	19
Table 2-2: Initial radio requirements for the 6G extreme data rate radios [HEX21-D21].	19
Table 3-1: Comparison of simulation abstraction levels.	22
Table 3-2: Receiver ADC analysis for 6G receiver to support 100 Gbps.	25
Table 3-3: Dominant RF impairments for different kind of research problems	26
Table 3-4: Power consumption modelling and scaling for an illustrative system.	30
Table 3-5: Available area per RFIC in an antenna array for the upper mmW frequency bands.	35
Table 3-6: Empirical expressions of the best LNA noise figure achieved by different technologies based on published works.	37
Table 4-1: Measurements of [NJK+18] used in simulation	47
Table 4-2 Simulation Parameters	49
Table 4-3 Summary of performance gain of System with convolutional encoder	49
Table 4-4 Summary of performance gain of system with LDPC encoder	50
Table 4-5 Probability of equalization iterations for system with convolutional encoder for highest SNR point of Figure 4-7.	51
Table 4-6 Probability of equalization iterations for system with LDPC encoder for highest SNR point of Figure 4-7.	51
Table 4-7: Setting parameters	53
Table 4-8: System parameters for OFDM/DFTS-OFDM comparison study	55
Table 4-9: System parameters for OFDM/DFTS-OFDM comparison study	60
Table 5-1 Summary of the simulator modules.	79
Table 5-2 Antenna arrays geometry parameters.	81
Table 5-3 Signal and channel parameters	82
Table 6-1: Simulation Parameters	91
Table 6-2: Simulation parameters	99
Table 7-1: Frequency bands and associated equipment	102
Table 7-2: Measured material samples and their thickness	104
Table 7-3: Measurement Uncertainties [MMK21]	107

List of Acronyms, Abbreviations and Mathematical Notations

Term	Description
III-V	Compound semiconductor combining element group three and five
3D	3 Dimensional
3GPP	3rd Generation Partnership Project
5G	5th Generation mobile communication
5G-PPP	5G Public Private Partnership
6G	6th Generation mobile communication
ABB	Analog BaseBand
ACLR	Adjacent Channel Leakage Power
AD	Analogue to Digital
ADC	Analogue to Digital Converter
AGC	Automatic Gain Control
AiP	Antenna in Package
AP	Access Point
ARoF	Analog Radio over Fibre
AWGN	Additive White Gaussian Noise
B5G	Beyond 5G
BB	BaseBand
BER	Bit Error Rate
BiCMOS	Bipolar CMOS
BLER	BLock Error Rate
BW	BandWidth
CCDF	Complementary Cumulative Density Function
ceCPM	constrained envelope CPM
CMOS	Complementary Metal Oxide Semiconductor
CPE	Common Phase Error
CP-OFDM	Cyclic Prefix OFDM
CPM	Continuous Phase Modulation
CPU	Central Processing Unit
CSI	Channel State Information
CU	Centralized Unit
D-MIMO	Distributed MIMO
DAC	Digital to Analogue Converter
DFT	Discrete Fourier Transformation
DFTS-OFDM	DFT Spread OFDM

DL	DownLink
DSP	Digital Signal Processing
DU	Distributed Unit
EC	European Commission
EIRP	Effective Isotropic Radiated Power
EM	Electro Magnetic
EU	European Union
EVM	Error Vector Magnitude
F	Noise Factor
FER	Frame Error Rate
FOM	Figure Of Merit
FR1	Frequency Range 1
FR2	Frequency Range 2
FTN	Faster Than Nyquist
GaAs	Gallium Arsenide
GaN	Gallium Nitride
Gbps	Giga bits per second
Gsps	Giga symbol per second
H2020	Horizon 2020
HIB	Hardware in Between
HPA	High power amplifier
HW	HardWare
IAB	Integrated Access and Backhaul
IC	Integrated Circuit
ICI	Inter-Carrier Interference
IF	Intermediate Frequency
InP	Indium Phosphide
IRR	Image Rejection Ratio
ISI	Inter Symbol Interference
IQ	In-phase and Quadrature
JT-CoMP	Joint Transmission Coordinated Multi-Point
KPI	Key Performance Indicator
KVI	Key Value Indicator
LMMSE	Linear Minimum Mean Squared Error
LNA	Low Noise Amplifier
LO	Local Oscillator
LOS	Line Of Sight
LTE	Long Term Evolution

MAC	Medium Access Control
MBS	Macro Base Stations
MCL	Maximum Coupling Loss
MIMO	Multiple Input Multiple Output
MMSE	Minimum Mean Square Error
MMSE-PIC	Minimum Mean-Square-Error Parallel Interference Cancellation
mmW	Millimetre-wave
NF	Noise Figure
NLOS	Non Line Of Sight
NR	New Radio
OBO	Output Back Off
OFDM	Orthogonal Frequency Division Multiplexing
OFDMA	Orthogonal Frequency Division Multiple Access
OTA	Over The Air
PA	Power Amplifier
PAPR	Peak to Average Power Ratio
PLL	Phase Locked Loop
PN	Phase Noise
PT-RS	Phase Tracking Reference Signal
QAM	Quadrature Amplitude Modulation
RAN	Radio Access Network
RF	Radio Frequency
RFIC	Radio Frequency Integrated Circuit
RIS	Reconfigurable Intelligent Surfaces
RMCL	Relative Maximum Coupling Loss
RMS	Root Mean Square
RRC	Root Raised Cosine
RSSD	Reduced State Sequence Detection
Rx	Receiver
RX	Reception
SC-FDE	Single-Carrier Frequency Domain Equalization
SC-FDMA	Single-Carrier Frequency Division Multiple Access
SE	Spectral Efficiency
SiGe	Silicon germanium
SINR	Signal-to-Interference and Noise-Ratio
SISO	Single Input Single Output
SNDR	Signal-to-Noise and Distortion-Ratio
SNR	Signal-to-Noise Ratio

SotA	State of the Art
TDD	Time Division Duplex
Tx	Transmitter
TX	Transmission
UE	User Equipment
UL	UpLink
VCO	Voltage Controlled Oscillator
WDM	Wavelength Division Multiplex
WP	Work Package
w.r.t	with respect to
ZF	Zero Forcing
ZXM	Zero-crossing Modulation

Symbol	Description	Section or equation
$(\cdot)^H$	conjugate transpose operation	6
$\delta(\cdot)$	delta function	(7-6)
τ	propagation delay	(7-6)
Ω	angle (of arrival)	(7-6)
α	steering angle of a beam	(7-7)
$G(\Omega)$	antenna/beam gain to angle Ω	(7-7)
ψ	phase of complex channel coefficient	(7-8)
f	frequency	(7-9)
$\overline{(\cdot)}$	complex conjugate operation	(7-9)

1 Introduction

Hexa-X is one of the 5G-PPP projects under the EU Horizon 2020 framework. It is a flagship project that develops a Beyond 5G (B5G)/6G vision and an intelligent fabric of technology enablers connecting human, physical and digital worlds.

This document is the second deliverable of Work Package 2 (WP2) - “Novel radio access technologies towards 6G”. The work in WP2 focuses on physical layer and Radio Frequency (RF) implementation aspects for future mobile communication systems. The research focuses on the following key aspects:

- Radio enablers and technology roadmap
- Radio and antenna implementation aspects, hardware component models and architecture
- Hardware-aware waveform and modulation design
- Hardware-aware beamforming design
- Distributed large multiple input multiple output (MIMO) systems for beyond 5G/6G
- Channel measurement and modelling for beyond 100 GHz

1.1 Objective of the document

The main target of this deliverable is to deepen the insights on radio modelling, beam forming, distributed MIMO (D-MIMO) and channel propagation from the first project deliverable D2.1 namely “Towards Tbps Communications in 6G: Use Cases and Gap Analysis” [HEX21-D21]. The wireless technologies which are studied are operating at the frequency range of 100 to 300 GHz which is one of the first options for the 6G extreme data rate communications.

This report provides new insights on the upcoming 6G radio implementations by providing initial simulation models and frameworks which will be utilized during the Hexa-X project. The development on the Hexa-X project will use and further refine the initial system level evaluations and analyses, simulation methods and models described in the deliverable to the next project deliverables.

1.2 Structure of the document

A short summary of the main radio requirements from the Hexa-X project documents is presented in the section 2. Those requirements are based on Key Performance Indicators (KPIs) and Key Value Indicators (KVIs), which have been introduced in the project documents D1.1 [HEX21-D11] and D1.2 [HEX21-D12] and those have been evaluated from a WP2 perspective in the document D2.1 [HEX21-D21]. As part of the ongoing work within Hexa-X, note that harmonization and alignment of the initial use cases and KPIs/KVIs of D1.1 and D1.2 with findings from technical work packages will be performed in WP1 and the outcome will be disseminated in D1.3, but the document D1.3 will be published later than this deliverable.

The main content of this document concentrates on radio system level, beam forming, D-MIMO and channel models, which are the first outputs of the modelling aspects of the project. The presented models are the first outputs, which will be further developed at a later phase of the project based on new simulations and measurement results towards the deliverable D2.3 called “Radio models and enabling techniques towards ultra-high data rate links and capacity in 6G”. The D2.4 will be the final deliverable of WP2 and it will concentrate on future technology outlook and technology roadmap views towards the first 6G implementations. More details on the next steps towards D2.3 based on the current work is presented in the last chapter.

2 Main requirements for the 6G radio system studies

Frequency band definitions and terminology which are used in this document are presented in Table 2-1. The Hexa-X encourages everyone to define the targeted frequency range in terms of the physical properties of either the wavelength or frequency for propagation in vacuum.

Table 2-1: Definition of frequency bands in the context of Hexa-X WP2 [HEX21-D21].

Term	Frequency band
mmW	30 – 300 GHz
lower mmW	30 – 100 GHz
upper mmW	100 – 300 GHz
THz	300 GHz – 3 THz

In 5G New Radio (NR), current 3rd Generation Partnership Project (3GPP) core specification supports operation up to 52.6 GHz and the first step towards the extension of operating spectrum beyond 52.6 GHz is under development for 3GPP Release 17, with finalization in September 2022 [HEX21-D12].

As an initial effort to enable and optimize 3GPP NR system for operating in spectrum above 52.6 GHz, 3GPP radio access network (RAN) has studied requirements for NR beyond 52.6 GHz up to 114.25 GHz in various potential use cases spanning over several deployment scenarios. As part of the 3GPP Release 17, spectrum support will be extended to up to 71 GHz [38.808], as frequencies between 52.6 GHz and 71 GHz are especially interesting in the short term because of their proximity to sub-52.6 GHz for which the current NR system is optimized and the imminent commercial opportunities [HEX21-D12].

A total bandwidth of 21.2 GHz of spectrum has been made available for use by unlicensed devices in four frequency bands (i.e., 116-123 GHz, 174.8-182 GHz, 185-190 GHz, and 244-246 GHz) with suitable propagation characteristics that would allow large unlicensed use, while limiting the potential for interference to existing governmental and scientific operations in the above-95 GHz bands, such as space research and atmospheric sensing [HEX21-D12].

Currently, spectrum allocations generally stop at 275 GHz worldwide, however frequency bands have been identified in the range 275-450 GHz for the implementation of land mobile and fixed service applications and for radio astronomy and Earth exploration-satellite service and for space research service in the range 275-1,000 GHz [HEX21-D12].

Based on the use case information and technical system capabilities presented in [HEX21-D12] and [HEX21-D21], initial technical requirements for 6G radio systems have been derived and those are presented in Table 2-2. The requirement targets fare or a non-fixed backhaul application, since fixed backhauled may require significantly longer link ranges.

Table 2-2: Initial radio requirements for the 6G extreme data rate radios [HEX21-D21].

Parameter	Initial release of 6G radio	Long-term vision for 6G radio
Data rate	100 giga bits per second (Gbps)	1 Tbps
Operational/carrier frequency (fc)	100 – 200 GHz	Up to 300 GHz
Radio link range	100 – 200 meters	10 – 100 meters
Duplex method	Time Division Duplexing (TDD)	TDD
Initial device class targets	Device to infrastructure, mobile backhaul/fronthaul	Infrastructure backhaul/front haul, local fixed links, and interfaces (data centres, robots, sensors, etc.)

3 RF system level analyses and simulations of initial 6G radio

RF system level analyses and modelling requires an initial 6G radio architecture defined for such purpose. The 6G RF architecture and preliminary implementation feasibility studies are presented in the following sub-sections. First general 6G RF architecture is discussed, and then different RF modelling levels are addressed. Analog to digital converter (ADC) analysis is given to indicate how feasible is to implement the 6G radio with currently available industrial converters. After the ADC analysis, multiple RF block level models are presented which can be used for RF system and waveform level simulations. Additionally, effects of multiple radio frequency integrated circuit (RFIC) processes to the noise figure (NF) of low noise amplifier (LNA) at upper millimeter wave (mmW) frequency band is analysed.

3.1 Initial 6G radio architecture for simulation purposes

A simplified RF block diagram of radio transceiver with one transmitter (Tx) and receiver (Rx) signal path is shown in Figure 3-1. This kind of one RF signal path transceivers are used in the current 4G radios and 5G frequency range 1 (FR1) implementations. The 5G frequency range 2 (FR2) devices which are supporting lower mmW frequencies from 24.2 up to 48.2 GHz [38.104] uses Tx and Rx array implementations to combat increased path loss compared with FR1 radios and to enable electrical beam steering with RF signal phase control. The Tx and Rx array combines multiple RF signals into a single common signal path, which is connected to analog-digital converters. The higher mmW frequency 6G transceivers will combine learnings from previous generation radios. The parallelism in the 6G Rx and Tx will most probably increase compared to lower mmW frequency counterparts. This is due to the limited Tx power of individual power amplifier at high mmW band and parallelism with focusing functionality (electrical beam steering and / or focusing antennas) will enhance effective isotropic radiated power (EIRP) and thus coverage of the 6G system [RKL+20]. A single RF path direct conversion RF architecture with in-phase and quadrature (IQ) modulator and demodulator is presented in Figure 3-1 for simplicity purposes. Two alternative frequency synthesis approaches are shown in the block diagram: a final operational frequency voltage controlled oscillator (VCO) or a lower frequency VCO with a frequency multiplication. Only one analog to digital (AD) and digital to analog (DA) converter is shown in the block diagram. The TRX function block refers a RF switch, which can connect receiver or transmitter to the antenna.

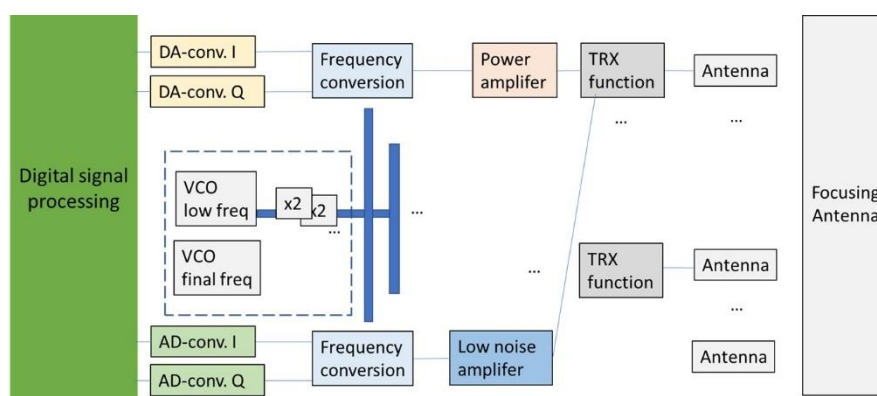


Figure 3-1: Potential one frequency conversion 6G transceiver architecture [HEX21-D21].

3.2 Simulation and modelling framework for RF impairments

3.2.1 Link level impacts of different RF impairments

A generic principle of a link error vector magnitude (EVM) behaviour as a function of Rx input power is presented in Figure 3-2. The RX EVM is measured at the analog output of the receiver. Similar analysis can be converted even to a cell size estimation as done in [LJT+19]. The curve can be divided into multiple different regions that usually have few dominant RF nonidealities [LTJ+19], [LJT+19], [TTP17]. In the low signal to noise (SNR) region, the receiver performance is inevitably noise limited, while in the higher powers the performance is limited by the nonlinearity. The desired link operation region is in the middle where EVM is minimum. The automatic gain control (AGC) aims usually to enable the transceiver to operate in the region where the EVM is at the minimum. In this region, the limiting RF nonidealities are phase noise, quantization, and IQ-imbalance. The generic link performance and behaviour in Figure 3-2 depends highly on the assumptions, for example, the waveform and modulation selection, in addition to the actual RF models. While these selections are under research within the project, it is inevitable that we need to consider many different levels of modelling to gain realistic results from the system level simulations.

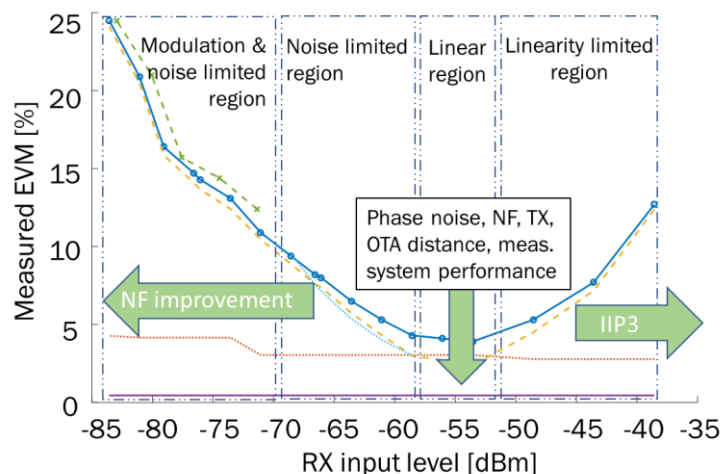


Figure 3-2: An example how RF parameters such as noise figure (NF), transmission power (TX), over the air (OTA) distance affect receiver EVM performance [PLT21].

3.2.2 Abstractions for modelling RF impairments for 6G Radio

Different research problems have very different modelling requirements when it comes to RF impairment modelling. In this section, the RF modelling framework is divided to three abstraction levels that can be used to simplify the models for different research problems. These modelling principles can be considered for each key building block of the RF transceiver. To estimate the realistic performance, it is important to include all dominant RF nonidealities to the system. The overall link level transceiver model may be a mixture of all three types of models. For example, power amplifier (PA) and phase noise can be modelled in more details, while the impacts of quantization and rest of the RF nonidealities are modelled as a static EVM/SNR performance. Such modelling principles helps to evaluate realistic performance results. In addition, more accurate models can be used to generate the lower-level models. The aforementioned three abstraction levels and their impacts to studied figures of merits (FOMs) are summarized in Table 3-1.

The first level of abstraction is based on simple power and noise calculations mainly used for initial link level range and coverage analysis. The same signal power analysis method is used for RF system analysis for different RF blocks, e.g., cascaded TX and RX signal power and noise level analyses and as example output signal level with noise is

$$P_{out}(dB) = P_s (dB) + P_n(dB), \quad (3-1)$$

where P_{out} is the total output power, P_s is the signal power and P_n is the noise power.

The level 1 models are mostly used in the link budget to evaluate system level performance and potential link ranges, specify the key building blocks, and detect the dominant sources of nonideality. Level 1 models mostly deal with power levels and SNRs sums with respect to individual SNR contributors together as root mean square (RMS) powers. In order to link the calculations to the system level performance, one must have information about the waveform selections in order to properly map the actual signal powers to the potential signal dynamics. Level 1 models for 5G system evaluations are used in [TTP17][LJT+19]. Note that in [LJT+19], the approach is validated by measurements. The approach can be expanded to MIMO scenarios if done in beam-basis as in [TTP17].

A second abstraction layer, which is named level 2, where the RF impairments are modelled as additive nonidealities, but the signal model is a complex valued signal instead of just signal power as in level 1 models. Level 2 models are tailored especially for simulations that require numerous realizations to estimate statistical performance which is not possible with more complicated models with reasonable simulation time. The general level 2 signal model for non-linear RF signals

$$y[n] = hx[n] + z[n] + v[n], \quad (3-2)$$

where the $y[n]$ is the output signal, $x[n]$ is the input signal, $v[n]$ is the noise signal and $z[n]$ is the signal component due to non-linearity of the respective RF block.

Level 3 models deal with signal samples using a specific waveform. They are especially tailored for simulating a waveform performance under nonideal RF, for example in presence of nonlinear PA or LO phase noise. The models can be extracted from measurements or circuit simulations. The models are mostly memory dependent, and the simulations require sometimes long signals to estimate a realistic performance as the results may vary over time. This approach can be used for example to simulate phase noise. Level 3 models can be also used to study compensation techniques of the RF nonidealities. A general signal model of the level 3 simulations is

$$y[n] = f(x[n]) + v[n], \quad (3-3)$$

where the $f()$ is a non-linear function applied to the input signal.

Table 3-1: Comparison of simulation abstraction levels.

Abstraction level	1	2	3
Typical signal model	$P_{out}(dB) = P_s (dB) + P_n(dB)$	$y[n] = hx[n] + z[n] + v[n]$	$y[n] = f(x[n]) + v[n]$
Typical FOMs	power, link range, SNR, coverage	Capacity, bit error rate (BER), block error rate (BLER), outage probability	EVM, Adjacent Channel Leakage Power (ACLR), SNR, Robustness against RF nonidealities (e.g. fading, phase noise, nonlinearity), Ambiguity function
Typical research problems	Link budget, component specifications, chain power and SNR calculations, chain nonlinearity analysis	Beamforming techniques, Algorithms, statistical simulations, Monte-Carlo simulations, equalization	Waveform design, link performance analysis, compensation of RF nonidealities, equalization
Special note	Impact of nonlinearities on EVM/SNR, power dependent EVM/SNR models	Nonidealities abstracted to the effective channel model, signal and nonidealities separated, nonidealities additive.	Nonidealities modeled with behavioral models from sample to sample.

Simulation time/count	Fast, Reference cases	Slow, Large number of realizations	Moderate, Depends on research problem
-----------------------	-----------------------	------------------------------------	---------------------------------------

When composing a complete link level simulation model, one can combine models from multiple abstraction layers together, or use more complex models to generate the higher-level models. In addition, the model validation can use the same principle such that some parts of the link are replaced by real or emulated hardware. Such arrangements are called as hardware in between (HIB) tests and demonstrations. The possible transitions between the modelling approaches, including the validation with the real or emulated hardware is illustrated in Figure 3-3. Physical models in the figure may also refer to circuit simulations, electro-magnetic (EM)-simulations, look-up-tables (LUTs), etc. These models can be generated with very different signal model in RF circuit simulators or using standard measurement equipment such as network analysers.

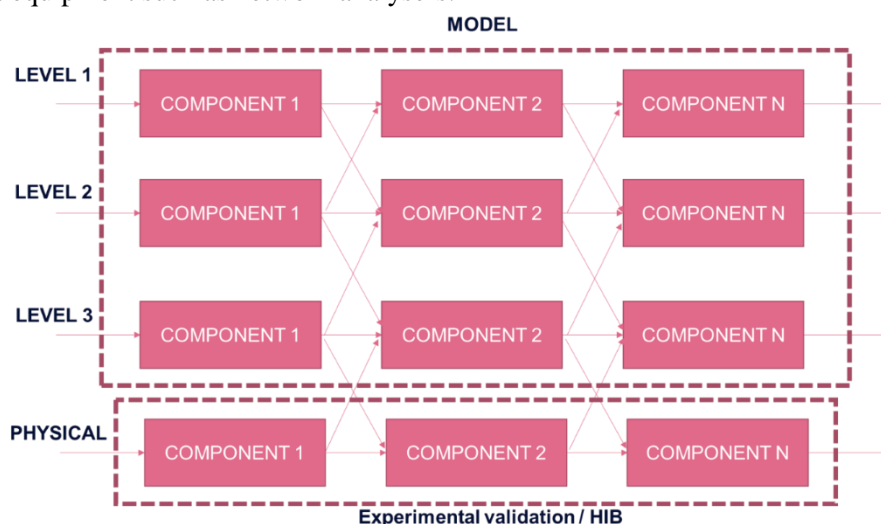


Figure 3-3: Different component simulation models can be mixed on a need basis to answer the research question.

3.3 RF system calculations of the RF reference architecture

A generic RF block diagram of the 6G transceiver is shown in Figure 3-1. The first wave of 6G radios are expected to support 100 Gbps data rate, and some selected of RF system level analysis for such receiver is presented in following sub-sections.

3.3.1 High performance analog to digital converter analysis and modelling

One of the most demanding component implementation of the envisaged 6G receiver is a low current consumption and high performance ADC. The operational bandwidth (BW) of the ADC limits the signal BW, which can be supported by the corresponding baseband (BB) receiver chain. Industrial state of the art (SotA) high performance ADCs are marked with brown and green dots in the Figure 3-4. The Nyquist frequencies of those are spanning from 1 GHz to 10 GHz enabling such baseband signal bandwidths. However, oversampling of the RX signal is required in ADC to avoid aliasing and signal regrowth problems due to non-linearities of the receiver components. The needed amount of oversampling in 6G receivers is not known at the time of the writing, while one may expect e.g., 4 times oversampling in the ADC, which limits the usable BW of the ADC.

A trendline model for present of SotA of published academic ADCs is shown in Figure 3-4 with a purple solid line. The power consumption trendline model for the academic SotA ADCs is shown with the y2 line equation. The SotA of the industrial ADCs is shown in the red solid line in Figure 3-4 and the regression line is presented with the y3 line equation. There is a significant difference between the academic and industrial ADCs in the current consumption estimates and the difference is 2.5 decades

based on the analysis below. The academic ADCs are typically reporting the current and power consumption of the converter block, only, while the industrial ADCs report a complete component current and power consumption including, e.g., clocking circuits and output driving stages.

The maximum achievable signal to noise distortion range (SNDR) for both academic and industrial ADCs follows the same model, which is shown in Figure 3-4 with the $y1$ line equation.

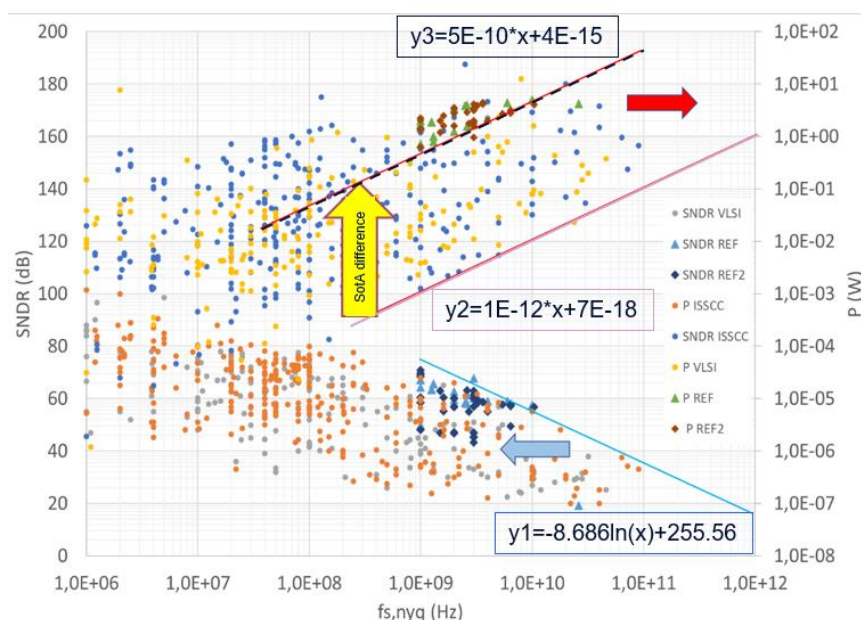


Figure 3-4: SNDR and power consumption of ADCs as a function of bandwidth based on data from [MUR21] and commercial data sheets.

3.3.2 Illustrative system level calculation for 100 Gbps RF architecture

A single signal path receiver analysis of the 6G RF architecture presented in Figure 3-1 considering ADC requirements such as clocking rate, number of bits and power consumption estimate is summarized in Table 3-2.

The analysis is performed based on the 6G radio requirements mentioned in Table 2-1, and based on those, input values at rows which are marked with a ***bold italic*** font at name column are placed to the analysis table. Other values in the analysis table are calculated based on input values.

The analysis starts from the user throughput data rate which targets 100 Gbps for the first wave 6G devices. In order to guarantee the user data rate, some coding is needed, and in this analysis, a 5/6 coding rate is used (on the row B) and the total data rate is shown at the row C. A 4 bits/symbol modulation order is used in the analysis, which refers to 16 quadrature amplitude modulation (16-QAM) modulation and symbol rate of the link is calculated in the row E. The selection of the modulation order is a trade-off of multiple factors, e.g., availability of the RF spectrum, linearity and power consumption of the Rx, Tx, PA. The air-interface signal needs to be band limited and most common method is to use raised root cosine (RRC) filter to cope with this limitation. A roll-off factor alpha of 0.25 is used in the analysis, as shown at the row F, and the total pulse shaped RF bandwidth is shown in the row G.

The number of base band streams in the row H is the same than number of RF channels over the air (OTA) which can be separated by polarization, RF channel frequency or used RF band. The final frequency of the RX down-conversion depends at least on the available ADC conversion bandwidth, digital signal processor (DSP), e.g., effectiveness of channel rejection and DC-removal, supported BB

signal bandwidth and width of the signal lanes. A direct down-conversion is studied in the analysis (marked in the row L) and the analog baseband (ABB) signal's bandwidth is calculated in the row M.

Table 3-2: Receiver ADC analysis for 6G receiver to support 100 Gbps.

Row	Parameter	Value	Unit
A	User datarate	100	Gbps
B	Coding rate of user data (5/6 coding=0.8333)	0.833	
C	Total data rate for radio link	120	Gbps
D	Modulation order (bits/symbol)	4	bits/symbol
E	Symbol rate (or raw RF BW)	30	Gsps
F	Roll-off value of pulse shaping filter (alpha)	0.25	
G	Pulse shaped RF BW (1+alpha)*RF BW	37.5	GHz
H	Number of BB (I/Q) streams	9	
I	Number of BB ADCs (I and Q own conv.)	18	
J	RF bandwidth for each BB stream	4.166	GHz
K	BB BW for each I and Q BB stream	2.083	GHz
L	BB center freq. (0 Hz = DiCo)	0	GHz
M	Total BB BW (BB center + BB BW)	2.083	GHz
N	Oversampling ratio of ADC	4	
O	ADC clocking frequency	8.333	GHz
P	ADC Nyquist frequency	4.166	GHz
Q	SNR required for modulation order	17.50	dB
R	Quantization level compared to SNR requirement	-6.0	dB
S	Crest factor of the modulation	2.6	dB
T	SNR requirement for ADC from modulation	26.1	dB
U	Req. For ADC effective number of bits for SNR	4.04	bits
W	Fading/AGC/DC-leakage accuracy implementation margin	1	bits
X	Total ADC bit requirement	5.04	bits
Y	ADC SNR requirement	32.12	dB
Z	Walden's figure of merit (FOM) for ADC, literature state-of-art	16.667	fJ/conv. step
AA	Power dissipation of ADC, literature state-of-art	4.58	mW
AB	Total power of SotA ADCs	41.22	mW
AC	Industrial ADC est. (2.5-decade power dissipation shift)	2290	mW
AD	Total industrial ADCs power consumption	41216	mW
		41.2	W
AE	Implementable ADC SNR based on trend line of analysis	57.6	dB
AF	Number of RF channels, dual polarization channels	5	
AG	Number of RF channels, linear polarization channels	9	

An oversampling ratio of four is given as an input parameter (shown in the row N), and then ADC clocking frequency of 8.333 GHz is calculated (in the row O) for nine IQ-base band streams with 18 ADC converters to support 100 Gbps user data rate. The SNR value of 17.50 dB is used for the 16-QAM [RKL+20] and given as input in the row Q. A quantization margin over the modulation SNR is shown in the row R on Table 3-2, which can be adjusted based on the used DSP algorithms. A crest factor of 2.6 dB is used for 16-QAM (row S) and the total SNR requirement for the modulation in the ADC is calculated by combing information from rows Q, R and S.

In the modern telecommunication systems like 3G, 4G and 5G, a fading margin is reserved for the ADC operation at mobile and base station ends of the wireless links. Only one bit, as shown in the row W, is reserved for the fading margin for the 6G over the previous generations due to smaller scattering environment, which is studied more in details in the section 7.2 of this document. The total SNR

requirement for ADC combines modulation SNR and fading margin in the row Y. The total SNR is converted to the corresponding requirement for the number of ADC bits in the row X. The total SNR requirement of the ADC (row Y) can be compared to implementation ADC trendline in the row AE and conclusion is that required ADC performance can be implemented with present day technology.

The power consumption of the ADC, which is based on the number of bits and the sampling frequency, can be estimated using the trendlines presented in Figure 3-4, which is presented more in details in Figure 3-5. The requirements of ADCs of nine IQ-data streams is highlighted with a red box. It can be seen from the figure that nine IQ-data stream requirement to support 100 Gbps can be implemented with currently available high performance ADC technology. The requirement is just on the industrial SotA trendline and in coming years power consumption will be scaled towards academic SotA trendline. This technology improvement is needed that 100 Gbps performance can be implemented in mobile 6G devices.

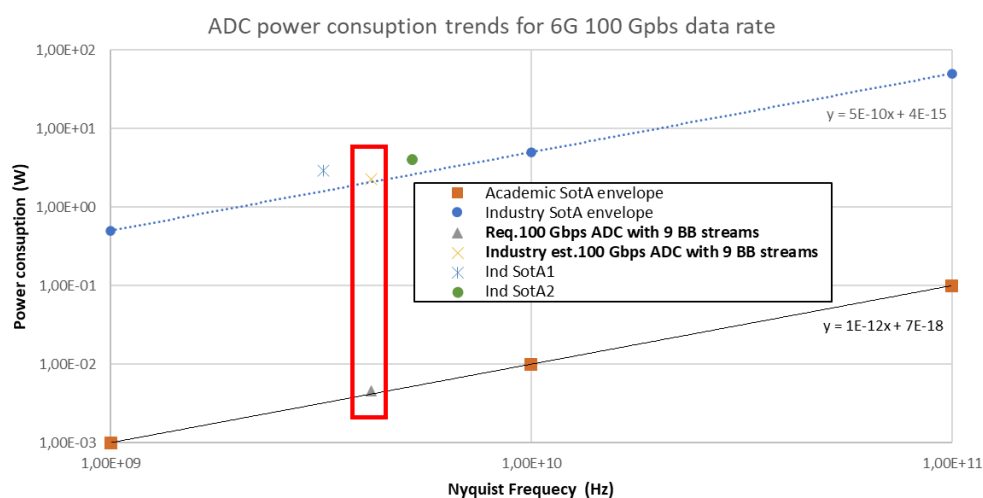


Figure 3-5: Analysis of number of needed ADCs and their power consumption a 6G receiver to support 100 Gbps.

3.4 Initial RF models and simulation examples

In this section, we briefly describe the initial RF impairment models used in level 3 simulations. One should note that at this stage, the models are initial, and not yet parametrized nor verified by measurements using 6G compliant hardware. This section briefly describes the behavioural component models with illustrative simulations by using a single carrier (SC) with existing QAM modulation as the waveform to be evaluated the functionality of the simulator. A summary of RF non-idealities which can be incorporated to different simulation purposes is shown in Table 3-3.

Table 3-3: Dominant RF impairments for different kind of research problems

	Waveform design	RF beamforming	Digital beamforming	Link budget / system calculations
Quantization (ADC / digital to analog converter (DAC))	Quantization impact, signal dynamics & number of bits	Limit the achievable SNR/SNDR, impact common for all antennas	Correlation of the quantization between DACs/ADC to be considered	Effective number of bits / impact to SNDR/EVM, power consumption

Filter responses*	Frequency response of analog filters has impact on the RF signal peak to average power ratio (PAPR) if input signal has very low (nearly zero) PAPR.	May have impact if frequency selectivity of the beamforming is modelled. Otherwise not important	Impact of analog filters can be seen in part of effective channel. May have effect if frequency selectivity is modelled	Not important. Can be taken into account as fixed EVM/SNR contributor
Phase noise	Important to model the time evolution/frequency selectivity. Dominance of slow/fast phase variations depends on how the data is distributed over the band. Different waveforms have different means to compensate phase noise	Limit the achievable SNR/SNDR. Impact common for all antennas,	Important to model the correlation of the phase noises between the analog/digital chains. Impact depends on the frequency synthesis architecture / LO distribution	Average impact on EVM/SNR. Requires assumptions waveform and potential compensation techniques to properly map the impact on the SNR.
IQ imbalance	Impact mostly in the static behaviour. Image rejection ratio (IRR) may be frequency selective	Static impact, not important	Not important unless the IQ imbalances are different over the individual signal paths	Average impact on the overall EVM/SNR and IRR requirements
PA nonlinearity	High priority. Impact is waveform dependent. For waveform studies the PA model should be validated for the given waveform, potential signal dynamics, PAPR etc.	Impact important in case the RF beamforming varies also the amplitudes. Important to model antenna/PA path specific impacts	Impact important especially if the individual PAs/arrays have different kind of signals.	Achievable output power and EVM with a certain modulation are the most important
Rx noise figure	In demodulation side, the noise impact is important.	Direct impact on Rx sensitivity	Direct impact on Rx sensitivity	Direct impact on Rx sensitivity / achievable link ranges / system level performance
LNA + mixer nonlinearity	RX Spectrum regrowth at short link ranges	RX desensitization due to nearby interference, null steering	RX desensitization due to nearby interference, null steering	RX blocking signal / interference analysis

*ABB/RF filter responses induces memory effect that has impact on the frequency response

3.4.1 Waveform assumptions, digital transceiver, and signal model

In waveform level models, the input and output signals are discrete-time domain samples specified with a certain sampling rate, F_S . Typically, one uses oversampled signals with 2-4x oversampling to properly

cover both in-band and out-of-band impacts. Additionally, it covers the impacts of the pulse shaping to PAPR of the signal in case of single carrier modulations, that in turn has further impact on the waveform behaviour with nonlinear RF devices. In addition, in PA nonlinearity studies, one should note that oversampling is usually essential to properly model the nonlinear memory effects of the PA.

In general, the behavioural RF impairment models are rarely valid for all possible input signals. Hence, especially the nonlinear models should be validated for different kind of waveforms individually if the waveforms have different characteristics (i.e., different power distribution, different PAPR etc.). On the other hand, for example thermal noise model (noise figure) is not dependent on the waveform as such. The basic signal flow in the waveform level simulations is given in the Figure 3-6. In order to show the basic functionality of the initial RF impairment models, the given simulation results are derived with QAM modulated signals using RRC pulse shaping with roll-off factor of 0.25 and the oversampling factor is set to 4. In the example simulations, the results are mostly expressed by using RMS error vector magnitude. For an EVM calculation, we use a simple ideal digital receiver is used that performs the receiver pulse shaping and down sampling. Because the models are likely memory dependent, time and phase synch, including a simple ideal equalization is also considered before the received symbols can be derived. Two different EVM definitions are used, where the first one is calculated against the reference constellation, while the second one is calculated against the original input symbols. Note that they diverge from each other when the EVM is large. The region where the metrics are the same depends on the used modulation and waveform. Note that the digital blocks will be replaced by the corresponding blocks generating and analysing 6G waveform. The aim of such simulator framework is to analyse the link behaviour with different waveforms, transceiver models, and link conditions. Furthermore, the waveform level simulations can be used to generate lower-level models for more simplified analysis as discussed in the previous sections.

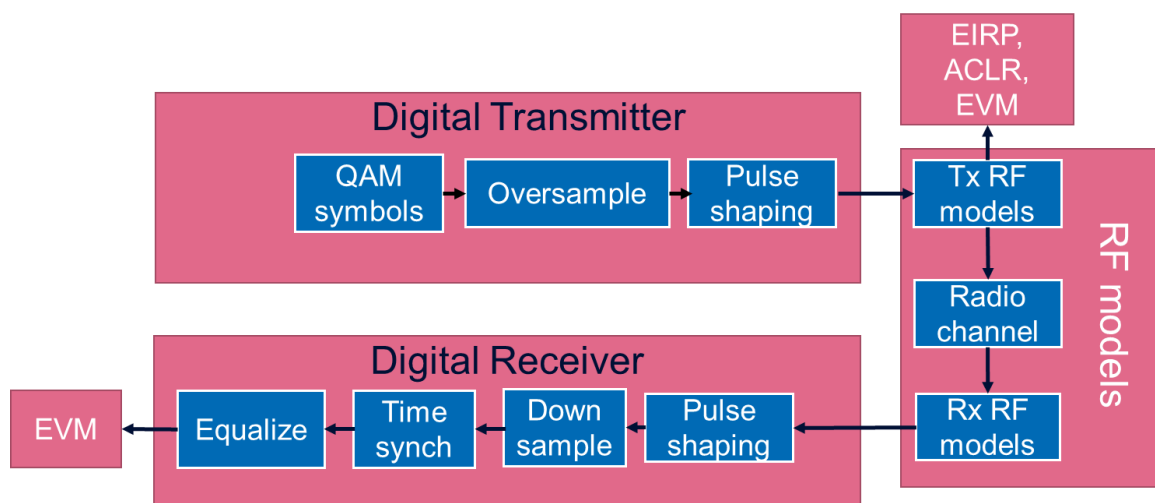


Figure 3-6: Overall signal flow of the whole link with the required reference digital transmitter and receiver. The digital blocks are required to generate and analyse the waveform and can be replaced by different 6G waveform candidates. The digital blocks may also include potential calibration and compensation routines for mitigating different RF impairments.

3.4.2 Reference transceiver and receiver overview

A block diagram of the envisaged RF transmitter phased array model is given in Figure 3-8. Since this is a behavioural model, RF blocks are described based on their functionality. This generally mean that a single block in the model may contain impacts from multiple actual RF blocks. As a reference architecture, we use direct conversion transmitter. The overall transmitter model contains the impacts of DAC quantization, I/Q imbalance, phase noise, analog beamforming, PA nonlinearity, and the antennas. In this stage, the interaction between the PAs and antenna array is not modelled but it may be considered later in the project. Note also that the overall system contains several parallel phased arrays, while only one is described in this phase of the modelling.

Block diagram of the phased array receiver model is described in Figure 3-8. The receiver model consists of antennas, LNAs, analog beamformers (analog amplitude weighting and phase shifting), common path RF response, IQ mixers with phase noise, analog baseband responses with IQ-imbalance, and ADC quantization. LNA model may be linear or nonlinear, depending on the simulation scenario. If the receiver nonlinearity is considered, also the AGC should be properly modelled and distributed over the different receiver blocks. Note that this has not been added yet to the current model but may be considered later in the project.

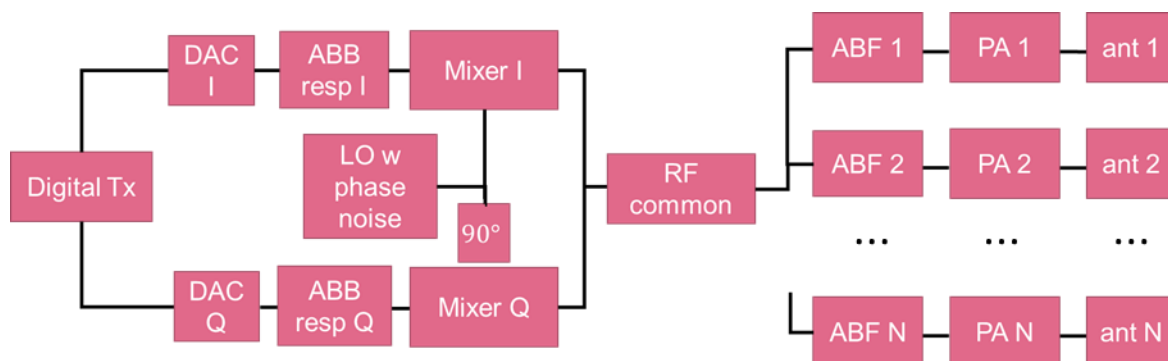


Figure 3-7: Functional RF blocks of a single phased array transmitter.

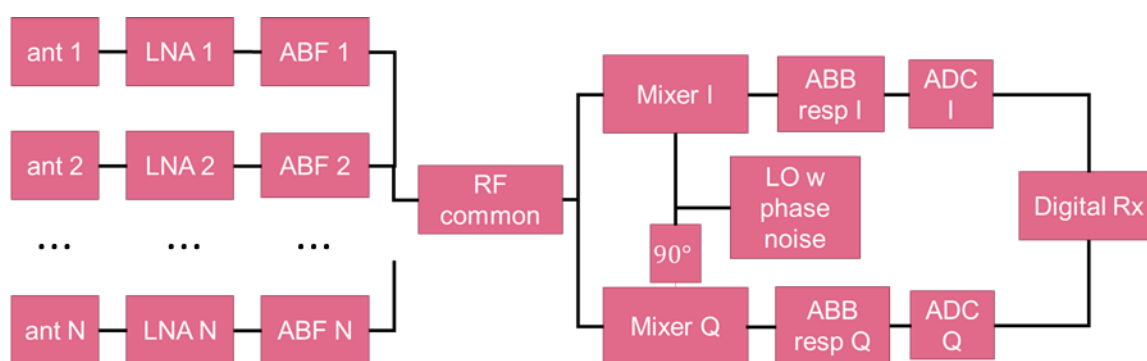


Figure 3-8: Functional RF blocks for a single phased array receiver.

3.5 Modelling energy efficiency/power consumption

The power consumption of large antenna arrays transmitting with relatively large power, can become a key limiting factor in the upper mmW band. A power consumption model, covering the RF frontend of a transceiver, has been derived in [HW21]. The main building blocks of transmitter and receiver are shown in Figure 3-8. Those are similar to RF architecture blocks presented in [HW21], which is based on an integrated solution with RFICs, and related power consumption values taken from [SH+19].

Digital signal processing is subject to further enhancements in RX and TX operations. The power consumption parameters can be set flexibly according to carrier frequency, beamforming architecture and models or data of considered devices.

To compare different architectures, the power consumption model takes into account the numbers of the different building blocks with their individual power consumption, and the scaling according to the architecture. Similarly, the ADC, DAC, analog BB and up/downconverter blocks scale with the number of signal paths or MIMO layers, whereas the number of LNAs, PAs and phase shifters scale with the number of antenna elements. The following Table 3-4 shows the scaling for different architectures, exemplarily based on illustrative device data and models taken from [SH+19].

Table 3-4: Power consumption modelling and scaling for an illustrative system.

Building blocks	Scaling			Power consumption @ 90 GHz (mW) [SH+19]
	Analog BF	Hybrid BF	Digital BF	
TX parts				
PA, active phase shifter, splitter	N	N	N	275
Analog BB and upconverter	1	M	N	500
LO + synthesizer	1	1	1	100
DAC	2	2M	2N	750
Digital signal processing	1	1...M	1...N	n.a.
RX parts				
LNA, active phase shifter, combiner	N	N	N	225
Downconverter and analog BF	1	M	N	500
LO + synthesizer	1	1	1	100
ADC	2	2M	2N	40-200*
Digital RX processing	1	1...M	1...N	n.a.
Max no. MIMO streams	1	M	N	

* Depending on selected model: Walden's FOM envelope or circuit theoretical approach

The numerical power consumption calculation can be summarized in the following

$$\begin{aligned}
 P_{tx} &= N \cdot P_{PA} + k \cdot P_{uc,aBB} + P_{LO,synth} + 2 \cdot k \cdot P_{DAC} + P_{dBB,tx} & \text{analog: } k = 1 \\
 P_{rx} &= N \cdot P_{LNA} + k \cdot P_{dc,aBB} + P_{LO,synth} + 2 \cdot k \cdot P_{ADC} + P_{dBB,rx} & \text{hybrid: } k=M \\
 P_{tot} &= P_{tx} + P_{rx} & \text{digital: } k=N
 \end{aligned}
 \tag{3-4}$$

In the upper mmW band the main impacts expected on power consumption are the reduced PA output power and PA efficiency with increasing carrier frequency, and the power consumption of DAC and ADC scaling with the channel bandwidth (sampling rate) and the number of parallel signal paths. First assessments based on the exemplary device data and models described above show that the components contributing most to the overall power consumption depend on the deployment scenario, signal bandwidth and beamforming architecture.

An exemplary result is shown in Figure 3-9. The impact of increasing frequency on path loss is compensated by increased number of array elements to increase the array gain according to the additional path loss. This leads to increase of the parameter N. The comparison of analog beamforming with one signal path, hybrid architecture with 4 signal paths, and a fully digital architecture with as many signal paths as array elements shows that for a low number of signal paths the power consumption of the transmitter is dominating, while for the digital architecture the receiver dominates, and the overall power consumption increases significantly. With this specific architecture the contribution of the RF frontends is similar, since the number of PAs does not change for the same carrier frequency. But the number of analog baseband and data converter blocks scales with the number of signal paths.

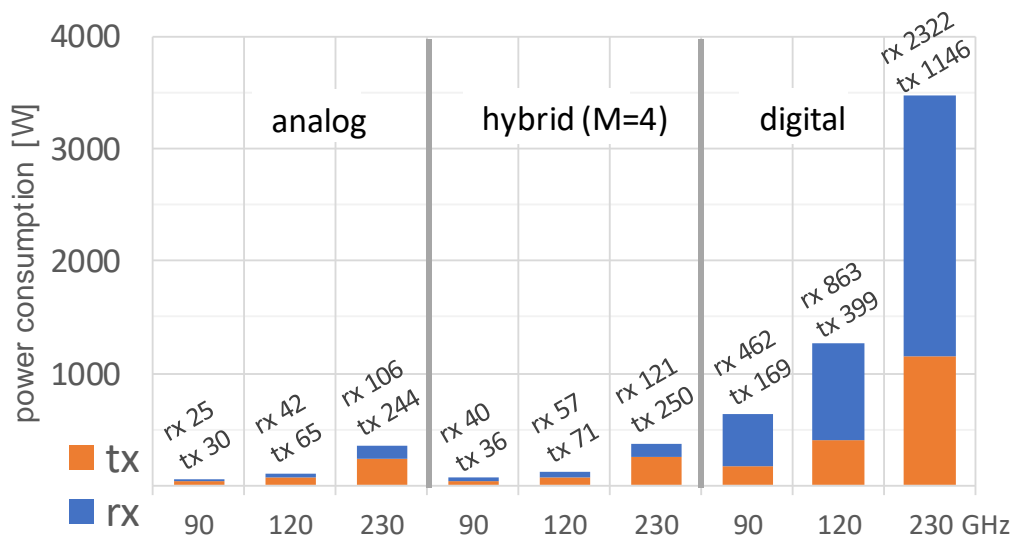


Figure 3-9: Total power consumption of TX and RX part (analog, hybrid and digital architecture, 90 – 230 GHz carrier frequency with 90, 168 and 452 array elements, respectively). Labels indicating power consumption in Watt.

Besides the power consumption the achievable spectral efficiency (SE) is the parameter of major interest since energy saving design should not compromise SE too much. It is important to know how many signal paths can be applied in specific channel conditions to benefit from spatial multiplexing with increasing data rates. This leads towards the analysis of power consumption per transmitted bits, which should be minimized. So, the optimum beamforming architecture depends on the deployment scenario with the related channel conditions. For the related evaluation a system simulation with different architectures, dimensioning of signal paths, and channel conditions is needed.

To enhance the accuracy of the model further, parameters and models derived in Task 2.2 can be included, and architectural variants can be added. Also models for digital processing need to be added for the complete picture. It can be concluded that the increase in number of array elements and PAs according to frequency increase has less impact than the increase in RF chains to the maximum number. A reasonable design therefore should consider (besides the device properties) only to increase the number of RF chains only as far as spatial multiplexing capability is fully exploited. This is depending on the channel properties of the specific deployment scenario.

3.6 Preliminary models for transceiver building blocks

This subsection includes modelling approaches of individual building blocks that require specific attention in the modelling. On the top of that there are parameters that need to be considered in the models. For example, noise of the receiver is not only defined by the LNA and components between antenna and LNA. However, the modelling approach will be similar and the components after LNA can be included in a similar manner. Future work is needed to define more accurate performance estimates for the block level performance in many cases and evaluate them more comprehensively together. At the end of this section, review for current models used in 3GPP standardization are reviewed. Those are adopted in the initial waveform studies in the next chapter. Future work includes refinements for those over a larger frequency range anticipated in 6G systems.

3.6.1 Behavioural ADC/DAC models

As the signal bandwidths are expected to be large in 6G systems, the power consumption of the digital converters becomes rather significant. This generally means that the number of bits have to be lowered

and hence the quantization impacts become severe source of nonideality that cannot be neglected. In phased arrays, converters are shared by multiple parallel antennas.

From behavioural modelling perspective, DAC and ADC have the same functionality, i.e., they add impairments to the signal due to the nonlinearity and quantization effects. This is because in waveform level simulations, the input signal is typically not quantized whereas in real system it is. Hence, the actual DAC model must first quantize the complex-valued input signal with an ADC model before the signal can be reconstructed. For already quantized and oversampled input signal, the DAC model is then eventually a reconstruction filter [OS13], if we neglect the implementation related to such nonidealities of the converters. The reconstruction filter cuts out the sampling harmonics of the input signal. As in the baseband equivalent (or passband) models, the harmonics are not typically modelled, the reconstruction filter is neglected in this phase of the modelling. In principle, it has impact also on the band as its frequency response is not perfectly flat. Hence, its impacts may be considered in the final models. If the input has fixed point representation, it still must be resampled and quantized to match the DAC quantization levels and sampling rate. Due to the above-mentioned reasons, the DAC model is basically equivalent to the ADC model.

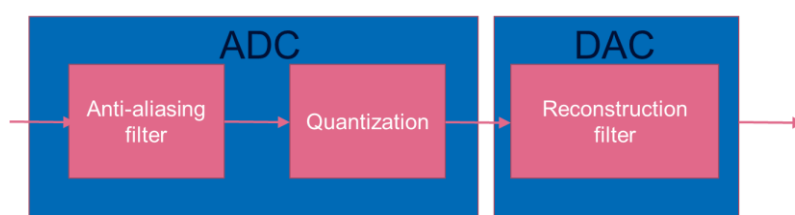


Figure 3-10: DAC modelling principle is similar with the ADC modelling, if the impact of the reconstruction filter is neglected, since DAC model requires first to quantize the input signal for DAC quantization levels.

The baseline for the ADC model is simply to quantize the signal. The basic modelling principles are depicted in Figure 3-11. Before the actual quantization, the signal must be scaled according to the converter's dynamic range. Usually, the scaling is performed by using the instantaneous input signal value. However, it is possible to let ADC also clip the input signal which may be beneficial if the number of bits is small. Another way to model the ADC is to add quantization noise to the signal. This is usually done by approximating the quantization noise as a Gaussian-distributed noise that depends on the ADC resolution. The approach is valid also in practice, but especially if the input signal SNR is high, the quantization noise may have some correlation with respect to the input signal. This may be important to consider in digital beamforming simulations and must be considered.

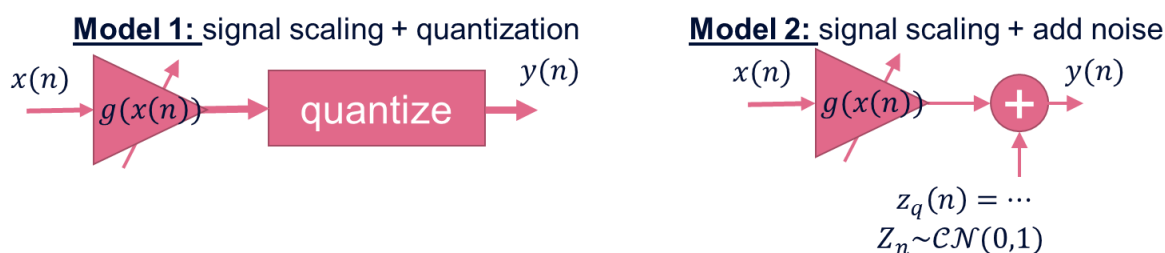


Figure 3-11: Two different generic ADC modelling principles are (1) quantize the signal and (2) add normal-distributed quantization noise. Both approaches may be used in different simulation scenarios, depending on the assumptions.

3.6.2 Power amplifier

PA semiconductor technologies

Power amplifiers (PAs) with high output power are very important for 6G communication with high transmission loss. Figure 3-12 presents the saturated output power versus operating frequency based on

different PA semiconductor technologies, indicating that for now Indium phosphide (InP) is the leading technology for PA working frequency ranges above 100 GHz. The SotA InP PAs can reach 30 dBm in the frequency range of 200 GHz to 230 GHz.

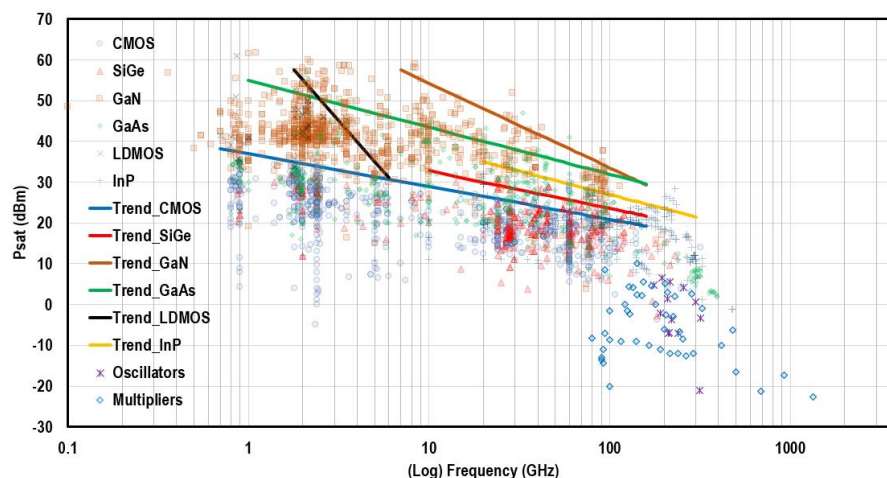


Figure 3-12: PA saturated output power versus frequency [WHM+21].

Baseband memory polynomial PA model

Both nonlinearities and memory effects are very important in PA modelling, since the signal bandwidth for 6G communication will be comparable to the inherent bandwidth of PAs. The baseband memory polynomial model based on measured data in the discrete-time domain is widely used to describe nonlinear effects of PA with memory effects. The general form of model can be written as [SDG+09]:

$$V_{out}(s) = \sum_{q=1}^Q \sum_{k=1}^K \tilde{a}_{kq} V_{in}(s - q) |V_{in}(s - q)|^{2(k-1)} \quad (3-5)$$

where s is the number of samples, k is the polynomial order and q is the memory interval. $V_{in}(s)$ and $V_{out}(s)$ are the measured discrete input and output complex envelope signals of the s^{th} sample respectively. Q and K are the maximum memory and polynomial orders respectively. The complex polynomial coefficients \tilde{a}_{kq} can be extracted by using the least-squares error method. With polynomial coefficients based on different technologies and parameters, we can estimate the output signal from the input signal as depicted in Figure 3-13.

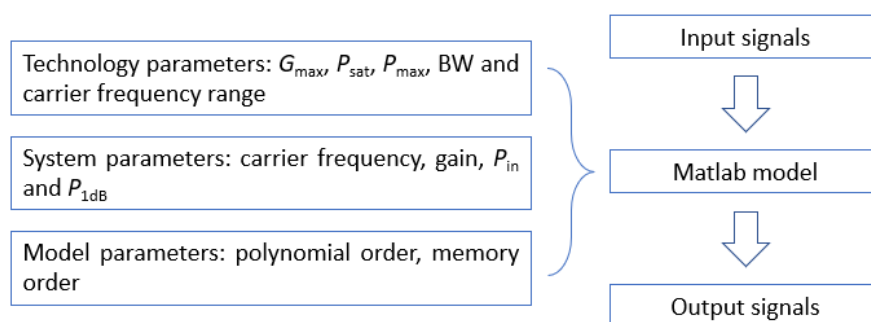


Figure 3-13: Structure for PA modelling.

Demo for PA modelling

To illustrate the baseband memory polynomial PA modelling approach, a Gallium nitride (GaN) PA (Cree CGH40006-TB) from Chalmers RF WebLab is used for demonstration. The input signal is a

bursty OFDM-like signal with 40 MHz bandwidth and a carrier frequency of 2.14 GHz. Figure 3-14 shows the input and output signals to the PA in frequency domain and time domain.

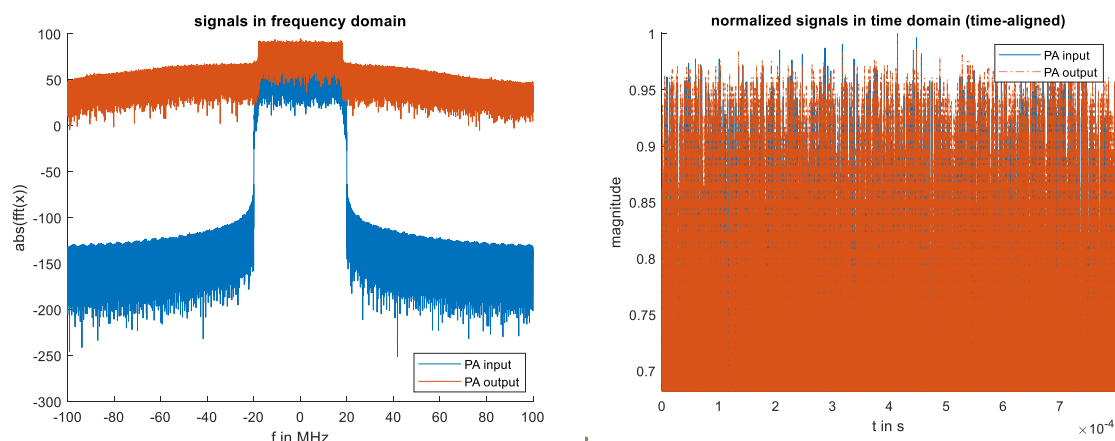


Figure 3-14: Input and output signals to the GaN PA in frequency domain (left) and time domain (right).

The measured and modelled amplitude-dependent amplitude distortion (AM-AM) and amplitude-dependent phase distortion (AM-PM) characteristics are shown in Figure 3-15. The modelled data without memory effects are also included for comparison. A more accurate modelling can be obtained when considering memory effects and similar PA modelling can be done for 6G when appropriate data is available.

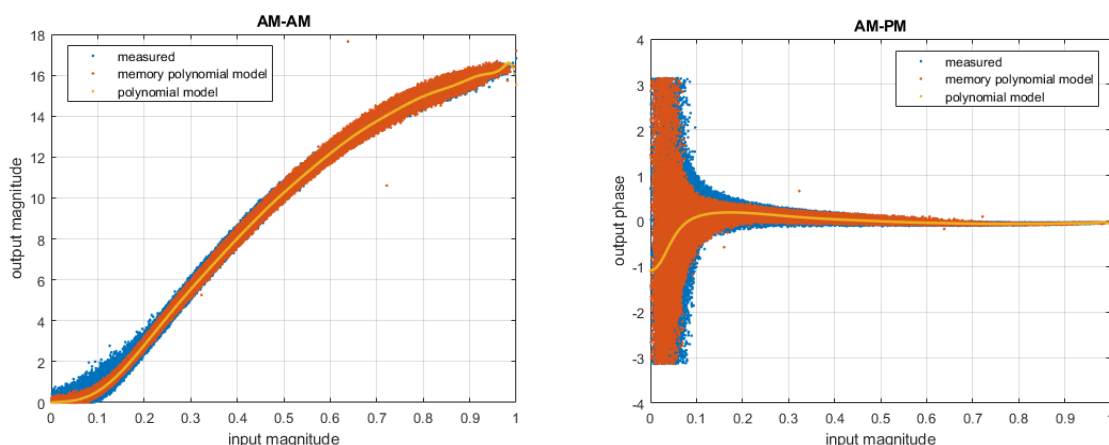


Figure 3-15: Measured and modelled AM-AM (left) and AM-PM (right) results of the GaN.

3.6.3 Noise figure model of analog Rx front-end

The analog front-end of a receiver, namely the LNA and the passive components before the LNA, contributes directly to the total noise figure (NF) of the receiver. A noise figure contribution from components after the LNA is downscaled by the power gain of the LNA. This initial modelling effort focuses on the analog front-end part. In microwave frequency range, it is the NF of the LNA that dominates. As frequency increases, the insertion loss of the passives (e.g., routing, filter, switch) increases progressively until their contribution is no longer negligible, especially in case when the operational frequency is above 100 GHz. RF block diagrams for array transmitter and receiver are shown in Figure 3-7 and Figure 3-8, here called Antenna Array Systems (AASs). The integration analysis of AAS is performed with an antenna in package (AiP) approach where RFICs and their associated interconnect are inherently embedded/formed in the package. The AiP reduces considerably the loss of interconnect from and to the die and the RF routing loss when it is compared to conventional

PCB-based implementation. More importantly, the AiP offers the possibility to overcome the stringent space limitation and meet the challenging multi-technology integration requirement of the analog front-end for the AAS.

3.6.3.1 LNA noise figure

The antenna element (AE) pitch is 1.5 mm ($\lambda/2$) at 100 GHz in the AAS. Assuming that each RFIC supports 16 AEs, the area available for a transceiver integrated circuit (IC) (consisting of both Rx and Tx circuits) is typically less than 6 mm x 6 mm. For higher frequencies, or when supporting less AEs per IC, the area becomes even smaller, as shown in Table 3-5. Therefore, only complementary metal oxide semiconductor (CMOS) and silicon germanium (SiGe) are considered to be the feasible technologies that can offer the required high degree of integration in the upper mmW range. While we focus on these silicon-based technologies, the III-V semiconductor technologies such as Gallium Arsenide (GaAs) and InP will be included for comparison in the next deliverable D2.3, since these III-V technologies offer much better noise performance than CMOS and SiGe.

Table 3-5: Available area per RFIC in an antenna array for the upper mmW frequency bands.

Frequency (GHz)	100	150	200	250	300
AE pitch ($\lambda/2$) (mm)	1.5	1.0	0.75	0.6	0.5
RFIC area with 4 AEs (mm x mm)	3.0 x 3.0	2.0 x 2.0	1.5 x 1.5	1.2 x 1.2	1.0 x 1.0
RFIC area with 16 AEs (mm x mm)	6.0 x 6.0	4.0 x 4.0	3.0 x 3.0	2.4 x 2.4	2.0 x 2.0

Our analysis of the LNA's noise figure is based on a NF survey provided by University of Calgary (Canada) [BJ20]. We corrected the erroneous data of the study, and we removed the data that are not really for LNA but for more complex Rx sub-system. Additionally, we improved the data by adding new additional NF data available which was missing in the survey. Moreover, we identified data as measured or simulated, and the final data set of the SiGe LNAs is shown in Figure 3-16.

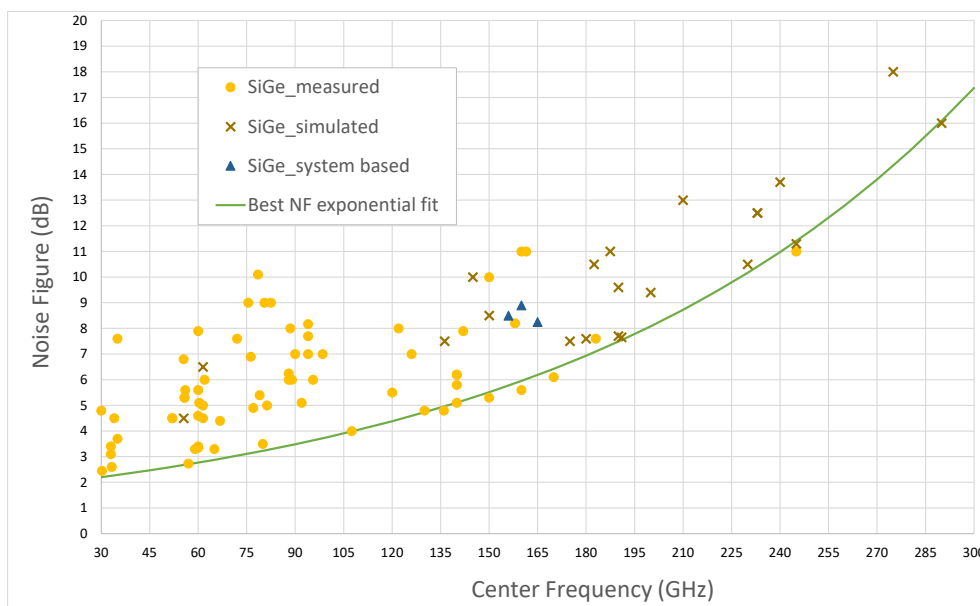


Figure 3-16 Noise figure of SiGe LNA MMICs over 30- 300 GHz: measured (circle), simulated (cross), extracted from Rx module (triangle), and exponential fitting of the minimum NF over the whole mmW range (solid line).

As a result of the active R&D at D-band (110 – 170 GHz) during the past decade, we have sufficient amount of measured NF data up to 170 GHz. Apparently, data is clustered around E-band (60 – 90 GHz) and 120 - 165 GHz, reflecting the stronger interest in these bands due to regulatory allocations

for wireless communications in the V- (50 – 75 GHz), E- and D-band. We expect that more NF data will be available in the W-band (92 – 114 GHz) which is currently under exploitation targeting for B5G and 6G applications.

Above 170 GHz, there are two measured data points available at 180 and 245 GHz, respectively. They are fortunately complemented by the simulated NF for LNAs designed using transistor models for realistic SiGe processes. The simulated NF follows well the trend of the measured data which can be seen from the Figure 3-16. Interestingly, a simple exponential frequency-dependence fits well to the best NF achieved over the whole mmW range (the solid line in Figure 3-16), a total span of 270 GHz. The resulting fitting curve for the minimum noise figure is

$$\min NF = 1.75 \exp(0.00765 f_c) = 1.75 \exp\left(\frac{f_c}{130.7}\right) \quad (3-6)$$

where f_c is the center operation frequency in GHz. Equation (3-6) gives a lower bound on NF (i.e., best case) for mmW SiGe LNAs, which may find useful when hardware (HW) impairment needs to be considered in waveform design, system simulation or link budget calculation.

Similar analysis is applied to LNAs in CMOS (standard as well as SOI), GaAs (pHEMT as well as mHEMT), and InP (HEMT as well as HBT). The data are collectively shown in Figure 3-17, together with NF from SiGe.

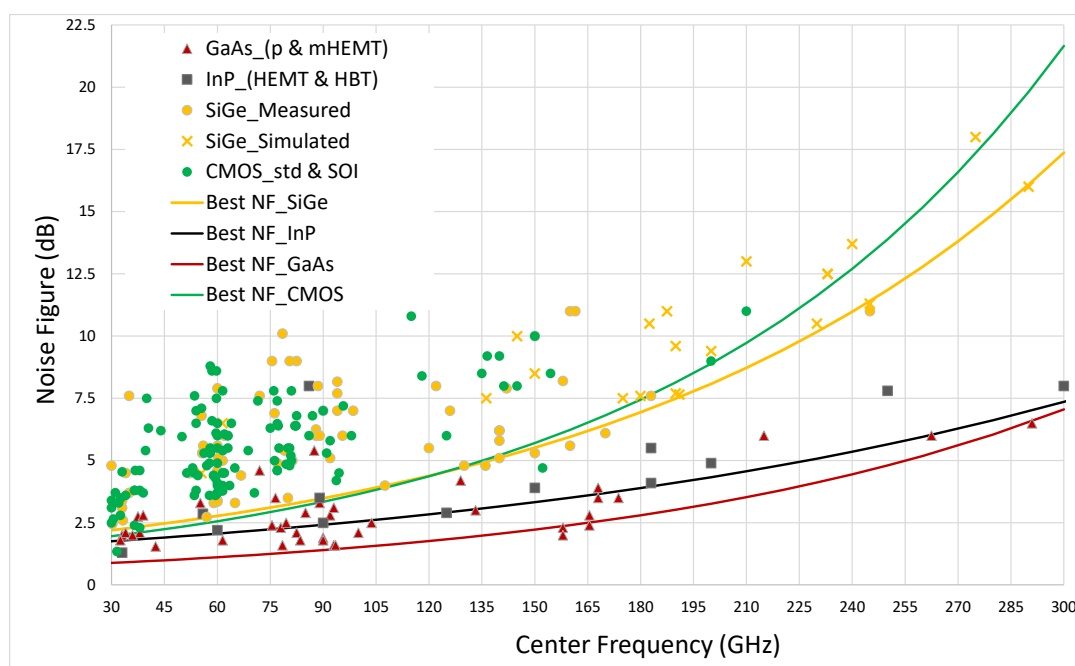


Figure 3-17: NF data of LNA ICs in CMOS (green circle), SiGe (orange circle), GaAs (red triangle) and InP (black square). The lines are exponentially fitted to the best NF of the respective technologies.

The fitting of the CMOS data is relatively less reliable, since the available data points are very limited above 160 GHz, either simulated or measured. It is clear that the NF of CMOS LNAs increases rapidly when frequency goes beyond the E-band (90 GHz). Initially, we attempted to fit the best CMOS NF using the linear frequency dependence of the noise factor (F) for CMOS [TL19]:

$$F_{min} \approx 1 + 2.4 \frac{g}{a} \left(\frac{f_c}{f_T}\right), \quad (3-7)$$

where a (≤ 1) is the normalized drain-source conductance and g ($\approx 2-3$) is a parameter describing the drain current noise. It turned out that the curve fitting based on (3-6), a logarithmic fit by the definition, worked well in the lower mmW frequency range but could not cover the whole 270 GHz mmW range.

Therefore, we consider the exponential fitting used in Figure 3-17 to be more likely representing the correct trend. A summary of the empirical trendlines for the best (i.e., the lowest-value) NF for each analysed technology from Figure 3-15 are presented in Table 3-6.

Table 3-6: Empirical expressions of the best LNA noise figure achieved by different technologies based on published works.

Technology	Empirical model
CMOS LNA	$\min NF = 1.50 \exp\left(\frac{f_c}{112.4}\right)$
SiGe LNA	$\min NF = 1.75 \exp\left(\frac{f_c}{130.7}\right)$
GaAs LNA	$\min NF = 0.70 \exp\left(\frac{f_c}{129.9}\right)$
InP LNA	$\min NF = 1.50 \exp\left(\frac{f_c}{188.7}\right)$

There is a trade-off at the upper mmW bands between the integration and the noise performance. CMOS and SiGe Bipolar CMOS (BiCMOS) offer the best opportunity to meet the stringent integration requirement necessary for the AAS. Unfortunately, their noise performance degrades too rapidly as frequency goes beyond 100 GHz, approaching NF of 10 dB at 200 GHz and NF of 18-20 dB at 300 GHz (which is deemed as practically unusable). GaAs and InP devices, on the other hand, deliver decent noise performance in the whole mmW range, maintaining the best NF level to within 8 dB even at 300 GHz. However, their integration capability is relatively limited and is considered to be unsuitable for AiP systems at the upper mmW bands. The performed NF analysis reveals that CMOS and SiGe are the optimal candidates offering a balanced performance in terms of integration and Rx noise figure for the 170 GHz band and below. For frequencies above 170 GHz, there is no single technology that meet both requirements, thus, advanced heterogeneous combination of the technologies can become necessary.

3.6.3.2 Loss of Rx front-end passives

Chip interconnect and RF routing inside of the AiP are very different from those in the conventional PCB-based packaging counterparts. The SotA AiP technology offers low-parasitic die interconnect and waveguide-based short RF routing path, reducing insertion losses of the passives. A conceptual cross section of the AiP is illustrated in Figure 3-18.

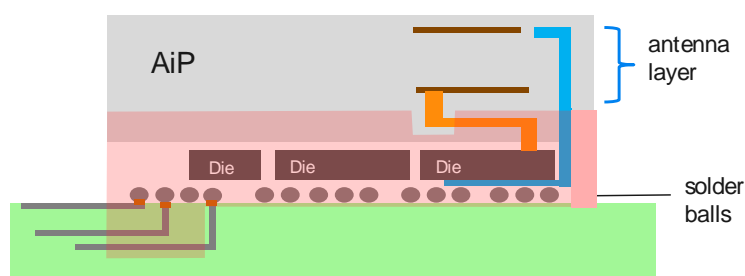


Figure 3-18 A conceptual drawing of basic AiP build up (the thick orange line is the RF routing path)

RF routing: The routing waveguide from the die I/O port to the AE feed layer (orange path in Figure 3-18) consists of vertical and horizontal parts. The length of the vertical path is determined mainly by the AiP process and will not depend much on f_c . The path length of the horizontal routing, however, is inversely proportional to the operation frequency, offsetting to a large extent the increased insertion loss of the waveguide when frequency increases. Therefore, the routing loss is expected to be a weak function of f_c . The total routing path length is typically 1.5-2 mm at 100 GHz. The total insertion loss

is estimated to be in the range of 0.5-1.0 dB per routing at 100 GHz, including the loss of die interconnect, based on simulation.

RF switch: RF switches are normally used in TDD systems. Integrating RF switches with the transceiver front-end circuits (PA and LNA) is the possible way of implementation for AAS, since there is no space for discrete switches in the AiP module. This on-chip integration induces extra loss, even if, a shunt connection topology is adopted for the switches. For example, a 1.8-2.0 dB loss is estimated at 71-76 GHz in a 64-element phased-array transceiver module implemented in 22nm FinFET CMOS [PCS+19]. For this reason, realization of TDD operation without using RF switches is under investigation for AAS.

RF bandpass Filter: RF Filter is another challenging component in the AAS implementation. Similar to the RF switches, there is simply no space in the AiP module for discrete filters which normally has sufficiently good quality factor. On-chip or package-embedded filters are lossy, and their quality factor is not high enough to fulfil the filter specification set by the system requirement. Therefore, applying filters in the analog front-end of a AAS should be avoided whenever possible, as there is no suitable mmW filter technology for AAS, especially in 100-300 GHz. If it is inevitable to integrate the filters on chip or packaging, at least 2-3 dB degradation in Rx noise figure should be counted due to the filter loss [YCC14].

To conclude this initial modelling effort on Rx noise figure, the contribution of the analog front-end to the total Rx NF can be expressed as:

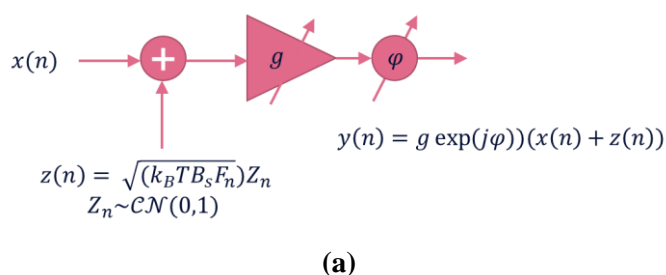
$$NF = IL_p + NF_{LNA} = IL_p + a * \exp\left(\frac{f_c}{b}\right). \quad (3-8)$$

where IL_p (in dB) represents the insertion loss of all passives between LNA and the AE. The values of parameter a and b are presented in Table 3-6. The total insertion loss values of IL_p at 100 GHz and above are typically:

$$IL_p = \begin{cases} 1 \text{ dB, routing+ interconnect} \\ 2 \text{ dB, with on-chip switch} \\ 3 \text{ dB, with integrated filter} \end{cases} \quad (3-9)$$

3.6.4 Analog beamforming nonlinearities

Antenna path specific amplitude and phase control is performed before the PA at the transmitter, and after the LNA at the receiver. Numerous passive and active phase shifting approaches can be considered. Analog phase shifting and amplitude control has mainly two nonidealities that should be considered namely quantized beamforming weights and noise. In most of the cases, LNA dominates the receiver noise figure and the noise added by the phase shifters can be neglected. However, especially if the amplitudes are also controlled, modelling the noise of the VGA/phase shifter may be considered. Model description for analog signal weighting and phase shifting in single RF path is depicted in Figure 3-15(a) and Figure 3-15(b). The model can be active or passive, depending on the respective implementation. In the active model, the noise is added prior to the beamformer, while in the passive model it is added afterward it. In both cases, the amplitudes are normalized such that they get maximum value of 1. Note that each antenna/LNA path has a dedicated analog amplitude and phase control. In the Tx side, the noise may be neglected, but one must guarantee that the signal is not scaled too low such that transmitter noise would have impact.



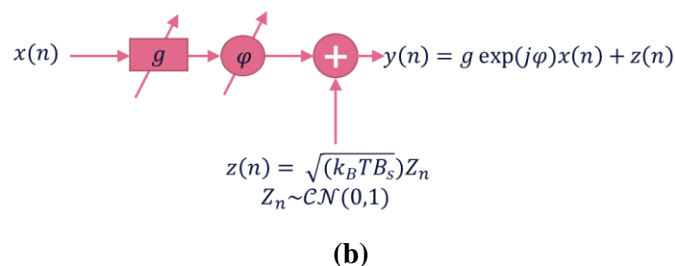


Figure 3-19: Analog phase shifter models (a) active model, where noise is added before amplitude and phase controls, and (b) passive model, where noise is added after amplitude and phase controls.

3.6.5 Frequency synthesis considerations and phase noise

Local oscillator (LO) frequency generation of 6G radios will utilize multiple multiplications by two or three of the VCO signal in series and thus the operation frequency of the VCO can be lowered. Typically, lower frequency VCOs are easier to implement with better performance and lower current consumption. However, the doubling of the LO frequency effectively raises the respective phase noise by 6 dB since the same signal is in intermediate frequency (IF) and LO port of the mixer and correlated noises are multiplied into the RF port of the mixer. This kind of frequency duplication is shown with 2X block in Figure 3-20. An example LO generation tree for 150 GHz frequency with a phase locked loop (PLL) topology is shown in Figure 3-20. This LO architecture has the 16 times VCO frequency multiplication which is similar to the 100 Gbps radio transceiver published in [RLG+20]. In the example, the crystal (XTAL) operates on 100 MHz frequency which is used as reference frequency in phase detector (PD). A RF signal generator was used as XTAL in [RLG+20]. The VCO operates on 9.375 GHz, and it is multiplied 16 times to 150 GHz final frequency, which is considered to be transmission (TX) and reception (RX) frequency of the 6G system. The PLL structure is simplified for illustration purposes in Figure 3-20.



Figure 3-20: Example local oscillator generation architecture to support 150 GHz frequency.

The overall phase noise depends highly on the frequency synthesis approach of the transceiver. The approach used in the initial phase of the modelling relies on phase noise spectra. This approach follows terminology adopted from 3GPP document [38.808, Section 4.2.3.1] and the phase noise power spectrum can be defined as

$$S(f_o) = PSD0 \frac{\prod_{n=1}^N \left(1 + \left(\frac{f_o}{f_{z,n}}\right)^{\alpha_{z,n}}\right)}{\prod_{m=1}^M \left(1 + \left(\frac{f_o}{f_{p,m}}\right)^{\alpha_{p,m}}\right)}, \quad (3-10)$$

where S is the single sideband phase noise power spectral density, f_o the offset frequency, $f_{z,1} \dots f_{z,N}$ the zeros, $f_{p,1} \dots f_{p,M}$ the poles, $\alpha_{z,1} \dots \alpha_{z,N}$ the order of the zeros, and $\alpha_{p,1} \dots \alpha_{p,M}$ the orders of the poles.

An example phase noise power spectrum with the type-1 parametrization of the model is given in Figure 3-21. Such model generally contains four different slopes that dominate the power spectrum shape with different offset frequencies. The slopes are mainly caused by the crystal, bandwidth of the loop filter in the PLL and phase noise performance of the VCO. The flat region models the wideband white phase noise. The overall model parametrization depends highly on the implementation.

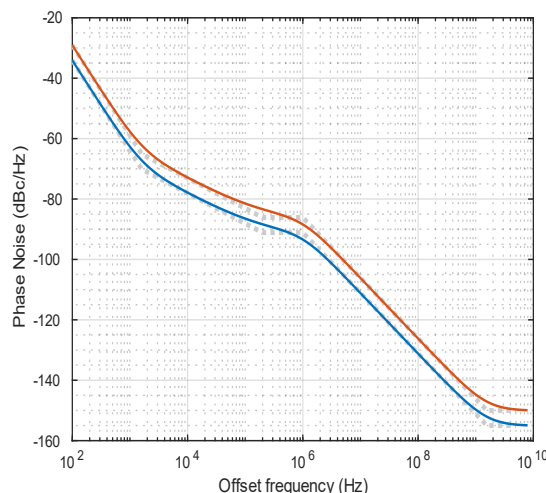


Figure 3-21: Example phase noise spectra with parametrization taken from 3GPP [38.808, Section 4.2.3.1]

Phase noise models are usually defined in frequency domain to represent the phase noise power spectrum of the LO. To estimate the average system level phase noise impacts, often the phase noise is integrated over the band to calculate the average RMS phase jitter, which can be further converted to an equivalent SNR or EVM. The RMS phase jitter can be calculated as

$$\sigma_{rms} = \sqrt{2 \int_0^{f_m} S(f) df}, \quad (3-11)$$

where $S(f)$ represent the phase noise power spectra and f_m is the maximum offset frequency ($F_s/2$). For simulations, this model can be simply by generating the LO signal as

$$x_{LO}(n) = \exp(j\varphi_{pn}(n)), \text{ where } \varphi_{pn}(n) \sim N(0, \sigma_{rms}^2), \quad (3-12)$$

and multiplying it by the original signal as

$$y(n) = x(n) \exp(j\varphi_{pn}(n)). \quad (3-13)$$

However, the average RMS phase jitter model assumes that the whole phase noise power is spread evenly over the whole band. This model holds if the symbols are short and applies well for many single carrier waveforms. However, it does not properly model the coloured phase noise impact, which is important when simulating, for example, multicarrier waveforms, where the actual symbol rate (for example orthogonal frequency division multiplexing (OFDM) symbol is rather long. A better model for that case is to generate a normal distributed phase noise and filter that by the phase noise spectra. This can be represented by using the Fourier transform

$$\varphi_{LO}(t) = \int_{f_1}^{f_2} H(f) \varphi_w(f) \exp(2\pi f t) df, \quad (3-14)$$

where $H(f) = \frac{1}{\sqrt{2}} \sqrt{S(f)}$ is the filter to color the normal distributed phase noise, and f_1 and f_2 are the lower and upper frequencies where the model applies. This is illustrated in Figure 3-22. The white Gaussian noise $\varphi_w(f)$ can be generated either in time or frequency domain as long as one takes care of the proper scaling when using discrete Fourier transform.

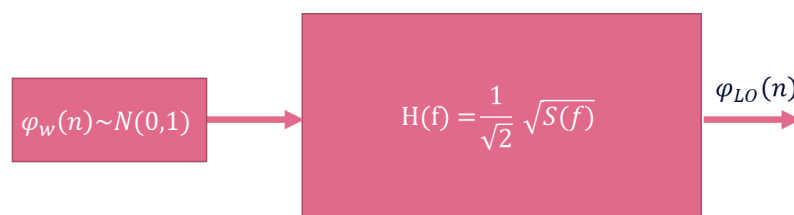


Figure 3-22: Normally distributed white noise is filtered with a phase noise spectrum frequency response to generate the phase noise model.

As an example of such phase noise simulation with 10 realizations by using both models are presented in Figure 3-23. The waveform used in the simulation is a 16-QAM signal with 0.25 RRC pulse shaping with 1 GHz of signal bandwidth. The parameters for the phase noise model are derived from the 3GPP specifications. LO is set to 140 GHz in the model. Note that as the model parameters are verified in 3GPP only up to 70 GHz, this example is just to show the basic functionality of the model.

In the figure, Model 1 represents the RMS phase jitter approximation, while the model 2 is the coloured phase noise model. As one can see, the overall impact on the EVM is approximately the same for both models. However, the spectra and the constellation are still very different, which emphasize the importance of the selection of modelling approach in frequency or in time domain of the phase noise.

The challenge with the coloured model is that the filter, to colour the phase noise, is rather long and hence requires large memory. It simply means that one needs significant amount of waveform samples to simulate the impact with both slow and fast phase variations properly. When simulating signals with very high sampling rate, this eventually means huge amount of memory and rather long simulations with large amount of realizations. For faster system level simulations, the white phase noise model would then work better to approximate the average impact.

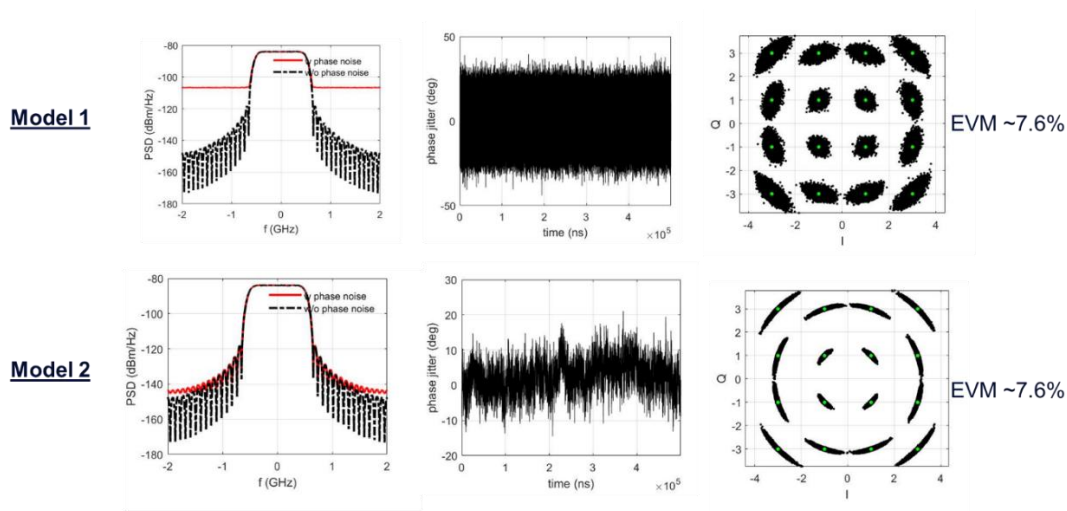


Figure 3-23: Building blocks of RF transceiver for upper mmW band (one signal path).

Different waveforms have also different means to compensate for the phase noise impacts. For example, in case of OFDM, the slow phase noise behaviour causes common phase error (CFE) which can be compensated. The remaining phase noise is the flat part of the phase noise spectra, which can be approximated with normal distributed phase noise. Hence, different simplified models can be later on derived for different waveforms to approximate better the average system level impacts with less complexity.

In MIMO systems, the phase noise model should include the correlation of the phase noises between the individual LOs. The correlation depends highly on the LO distribution strategy between the

individual arrays/RF chains and thus it need be considered when the phase noise for the digital and hybrid beamforming is modelled.

3.6.6 Review of current 3GPP models used for preliminary waveform studies

In this subsection, RF impairment models used in the waveform studies in Section 4 will be outlined. Furthermore, a general discussion on simplistic RF impairment modelling and its potential shortcomings in the context of transmitter/receiver architectures for 6G radio nodes is given.

3.6.6.1 3GPP power amplifier models

PA model I is a memoryless polynomial model of a GaN PA design at 28 GHz, based on circuit simulations and described in detail in [3GPPR4-165901, Section 2.1.4]. Following the presentation in [3GPPR4-1610279], PA model I can be considered approximately valid also at 45 and 70 GHz, as the ACLR characteristic with respect to PA output power is merely shifted according to the expected downscaling of maximum PA output power when going from 28/30 GHz to 45 and thereafter 70 GHz. It can therefore be concluded that the PA model I is applicable in the entire range 30 – 70 GHz. As an example, the AM/AM and the AM/PM characteristics of PA model I for 30 to 60 GHz range are shown in Figure 3-24.

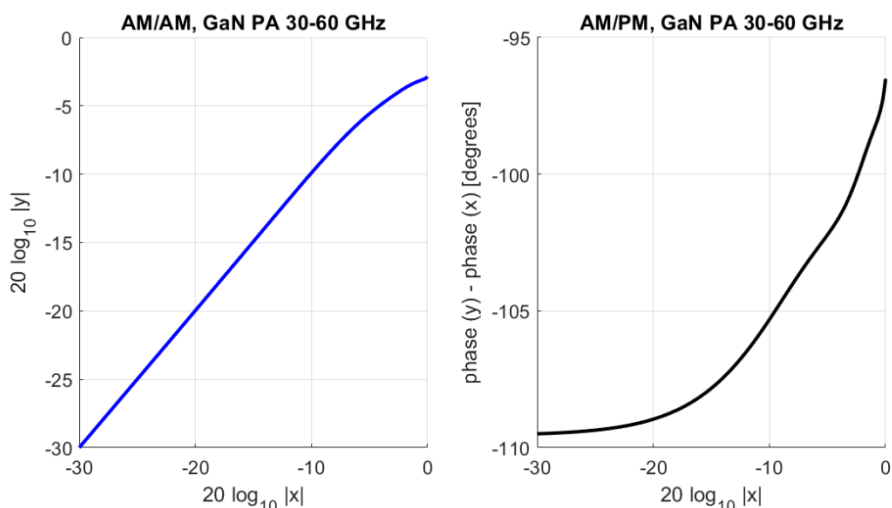


Figure 3-24: AM/AM and AM/PM characteristics of PA model I

3.6.6.2 3GPP phase noise models

The phase noise (PN) model I, taken from [38.808, Section 4.2.3.1], is a parametrized model which is defined in terms of a power spectral density (PSD) and is based on the investigation of many measured PLL PN characteristics. The PN characteristics of the PLLs are used to define an average PSD, still depending on one parameter called design margin (DM). The DM is used to model the severity of the PN, which is in general lower for base stations (BS) than for user equipment (UE) and DM values 5 and 0 dB are used. The PSD is used to generate coloured Gaussian noise which is then taken as the argument of a complex phasor. The model is valid for a carrier frequency of 70 GHz.

PN model II, as defined in [38.808, Section 4.2.3.2], is a multi-zero/pole model with the parameters taken from [3GPP803, table 6.1.11.2-1] for the receiver side. At the transmitter side an approximate of the measured PSD from the commercially available 20GHz wideband RF synthesizer LMX2595 Texas Instrument is used. Figure 3-25 depicts the PSD of the PN model II. For the needed carrier frequency of 120GHz in the study, the PSD is scaled up using the 20 dB per decade rule.

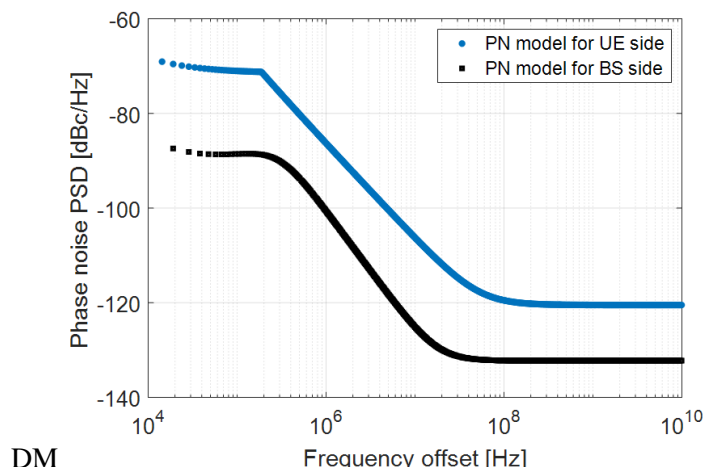


Figure 3-25: PSD of the phase noise model II at both transmit and received side, scaled up to 120 GHz carrier frequency

3.6.6.3 Discussion on shortcomings of simplified RF impairment modelling

The transmitter and receiver front-end aspects that should be modelled for waveform investigations are shown in Figure 3-26. It is obvious that modelling the equivalent baseband of the beamforming is a challenge if considering the already high processing requirement for waveform performance evaluation. In addition, it is the actual implementation would experience gain differences and process variations for example in the different PAs of one antenna array. The modelling of the phase noise is also often considering the same phase noise at different antenna panels. This cannot always be assumed as this would assume the distribution of the local oscillator at the carrier frequency (assuming a direct conversion receiver). This aspect is dependent on the front-end architecture. If this is not the case the phase noise at different arrays will be different as the oscillator signal that is used in the mixer would be derived from a lower frequency clock distributed in the device separately at each antenna array.

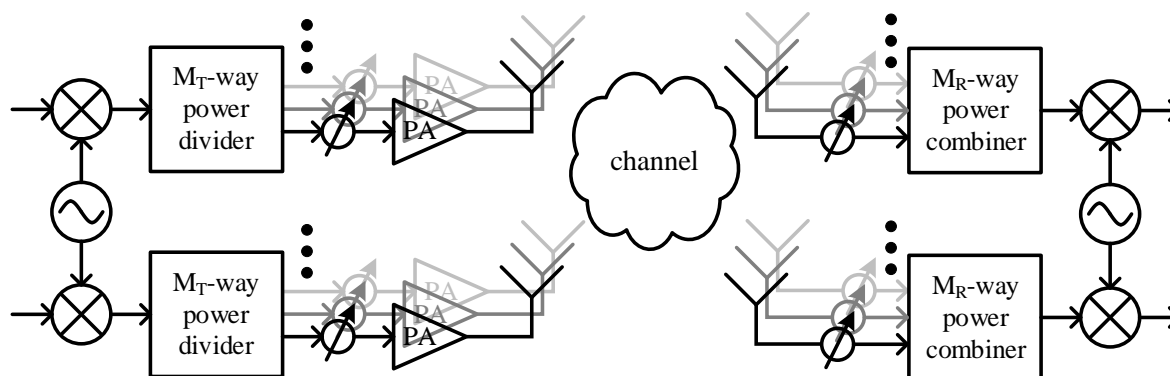


Figure 3-26: Illustration of the transmitter and receiver front-end aspects that has the main influence on waveform performance.

The model that we considered for this preliminary investigation is the one shown in Figure 3-27. It is obvious that the transmitter PA in this model is representing the equivalent baseband model of the linear and non-linear aspects of all PAs in an array shown in Figure 3-26. As the model in Figure 3-27 does not include beamforming the non-linearity of the PA in it represents the portion of the non-linearity of all PAs in Figure 3-26 that coherently add after the channel and receiver beamforming. The same holds true for the transmitter's phase noise. All other contributions of the PAs and the phase noise that do not coherently add after the receiver beamforming contribute to the EVM of the system. Therefore, this system modelling can be viewed as beam specific. Further discussion on the validity of this approach

that is very common in academic literature and standardization needs to be addressed before a final model for waveform investigations can be agreed for this project. It also needs to be discussed if the contribution from LO distribution at a lower frequency needs to be modelled.

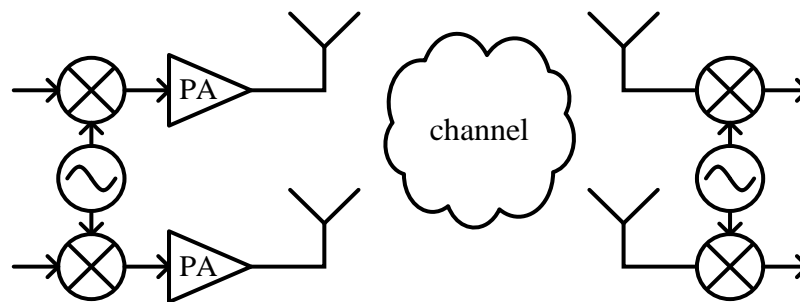


Figure 3-27: Illustration of the transmitter and receiver front-end model used for the preliminary waveform investigation.

4 Waveform candidates for 6G: impact of hardware impairments and complexity-performance trade-offs

Design of waveforms for systems operating at mmW frequencies will be heavily influenced by hardware limitations. Unfavourable scaling of phase noise with carrier frequency puts a demand on waveforms to be robust to phase noise impact. Limited peak output power at the PA at mmW frequencies will reduce the available link budget and range; choosing waveforms with low envelope variation (and consequently, output power backoff) can help regain some of the lost link budget headroom. Another important aspect of mmW waveform-related system design is processing complexity, which should be kept low in order to save power. This section presents several studies touching upon the aforementioned issues.

4.1 Short description of studied waveforms

Before presenting the studies themselves, a short description of studied waveforms is given.

4.1.1 OFDM-like waveforms

A number of waveforms studied in this contribution can be described as OFDM-like waveforms, and a generalized block diagram of the transmitter digital baseband for this family of waveforms is given in Figure 4-1. The key blocks here are the precoder and the bit-to-symbol mapper, and waveforms in this family differ in the structure of the precoder alone, while having all the other Tx blocks in common. Precoder is a very general structure with M inputs and N outputs. For OFDM, precoder is linear and consists of a $M \times N$ binary matrix performing the mapping of symbols to subcarriers. For discrete Fourier transformation (DFT)-spread-OFDM (DFTS-OFDM), the precoder is also linear and consists of a concatenation of an $M \times M$ DFT matrix and the $M \times N$ symbol-to-subcarrier mapper. On the other hand, constant-envelope-precoded DFTS-OFDM (CEP-DFTS-OFDM) has the same precoder structure as DFTS-OFDM, while performing constant-envelope phase modulation in the bit-to-symbol mapping block (OFDM and DFTS-OFDM typically perform mapping of coded bits to QAM symbols).

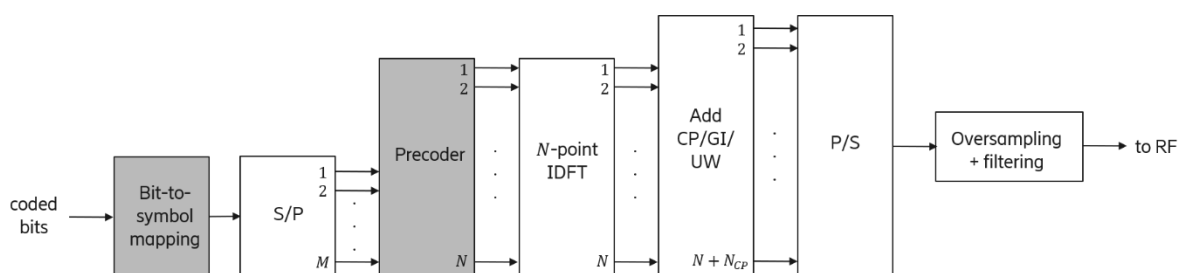


Figure 4-1: diagram of Tx digital baseband for OFDM-like waveforms

4.1.2 Single-carrier

Another type of waveform is the pure single carrier with frequency-domain equalization (SC-FDE), the transmitter diagram of which is shown in Figure 4-2. The addition of a cyclic prefix enables frequency-domain equalization at the receiver.

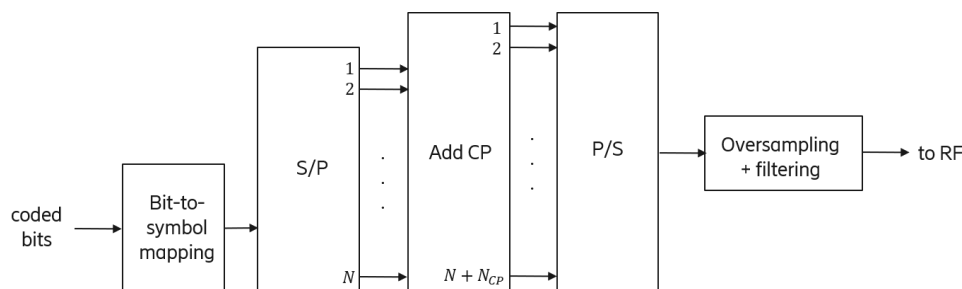


Figure 4-2: diagram of Tx digital baseband for SC-FDE

4.1.3 Constrained Envelope Continuous Phase Modulation (ceCPM)

Constrained envelope continuous phase modulation (ceCPM) [SS03] is a true single carrier scheme generalizing CPM by allowing controlled small envelope variations. The signal is designed such that the receiver sensitivity can benefit proportionally from the allowed envelope energy variations energy. ceCPM is based on the extended Laurent decomposition of CPM [MM95], allowing non-binary modulation alphabets for increased spectral efficiency. ceCPM has better receiver sensitivity than CPM-DFTS-OFDM, but a more complex equalizer. Both can be detected by Reduced State Sequence Detection (RSSD) with 8-16 states [SS09].

4.1.4 Zero-crossing modulation (ZXM)

The main motivation behind zero-crossing modulation (ZXM) [FDB+19] is energy efficiency. For large bandwidths, as envisioned for 6G, the power consumption of the ADCs starts to rise quadratically with the sampling frequency [Mur21]. Especially for systems with large antenna arrays, with many RF chains, ADCs will likely become one of the main contributors to the system's power consumption [NDF19]. ZXM is based on the idea, that sampling at high frequencies might still be feasible, if the ADC complexity, i.e., the amplitude resolution is reduced, as the ADC power consumption grows exponentially with the number of bits. With 1-bit ADCs the receiver is effectively only able to detect the zero-crossings of the received signal. Therefore, ZXM aims to encode the information in the distance of the zero-crossings of the transmit signal.

In this contribution, ZXM is combined with faster-than-Nyquist (FTN) signalling and sequence design with so called run-length-limited (RLL) sequences [LDF18]. RLL sequences [Imm90] can be constructed from (d, k) sequences, which are constrained binary sequences, where every 1 has to be followed by at least d and at most by k 0s. To maximize the entropy rate of the transmit signal we omit the k -constraint, i.e., $k = \infty$. RLL sequences can be constructed from (d, k) sequences by non-return-to-zero-inverse (NRZI) encoding, which is illustrated in the following example for $d = 1$:

$$\begin{aligned} (d, k) \quad \bar{\mathbf{a}}_m &= [\dots, 0, 1, 0, 1, 0, 0, 1, \dots]^T \\ \text{RLL} \quad \mathbf{a}_m &= [\dots, -1, 1, 1, -1, -1, -1, 1, \dots]^T \end{aligned} \quad (4-1)$$

In essence, the d -constraint controls the minimum distance between amplitude transitions.

FTN signaling allows to align zero-crossings on a finer grid and thus, increases the entropy rate of the transmit signal. However, it comes at the cost of self-introduced inter symbol interference (ISI). The amount of ISI is controlled by the d -constraint of the RLL sequence. Figure 4-3 shows a schematic overview of the transmitter for ZXM.

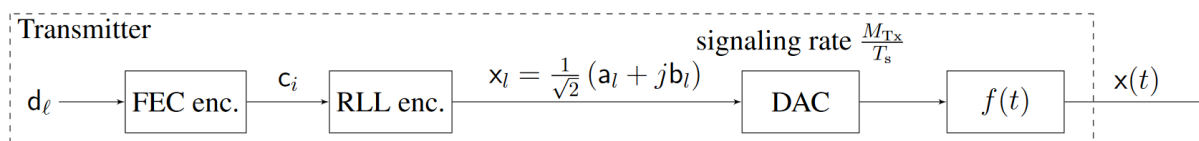


Figure 4-3: Block diagram of the transmitter for ZXM systems, taken from [NDH+20b].

4.2 Complexity-performance trade-off for DFTs-OFDM with an iterative receiver design

The works in [NJK+18, NHJ+21] and also those of Section 7 have shown that the sub-THz wireless channel at 140 GHz is time-dispersive in general, meaning that the DFT-s OFDM symbols will suffer from ISI, which happens because the symbols are localized in the time domain. Thus, this section has the objective of investigating the impact of iterative equalization of DFTs-OFDM under an empirical sub-THz channel model to mitigate ISI effects. Information about iterative equalization is found in the references [TS11, DCJ+95, TKS02, RS00]. Therefore, in this report we consider the low-complexity minimum mean-square-error parallel interference cancellation (MMSE-PIC) receiver [BCF19], where we want to compare the performance of two different single-input single-output (SISO) encoders, namely, convolutional, and low-density parity-check (LDPC). We consider the convolutional encoder because it has been commonly used in conjunction with iterative equalization in several recent works in literature [BNC+21, ZHL+18]. Regarding the LDPC code, it is well accepted that it provides superior coding performance than convolutional codes under additive white Gaussian noise (AWGN) channels, and it has been selected in 5G new radio (NR) for long packet sizes due to its good performance and good implementation aspects [38.212].

4.2.1 Empirical sub-THz Channel Model

In the following the empirical 140 GHz sub-THz channel model is described. We utilize the measurements presented in [NHJ+18] [NHJ+21], which were collected via the spatio-temporal channel sounder from Aalto University, Finland. Details about the measurement setup are discussed more in detail in Section 7. In this investigation, we consider the measurements performed on the shopping mall ‘‘Sello’’ in Espoo, Finland. The measured channel data consists of power angular-delay profile (PADP) measurements with significant local maxima within the utilized dynamic range, which is described in equation (7-5) as $\mathcal{P} = \{\phi_m, \tau_m, \hat{P}_m\}_{m=1}^{N_p}$. The delays in the PADP \mathcal{P} are defined in continuous time. In order to have a discrete time model, we define the PAPD as

$$\rho_{n,\phi} = \sum_{m=1}^{N_p} \hat{P}_m \delta(\phi - \phi_m) \quad (4-2)$$

where $n = \text{round}(\tau_m B)$ is the n^{th} discrete time tap and B is the bandwidth. The term $\delta(\phi - \phi_m)$ is used to extract all taps from the angle ϕ , and $\delta(\cdot)$ is the delta function. In order to create random channel realizations, we follow a similar approach of [PBH+21] where each multi-path component has a uniformly distributed random phase. Next, we analyse the channel measurements used in the numerical results of numerical results subsection. We selected three measurement sets from [NJK+18] which are given in Table 4-1, where the Tx ID is related to the transmitter location.

Table 4-1: Measurements of [NJK+18] used in simulation

Channel	Tx ID	Distance (m)	ϕ (deg)
I	1	5.10	42
II	13	15.04	223
III	13	15.04	209

We plot the PAPD of equation (4-2) for these channels in the left side of Figure 4-4. Channel I is flat, and channels II and III have multi-path components for $n > 0$. In order to better understand the frequency

² Here we changed the original index variable n to a new variable m because we use n to describe the tap index.

selectivity of channels II and III, the right side of Figure 4-4 depicts the overlaid channel power in the frequency domain for different realizations, for $N = 512$ subcarriers and bandwidth of 1 GHz. For Channel II, one observes a difference of approximately 18 dB between the sub-carrier with maximum and minimum power. For Channel III, this difference is approximately 38 dB, that is 20 dB more than Channel II, showing that it is more selective in frequency.

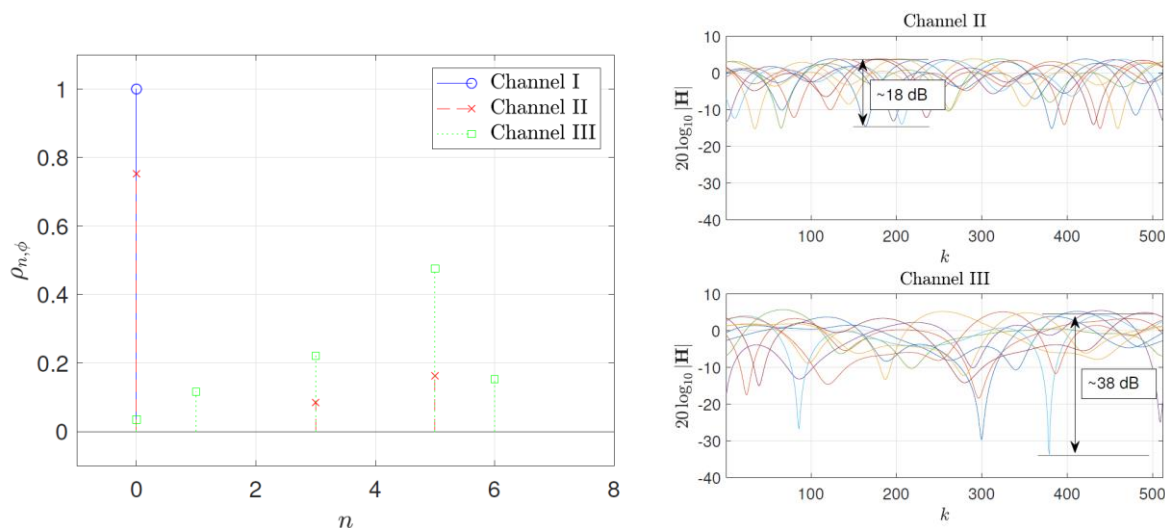


Figure 4-4 PADP of the used channels (left), and overlaid channel power (right).

It is important to highlight that we have considered Channels I, II and III in our experiments due to their level of selectivity shown in Figure 4-4. However, there are other major aspects to be considered that should be investigated in future works. Basically, it is more meaningful to have a statistical channel model such that more general conclusions are possible. This can be done by considering a larger set of measurements described in Section 7. Also, Channels I, II and III have relatively low time dispersion, with the last path arriving at $n = 6$, meaning that the DFTs-OFDM with frequency domain equalization needs a small CP overhead for $N = 512$ that is used in the numerical evaluations. However, in general there are channels in the entire measurement set whose time dispersion is much higher. This aspect should be considered while choosing the system numerology.

4.2.2 Results

We evaluate the performance of convolutional and LDPC³ encoders in terms of frame error rate (FER) with the channel model of the previous subsection. The 1/2 code rate recursive systematic convolutional (RSC) encoder has generating polynomial $\{133,171\}_8$, and a higher code rate of $R = 3/4$ is obtained by puncturing. The QC-LDPC code work utilizes the 5G NR base graphs BG_1 and BG_2 [38.212]. In particular, the system with $R = 1/2$ and $R = 3/4$ code rates utilizes BG_2 and BG_1 , respectively. The remaining parameters used in the simulations are shown in Table 4-2. Also, the system assumes perfect synchronization, perfect channel knowledge and no hardware impairments.

³ The 5G NR LDPC encoder and decoder has been obtained via the joint Sino-German research project "Large-Scale and Hierarchical Bayesian Inference for Future Mobile Communication Networks" [XWX+19].

Table 4-2 Simulation Parameters

Parameter	Value
n. of symbols (FFT size), N	512
Bandwidth	1 GHz
MCS	$\frac{1}{2}$ QPSK, $\frac{1}{2}$ 16QAM, $\frac{3}{4}$ QPSK, $\frac{3}{4}$ 16QAM
Convolutional decoder	BCJR log-MAP
LDPC decoder	SPA with 15 iterations

4.2.2.1 Performance Analysis

The Figure 4-5 shows the results with convolutional encoder. The initial analysis evaluates the impact of having several iterations in the receiver. For this, we show the results for iterations $I = (0,2,4)$. Iteration zero means that the receiver has no iteration, i.e., it can be seen as the regular linear receiver with equalization and decoding. A summary of the performance gain of the system with iterative equalization in relation to the system with linear equalization is given in Table 4-3. We see that the performance is indeed improved. For example, in the results using Channel II there is an improvement of approximately 2 dB and 2.5 dB for $\frac{1}{2}$ QPSK and $\frac{1}{2}$ 16QAM systems, respectively. In general, we observe a trend where this gain increases with the channel selectivity and MCS. This is expected because higher selectivity in frequency is translated in larger levels of ISI in time, therefore the iterative equalization will have a higher impact. In addition, as the MCS increases, the system becomes more sensitive to ISI, thus the gain of using iterative equalization is larger.

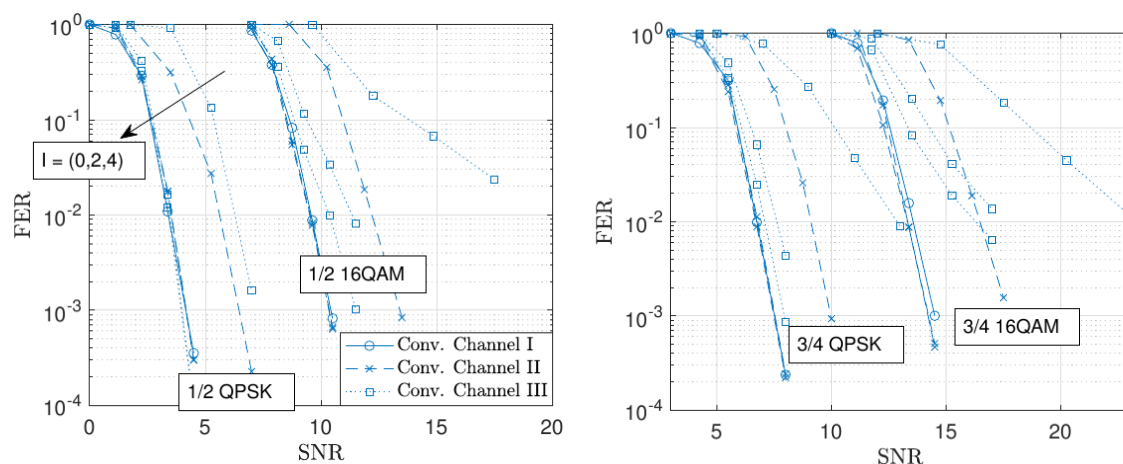


Figure 4-5: FER with convolutional encoder for maximum iterations of 0, 2 and 4.

Table 4-3 Summary of performance gain of System with convolutional encoder

Encoder	Convolutional							
	Channel II				Channel III			
Channel	$\frac{1}{2}$ QPSK	$\frac{3}{4}$ QPSK	$\frac{1}{2}$ 16QAM	$\frac{3}{4}$ 16QAM	$\frac{1}{2}$ QPSK	$\frac{3}{4}$ QPSK	$\frac{1}{2}$ 16QAM	$\frac{3}{4}$ 16QAM
Performance gain	2dB	2.5dB	2.5dB	3dB	3dB	6dB	7dB	7dB

Figure 4-6 shows the results with the LDPC encoder, with a performance summary in Table 4-4. Generally similar conclusions to the system with convolutional encoder can be drawn. The main

difference is that the iterative receiver provides less performance improvement than the system with convolutional encoder.

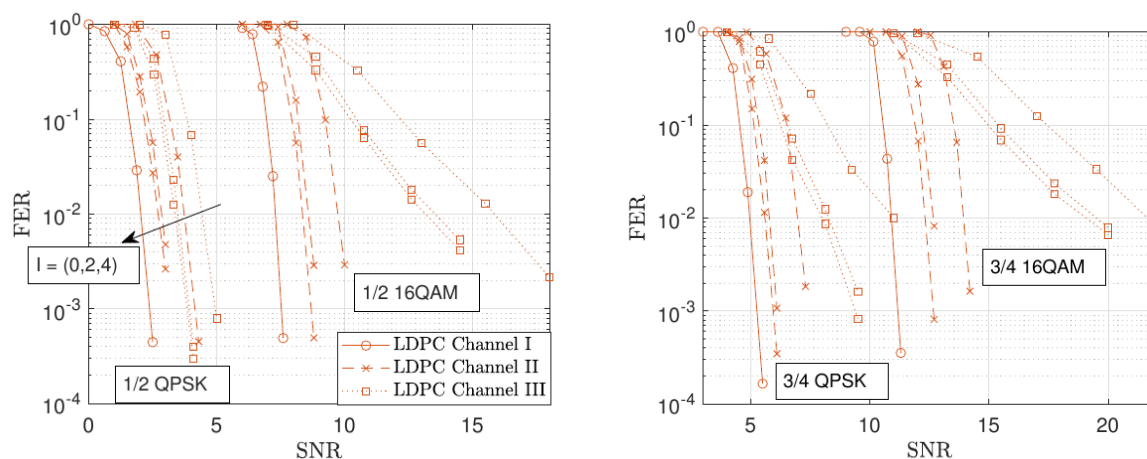


Figure 4-6: FER with LDPC encoder for maximum iterations of 0, 2 and 4.

Table 4-4 Summary of performance gain of system with LDPC encoder

Encoder	LDPC							
Channel	Channel II				Channel III			
MCS	½ QPSK	¾ QPSK	½ 16QAM	¾ 16QAM	½ QPSK	¾ QPSK	½ 16QAM	¾ 16QAM
Performance gain	1dB	1.5dB	1.5dB	1.75dB	1dB	3dB	3dB	3dB

In Figure 4-7 we compare the system with both encoders with a maximum of 4 iterations. As expected, the system with LDPC encoder outperforms the system with convolutional for the Channel I, that is the AWGN channel. For Channel II, the results still show that LDPC system is better, while the transmission under the Channel III has a better performance with the convolutional encoder. To explain this result, the first aspect to be considered is that, although the convolutional encoder has notably worse performance than the LDPC in the AWGN channel, it is less sensitive to the channel selectivity. One manner of explaining this is that the convolutional encoded signal that is applied to a dispersive channel can be interpreted as a type of serially concatenated convolutional encoder. On the other hand, the system with LDPC code decreases its performance as the channel becomes more selective in all cases. Similar results to this have already been reported in the literature. For instance, in [MZ18] it has been shown that LDPC decoder provided worse performance than the convolutional decoder in a MIMO setting, where the ISI level is very high. The outcomes of Figure 4-7 are relevant because they reveal that there is a channel selectivity level from which the LDPC code provides better performance than the convolutional, with the iterative MMSE-PIC equalizer.

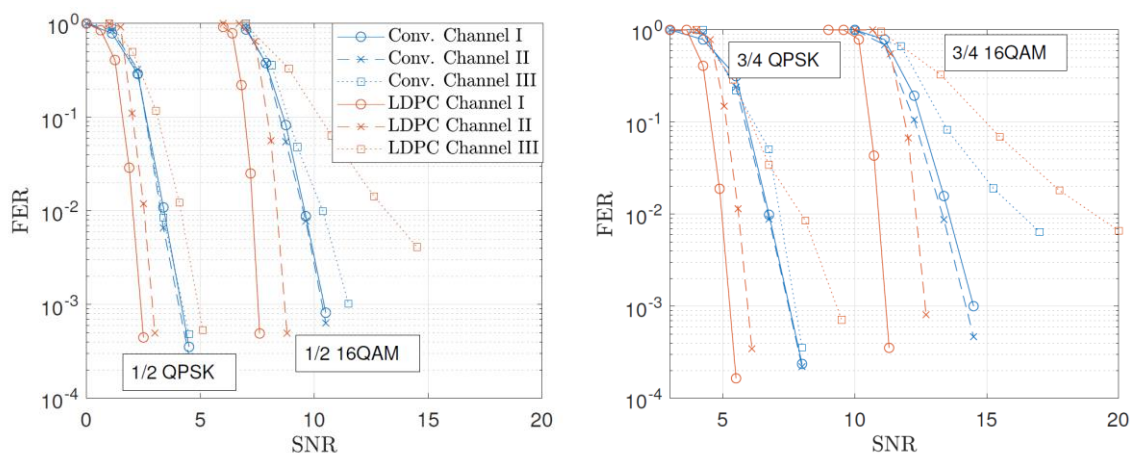


Figure 4-7: FER comparison between convolutional and LDPC encoders for a maximum of 4 equalization iterations.

4.2.2.2 Complexity Analysis

In this subsection we analyse additional complexity required when iterative equalization is employed. To this end, we show the probability of equalization iterations for the results of Figure 4-7 for the highest SNR point. Also, this analysis assumes that a cyclic redundancy check (CRC) is performed after the decoder. Thus, if the CRC indicates that the code word has been correctly detected, the receiver stops iterating. Under this assumption, 0 iterations mean that the receiver is capable of correctly decoding the data bits without iterations. 1 iteration means that one more request of equalizer and decoder is needed, and so on. Since the maximum number of iterations is set to 4, when the code word is not correctly detected, the receiver will necessarily perform 4 equalization iterations. Thus, the higher the FER, the higher is the probability of the receiver performing 4 iterations.

The results are shown in Table 4-5 and Table 4-6 for the systems with convolutional and LDPC encoders, respectively. In general, we can conclude the systems that employ the iterative receiver do not require very high additional processing, 0 iterations and 1 iteration are cases that happen with highest probabilities. Another aspect to be noticed is that the system with convolutional encoder requires more iterations under Channel III. For instance, the systems with $\frac{3}{4}$ 16QAM, the system with convolutional code utilizes 1 iteration 28.7% while the system with LDPC utilizes 1 iteration only 1%. This result indicates that convolutional code would require more additional computational complexity under Channel III. For Channel II, it is shown that LDPC encoder requires more iterations than the convolutional code, meaning that now the system with LDPC code requires more additional complexity.

Table 4-5 Probability of equalization iterations for system with convolutional encoder for highest SNR point of Figure 4-7.

Encoder	Convolutional							
	Channel II				Channel III			
	1/2 QPSK	3/4 QPSK	1/2 16QAM	3/4 16QAM	1/2 QPSK	3/4 QPSK	1/2 16QAM	3/4 16QAM
0 Iterations	92%	92.3%	77.7%	55.5%	76.8%	53.1%	54.74%	67.4%
1 Iterations	7%	7.64%	22.5%	44.4%	23.1%	44%	38.9%	28.7%
4 Iterations	0.04%	0.02%	0.05%	0.05%	0.03%	0.08%	0.18%	1%

Table 4-6 Probability of equalization iterations for system with LDPC encoder for highest SNR point of Figure 4-7.

Encoder	LDPC							
Channel	Channel II				Channel III			
MCS	½ QPSK	¾ QPSK	½ 16QAM	¾ 16QAM	½ QPSK	¾ QPSK	½ 16QAM	¾ 16QAM
0 Iterations occ.	76.5%	70.6%	53.9%	23.12%	95.5%	96.3%	98.41%	98.1%
1 Iterations occ.	22%	28.6%	44.5%	70.26%	4.4%	3.26%	0.63%	1%
4 Iterations occ.	0.44%	0.05%	0.11%	0.24%	0.01%	0.08%	0.58%	0.6%

Next we comment on the computational complexity of each equalization iteration. We have employed the low-complexity minimum mean square error (MMSE) equalizer of [BCF19], which requires 2 FFT with size N per iteration. For the soft demapper and mapper, we considered the low-complexity solution of [SFS11] that requires J complex multiplications per symbol to compare the symbol estimate to all constellation points, where J is the QAM order. The soft mapper is required from the first iteration on and requires $\log_2(J)$ multiplications to convert a-priori log likelihood ratios (LLRs) to symbol probabilities and $2*J$ complex multiplications to convert symbol probabilities to mean and variance of a-priori symbol estimates. Regarding the decoders, computing the exact complexity is out of the scope of this report, since there are several possible implementations of these components. For instance, for both decoders we have selected optimal decoding algorithms for performance assessment. In particular, we have used the BCJR log-MAP implementation, sub-optimal solutions are the max-log-MAP and soft-output Viterbi algorithm (SOVA) [RVH95]. For the LDPC decoder, we have used the SPA algorithm, which has product operations that are not desired for practical implementations. Thus, low-complexity algorithms that rely only on summations have been developed in [FMI99] with good performance-complexity trade-off.

4.2.3 Conclusions

The outcomes of our analysis revealed that the sub-THz channel can be sufficiently selective in frequency, such that the performance of DFTs-OFDM is degraded due to ISI. Thus, the iterative equalization structure was investigated in order to mitigate the ISI with the cost of extra hardware complexity. For instance, for the Channel III (more selective), the performance gain is in the range of 1.5-3 dB for the LDPC encoder, and 3-7 dB for the convolutional encoder. Typically, higher MCS leads to a higher gain. Another interesting result is that the best encoder, in terms of performance, depends on how much the channel is selective. In particular, the results have shown that for Channel I and II, the LDPC code has better performance and requires more additional iterations, while for Channel III, the convolutional code has better performance and requires more additional iterations. An important point to make here is that, based on our initial data analysis, the Channel III situation happens rarely among the complete data set, while situations like Channel I and Channel II are more common. This fact favors the LDPC encoder choice in general in terms of performance. In any case, a more general investigation with a larger set of measurements or with statistical model is expected in future work. Lastly, we have shown that amount of necessary equalization iterations is relatively low, i.e., in most of the cases the receiver runs no or 1 iteration. This indicates that the extra signal processing due to iterative equalization is not very high.

4.3 Impact of RF impairments on the performance of CP-OFDM, DFTS-OFDM and SC-FDE

4.3.1 Impact of phase noise

In this subsection the robustness against phase noise of cyclic prefix OFDM (CP-OFDM), DFT-S-OFDM and SC-FDE is assessed. In particular, the ability to mitigate its impact using realistic compensation algorithms with tolerable processing complexity is in focus.

A single TX, RX antenna system model is considered (analog beamforming) with parameters mostly follow NR design. A carrier frequency of 120 GHz with a bandwidth of 3.93 GHz and a subcarrier spacing of 960 kHz are chosen for this study. LDPC channel coding with code rate $\frac{3}{4}$ is applied. For each transmission type a maximal occupied channel bandwidth is used, namely 3.17 GHz, 2.95 GHz, and 3.92 GHz for CP-OFDM, DFT-S-OFDM and SC-FDE, respectively. For this preliminary study an AWGN channel is considered. Phase noise model II (described in Section 3.6.6.2) was used in the analysis. For compensation purpose Phase Tracking Reference Signal (PT-RS) are inserted, closely follows the NR mechanism [38.211]. In case of SC-FDE transmission a root raise cosine pulse shaping filter is applied to limit the spectral bandwidth. As in NR standard no filtering and windowing is used for CP-OFDM and DFT-S-OFDM transmissions. Simulation parameters are summarized in Table 4-7.

Table 4-7: Setting parameters

Parameter	Value
Carrier frequency (GHz)	120
FFT size	4096
Occ. BW (GHz)	O:3.17 / D:295 / S:3.92
Coding	LDPC 3/4
RRC β	0.3 (SC-FDE only)
Cyclic Prefix (%)	7
PT-RS (%)	3
Nr.of T_x, R_x Antenna	1,1

Simple least square algorithm and a subsequent interpolation can be used to mitigate the phase noise effect for DFT-S-OFDM and SC-FDE. For CP-OFDM case phase noise induces common phase error (CPE) and inter-carrier interference (ICI). CPE can simply be corrected by an average de-rotation phase value measured on PT-RSs. The processing complexity is comparable to that of the above mentioned compensation algorithm applied to DFT-S-OFDM and SC-FDE. However, to further suppress the phase noise induced ICI contribution, knowledge on correlation of each sub-carrier to many other neighbored sub-carriers is required. Such compensation algorithm is of much higher processing complexity. Therefore, to keep the implementation complexity comparable, ICI mitigation for CP-OFDM is not considered.

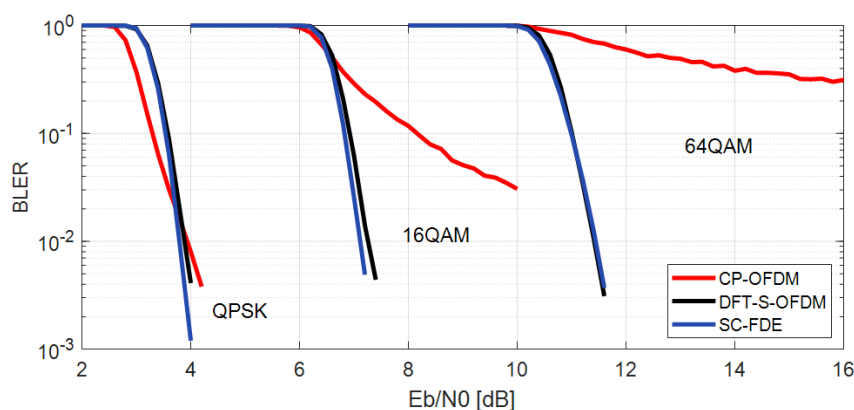


Figure 4-8: BLER performance for different modulation orders and waveforms. Phase noise is compensated applying the described algorithms

Figure 4-8 shows the BLER performance as a function of $\frac{E_b}{N_0}$ after phase noise compensation for the different modulation orders and waveforms. As can be seen, CP-OFDM clearly suffers from the strong remaining ICI, except for the low modulation order case QPSK. Compared to DFT-S-OFDM and SC-FDE, CP-OFDM benefits from averaging over higher number of available PT-RS such that a better noise suppression can be achieved. This effect is more pronounced and hence can be observed in the low $\frac{E_b}{N_0}$ region. Phase noise can be well mitigated in case of DFT-S-OFDM and SC-FDE transmissions using the same simple algorithm. Both exhibits similar BLER performance for all modulation orders. Note that the number of deployed PT-RS for different waveforms with different occupied channel bandwidth is appropriately scaled, such that the same PT-RS overhead is accounted for all waveform candidates.

Further extensions of the study are needed to include important effects of e.g. multi-path channel, hybrid beamforming.

4.3.2 Impact of PA nonlinearity and effects on the link budget

4.3.2.1 PAPR Results

PA is identified as the most power consuming component in the transmitter, it is therefore highly desired to allow PAs to operate at their optimal efficiency, e.g. with output power backoff (OBO) as low as possible. PAPR directly affects the PA efficiency and hence is an important design parameter. Different waveform inherently exhibits different PAPR characteristics. Figure 4-9 shows complementary cumulative density function (CCDF) of the PAPR level of the multi-carrier CP-OFDM, the DFT-S-OFDM and the true single-carrier SC-FDE for standard 256-QAM modulation. The setting parameters are the same as in section 4.3.1 For the PAPR computation, the baseband analog sampled signal is considered.

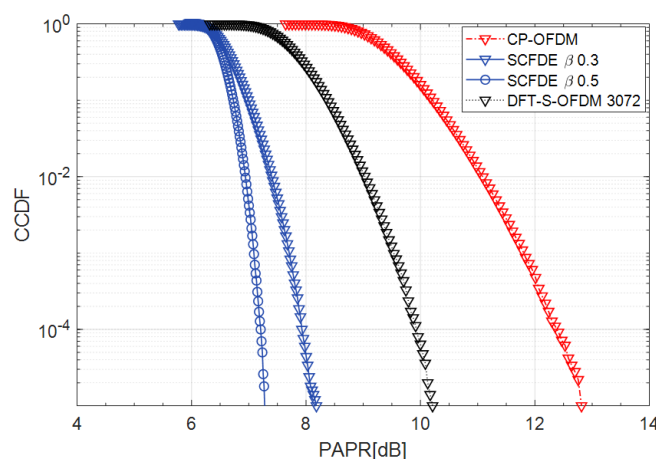


Figure 4-9: PAPR characteristics of CP-OFDM, DFT-S-OFDM and SC-FDE with 0.3 and 0.5 rolloff

High PAPR is a well-known characteristic of multi carrier transmission like CP-OFDM (red curve) and stemming from the superposition of the individual subcarriers carrying the signals during the FFT operation. The larger the FFT size the higher the resulting PAPR. For the studied case a PAPR of 12.8 dB is reached at 10^{-5} of the CCDF. In case of DFT-S-OFDM, the additional DFT before the iFFT spreads out the phase and helps to reduce the PAPR level (black triangle in Figure 4-9). The PAPR reduction amounts to 2.6 dB compared to the CP-OFDM case. Single carrier block transmission SC-FDE - avoiding the FFT operation in the transmissions - features the lowest PAPR level. Envelope fluctuation introduced by signal modulation and pulse shaping filter determine the PAPR level in that

case. A RRC pulse shaping filter was applied to confine the signal spectrum. Depending on the shape of the RRC (i.e. the roll-off factor β) the PAPR level varies. An increase by 0.8 dB in PAPR is induced when changing β from 0.5 to 0.3 (blue triangle vs. blue circle in Figure 4-9). Compared to multi-carrier CP-OFDM and DFT-S-OFDM transmissions, a reduced PAPR up to 5.5 dB and 3 dB can be observed. In upper mmW scenario this can beneficially be translated into to a highly desired range extension. Under assumption of free space path loss in line of sight conditions a gain of 3dB in the signal power corresponds to approximately a factor of 1.4 in range extension.

4.3.2.2 PA output backoff and link budget comparison of OFDM and DFTS-OFDM

DFT-spread OFDM (DFTS-OFDM) can be considered a variation of a standard OFDM waveform, where the DFT precoding of the symbols before mapping onto subcarriers helps reduce the overall PAPR and, consequently, output backoff of the PA, leading to an improvement of the link budget. Due to this favourable property and relative ease of incorporation into the overall design of layer-1 procedures, DFTS-OFDM was adopted for the uplink (UL) of the Long-Term Evolution (LTE) and NR standards.

Methodology and system setup

PAPR is often used for quantifying envelope variations of waveforms but is a relatively poor predictor OBO of PA. Cubic metric is a better OBO predictor [KNS16]. The best OBO estimate, naturally, is obtained by taking into account constraints on in- and out-of-band distortion generated when a signal with non-constant envelope passes through a nonlinear PA and determining the OBO that will meet these constraints.

The above-mentioned approach for finding the exact value of OBO comprises the first step of the study. In-band distortion (measured by error vector magnitude, EVM) and out-of-band distortion (measured by adjacent channel leakage ratio, ACLR) of a signal at the output of a nonlinear PA are tracked as the value of OBO is swept. ACLR constraint is chosen to fit the out-of-band emissions requirements in the 60 GHz band. A standard set of PSK/QAM modulations is used. In the second step of the study, OBOs found in the first step are applied (as a regulator of the level of nonlinearity distortion) in link-level simulations under the influence of a nonlinear PA, for a set of modulation and coding schemes (MCS) taken from 5G NR specifications. In the third and final step, information from the first two steps is combined with the goal of comparing the differences in link budget between the two waveforms as a function of throughput.

Table 4-8 gives the set of basic system parameters used in the study. Nonlinear distortion introduced by the PA is observed as in- and out-of-band changes of the transmitted signal. One way of quantifying the in-band distortion is the EVM. In this study, the set of requirements on EVM for different modulation schemes is taken from [38.104] and [38.101 – 2]. The procedure to calculate EVM follows the specifications outlined in [38.104, Annex B.6] and [38.104, Annex B.7]. Values of EVM constraints are given in Table 4-8.

Table 4-8: System parameters for OFDM/DFTS-OFDM comparison study

RF impairment	PA nonlinearity
PA model	30-70 GHz memoryless GaN (PA model I, cf. section 3.6.6.1)
Carrier frequency	60 GHz
Subcarrier spacing	960 kHz
Channel BW (data subcarriers + guard bands)	2.16 GHz
Configured BW (only data subcarriers)	1.88 GHz
FFT size	8192

Time period for waveform metric averaging	10 ms
Modulations for OBO estimation	<ul style="list-style-type: none"> – $\frac{\pi}{2}$ BPSK, QPSK, 16-QAM, 64-QAM – Additionally, $\frac{\pi}{2}$ – BPSK with pulse shaping for DFTS-OFDM
Number of BSs/number of UEs	1/1
Number of Tx antennas/Number of Rx antennas	1/1
DMRS included in ACLR/PSD calculation	no
PS filter for $\frac{\pi}{2}$ – BPSK, DFTS-OFDM	$\delta[n] - 0.28\delta[n - 1]$
ACLR constraint	26 dB
EVM constraint (BPSK/QPSK/16-QAM/64-QAM)	30%/17.5%/12.5%/8%
Channel model (link-level simulations)	TDL-A, 10 ns delay spread, 3 km/h UE speed
Modulation and coding schemes (link-level simulations)	DFTS-OFDM: MCS 0/2/4/6/8/10/12/14/16/18/20/22/24 [38.214, Table 5.1.3.1 – 1], $q = 1$ OFDM: MCS 0/2/4/6/8/10/12/14/16/19/21/23/25 [38.214, Table 5.1.3.1 - 1]

Step 1: PA OBO as a function of EVM, ACLR and spectral emission constraints

One metric for quantifying the level of out-of-band distortion is ACLR. Following the specification in [38.104, Section 6.6.3.1], and [38.104, Table 9.7.3.3 - 1], ACLR is calculated as the ratio of signal power contained in the band with the bandwidth equal to configured system bandwidth BW_{config} , centered on the system carrier frequency and the power in the band with bandwidth equal to BW_{config} , centred on a frequency whose distance from system carrier frequency is equal to the nominal channel bandwidth $BW_{channel}$ of the system. Figure 4-10 illustrates these relations.

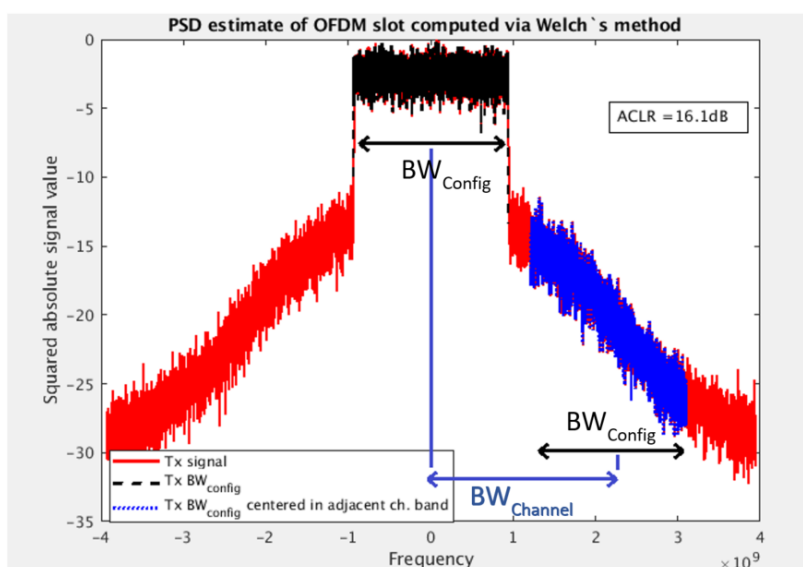


Figure 4-10: illustration of terms essential for ACLR calculation as per 3GPP specification

Finally, by following the recommendation in [38.104, Table 9.7.3.3 - 1], the minimum ACLR is set to 26 dB. With these constraints in place, OFDM and DFTS-OFDM waveforms are generated for each of the four modulation schemes and a nonlinear PA model with a certain value of OBO is applied on the resulting waveforms. The value of OBO is swept until the minimum OBO is found where both EVM and ACLR constraints are satisfied. The results of this simulation are shown in

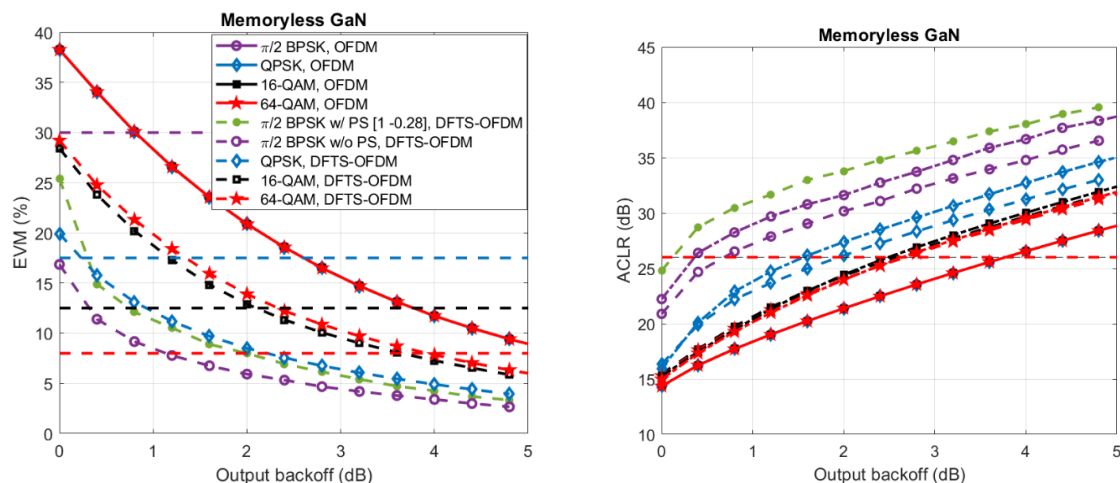


Figure 4-11: EVM and ACLR as function of OBO for 60 GHz memoryless GaN PA

It can be noted that ACLR is the dominant performance constraint at lower modulation orders (BPSK – 16-QAM) and that EVM begins to dominate at higher modulation orders (64-QAM). Minimum OBO values are shown in Figure 4-12.

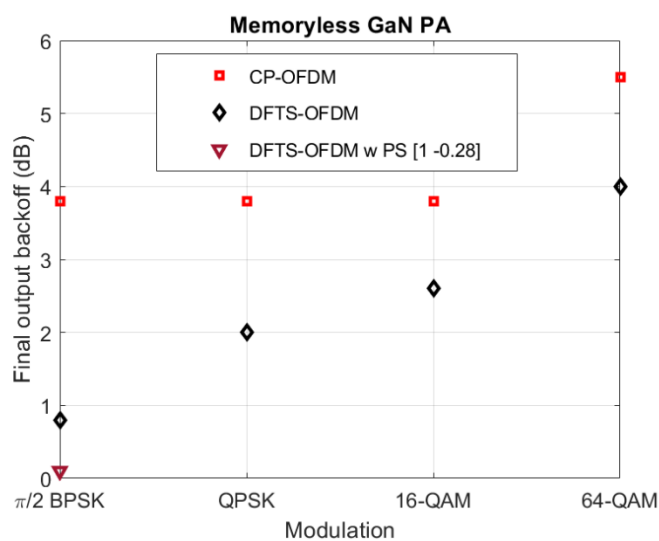


Figure 4-12: Minimum OBO needed for satisfying EVM and ACLR constraints

Rather expectedly, OBO needed for OFDM does not depend on modulation order as envelope variability stays approximately the same for all modulation orders. As DFTS-OFDM is closer to (or rather, equivalent to) a single-carrier waveform, impact of constellation size on envelope variability and therefore minimum OBO is clearly visible. Remarkably, $\frac{\pi}{2}$ -BPSK with pulse shaping has such low envelope variations that minimum OBO is almost 0 dB.

Step 2: BLER simulations under the influence of nonlinear PA

In the next step of the study, the performance of 5G NR modulation and coding schemes defined in [38.214] is simulated for both OFDM and DFTS-OFDM under the influence of the nonlinear PA.

Backoffs applied to each MCS are the ones determined in the previous step (e.g. for an MCS with 16-QAM and DFTS-OFDM, PA OBO is set to 2.6 dB). A selection of link-level results is given in Figure 4-13 and Figure 4-14 as illustration (MCSs 0, 10 and 20).

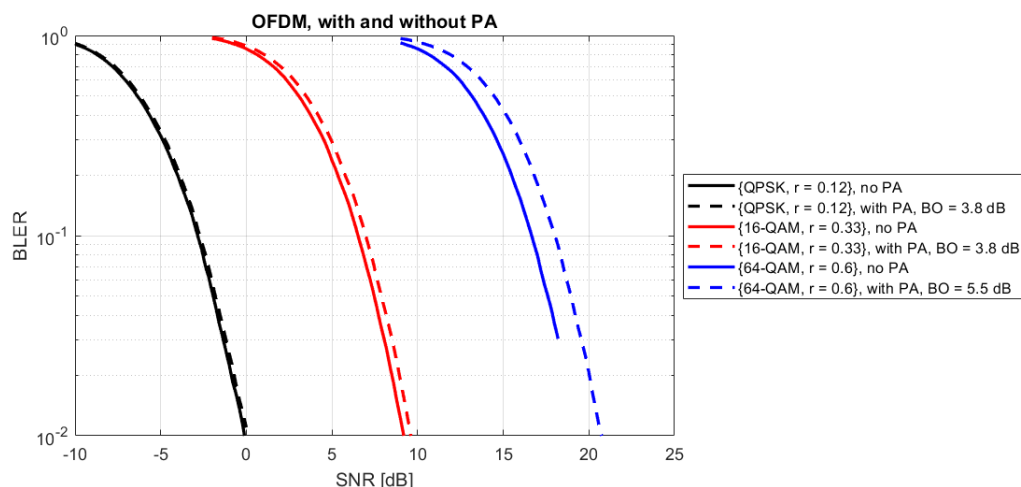


Figure 4-13: selection of BLER simulation results, OFDM

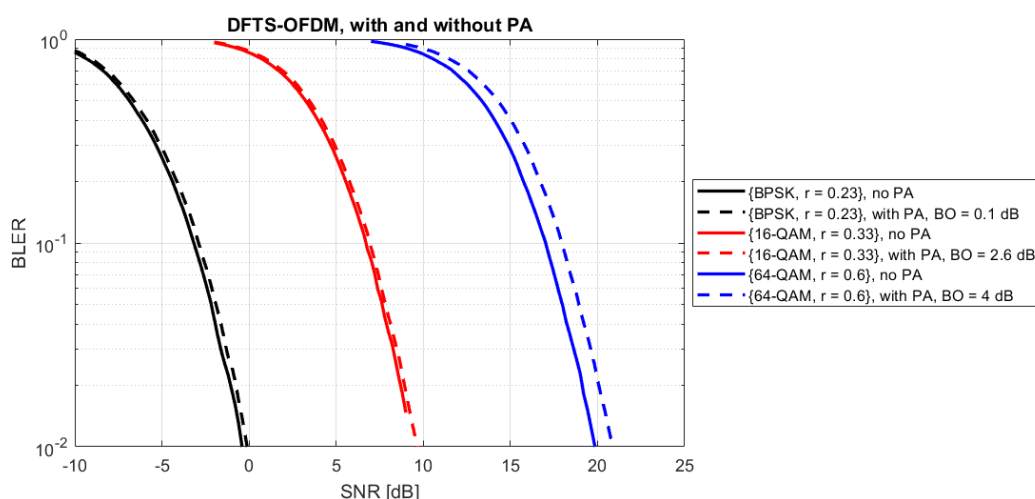


Figure 4-14: selection of BLER simulation results, DFTS-OFDM

Step 3: Link budget comparison between OFDM and DFTS-OFDM

PA OBO needed for satisfying in-and out-of-band distortion constraints and performance degradation due to nonlinear distortion (measured e.g. as the SNR loss, i.e. horizontal distance between “no PA” and “with PA” curves in Figure 4-13 and Figure 4-14) will adversely impact the link budget and with that the maximum distance between radios (e.g. base station and UE). This “link budget shrinking” will be different for OFDM and DFTS-OFDM. Results obtained in steps 1 and 2 need to be combined and presented on a fair basis in order to infer which of these two waveforms provides better link budget/coverage, under which circumstances and by how much. To this end, we define first the maximum coupling loss (MCL) as

$$\begin{aligned}
 MCL &= P_{tx, desired} - OBO - RX_{sens} \\
 &= P_{tx, desired} - OBO - (SNR + P_{noise} + NF),
 \end{aligned} \tag{4-3}$$

where $P_{tx,desired}$, RX_{sens} , P_{noise} are expressed with dBm values, and OBO , SNR and NF are expressed with dB values. Normalizing this metric with noise power and NF (and thus removing the effects of bandwidth) we arrive at the relative MCL (RMCL):

$$RMCL = P_{tx,desired} - OBO - SNR. \quad (4-4)$$

On the other hand, per-user throughput as a function of SNR can be calculated as

$$Th(SNR) = SE[1 - BLER(SNR)]. \quad (4-5)$$

Evidently, RMCL and throughput are connected through SNR. One way of connecting the results from steps 1 and 2 is to sweep the SNR points, determine maximum throughput at that SNR among all possible MCSs, note the OBO being used and thus obtain RMCL. For fairness and simplicity, $P_{tx,desired}$ can be set to a dummy value such as 0 dBm for all MCSs and both waveforms. Results thus obtained are shown in Figure 4-15.

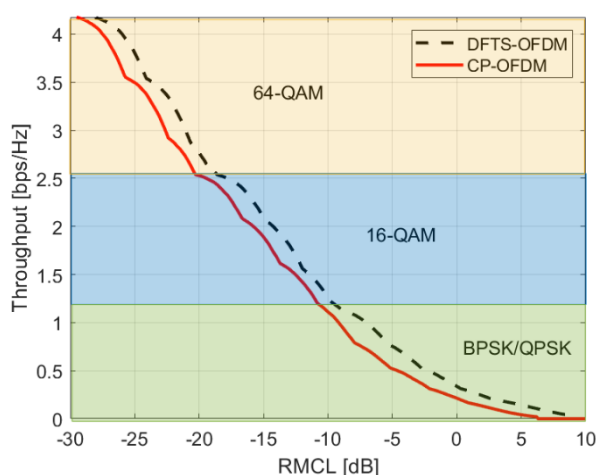


Figure 4-15: Throughput as function of RMCL for OFDM and DFTS-OFDM

It can be seen from the preceding discussion that RMCL is a measure of link budget needed to support a certain performance, remaining after one normalizes for other factors such as antenna array gains, pathloss and noise. For a particular throughput, therefore, a waveform having a larger RMCL will be able to support operation on a larger maximum distance. The above result is then reformulated by calculating the difference in RMCL, $RMCL_{diff} = RMCL_{DFTS-OFDM} - RMCL_{OFDM}$ for a constant throughput. This result is shown in Figure 4-16.

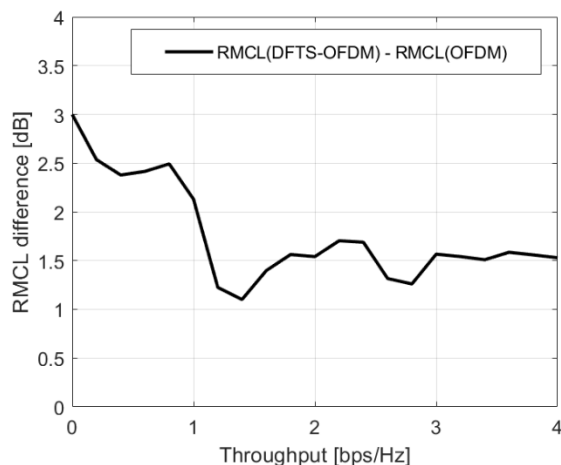


Figure 4-16: Difference in RMCL between DFTS-OFDM and OFDM as a function of throughput

If one wants to go a step further, $RMCL_{diff}$ can be converted into range extension when using DFTS-OFDM instead of OFDM. Namely, assuming free-space propagation (propagation factor 2), it is relatively easy to show that the ratio of achievable propagation distances for which performance (throughput) and Tx power are the same can be calculated as

$$\frac{d_{DFTS-OFDM}}{d_{CP-OFDM}} = \sqrt{10^{\frac{RMCL_{diff}}{10}}}. \quad (4-6)$$

For example, following the result shown in Figure 4-16, for a system using DFTS-OFDM and a system using OFDM, where both systems have the same Tx power and same throughput, the system using DFTS-OFDM can operate at a 30-40% larger propagation distance between the Tx and Rx compared to the system using OFDM. For larger throughputs, the DFTS-OFDM system will be able to support a propagation distance that is around 20% larger than the OFDM system.

4.3.3 DFTS-OFDM under joint impact of PN and PA nonlinearity

In this part we investigate the impact of the non-linear distortion of the PA at the transmitter with the PN at the receiver in a downlink (DL) scenario. The same PN model also used in section 4.4.1 is used (details are described in section 3.6.6.2). The PA model is the same as the one used in section 4.3.2 (details of the model can be found in section 3.6.6.1). This investigation is only considering DFT-s-OFDM. The simulation parameters are described in Table 4-9.

Table 4-9: System parameters for OFDM/DFTS-OFDM comparison study

RF impairment	PA nonlinearity
PA model	70 GHz memoryless GaN (PA model I)
Carrier frequency	70 GHz
Subcarrier spacing	960 kHz
Channel BW (data subcarriers + guard bands)	400 MHz
Time period for waveform metric averaging	10 ms
Number of BSs/number of UEs	1/1
Number of Tx / Rx antennas	1/1
Code Rates	0.75

Modulation format	QPSK, 16-QAM, 64-QAM
PN compensation	Ideal per DFT-s-OFDM symbol
Channel	AWGN
RxType	linear (MMSE CE + MMSE equalization)
DMRS	NR
FEC	NR LDPC
PA output power back-off dB	4 (QPSK), 5 (16-QAM), 6 (64-QAM)

The results of this comparison are shown in Figure 4-17. It is obvious that for QPSK modulation the influence on the performance is minimal (0.2 dB SNR range). As for 16-QAM the PAPR is higher there and the ICI due to the PN is the same the performance with RF impairments is about 1 dB worse than without considering these aspects. For a 64-QAM modulation format we cannot even reach 0.01 BLER at a very ideal SNR of 30 dB. Considering that in this initial result we only consider some RF impairments models at 70 GHz we expect a larger influence of these by the time the models at 100 + GHz carrier frequency are available.

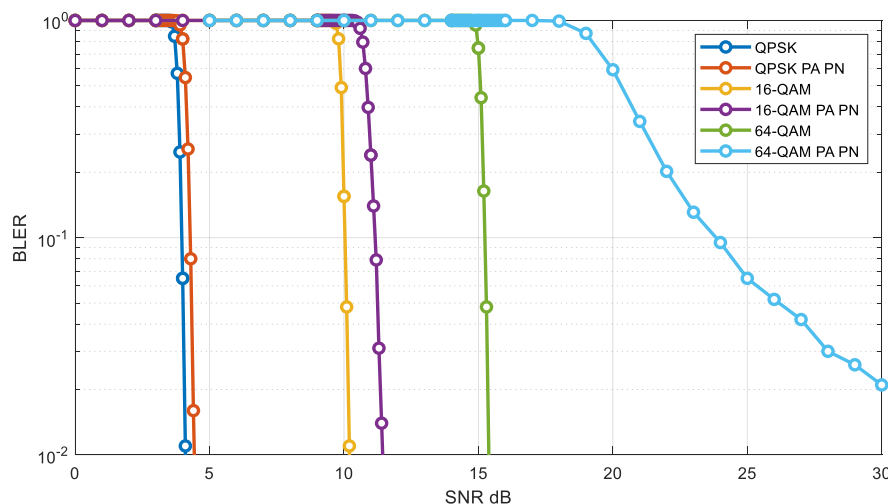


Figure 4-17: DFT-s-OFDM performance with RF impairments.

4.4 Performance of zero-crossing modulation under the influence of phase noise

In the following, the influence of phase noise on the performance of systems employing ZXM with 1-bit quantization and temporal oversampling at the receiver is investigated in terms of the uncoded BER. The results presented are, however, preliminary results and may only partly reflect the complete influence of phase noise on the system, in particular the simulations have been conducted without a phase noise tracking unit.

The baseband representation of the system model considered in this section is depicted in Figure 4-18.

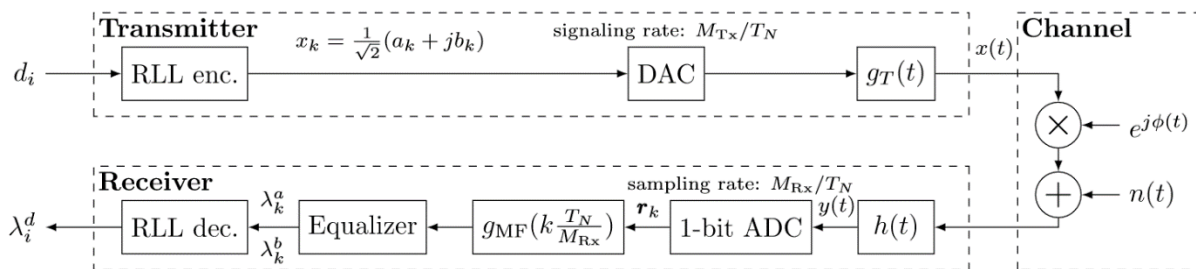


Figure 4-18: Baseband system model.

We assume ZXM by combining faster-than-Nyquist (FTN) signalling and RLL encoding for in-phase and quadrature component independently. At the transmitter i.i.d. input bits are encoded using the finite state machine RLL encoders derived in [NDH+20a] and converted to an analog signal by the DAC. The analog transmit signal is shaped by a real valued transmit filter $g_T(t)$ and is therefore given by

$$x(t) = \sum_{k=-\infty}^{\infty} x_k g_T\left(t - k \frac{T_N}{M_{Tx}}\right), \quad (4-7)$$

with $x_k \in \left\{\frac{1+1j}{\sqrt{2}}, \frac{1-1j}{\sqrt{2}}, \frac{-1+1j}{\sqrt{2}}, \frac{-1-1j}{\sqrt{2}}\right\}$, M_{Tx} being the FTN signalling factor and T_N denoting the Nyquist interval, respectively. Increasing the signalling factor to values larger than 1 introduces ISI, which is mitigated by the RLL sequences. In the scope of this investigation the d-constraint of the RLL sequence is always set to $d = M_{Tx} - 1$, as proposed in [NDH+20].

The channel introduces phase noise, which is generated according to PN model I, described in Section 3.6.6.2, and additive white Gaussian noise. At the receiver the signal is filtered with a real valued analog receive filter $h(t)$, such that the unquantized received signal is given by

$$y(t) = (x \cdot e^{j\phi} * h)(t) + (n * h)(t), \quad (4-8)$$

where $\phi(t)$ is the PN process and $n(t)$ is the additive white noise. With 1-bit quantization, the receiver has only access to

$$r_k = \text{csign}\left(y\left(k \frac{T_N}{M_{Rx}}\right)\right) = \text{sign}\left(\text{Re}\left(y\left(k \frac{T_N}{M_{Rx}}\right)\right)\right) + j \cdot \text{sign}\left(\text{Im}\left(y\left(k \frac{T_N}{M_{Rx}}\right)\right)\right), \quad (4-9)$$

where $\text{sign}(x)$ is the signum function and M_{Rx} is the normalized sampling rate. Here, the ratio $M = \frac{M_{Rx}}{M_{Tx}}$ is termed the effective oversampling factor. Subsequently, the stream of 1-bit quantized samples is filtered by a digital matched filter $g_{Mf}(t) = (g_T * h)(-t)$ and is passed to the equalizer. For this investigation we use a low complexity approximation of the linear minimum mean square error (LMMSE) equalizer, which was proposed in [ZNS+21]. Based on the filtered, 1-bit quantized observations, the equalizer creates estimates for the RLL symbols. These are then used by the low-complexity, Viterbi-based RLL decoder from [NML+21], which creates estimates for the transmitted bits.

In this deliverable, the influence of PN on the performance of ZXM is observed in terms of the degradation of the uncoded BER. In conformity with PN model I, all simulations have been carried out with a carrier frequency of 70 GHz and a bandwidth of 3 GHz. The design margin (DM) parameter was set to 0dB. For the transmit filter $g_T(t)$, we assume a root-raised cosine (RRC) filter with a roll-off factor of $\beta = 0.6$. For the estimation of a constant phase offset the application of uniform phase dithering by sampling at a low IF has been proposed in [SDF21], which has also been used for an early

state PN tracking approach. With low IF sampling, the analog receive filter needs to be broadened correspondingly, however, as we do not consider PN tracking for this deliverable, we assume the receive filter $h(t)$ as an ideal rectangular filter with bandwidth $W_h = W_{g_T}$ and thus, $g_{M_f}(t) = g_T(t)$. Note, that for the communication performance this approach is suboptimal, as the receiver captures more noise power than necessary. Finally, for the investigations done here, we always assume an effective oversampling factor of $M = 3$.

In Figure 4-19, we see the BER performance over $\frac{E_b}{N_0}$ for different FTN signalling factors. In the presence of PN we observe an error floor, except for $M_{Tx} = 1$, likely because the error floor is too low to be simulated with reasonable effort. Since a higher FTN signalling factor means that the zero-crossings of the transmit signal are aligned on a finer grid, it is somehow intuitive that the influence of PN becomes more severe. Moreover, for $M_{Tx} = 3$ and no PN, we observe an up-rise of the BER curve at around 25 dB. This could be caused by stochastic resonance in the $\frac{E_b}{N_0}$ range from 14 dB to 18 dB, however, to give a definite answer, more investigation is needed.

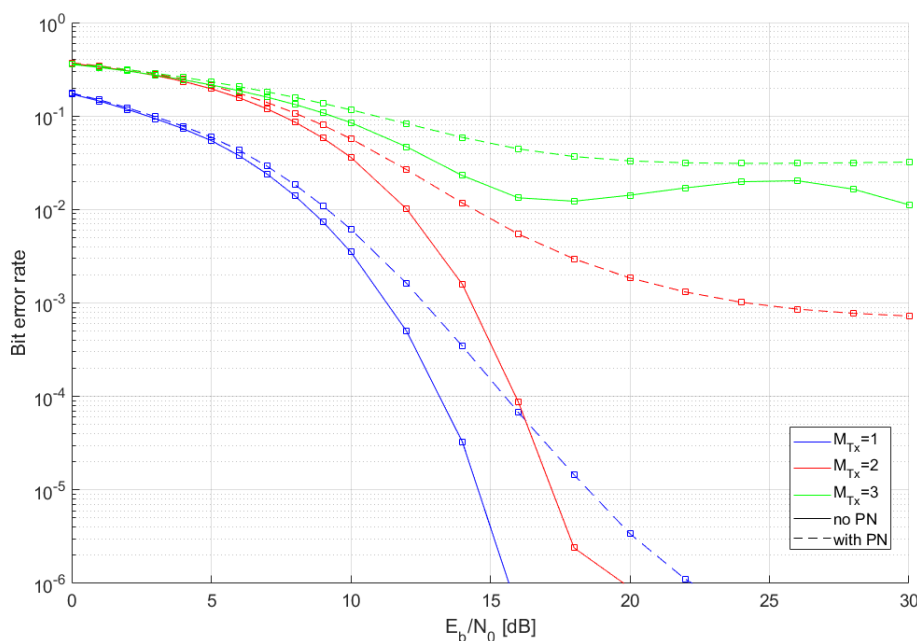


Figure 4-19: Performance comparison in terms of BER for different FTN signaling factors M_{Tx} , $M = 3$.

To conclude, the impact of PN on the communication performance is more severe for higher FTN signalling factors, as it can be expected. It has to be emphasized, that the results are only of preliminary nature, as we do not perform PN tracking. Moreover, due to the receive filter that captures too much noise power, the system model is not optimal from a perspective of communication performance. Further optimization is subject of ongoing research.

4.5 End-to-end performance analysis of constrained-envelope modulation under PA nonlinearity

Continuous Phase Modulation (CPM) [AAS86] has been the technique of choice in the field of *constant* envelope digital communications, due to its good spectral properties, well-studied receiver structures, and its ability to support advanced channel coding schemes via concatenated coding and turbo receivers [MA01]. With partial response CPM, using frequency pulses of several symbol durations, CPM becomes a coded modulation scheme. The envelope properties of the serially modulated signals after

digital to analog (D/A) conversion depends on the employed pulse-shaping filter. Even a constant envelope signal constellation such as M -ary Phase Shift Keying (MPSK) has typically substantial envelope variations after the pulse-shaping filter. Only continuously modulated phase signals such as CPM have a true constant envelope in the analog domain.

Constrained envelope modulation schemes have been considered before, e.g., in the 3GPP EDGE modulation scheme based on offset M -ary Phase Shift Keying (MPSK). The offset MPSK avoids zero crossing in the in-phase versus quadrature-phase (I/Q) diagram, but still yields quite significant envelope variations that could cause substantial spectral regrowth with highly non-linear amplifiers.

The envelope property of the modulated signal after D/A conversion is typically characterized by means of the peak-to-average power ratio (PAPR) [FKH08, eq. (15)], [NP00], or the Raw Cubic Metric (RCM) as defined in [FKH08, eq. (16)], which is closely related to the 3GPP Cubic Metric (CM) defined in [3GPP4-040367]. The rationale behind CM and RCM is the fact that the primary cause of transmit-signal distortion is the third order nonlinearity of the amplifier gain characteristic.

In Figure 4-20, we show how these metrics relate to the overall efficiency of a typical high power amplifier (HPA) for a set of signals having different envelope properties [SE10]. Here, the HPA overall efficiency is defined as $\eta_A = P_{\text{Out}} / (P_{\text{DC}} + P_{\text{In}})$, where P_{In} is the RF power at the input of the HPA, P_{Out} is the resulting RF output power and P_{DC} is the power at the Direct Current (DC) input of the amplifier. For signals with a large PAPR, the average input power must be reduced (this is known as input power backoff) in order to keep the peak power of the input signal less than or equal to the saturation input level of the HPA. If the input power is not backed off then signal distortion occurs, the most serious consequence of which is out-of-band spectral regrowth.

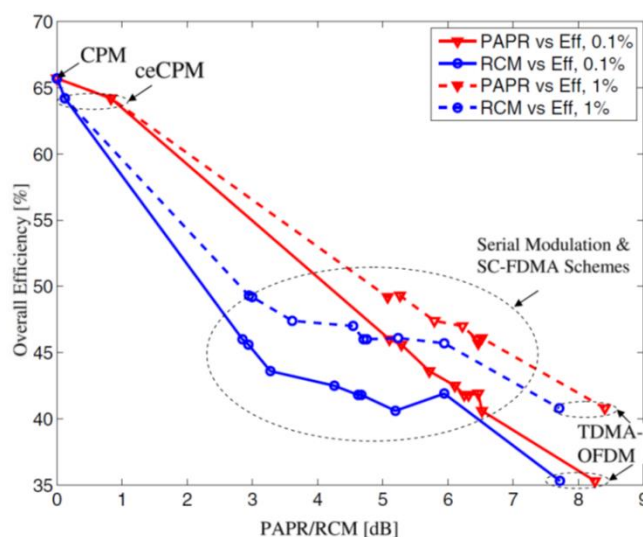


Figure 4-20. Maximum overall HPA efficiency versus mean PAPR and RCM of various modulated signals with 1% and 0.1% clipping level [SE10].

As seen in Figure 4-20, HPAs are most efficient when they are driven into saturation. Therefore, input power backoff reduces the efficiency of the HPA and is detrimental to battery-powered devices, which have limited power resources. Because of this, PAPR reduction has been the subject of numerous studies and various schemes have been developed to address this issue - such as coding and tone reservation [DJ99], [KJ04], [JA04], predistortion schemes [ALR01], and clipping [Arm02]. An alternative approach involves the transformation of OFDM signals into constant envelope waveforms by phase modulating the OFDM waveform. In [TAP+08], an OFDM waveform is used to phase-modulate a single carrier, and the result is a constant envelope waveform (i.e., the resulting signal has 0 dB PAPR). In [TS02], a similar approach is taken whereby the encoded data is first applied to a DCT (discrete cosine transform) and then passed through a continuous phase modulation (CPM) unit. Although both approaches are novel and result in a constant envelope waveform, neither approach retains the orthogonality of the subcarriers. This implies that some of the advantages of using OFDM, such as low

complexity frequency domain equalization and frequency multiplexing of user data on the uplink, are lost.



Figure 4-21. CPM-DFTS-OFDM precoder

In [WPS11], a scheme employing a sub-sampled CPM encoder as precoder of single carrier frequency division multiple access (SC-FDMA) with interleaved frequency division multiple access (I-FDMA) subcarrier mapping was proposed, which we here denote CPM-DFTS-OFDM, illustrated in Figure 4-21. An important property of the scheme is that it yields very good envelope properties while at the same time maintaining the orthogonal frequency division multiple access (OFDMA) structure. This allows for a simple multiple access scheme through frequency division and permit the reuse of the OFDMA transceiver structure currently in use in OFDMA-based systems. The scheme can provide a very low PAPR signal with very low side lobes, provided the CPM parameters, over-sampling factor and subcarrier mapping are suitably selected [WPS11]. In [WPS11], it is shown that a good PAPR vs spectral efficiency trade-off is obtained with an oversampling factor of two together with IFDMA mapping, but initial investigations have shown that a substantial fraction of the low PAPR properties remains also when using B-IFDMA [SFE+09] with two subcarriers per block, which should increase robustness to carrier frequency offset and Doppler spread. Insertion of trellis termination bits might be needed in case of few subcarriers per user.

Both CPM-DFTS-OFDM and ceCPM can be detected by a low-complexity close-to-optimal Viterbi detector using Reduced State Sequence Detection (RSSD) with 8-16 states [Sve02]. Such a low complexity detection is very beneficial for low energy consumption and low decoding delay. As mentioned, CPM-DFTS-OFDM supports frequency diversity towards fading and narrowband interference, but at the cost of lower spectral efficiency compared to ceCPM that is best suited for less frequency selective channels in order to avoid complex Viterbi equalizer. Both schemes can benefit from an optimization of minimum Euclidean distance under a spectrum constraint function, the higher allowed side-lobes the better receiver sensitivity [Sve02].

We are investigating the end-to-end energy efficiency of CPM-DFTS-OFDM over non-linear amplifiers in comparison with QPSK modulated DFTS-OFDM. Constrained envelope modulation typically needs less power backoff and has better side-lobe suppression than linearly modulated DFTS-OFDM, but also less receiver sensitivity. We are interested in understanding these trade-offs. We target the error probability for a given path loss on a line-of-sight link and evaluate the required power consumption at the transmitter side, under the same constraints on spectral efficiency and sidelobes suppression.

4.6 Concluding remarks

The preliminary waveform studies demonstrate the main analysis flows, design challenges and offer preliminary insights in ways forward for waveform design for 6G. It is evident that the impact of hardware impairments needs to be taken into account since it makes a decisive influence on the choice of waveforms and corresponding signal processing. This impact needs to be carefully and accurately modelled. Another important aspect of waveform design is the complexity of signal processing (digital as well as mixed-signal) since it directly determines the power consumption.

DFTS-OFDM and SC-FDE are shown to possess better robustness towards phase noise and PA nonlinearities compared with legacy OFDM. It is also shown that the complexity of an iterative receiver for DFTS-OFDM does not necessarily need to be high. Preliminary analysis of the sensitivity of ZXMM waveform to phase noise shows a performance degradation for higher FTN factors; however, phase noise compensation has not been assumed and its effects are left for future work. Finally, the concepts behind constrained-envelope modulations and their benefits in improving PA efficiency are demonstrated.

5 Hybrid beam forming analyses

In this section, we first present a generic hybrid beamforming architecture to derive the signal model under ideal assumptions. The goal is to derive a system model to study the theoretical performance limits that are used as references for the performance under realistic hardware. Additionally, we discuss the design constraints based on the hardware preliminary models presented in Section 3.4 and 3.6. As a study case, we study some challenges associated with pure analog beamforming, namely, the beam training strategies and beam tracking. These are influenced by the narrow beam resulting from the high gain requirements at the upper mmW, and the lack of full channel estimation at the input of the antennas, since only the combination of the wireless channel and beamforming is accessible at the baseband.

5.1 Hybrid beamforming architecture

In hybrid beamforming architecture [AMG+14], as shown in Figure 5-1, we consider a transmitter with M RF chains and a phased antenna array with $P > M$ antenna elements. The receiver is equipped with a phased array of $Q > N$ antenna elements, and N receive RF chains. The beamforming is achieved by means of digital precoding and analogue phase and gain control. In particular, at the transmitter a precoding matrix \mathbf{W}_D of size $M \times M$ is used at the digital baseband, and \mathbf{W}_A of size $M \times P$ is a matrix whose elements represent the phase and gain control. Similarly, the receiver employs analogue phase and gain represented by a matrix \mathbf{F}_A of size $N \times Q$, whereas the digital decoding is performed with a matrix \mathbf{F}_D of size $N \times N$. Note that, when $M = N = 1$, the RF architectures reduced to the one transmitter and receiver common path are shown in Figure 3-7 and Figure 3-8.

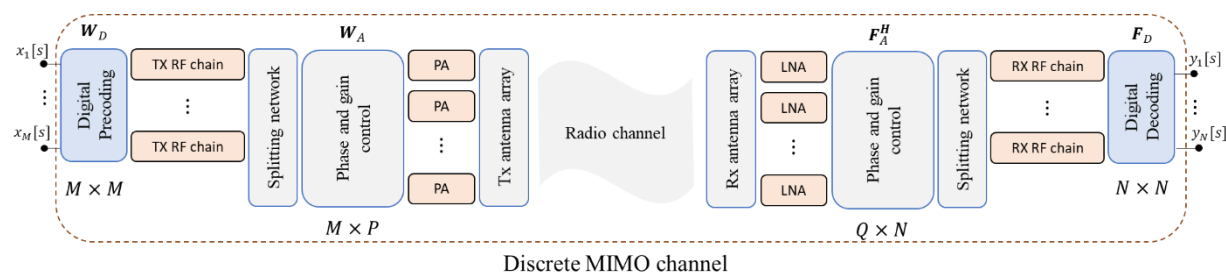


Figure 5-1 Generic hybrid beamforming architecture.

5.1.1 Signal model under ideal hardware

This section focuses on deriving the signal model under ideal hardware and refers to the corresponding HW impairment summarized in section 3.6. Let $\mathbf{x}[s]$ be the input sample vector at the s -th sample. After digital precoding, we get the complex vector $\bar{\mathbf{x}}[s] = \mathbf{W}_D \mathbf{x}[s]$ of size M , which is forwarded to the RF chains shown in Figure 3-7.

5.1.1.1 Ideal transmitted signal

After DAC and filtering, the m -th baseband signal is given by

$$\bar{x}_m(t) = \bar{x}_m^{(I)}(t) + j\bar{x}_m^{(Q)}(t) = \sum_s \bar{x}_m[s] \beta^{(tx)}(t - sT_s) \quad (5-1)$$

where $\bar{x}_m^{(I)}$ and $\bar{x}_m^{(Q)}$ are the in-phase and quadrature components, respectively, T_s the sampling interval, and $\beta^{(tx)}$ denotes the baseband overall response including up-sampling, interpolation, and filtering. Ideally, $\bar{x}_m[s] = \bar{x}_m(sT_s)$, however, in realistic hardware, quantization and sampling impact should be considered. The bandpass signal is generated by the mixer, and can be expressed as

$$s_m(t) = \text{mix}(\bar{x}_m^{(I)}(t), \bar{x}_m^{(Q)}(t)). \quad (5-2)$$

The mixer function $\text{mix}(\cdot)$ involves phase noise and IQ imbalance impairments. In ideal case

$$s_m(t) = \bar{x}_m^{(I)}(t)\cos(2\pi f_c t) - \bar{x}_m^{(Q)}(t)\sin(2\pi f_c t) = \text{Re}[\bar{x}_m(t)e^{j2\pi f_c t}]. \quad (5-3)$$

The bandpass signal is then passed to the splitter to get P signals. Considering the power gain after splitting is G_s , the output signals are given by

$$s_{p,m}(t) = \sqrt{G_s} s_m(t). \quad (5-4)$$

Thereafter, each signal is passed to a gain and shift node defined by $g_{p,m}$ and $\tau_{p,m}$. In theory, the M signals can be combined at the input of the PA, such that

$$s_p^{(PA)}(t) = PA\left(\sum_{m=0}^{M-1} g_{p,m} s_{m,p}(t - \tau_{p,m})\right), \quad (5-5)$$

where $PA(\cdot)$ denotes the PA response, which is subject of modelling in Section 3.6.2. In practical systems, such combining may not be feasible. However, the equation still holds by setting the corresponding unused gains to zeros. Assuming the PA operates in a linear region with power gain G_{PA} ,

$$\begin{aligned} s_p^{(PA)}(t) &= \sqrt{G_s G_{PA}} \sum_{m=0}^{M-1} g_{p,m} s_{m,p}(t - \tau_{p,m}) \\ &= \sqrt{G_s G_{PA}} \sum_{m=0}^{M-1} g_{p,m} \text{Re}[\bar{x}_m(t - \tau_{p,m})e^{-j2\pi f_c \tau_{p,m}} e^{j2\pi f_c t}]. \end{aligned} \quad (5-6)$$

Finally, the amplified signal is then radiated by the antenna element with gain $G^{(tx)}(\theta_a, \phi_a)$ in the direction defined by the elevation angle θ_a and azimuth ϕ_a , such that

$$s_p^{(tx)}(t) = \sqrt{G^{(tx)}(\theta_a, \phi_a)} s_p^{(PA)}(t). \quad (5-7)$$

Under the narrow band assumption, $\bar{x}_m(t - \tau_{p,m}) \approx \bar{x}_m(t)$ the equivalent baseband signal is

$$x_p^{(tx)}(t) = \sqrt{G_s G_{PA} G^{(tx)}(\theta_a, \phi_a)} \sum_{m=0}^{M-1} g_{p,m} e^{-j2\pi f_c \tau_{p,m}} \bar{x}_m(t). \quad (5-8)$$

The term $W_A[p, m] = g_{p,m} e^{-j2\pi f_c \tau_{p,m}}$ denotes the ideal analogue beamforming complex gain. The realistic HW model for analogue beamforming gain and phase shift is discussed in Section 3.6.4.

5.1.1.2 Planar array

For a general planar array with P antenna elements located at (x_p, y_p) , as shown in Figure 5-2, the array steering vector under far field and narrow bandwidth assumptions in the transmission mode is given by [IB05]

$$\mathbf{a}[p](\theta_a, \phi_a) = e^{-j2\pi \frac{\Delta_p}{\lambda}} = e^{-j2\pi \tau_p f_c}, \quad \Delta_p = d_{x,p} \sin \theta_a \cos \phi_a + d_{y,p} \sin \theta_a \sin \phi_a, \quad (5-9)$$

where $d_{x,p} = x_p - x_0$, $d_{y,p} = y_p - y_0$, λ is the wavelength, θ_a the elevation angle, and ϕ_a the azimuth angle. In the receiving mode,

$$\mathbf{b}[p](\theta_b, \phi_b) = e^{-j2\pi\frac{\Delta_p}{\lambda}}, \Delta_p = d_{x,p} \sin \theta_b \cos \phi_b + d_{y,p} \sin \theta_b \sin \phi_b. \quad (5-10)$$

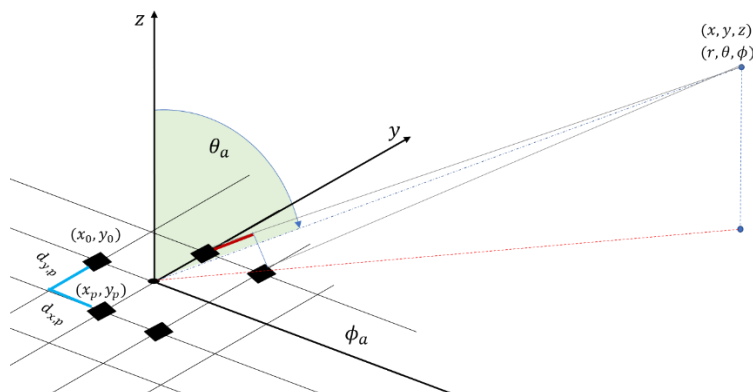


Figure 5-2 General planar array.

The far field assumption holds, when [VBPG15]

$$r > \frac{2L_a^2}{\lambda} = 2\lambda L_\lambda, \quad (5-11)$$

given that $L_a = \lambda L_\lambda$ is the maximum array dimension, which corresponds to the maximum distance between two antenna elements. The validity of the narrow band assumption requires that the signal bandwidth B and the maximum delay across the array τ_{max} fulfils $B\tau_{max} \ll 1$ [Zat98], which can be related to the array dimension and carrier frequency by the relation

$$B \ll \frac{f_c}{L_\lambda}. \quad (5-12)$$

As a result, the baseband signal observed in the direction (θ_a, ϕ_a) can be expressed as

$$\mathbf{x}^{(tx)}(t) = \sum_{p=0}^{P-1} x_p^{(tx)}(t) \mathbf{a}[p](\theta_a, \phi_a). \quad (5-13)$$

The corresponding bandpass signal is $s^{(tx)}(t) = \text{Re}[x^{(tx)} e^{j2\pi f_c t}]$. In a matrix form, the relation between the baseband signal vector $\mathbf{x}(t)$ and $\mathbf{x}^{(tx)}(t)$ is

$$\mathbf{x}^{(tx)}(t) = \sqrt{G_s G_{PA} G^{(tx)}(\theta_a, \phi_a)} \mathbf{a}^T(\theta_{a_a}, \phi_{a_a}) \mathbf{W}_A \mathbf{W}_D \mathbf{x}[t]. \quad (5-14)$$

5.1.1.3 Ideal received signal

Let $r^{(rx)}(t) = CH(s^{(tx)}(t))$ be the bandpass signal at the receiver through a channel with the function $CH(\cdot)$, the detected signal by the q -th antenna is given by

$$r_q^{(rx)}(t) = \sqrt{G^{(rx)}(\theta_b, \phi_b)} r^{(rx)}(t - \tau_q) + v_q^{(rx)}(t), \quad (5-15)$$

where $v_q(t)$ is the equivalent baseband noise. Here, $G^{(rx)}(\theta_b, \phi_b)$ is the antenna element gain at the receive array, $\tau_q = \frac{\Delta_q}{c}$ is the relative delay between the antenna elements, which is related to the steering vector $\mathbf{b}(\theta_b, \phi_b)$, and $v_q^{(rx)}(t)$ is additive noise. The signal is then amplified by LNA that

$$r_q^{(LNA)}(t) = LNA(r_q^{(tx)}(t)), \quad (5-16)$$

with $LNA(\cdot)$ represents the LNA response. In ideal case, the LNA is linear with constant NF. However, in realistic HW, LNA can be non-linear and the NF has non-flat frequency response, as presented in Section 3.6.3.1. Thereafter, the signals pass through beamforming delay and gain, and combiner network, which results in N signals given by

$$r_n(t) = \sum_{q=0}^{Q-1} f_{n,q} r_q^{(LNA)}(t - \tau_{n,q}). \quad (5-17)$$

Next, the receiver mixer is applied to get the baseband signal

$$\bar{y}_n(t) = MIX^{-1}(r_n(t)). \quad (5-18)$$

The realistic mixer introduces phase noise and IQ imbalance, as presented in Sections 3.6.5 and 3.6.6.2. Considering ideal mixer, the received baseband signal is given by

$$\bar{y}_n(t) = \sqrt{G^{(rx)}(\theta_b, \phi_b)} \sum_{q=0}^{Q-1} \mathbf{b}[q](\theta_b, \phi_b) f_{n,q} e^{-j2\pi f_c \tau_{q,n}} y^{(rx)}(t) + \sum_{q=0}^{Q-1} f_{n,q} e^{-j2\pi f_c \tau_{q,n}} v_q(t), \quad (5-19)$$

where $\mathbf{F}_A[q, n] = f_{q,m} e^{j2\pi f_c \tau_{q,n}}$ is the beamforming complex gain, $y^{(rx)}(t) = CH_b(x^{(tx)}(t))$ the baseband received through the baseband channel $CH_b(\cdot)$, $v_q(t)$ the equivalent baseband noise, whose power depends on the bandwidth, thermal noise power density N_0 and LNA noise figure N_F . Therefore,

$$\bar{\mathbf{y}}(t) = \sqrt{G^{(rx)}(\theta_b, \phi_b)} \mathbf{F}_A^H \mathbf{b}(\theta_b, \phi_b) y^{(rx)}(t) + \mathbf{F}_A^H \mathbf{v}(t). \quad (5-20)$$

This signal is then sampled and quantized by ADC, which is practically with limited resolution as discussed in Section 3.3.2. Then, digital decoding is performed such that

$$\mathbf{y}[s] = \sqrt{G^{(rx)}(\theta_b, \phi_b)} \mathbf{F}_D^H \mathbf{F}_A^H \mathbf{b}(\theta_b, \phi_b) y^{(rx)}[s] + \mathbf{F}_D^H \mathbf{F}_A^H \mathbf{v}[s]. \quad (5-21)$$

5.1.1.4 Received signal in multipath channel

As shown in Figure 5-3, the array steering vectors of the transmitter and are denoted as $\mathbf{a}(\theta_{a_k}, \phi_{a_k})$ and $\mathbf{b}(\theta_{b_k}, \phi_{b_k})$ of size P and Q , respectively. The angles θ_{a_k}, ϕ_{a_k} define the direction of departure (DoA), and θ_{b_k}, ϕ_{b_k} the direction of arrival DoA, either for line of sight (LoS) or indirect path via a scattering object located at position P_k . These angles depend on the relative position of the scattering object and arrays, and the relative orientation of the arrays. Accordingly, the corresponding baseband wireless channel matrix is given by [HSE+18],

$$\bar{\mathbf{H}}_k(\theta_{a_k}, \phi_{a_k}, \theta_{b_k}, \phi_{b_k}) = h_k \sqrt{G^{(rx)}(\theta_{b_k}, \phi_{b_k}) G^{(tx)}(\theta_{a_k}, \phi_{a_k})} \mathbf{b}(\theta_{b_k}, \phi_{b_k}) \mathbf{a}^T(\theta_{a_k}, \phi_{a_k}). \quad (5-22)$$

Here, h_k is the path complex gain, $G^{(tx)}(\theta_{a_k}, \phi_{a_k})$ and $G^{(rx)}(\theta_{b_k}, \phi_{b_k})$ are the antenna element gains at the transmit and receive arrays, respectively. Note that $\bar{\mathbf{H}}_k$ is a rank-1 matrix of size $Q \times P$. More details on channel modeling and measurements are presented in Section 7.

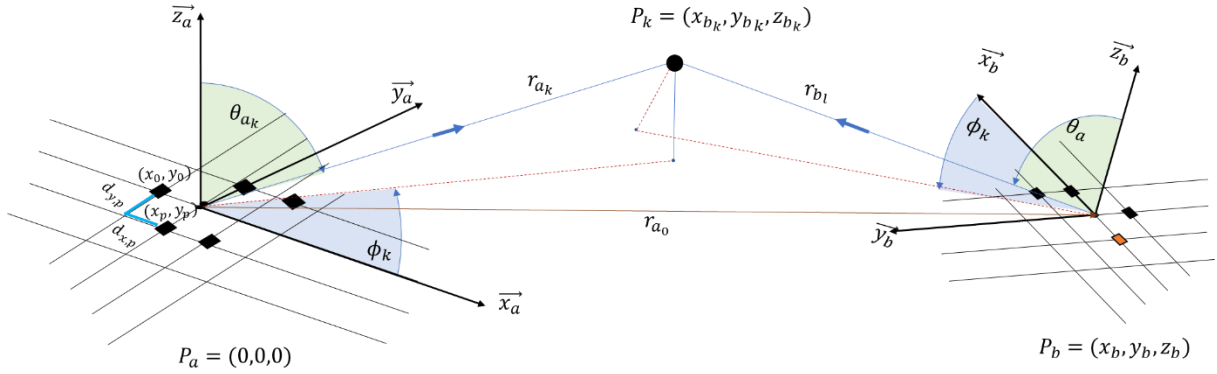


Figure 5-3 Array steering vectors for generic TX and RX planner arrays.

Considering multiple scattering points, which results in multipath channel, and each path reaches the receiver with a delay τ_k . Let $\mathbf{x}(t)$ be the transmitted baseband signal vector of size M , the received baseband signal vector $\mathbf{y}(t)$ of size N can be expressed as

$$\begin{aligned} \mathbf{y}(t) &= \mathbf{F}^H \sum_k \bar{\mathbf{H}}_k(\theta_{a_k}, \phi_{a_k}, \theta_{b_k}, \phi_{b_k}) \mathbf{W} \mathbf{x}(t - \tau_k) + \mathbf{F}^T \mathbf{v}(t) \\ &= \mathbf{F}^H \int \left[\sum_k \bar{\mathbf{H}}_k(\theta_{a_k}, \phi_{a_k}, \theta_{b_k}, \phi_{b_k}) \delta(\tau - \tau_k) \right] \mathbf{W} \mathbf{x}(t) d\tau + \mathbf{F}^T \mathbf{v}(t), \end{aligned} \quad (5-23)$$

where $\mathbf{W} = \mathbf{W}_A \mathbf{W}_D$ and $\mathbf{F} = \mathbf{F}_A \mathbf{F}_D$ are the hybrid beamforming matrices, and $\mathbf{v}(t)$ denotes the AWGN vector. Considering that several paths may have a similar delay τ_l , then the channel can be expressed by clustering the angles that have the same delay $\tau_k = \tau_l$, such that

$$\sum_k \bar{\mathbf{H}}_k(\theta_{a_k}, \phi_{a_k}, \theta_{b_k}, \phi_{b_k}) \delta(\tau - \tau_k) = \sum_l \sum_c \bar{\mathbf{H}}_{c,l}(\theta_{a_{c,l}}, \phi_{a_{c,l}}, \theta_{b_{c,l}}, \phi_{b_{c,l}}) \delta(\tau - \tau_l). \quad (5-24)$$

Therefore, the resulting multipath channel is

$$\mathbf{H} = \sum_l \mathbf{H}_l \delta(\tau - \tau_l) \quad (5-25)$$

where \mathbf{H}_l is the channel matrix corresponding to the delay τ_l is given by

$$\mathbf{H}_l = \sum_c \bar{\mathbf{H}}_{c,l}(\theta_{a_{c,l}}, \phi_{a_{c,l}}, \theta_{b_{c,l}}, \phi_{b_{c,l}}). \quad (5-26)$$

The rank of this matrix depends on the number of directions. During the coherence time of the channel

$$\mathbf{y}(t) = \mathbf{F}^H \sum_l \mathbf{H}_l \mathbf{W} \mathbf{x}(t - \tau_l) + \mathbf{F}^T \mathbf{v}(t). \quad (5-27)$$

and by computing the frequency response of each signal, the frequency-domain is

$$\tilde{\mathbf{y}}(f) = \mathbf{F}^H \tilde{\mathbf{H}}(f) \mathbf{W} \tilde{\mathbf{x}}(f) + \mathbf{F}^T \tilde{\mathbf{v}}(f), \quad (5-28)$$

such that $\mathbf{F}^T \tilde{\mathbf{H}}(f) \mathbf{W}$ is the equivalent MIMO channel, and $\tilde{\mathbf{H}}(f) = \sum_l \mathbf{H}_l e^{-j2\pi f \tau_l}$. Within the coherence bandwidth of the channel, $\tilde{\mathbf{H}}(f)$ can be approximated by a constant matrix.

The channel variation depends on the mobility and the dynamicity of the environment, such that

$$\mathbf{H}(t) = \sum_l \mathbf{H}_l(t) \delta(\tau - \tau_l(t)) \quad (5-29)$$

The time-frequency selectivity of the channel influences the design requirements for waveforms and channel coding as presented in Section 4.3.

5.2 Theoretical limitations under ideal assumptions

This section provides several introduces several limitations under the assumption of ideal hardware, which need to be considered in the implementation.

5.2.1 MIMO consideration

Recall that from (5-28) that $\tilde{\mathbf{y}}(f) = \mathbf{F}^H \tilde{\mathbf{H}}(f) \mathbf{W} \tilde{\mathbf{x}}(f) + \mathbf{F}^T \tilde{\mathbf{v}}(f)$. First, we consider a flat channel with respect to (w.r.t.) to the signal bandwidth, where $\tilde{\mathbf{H}}(f) = \tilde{\mathbf{H}} e^{-j2\pi f \tau_0}$, then

$$\tilde{\mathbf{y}}(f) = \mathbf{F}^H \tilde{\mathbf{H}} \mathbf{W} \tilde{\mathbf{x}}(f) + \mathbf{F}^T \tilde{\mathbf{v}}(f), \text{ and } \mathbf{y}(t) = \mathbf{F}^H \mathbf{H} \mathbf{W} \mathbf{x}(t) + \mathbf{F}^H \mathbf{v}(t). \quad (5-30)$$

In this case, the beamforming weights are independent of the frequency and can be theoretically chosen to maximize the achievable rate. The solution is given by the singular vectors corresponding to the maximum singular values [PRN+03], such that

$$\mathbf{F} = \mathbf{U}_H[:, 0:M-1], \mathbf{W} = (\mathbf{V}_H[:, 0:N-1]) \mathbf{\Lambda}_p, \text{ where } \mathbf{H} = \mathbf{U}_H \mathbf{\Sigma}_H \mathbf{V}_H^H, \quad (5-31)$$

and $\mathbf{\Lambda}_p = \text{diag}(P_0, \dots, P_{M-1})$ is the power allocation matrix, chosen to maximize the data rate under total power constraint. Therefore, with $M \leq N$, we get M SISO channels

$$\tilde{y}_m[f] = P_m \sigma_m \tilde{x}_m[f] + \tilde{v}_m[f] \quad (5-32)$$

The achievable mutual information is

$$R = \sum_{m=0}^{M-1} \log_2(1 + P_m \sigma_m^2 \rho), \text{ where } \rho = \frac{E[|\tilde{x}_m[f]|^2]}{E[|\tilde{v}_m[f]|^2]} \text{ is the signal SNR.} \quad (5-33)$$

As a result, employing a single user MIMO is influenced by the channel rank, where it is required to select $M \leq \text{rank}(\mathbf{H})$ in order to achieve spatial multiplexing. This design parameter is subject to study in the context of channel modeling.

The receiver has access to the combined channel $\mathbf{F}^H \mathbf{H} \mathbf{W}$. Estimating such channel requires more signal chains. In a fully digital approach ($P = M, Q = N$), the MIMO channel can be acquired by means of channel estimation, which enables full steering capability. On the contrast to pure analog approach ($M = N = 1$), only the combined channel is available and its strength can be used as an indicator to determine the beamforming coefficients. Hybrid beamforming provides a trade-off between both corner cases.

5.2.2 LoS scenario limitations

When considering LoS and far field assumption⁴, the channel rank is 1, and therefore considering MIMO diversity is irrelevant. Thus, the beamforming matrix in such scenario is reduced to vectors \mathbf{w} and \mathbf{f} of sizes P and Q , respectively. Therefore, using one signal chain

$$y(t) = \mathbf{f}^H \mathbf{H} \mathbf{w} x(t) + \mathbf{f}^H \mathbf{v}(t). \quad (5-34)$$

In particular, the channel is given by

$$\mathbf{H}(\theta_b, \phi_b) = \sqrt{G_{PL}} \sqrt{G^{(rx)}(\theta_b, \phi_b) G^{(tx)}(\theta_b, \phi_b)} \mathbf{b}(\theta_b, \phi_b) \mathbf{a}^T(\theta_b, \phi_b). \quad (5-35)$$

Here, (θ_b, ϕ_b) is the direction of the receiver, and G_{PL} is the path gain factor at a distance r given by

$$G_{PL} = \frac{\lambda^2}{(4\pi r)^2}. \quad (5-36)$$

When the beamforming gain are set such that $\mathbf{w} = \frac{1}{\sqrt{P}} \mathbf{a}^H$ and $\mathbf{f}^H = \frac{1}{\sqrt{Q}} \mathbf{b}^H$, and the direction is aligned towards the maximum antenna gains, the then, we get the equivalent AWGN model

$$y(t) = \sqrt{G_{PL} G^{(rx)} G^{(tx)}} \sqrt{PQ} x(t) + v(t). \quad (5-37)$$

Where $v(t) = \mathbf{f}^H \mathbf{v}(t)$. Note that, after such normalization of \mathbf{w} and \mathbf{f} , we get $E[v(t)^2] = BN_0 N_F$, which is equivalent to the noise at the output of LNA, and $E[x(t)^2] = P_s$ is the sum of the total power produced at the output of all PAs. However, when pure analogue beamforming is used, estimating the direction of arrival is not digitally possible, and finding such optimal solutions requires more efforts.

Ideally, we get the linear SNR is given by

$$\rho = G^{(rx)} G^{(rx)} P Q \frac{\lambda^2}{(4\pi r)^2} \frac{1}{N_F} \frac{P_s}{BN_0}. \quad (5-38)$$

Therefore, the achievable mutual information is

$$R = \log_2(1 + \rho) \Rightarrow \rho = 2^R - 1 \Rightarrow SNR = 10 \log_{10}(\rho) \approx 3R. \text{ [bit/sample]} \quad (5-39)$$

And therefore, the theoretical achievable data rate, which is given by RB [bit/s], can be increased with the increase of the bandwidth while preserving the SNR. This requires increasing the antenna arrays gain linearly with the increase of B for a fixed transmit power and range, i.e., using αB , requires increasing the arrays size to $\sqrt{\alpha} P, \sqrt{\alpha} Q$. However, increasing the bandwidth leads to violating the assumption of narrow bandwidth given in (5-12). An alternative solution is to increase R by increasing the SNR, where the narrow band assumption holds. This results in exponential growth of the array size, i.e. achieving $R_1 = \alpha R$, requires that $P_1 Q_1 = P Q 2^{(\alpha-1)R}$. The large growth may lead, on the one hand, to an array size that violates the narrow band assumption, and on the other hand, the beams becomes very narrow, which complicates the beam initial access and alignment.

⁴ When the distance between TX and RX is small enough in comparison to the antenna aperture, spatial multiplexing is possible in LoS conditions, where the rank of the channel matrix can be larger than 1.

5.2.3 Wideband consideration

When the signal bandwidth violates the narrow band assumption, the array steering response depends on the frequency. To illustrate that, assume a wideband signal of bandwidth IB that is composed of I narrow band signals, each of a bandwidth B such that $\tilde{\mathbf{x}}(f) = \sum_{i=-I/2}^{I/2} \tilde{\mathbf{x}}_i(f - iB)$, and using pure analogue beamforming. Considering the carrier frequencies $f_{c_i} = f_c + iB$ in computing the steering vectors from (5-9) and (5-10), the frequency-domain transmitted baseband signal can be expressed as

$$\tilde{\mathbf{x}}^{(tx)}(f) = \sum_{i=-I/2}^{I/2} \tilde{\mathbf{x}}_i(f - iB) \sum_{p=0}^{P-1} w_p e^{j2\pi\tau_p iB} \cdot \mathbf{a}[p](\theta_a, \phi_a). \quad (5-40)$$

Similarly, ignoring the noise term, the received signal can be written as

$$y(f) = \sum_{i=-I/2}^{I/2} \tilde{\mathbf{x}}_i(f - iB) \sum_{p=0}^{P-1} w_p e^{j2\pi\tau_p iB} \cdot \mathbf{a}[p](\theta_a, \phi_a) \sum_{q=0}^{Q-1} f_q^* e^{j2\pi\tau_q iB} \cdot \mathbf{b}[q](\theta_b, \phi_b). \quad (5-41)$$

This leads to a frequency selective channel, as in (5-28), even in the case of far field LoS. The beam search is more challenging, and equalization at the receiver is needed. The beamforming can only improve the SNR at a certain narrow band. One theoretical solution to cope with, is by means of analogue waveforms, which is introduced in [HEX21-D21].

5.3 HW design constraints and effects on the performance

The beamforming performance is influenced by the individual HW components in the transceiver chain, as thoroughly presented in Sections 3.4 and 3.6. These includes quantization errors by low resolution ADC, IQ imbalance and phase noise by the mixers, nonlinearities, especially, in the Pas, in addition to the loss by splitters and combiners at the beamforming network, and to the non-linearities of the individual phase and gain control. Other aspects are the implementation constraints in circuit design. In this section, we highlight some of the relevant aspects to the beamforming design itself.

Recall, the theoretical model of beamforming (5-28) $\tilde{\mathbf{y}}(f) = \mathbf{F}^H \tilde{\mathbf{H}}(f) \mathbf{W} \tilde{\mathbf{x}}(f) + \mathbf{F}^T \tilde{\mathbf{v}}(f)$. With $\mathbf{W} = \mathbf{W}_A \mathbf{W}_D$ and $\mathbf{F} = \mathbf{F}_A \mathbf{F}_D$. In theory, the analogue beamforming matrices can be full to enable the realization of the SVD precoding matrices in the case of MIMO. However, this requires a fully connected network of phase and gain, which practically may not be feasible. As a result, the structure of \mathbf{W}_A and \mathbf{F}_A need to be sparse, where non-zero values appear only once in each column and row. This can be translated to a single phase and gain control before the PA and after the LNA. This leads to the concept of subarrays, where each array is steered with independent analog beamforming. The digital precoding is performed across the subarrays. With this constraint, even with a full knowledge of the channel at both the transmitter and receiver, and ideal HW components, the theoretical rate cannot be achieved.

Other design constraint is associated with the array size and geometry, which have impact on the response of the array steering vector. As discussed in Section 5.2.3, the narrow band assumption is important to simplify the signal processing in terms of equalization and beam search. And while that conflicts with the need for a larger array to compensate for the small antenna aperture, it is required to achieve a trade-off by operating on parallel narrow band subarrays, which requires designing the sub arrays at multiple carrier frequencies.

From signal processing perspective, the selected beamforming architecture impacts the signal processing approaches. For instance, with a pure analogue beamforming, to align the beams with the absence of full channel estimation, beam search strategies based on SNR measurements need to be used. However, that may not guarantee establishing the link according to the highest singular value of the channel when multipath channel is available. Moreover, such search cannot practically be done with fine resolution, rather by evaluating several possible beams selected for a finite codebook. Once the

initial connection established, a smart beam tracking should be implemented to avoid long search. These aspects are discussed in Section 5.3 and 5.5.

5.4 Impact of HW limitations on Beam training strategies and initial access

Due to the specific propagation properties in the upper mmW band a link can be established only by applying high gain beamforming to achieve sufficiently high link budget. This leads to challenges especially for initial access and beam training since channel information per antenna element is not available and all procedures need to be realized in beam space. 5G NR [38.802] supports a beam scan procedure, where a number of synchronization signals (SS) are transmitted with different beam directions (SSB beams), so that a UE can detect and feedback the information about the best beam for connection. A more detailed description can be found also in [HA+21]. The number of SSB beams can be smaller than the maximum number of DFT beams. These beams then have larger half-power beam width (HPBW) than DFT beams, but also less gain (see Figure 5-4). Purpose is to keep the scanning time reasonably low. The lower number of widened beams can be scanned in less time, and once the optimum beam is found a refinement within the angular range of the widened beams can be done.

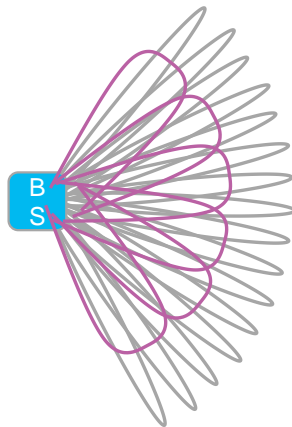


Figure 5-4: Beam shapes for initial access.

Such widened beams can be constructed e.g., according to [Tre02] by using a target function for the beam shape and find the corresponding antenna weights. A target function

$$f(\alpha) = \begin{cases} 1 & \text{for } \alpha_L < \alpha < \alpha_R \\ 0 & \text{else} \end{cases} \quad (5-42)$$

defines a constant gain between left and right coverage angle α_L and α_R . The corresponding beam weights for an even number of antenna elements N can be calculated then as

$$a_m = \frac{e^{-j(m-\frac{1}{2})\psi_L} - e^{-j(m-\frac{1}{2})\psi_R}}{-2\pi j(m-\frac{1}{2})}, \quad (5-43)$$

where $m = -\frac{N}{2} + 1, -\frac{N}{2} + 2, \dots, \frac{N}{2}$, $\psi_L = 2\pi \frac{d}{\lambda} \sin \alpha_L$, $\psi_R = 2\pi \frac{d}{\lambda} \sin \alpha_R$, m as antenna index ranging from 1 to N and d is the element distance in multiples of λ .

A major hardware impact for these widened beams comes from the fact that the resulting weights are no longer of unit power, like for DFT beams, but the amplitude can vary depending on the number of elements considered and with the steering angle. An example of beam weights according to equation (5-43) for the case of 64 elements and widened beam widths of 5° and 10° is shown in Figure 5-5.

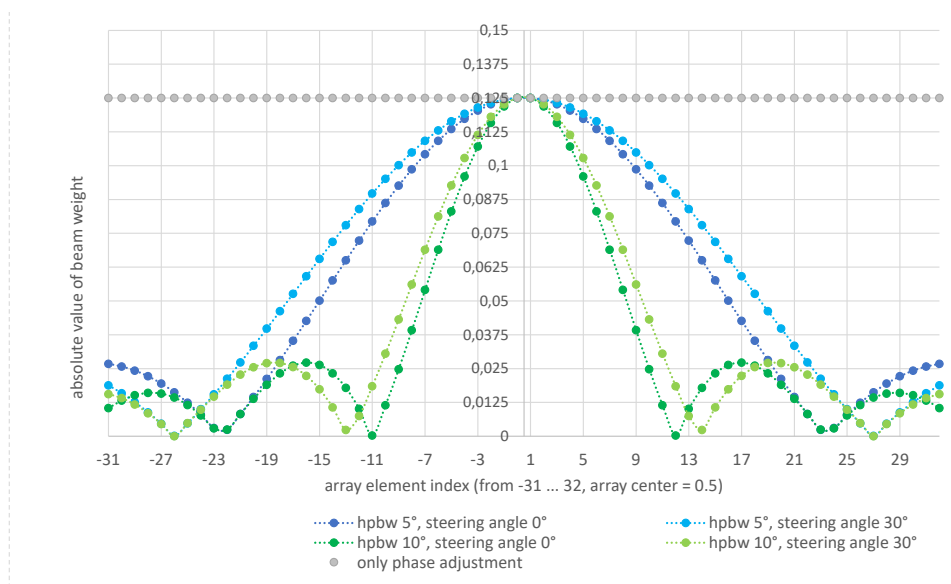


Figure 5-5: Absolute values of beam weights for widened beams according to equation (5-43), normalized to maximum allowed power per element of 1/64

When normalizing the beamforming weights so that the maximum power per element is respected, the total transmitted power is reduced. So, a loss in beam gain can become high and depends further also on the steering angle. Initial investigations show that the higher the relation between widened beam width and DFT beam width is, the larger is the difference between highest and lowest amplitude beamforming weight, and the higher the number of elements is, the larger is the resulting reduction of beamforming gain. This impact on beam gain during beam search becomes especially serious with respect to the targeted 6G upper mmW bands with the further increased path loss proportional to $20 \cdot \log(f)$. The fact that on UE side also high gain beamforming arrays with narrow beam widths are expected to be necessary for sufficient link budget will further increase the effort for beam alignment procedure.

5.5 Beam tracking and management

5.5.1 Beam Training Time Interval

Another important aspect of beam training is the time interval during which the training needs to be performed. This is dependent on the assumptions of the maximum mobility and the area that needs to be covered. For the evaluation in this work, we consider two simplified scenarios. The first one is only considering LOS connection. The second one models the spatial coherence and therefore, include non-line-of-sight (NLOS) scenarios. In both cases we assume that the maximum speed of a device would be 30 km/h. Essentially, this speed is modelling a streetcar, bus, or car in a dense urban environment. We model a system where a connection in the frequency range of 100 to 300 GHz is providing a high data rate connection to the vehicle, and the connectivity for the users inside the vehicle is provided via for example Wi-Fi or another technology.

5.5.1.1 LOS Based Model

In this model we only consider the LOS connection from the device to the access point (AP). We also ignore any possible blockage of the LOS path. Assuming the device can move in any direction, the maximum speed s together with the time between two phases of beam training τ_B define a possible movement radius $r_m = s \cdot \tau_B$. For the AP we assume that the area it should cover is divided into three sectors, each covering 120° . Each sector is equally divided into areas covered by distinct beams. In example in Figure 5-6 there are six beams each covering an angle of $\Delta = 20^\circ$. Figure 5-6 also illustrates

three example positions for devices (Device position P1, P2, P3) and the respective potential device movement area $A(x_1, y_1, r_m)$ to $A(x_3, y_3, r_m)$. The area covered by different beams A_i are illustrated with faded colors. The vibrant colours indicate the portion of the area inside the possible movement radius, where a device would transition between beams or leave the coverage area of the sector. These areas can be formed by intersecting the area covered by a beam with the disc describing the movement. In principle we integrate over the area that is inside the current beam for all possible devices starting in this beam. Dividing this by the area for all possible movements we can get the probability for the device to have the same beam-configuration in two consecutive beam training instantiations. In addition, with this tool it is also possible to generate the transition probability for a Markov-model, where each state is associate with a beam. It needs to be mentioned that this model does not take rotation of the mobile device into account. In fact, we assume that the mobile device can provide sufficient spherical coverage, thus, rotating the device does not change the best beam of the AP.

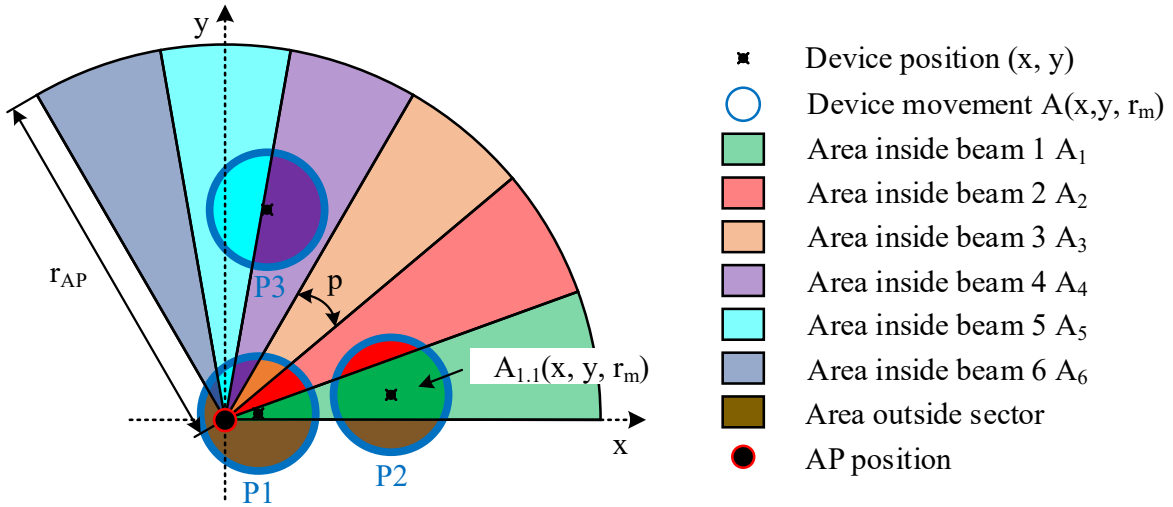


Figure 5-6: Illustration of the transition of devices at positions P1 at x_1, y_1 to P3 x_3, y_3 from the region covered by one beam to other regions, given a movement radius defined by the maximum speed and beam training time interval. The faded colours show the regions covered by beams 1 to 6 denoted as A_1 to A_6 . The other colors show the intersection of the movement at each the example device positions $A(x_i, y_i, r_m)$ with the beam coverage, resulting in the areas $A_{i,j}(x_i, y_i, r_m)$.

From the illustration in Figure 5-6 it is easy to see that all areas $A_{i,j}(x, y, r_m)$ can be formed by intersecting the area describing the device movement $A(x, y, r_m)$ with the beam coverage area A_i . This means assuming that the position x, y is inside the coverage area of beam i we can describe $A_{i,j}(x, y, r_m)$ as:

$$A_{i,j}(x, y, r_m) = A(x, y, r_m) \cap A_i. \quad (5-44)$$

In this case we are mainly interested in the probability that given a movement radius r_m , the beamwidth Δ in radian, and the cell radius r_{AP} we can calculate the probability that the coverage of one beam is:

$$P_l = 1 - \frac{1}{O_t} \int_0^{r_{AP}} \left(\int_0^{\min(\tan(\Delta)x, \sqrt{r_{AP}^2 - x^2})} A_{i,i}(x, y, r_m) dy \right) dx, \quad (5-45)$$

with O_t being a normalization factor equal to $O_t = \frac{\Delta}{2\pi} r_{AP}^2 \pi r_m^2 \pi$. This integral is calculating the full area of the device staying in beam i given that it is already in beam i at the start. As the areas $A_{i,i}(x, y, r_m)$ are dependent on the movement radius r_m and thus implicitly dependent on the time between beam training τ_B we can evaluate this equation for different values of the beam training interval τ_B .

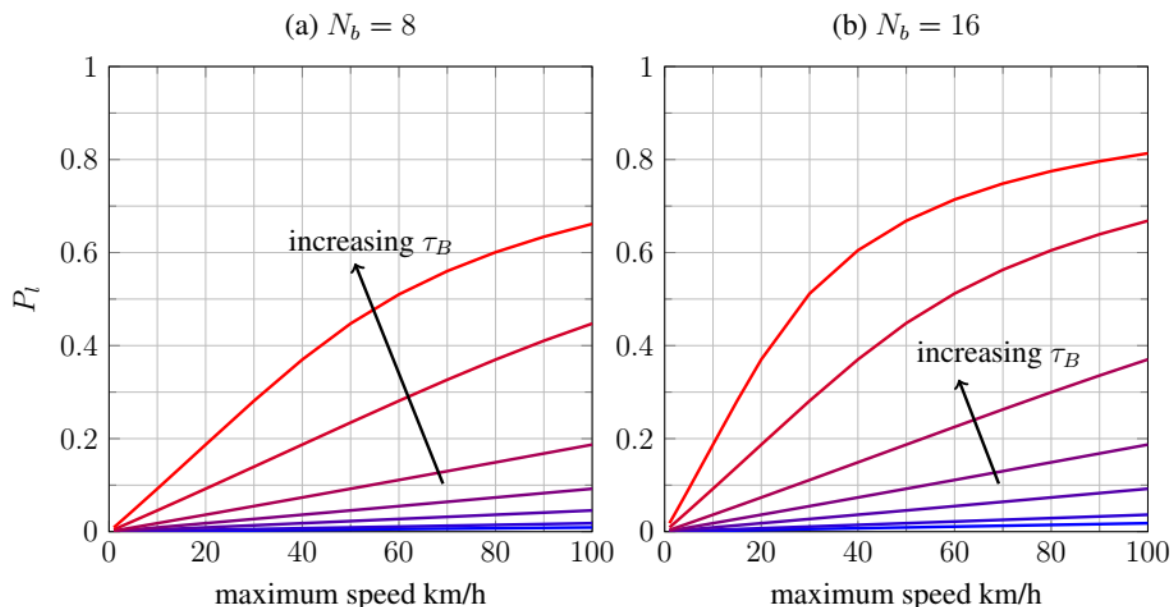


Figure 5-7: Probability P_l of devices leaving a given coherence area given different beam training intervals $\tau_B \in \{10 \text{ ms}, 20 \text{ ms}, 50 \text{ ms}, 100 \text{ ms}, 200 \text{ ms}, 500 \text{ ms}, 1\text{s}\}$ and number of beams (a) $N_b = 8$ and (b) $N_b = 16$ for cell radius $r_{AP} = 50 \text{ m}$.

Figure 5-7 shows the evaluation results for one 120° sector of a cell with radius $r_{AP} = 50 \text{ m}$. In the evaluation different number of beams were used. The results show that to have a probability below 10% of leaving the cell in between two beam training intervals given a speed of 30 km/h, τ_B should be below 100 ms. However, this model does only capture LOS connections. To cover all possible propagation aspects in the next paragraphs a model not restricted to only LOS is developed.

5.5.1.2 Spatial Coherence Based Model

Since the first model was only considering LOS channels, it is also interesting to investigate a model not limited by this assumption. For all the aspects in this model it is important to note that the beamforming should only adapt to the large-scale parameters of the system. Adapting to small scale parameters would result in a prohibitive beam training overhead, as they too frequently change. The spatial correlation distance is defined in [WSH+16] and [JR18]. Essentially, it describes the spatial distance at which the large-scale parameters are highly correlated. In [JR18] measurements of this parameter at 73 GHz carrier frequency are shown. The resulting correlation distance is in the range of 5 to 10 meters.

In a two-dimensional model these aspects can be captured by defining a circle in which the large-scale parameters are highly correlated. This results in the system using the same beamforming configuration if the device remains in this area. This model is illustrated in Figure 5-8. The area of spatially coherent large-scale parameters of the channel is modelled as a circle. As the mobile device is currently using the specific beam for this area it must be inside the circle. Now again assuming a certain time interval of the beam training a device could move inside a circle around the starting position. The radius of the circle is defined by the maximum possible speed and the beam training time interval.

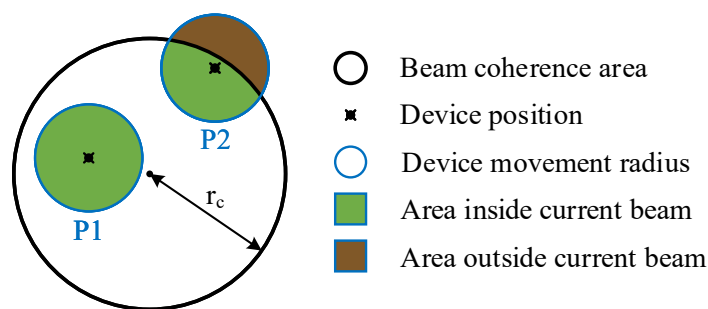


Figure 5-8: Illustration of the area in which the one beam is optimal including two device positions (P1 and P2) and the respective areas for staying inside the area of this beam or transitioning to another one.

The area in which the beam defined for the NLOS model is no longer optimal given a device location x, y and the same device movement model as in the LOS case is define as $A(x, y, r_m)$. From Figure 5-8 it is evident that for all possible location x, y inside the area served by the same beam, here defined by a circle with radius r_c , this $A(x, y, r_m)$ can be calculated by simple geometric objects like triangles and circles. Combining these for all possible location we get the probability that a device leaves the area:

$$P_l = 1 - \frac{1}{O_t} \int_0^{r_c} A(r, 0, r_m) \cdot r dr, \quad (5-46)$$

where we used the rotational symmetry to simplify the calculation. In this case O_t is a normalization factor equal to $O_t = r_c^2 \pi r_m^2 \pi$. The time interval between consecutive beam training periods is defined as τ_B .

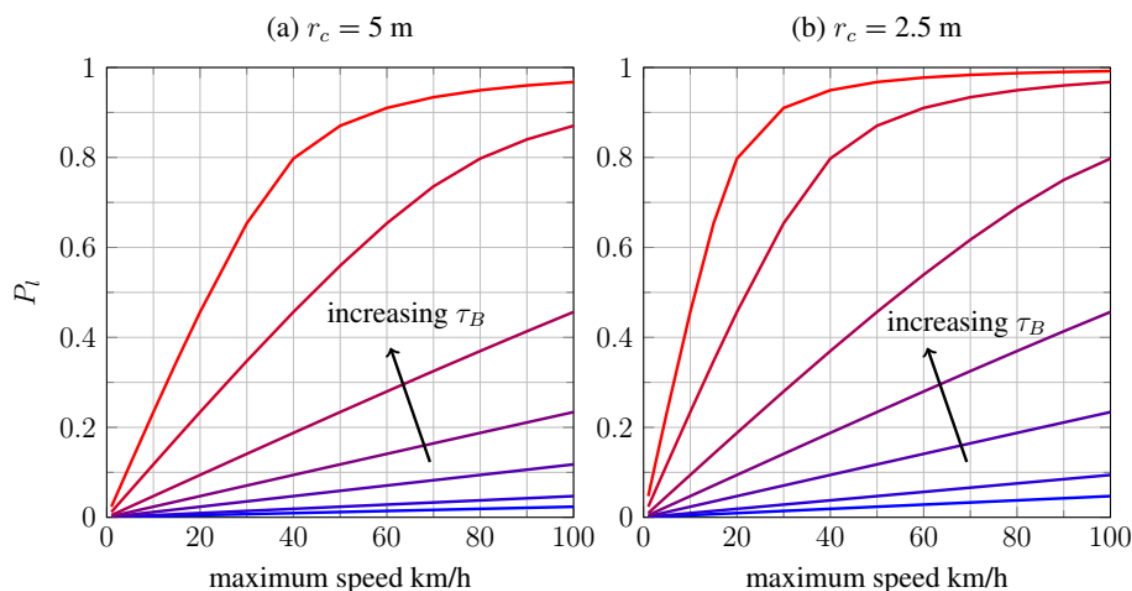


Figure 5-9: Probability P_l of devices leaving a given coherence area given different beam training intervals $\tau_B \in \{10 \text{ ms}, 20 \text{ ms}, 50 \text{ ms}, 100 \text{ ms}, 200 \text{ ms}, 500 \text{ ms}, 1\text{s}\}$ and coherence radii (a) $r_c = 5$ m, and (b) $r_c = 2.5$ m.

In Figure 5-9 the probability of leaving the area of one beam being the optimal one in between two consecutive beam training intervals is presented. Based on the measured correlation distance of 5 to 10 meters in [JR18] the coherence radius of r_c was setup to be between 2.5 and 5 meters. As leaving the

area for one beam would likely result in a link failure, the probability P_l should not be too large. However, the time between two consecutive beam training intervals τ_B should also not be too large as this would result in a prohibitive large overhead. Thus, judging from the results in Figure 5-9 see that a $\tau_B = 50$ ms beam training interval will keep the probability $P_l < 10\%$ for a maximum speed of 30 km/h.

5.6 Simulation framework

In this section, we present a simulation framework to study the link level performance under different theoretical and practical assumption considering the RF impairments listed in 3.4. The idea is to break the simulator into multiple modules, as shown in Figure 5-10, namely, DSP including waveform and digital precoding, RF chain, and beamforming. Each module may contain several submodules with a particular focus on certain functionality.

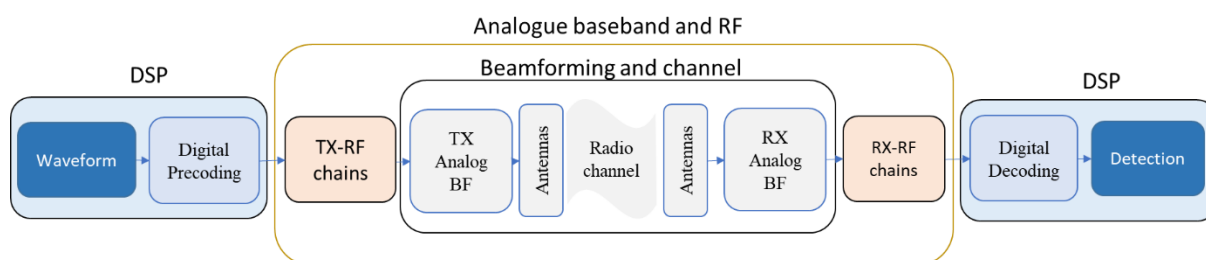


Figure 5-10 Simulator framework architecture.

The DSP can be further interfaced with realistic hardware in loop corresponding to (analogue baseband and RF) for proof-of-concept of the signal processing algorithm, as presented in Section 8. The highlighted box can be replaced by hardware in loop.

5.6.1 Structure

For each transmitter module there is a counterpart receiver module that can be directly evaluated independently from other modules. In particular, waveform generator and detection, TX-RF chains and RX-RF chains, TX Beamforming and RX beamforming. Each module should be abstracted by a function with input data vector (matrix in the case of multiple inputs), a structure defining the required parameters, and output data vector (matrix in the case of multiple outputs). There are mainly four data types across the modules, bits and floating/fixed points at the DSP, quantized and complex float numbers for the hardware. Note that, to simulate the analogue signals, we use oversampling. A similar structure can be used per each module to interconnect the functions of its submodules. The overall goal is to have reusable function library to study different performance metrics (e.g. BER, EVM) in a form of top-level application. Table 5-1 provides a summary of the supported modules.

Table 5-1 Summary of the simulator modules.

Module	Input signal	Output signal	Parameters	Submodules	Evaluation metrics
Waveform (TX)	Bit stream	Complex-valued signal	Waveform parameters MIMO configuration	Bit processing (Encoding, scrambling, interleaving, etc.) QAM mapping, Linear/non-linear transforms	PAPR Ranging Ambiguity function

Detection (RX)	Complex-valued signal	Bit stream	Waveform parameters MIMO configuration Reference signals	Synchronization Channel estimation Equalization Soft-demapping Decoding	FER, BER Estimation error
Digital precoding (TX)	Complex-valued signal	Quantized IQ samples	Number of RF chains	Precoding Convert from floating point to quantized signal	Diversity Spatial multiplexing
Digital Decoding (RX)	Quantized IQ samples	Complex-valued signal	Number of RF chains	Decoding Quantized signal to floating point	Diversity Spatial multiplexing
TX-RF chain	Quantized IQ samples (with sample rate of the system)	Oversampled analogue complex baseband signal	DAC resolution Bandwidth Transmit power IQ imbalance Phase noise Carrier frequency	Interpolation Predistortion Channel filtering DAC model Mixer model	EVM
RX-RF chain	Oversampled analogue complex baseband signal	Quantized IQ samples (with sample rate of the system)	ADC resolution Bandwidth RX Gain IQ imbalance Phase noise Carrier frequency Noise figure	AGC Mixer model ADC model Dissemination	EVM
Beam forming and antennas	Complex baseband signal or oversampled analogue signal	Complex baseband signal or oversampled analogue signal	Architecture Number of antennas coupling in array Carrier frequency and bandwidth Antenna: library of different abstractions Beam squint	Array steering vectors Geometry and orientation Splitter Combiner Phase and gain PA model LNA model	Link budget SNR Beam alignment Beam tracking Capacity

			TX power NF Channel		
Channel	Complex baseband signal or oversampled analogue signal	Complex baseband signal or oversampled analogue signal	TX, RX location (range, orientation) Environment Far field Near field	Channel model (statistical/geometrical)	Link budget Capacity

5.6.2 Beamforming initial simulation module

To simulate the beamforming in ideal scenario, we use the generic planner array model discussed in Section 5.1.1.2, and the received multipath channel mode of Section 5.1.1.4. The relevant geometry and location parameters are listed in Table 5-2, whereas Table 5-3 summarizes the signal parameters.

Table 5-2 Antenna arrays geometry parameters.

Parameter	Description
L_λ	Maximum array dimension in number of wavelength
(x_p, y_p)	Antenna element coordinate
$\vec{e}_p = (d_{x,p}, d_{y,p})$	Vector relative to reference element (x_0, y_0) , $\vec{e}_p = (x_p, y_p) - (x_0, y_0)$
$a[p](\theta, \phi) = e^{-\frac{j2\pi\Delta_p}{\lambda}}$	Array steering vector $\Delta_p = d_{x,p} \sin \theta \cos \phi + d_{y,p} \sin \theta \sin \phi$
$\vec{x}_a, \vec{y}_a, \vec{z}_a$	Local coordinate of TX array, used as reference
ψ_x, ψ_y, ψ_z	Rotation angles of RX w.r.t.. to TX array around $\vec{x}_a, \vec{y}_a, \vec{z}_a$ with rotation matrices $\Omega_x, \Omega_y, \Omega_z$.
$\vec{x}_b, \vec{y}_b, \vec{z}_b$	Local coordinate of RX array, used as a reference.
$\Omega = [\vec{x}_a, \vec{y}_a, \vec{z}_a]$	Rotation matrix $\Omega = \Omega_x \Omega_y \Omega_z$
$P_b = (x_b, y_b, z_b)$	Location of RX antenna array relative to TX array location $P_a = (0,0,0)$
$P_k = (x_k, y_k, z_k)$	Location of the $k - th$ scattering object
$\vec{v}_{a_k} = \frac{1}{r_{a_k}} (P_k - P_a)$	DoD from TX towards the $k - th$ scattering object at a distance r_{a_k} For line of sight $P_k = P_b$
$\vec{v}_{b_k} = \frac{1}{r_{b_k}} (P_k - P_b)$	DoA from the $k - th$ scattering object at a distance r_{b_k} to RX For line of sight $P_k = P_a$
$(\theta_{a_k}, \phi_{a_k})$	Direction of departure, $\sin \theta_{a_k} \cos \phi_{a_k} = \vec{x}_a \cdot \vec{v}_{a_k}$, $\sin \theta_{a_k} \sin \phi_{a_k} = \vec{y}_a \cdot \vec{v}_{a_k}$, $\cos \theta_{a_k} = \vec{z}_a \cdot \vec{v}_{a_k}$
$(\theta_{b_k}, \phi_{b_k})$	Direction of arrival $\sin \theta_{b_k} \cos \phi_{b_k} = \vec{x}_b \cdot \vec{v}_{b_k}$, $\sin \theta_{b_k} \sin \phi_{b_k} = \vec{y}_b \cdot \vec{v}_{b_k}$, $\cos \theta_{b_k} = \vec{z}_b \cdot \vec{v}_{b_k}$

Table 5-3 Signal and channel parameters

Parameter	Description
f_c	Carrier frequency
c	Propagation speed (approximately, the speed of light)
$\lambda = \frac{c}{f_c}$	wavelength
B	Bandwidth
N_0	Noise power spectral density
N_F	Noise figure
P_s	Transmit power
$G_{PL} = \frac{\lambda^2}{(4\pi r)^2}$	Path gain factor at a distance r
M	Number of TX chains
N	Number of RX chains
P	Number of TX antenna elements
Q	Number of RX antenna elements
$G^{(tx)}(\theta, \phi)$	TX antenna element gain at direction (θ, ϕ)
$G^{(rx)}(\theta, \phi)$	RX antenna element gain at direction (θ, ϕ)
$\mathbf{a}(\theta, \phi)$	TX array steering vector of size P at direction (θ, ϕ)
$\mathbf{b}(\theta, \phi)$	RX array steering vector of size Q at direction (θ, ϕ)
$\mathbf{W} \in \mathbb{C}^{P \times M}$	TX beamforming matrix
$\mathbf{F} \in \mathbb{C}^{Q \times N}$	RX beamforming matrix
$\bar{\mathbf{H}}_k(\theta_{a_k}, \phi_{a_k}, \theta_{b_k}, \phi_{b_k})$	Channel matrix at DoD $(\theta_{a_k}, \phi_{a_k})$ and DoA $(\theta_{b_k}, \phi_{b_k})$, gain h_k and delay τ_k : $= h_k \sqrt{G^{(rx)}(\theta_{b_k}, \phi_{b_k}) G^{(tx)}(\theta_{a_k}, \phi_{a_k})} \mathbf{b}(\theta_{b_k}, \phi_{b_k}) \mathbf{a}^T(\theta_{a_k}, \phi_{a_k})$

6 D-MIMO radio architecture studies

6.1 Introduction and motivation to D-MIMO

6.1.1 What is D-MIMO for 6G?

Multi antenna systems have been always evolved during generations of wireless networks. First Single-Input Single-Output systems, then point-to-point MIMO has been introduced in 3G and subsequently the LTE system is based on multi-user MIMO. Heterogeneous Networks (HetNets) have been utilized in contrast to the homogenous cellular network architecture containing Base Stations (BS) possessing similar properties, where various transmission nodes (e.g., pico-cell, femto-cell, remote-radio-head, RRH) are installed within the same macro-cell containing a BS to improve the quality of service of cell-edge users as well as to improve the system-wide service quality. These transmission nodes are network components that work in coordination with the BS, but also differ from the BS in various aspects such as transmit power levels and hardware. For example, RRHs are composed of antennas and RF amplifiers, and connected to the BS via fibre cables or radio links using baseband signals, which turns the macro-cell into a distributed antenna system. Pico-cells communicate with the BS with limited capacity and some of the functionalities can be moved to local sites. On the other hand, femto-cells have the capability of working autonomously but less coordination capacity with BS.

Now the 5G NR standard has massive MIMO, where each BS is equipped with a large number of antenna elements, and it serves numerous UEs simultaneously by means of highly directional beamforming techniques. It is benefiting from channel hardening and favourable propagation utilizing the deterministic channel and hence potentially eliminates the need for combating small-scale fading [Mar10], [ABC+14], [JMZ+14], [BHS18].

Joint Transmission Coordinated Multi-Point (JT-CoMP), which enables coherent transmission from clusters of BSs to overcome the inter-cell interference within each cluster [GHH+10], [JMZ+14], has also attracted the attention during the past ten years, however it did not become part of the 5G NR standard as LTE standardization [LSC+12] did not deliver significant gains in practical deployments. This can be mainly attributed to the considerable amount of backhaul signalling for Channel State Information (CSI) and data sharing resulting from a network-centric approach to coherent transmission [IBN+19], whereby the BSs in a cluster cooperate to serve the UEs in their joint coverage region. The practical implementation of JT-CoMP was also hindered by other attributes of LTE, such as frequency division duplex operations and a rigid frame/slot structure, which did not allow for effective channel estimation.

One question for 6G is what the next evolution of MIMO will be, and what will be the demands and needs of 6G networks from multi-antenna systems? 6G should provide limitless connectivity with both functional and deployment values. It will utilize upper mmW frequencies and is expected to provide high spectral efficiency and predictable quality of service to the UEs. To ensure more consistent quality and non-intrusive, flexible, and robust networks, multi-point transmission is expected to become common [GPS+20]. It is envisioned that joint transmission and reception via spatially separated transceivers will be vital in upcoming systems [37.340].

Cell-free massive MIMO [IBN+19], [ZCL+19] combines the elements from small cells [JMZ+14], massive MIMO [BHS18], and UE-centric JT-CoMP [JMZ+14] and more recent works in [BDZ+19], as illustrated in Figure 6-1. In a cell-free context, the massive MIMO regime is achieved by spreading a large number of antenna elements across the network (even in the form of single-antenna BSs [NAY+17], [NAM+17]), which provides enhanced coverage and reduced pathloss. Moreover, a UE-centric coherent transmission extended to the whole network, where each UE is served jointly by all the BSs, allows to practically eliminate the interference, as shown in the Network MIMO paper [FKV06].

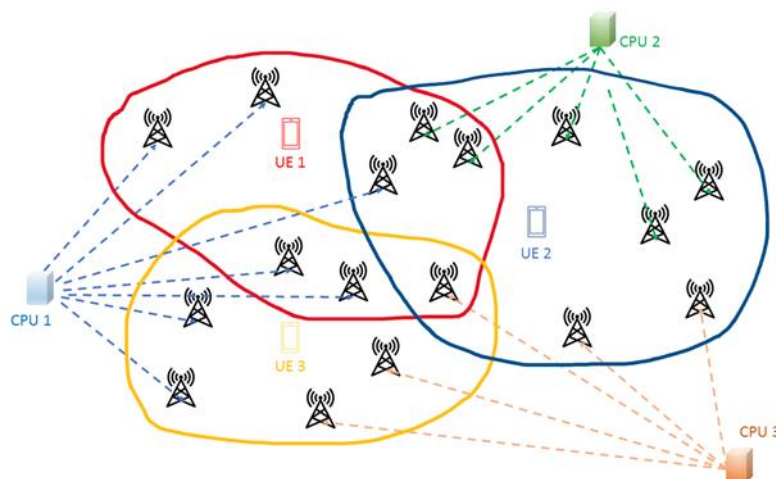


Figure 6-1: Illustration of distributed MIMO.

Large scale distributed MIMO systems (D-MIMO), aka cell-free massive MIMO, which can be thought of as the ultimate embodiment of concepts such as Network MIMO [FKV06], multi-cell MIMO cooperative networks [GHH+10], virtual MIMO [HJW+13], ultra-dense networks and JT-CoMP, is now regarded as a potential physical-layer paradigm shift for beyond-5G systems [ZBM+20]. All the transmission nodes (Access Points, APs) are assumed to be connected to a central processing unit (CPU) via fronthaul links, e.g., high-capacity fibre-optic cables, which conveys both the UE-specific data and processing weights that enable network-wide processing for the computation of the AP-specific precoding strategies [IBN+19]. Since APs can perform channel estimation and distributed precoding locally, D-MIMO constitutes a scalable way to implement the network MIMO concept. Moreover, precoding can be designed by using channel estimates acquired via uplink pilots by leveraging the channel reciprocity of TDD operation, therefore the overhead due to the channel estimation is independent of the number of APs, and scales with the number of transmission layers.

The terminology for the transmission nodes in Distributed MIMO needs to be clarified, where both BS and AP are used in the literature, however without expressing the functions placed in the units, any term like BS or AP do not provide sufficient information. Since BS can be interpreted with different functionalities, throughout this context, we prefer to use the term AP as a distributed antenna or transmission node. A gNB is introduced with functional splits in 5G era, e.g., Radio Unit (RU), Distributed Unit (DU) and Centralized Unit (CU), and the splits in D-MIMO have not been defined, yet. One interpretation is that the APs may have little processing capability, and CPU may be the DU as it involves low level functions. Herein, DU may be further split by centralizing the medium access control (MAC) and RLC layers w.r.t the PHY layer. In investigations, where the functional split is not fundamental BS/AP and AP can be used.

Research in MIMO can be linked with another terminology, e.g., reconfigurable intelligent surface (RIS). A RIS is a two-dimensional surface of engineered material whose properties are reconfigurable rather than static that can shape how the surface interacts with wireless signals enabling a new dimension to be fine-tuned: the wireless propagation environment [BWM+21]. The surface can include mainly passive elements without doing digital processing or any signal amplification. Nonetheless, some surfaces can have relaying capability such that it can provide signal amplification. Moreover, it can have active elements that can enable digital signal generation, i.e., can be interpreted as extra-large massive MIMO.

6.1.2 Potential

At lower carrier frequencies (sub-6 GHz), where coherent transmission is possible, D-MIMO can be used to increase the spectral efficiency of the system and in principle avoid inter-cell interference. Moving up in frequency available bandwidth becomes larger and spectral efficiency is not necessarily

the main concern anymore. Instead, reliability of the communication links becomes a primary concern. Reliability is impacted by the higher pathloss, lower available output power of semiconductors, narrower antennas beams and most importantly a higher level of signal blockage.

D-MIMO offers great potential to help and mitigate both, unreliable links due to blockage as well as increased path-loss. The fact that with D-MIMO a link between the network and a UE is provided by multiple APs, increases the likelihood that a link or combination of links with minimal blockage is available by macro diversity. D-MIMO also allows for densification of APs, with in the ideal case, no increase in interference. An increased density of APs cooperating will further reduce the likelihood of blockage and will also be necessary to have sufficient link margin due to output power limitations and increased pathloss at upper mmW and THz frequencies.

From a technical perspective, an increased number of cooperating APs will pose new challenges for providing front/back-haul access to all nodes. On the other hand, a lot of bandwidth will be available, and links will be supported by very directive antennas limiting the amount of interference. This opens for integrated access and backhaul solutions, sharing the same resources, but requires potentially new beamforming and scheduling concepts.

6.1.3 Roll-out considerations

To be successful, any new 6G technology component needs to provide some significant functional benefits, such as delivering very high radio performance. For D-MIMO this is achieved by a high degree of macro diversity that results in a predictable service quality over the entire service area. The line-of-sight probability for D-MIMO is very high which makes it suitable for deployment on very high frequency bands where radio propagation makes it challenging to provide a robust access link for mobile users. In theory under the assumption of full channel state information, there is no upper limit on the capacity of a D-MIMO system while densifying [FKV06], however the capacity will be limited by practical constraints such as cost, power, and hardware impairments, as discussed in Section 3.2.

The main challenge for large scale D-MIMO rollout is arguably the cost for installing many nodes in different places that need fast and high speed fronthaul connections. D-MIMO installations needs to be easy to deploy, have a small and none-intrusive visual footprint, and be flexible to scale and extend. Clearly, there are seemingly conflicting requirements that D-MIMO need to fulfil as shown in Figure 6-2.

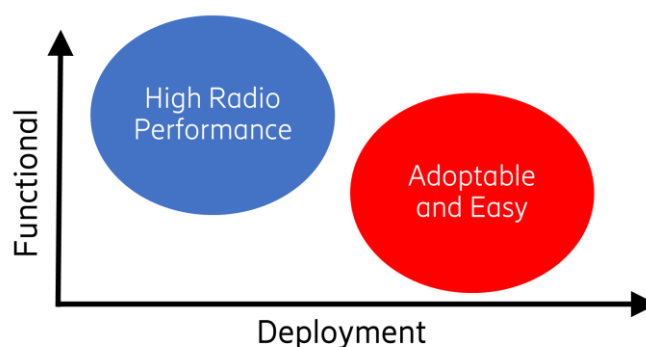


Figure 6-2: D-MIMO need to fulfil seemingly conflicting requirements on functional complexity and deployment costs.

If every D-MIMO access point will require a dedicated fronthaul cable, then there is no way to make large installation economically feasible. It must be possible to cascade multiple access points on the same fronthaul connection. Cascading or serializing the fronthaul may not be sufficient. If every access point requires separate cables to each of its neighbouring access points that will also make the installation complex, labor intense, and costly.

There are two different ways to provide fronthaul/backhaul to different APS: through fibre, or wirelessly. For D-MIMO deployments, both need to be highly efficient. An optimized wired fronthaul can be realized through so-called radio stripes, while wireless fronthaul/backhaul can be realized efficiently by integration with the access network.

Access points can be integrated into a “radio stripe” as depicted in the left part of Figure 6-3. The radio stripe provides the fronthaul data and power supply for each AP as well as physical protection and encapsulation. With similar low power techniques that are used in mobile phones the entire access point can be implemented in a system-on-chip (SoC) package that is denoted antenna processing unit (APU) in Figure 6-3. An APU may contain some digital processing function (e.g., a digital signal processing, or DSP unit), and antenna panel consisting of one or more antenna elements, and one or more external interfaces that can connect to other APUs or to CPU. D-MIMO may also make use of a meshed fronthaul, sometimes denoted a RadioWeave, as depicted in the right part of Figure 6-3. In a meshed fronthaul the actual fronthaul segments may be implemented using wires, but the fronthaul segments may also be wireless.

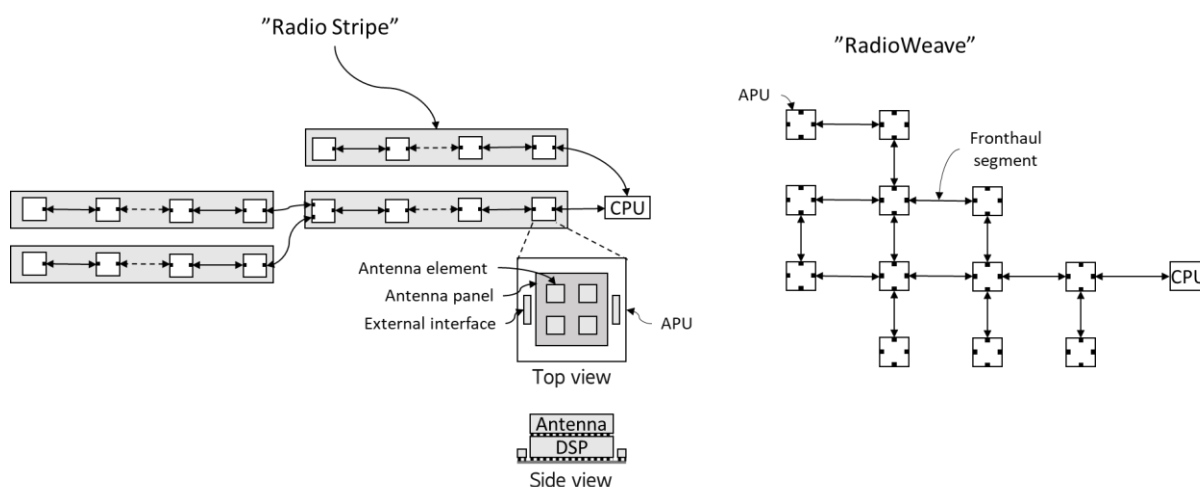


Figure 6-3: D-MIMO installation can be simplified if many distributed access points can be rolled out at once, which is the main purpose of a radio stripe (left). There is also need for both serialized (or cascaded) fronthaul connections as well as parallel (or meshed) fronthaul connections (right). The fronthaul segments may be wired or wireless.

Outdoor D-MIMO installations need to have a low visual footprint. With radio stripes, it is possible to hide the installation in existing construction elements in the environment, see Figure 6-4. To enable a small form-factor of the APs or of the APUs integrated inside of a radio stripe the power consumption needs to be very low. Fronthaul connections between APs or APUs can sometimes, but not always, be realized very easily with a cable. It is however not realistic to assume that every CPU can have a fibre backhaul connection. In dense urban areas the backhaul connection can then be provided wirelessly by an existing macro base station.

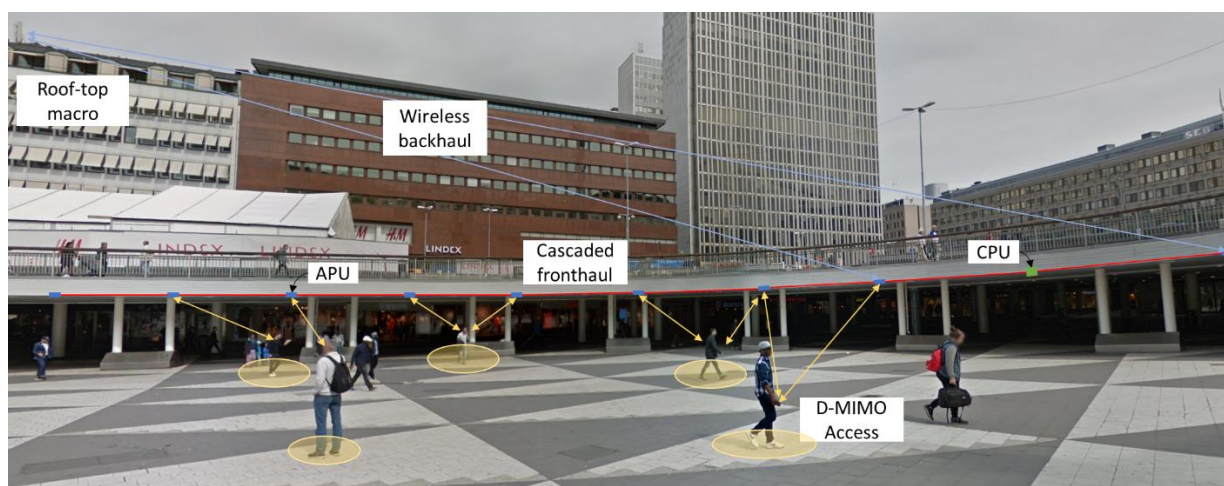


Figure 6-4: Outdoor D-MIMO is well suited for dense urban areas where it can provide invisible and high-capacity deployments.

Cascading or serializing the fronthaul connections is also important for indoor installations, such as in a factory environment, see Figure 6-5. Comparing to electrical lights that are also installed in large volume inside a factory, we note that this would not be possible if each electrical light required a separate cable installation. Just as one power cable can power up several lights, one fronthaul cable can connect several APs or APUs in a D-MIMO installation.

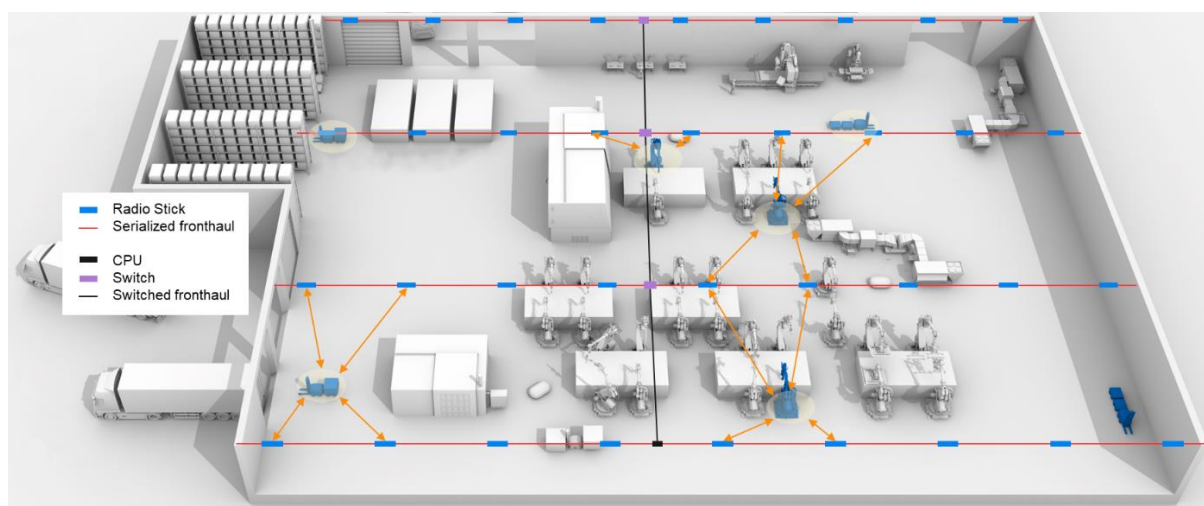


Figure 6-5: In indoor deployments, such as in a factory, D-MIMO can provide extremely reliable services with high capacity.

6.2 Transceiver and radio access/fronthaul/backhaul architecture considerations

6.2.1 Hardware constraints

As outlined in Section 3, signals transmitted at upper mmW and THz frequencies are subject to distortion by the transceiver hardware. In this section, we discuss the main hardware effects that are particularly relevant for D-MIMO systems:

- Phase and frequency coherency
- Output power
- Reciprocity

To utilize distributed antennas to their maximum extent, coherent transmission and reception would be desirable. This requires however that all antennas participating in coherent transmission are tightly synchronized. Going to THz frequencies, coherent schemes will be very challenging to realize due to phase noise and frequency errors. Techniques robust against coherency errors must be developed. In its simplest form this could for example be antennas selection.

Another key hardware effect with current semi-conductor technology at upper mmW and THz frequencies is that it is challenging to produce sufficient output power to maintain a robust communication links over a larger distance. As a result, devices are pushed harder, introducing more non-linear distortion. D-MIMO is a possibility to address this limited output power challenge: APs will have challenges to reach end-points due to output power limitations, but the inherent macro diversity in D-MIMO, and support for dense deployments enables more APs close to end-points. The effect of lower output power will result in transceiver designs with more parallel PAs combined with a higher number of antennas elements yielding higher EIRP. At lower mmW frequencies where the EIRP, rather than AP output power, might be the limiting factor at certain deployment scenarios, D-MIMO has the capability to allow for lowering the EIRP by dense AP deployment and still provide sufficient coverage.

To perform beamforming in a D-MIMO system, the channel has to be acquired. One way to do this is to assume channel reciprocity which means uplink and downlink channel are identical (in TDD mode). The channels estimated by a device contain the air-channel, but also the analogue transceiver chains. Reduced coherence time (of channel and hardware) and components that are driven more non-linearly, will make it more challenging to build D-MIMO systems based on channel reciprocity.

6.2.2 Architectural considerations

We need to develop techniques enabling scalable D-MIMO systems with converged access-backhaul & fronthaul, delivering extreme spectral efficiency, reliable access and robust mobility in scenarios ranging from low bands to sub-THz bands, taking hardware impairments and deployment options into account. In order to do that we need to understand how much distribution we need, where is the sweet-spot in terms of complexity versus robustness and performance considering the trade-off between distributed and centralized processing. We need to address beam management aspects and practical approaches to non-coherent operation in higher bands, and transport solutions, e.g., wired/wireless, optical/electrical, analog/digital, satisfying the requirements.

Sub-THz communication, i.e., mmW and higher frequencies, provides relatively large system bandwidth (e.g., several GHz), thus it is anticipated to substantially increase the average system throughput. Nevertheless, digital processing, ADCs and DACs in these bands will be power consuming and increases the chip cost and size of the processing unit. Small APs are essential in terms of deployment values, e.g., invisible, and aesthetic impacts, that is why we may need to move the digital processing from AP to the CPU, which means that fronthaul will become analog and needs to have a capacity on the level of fibre connection. On the contrary, in case of low frequency bands and limited bandwidth (e.g., 10-100 MHz), digital processing is feasible in the AP and can be carried out locally. Distributed processing means that there will be less information, e.g., channel estimation and precoding, exchange between the AP and CPU. Since baseband data will be transferred, there will be less load (compared to RF modulated data) on the fronthaul which can be handled without high capacity fronthaul links, e.g., a 10 Gbps Ethernet digital fronthaul may be enough.

It is always preferable if it is easy to connect the APs with cables. Some installations can be easy as one cable going through multiple APs, however wireless links are also an option for fronthauling. At higher frequencies (e.g., sub-THz), the spectrum is large and there is not much traffic in early phase of the utilization of these bands, even the UE is limited in how much bandwidth it can process, i.e., there will be available spectrum that can be utilized for the fronthauling. Since APs are generally not nomadic, robust fronthaul links will be easy to maintain. Random blockage due to moving objects can be handled by redundant links.

On low frequency bands (e.g., sub-6 GHz), the spectrum is scarce, but the traffic is high, thus there is a need to grow the spectral efficiency for increased capacity. One way is to have a distributed coherent

antenna system. In theory, D-MIMO and coherent multipoint transmission can enable higher capacity everywhere by adding additional coordinated APs. It is only sort of impairments and practical limitations that will eventually limit the performance.

But on high frequency bands (e.g., sub-THz), due to the large spectrum and less traffic, non-coherent transmission can be enough for early phases. Moreover, as frequency increases, antenna elements shrink and the antenna array will be relatively large, and beams become narrower. The main challenge in these bands is to realize and maintain a robust access link which supports mobility where the propagation environment is more challenging. Macro diversity brings an advantage to achieve the high reliability, especially in non-line of sight, and a D-MIMO can benefit from a much higher degree of macro diversity to overcome radio blocking in case of narrow beams and weak signal penetration.

To enable scalable D-MIMO, we need to understand how much distribution we need and need to address practical approaches to non-coherent operation in higher bands, and transport solutions satisfying the requirements. Optimum solution would be phase-coherent transmission and one centralized processor, but it will be difficult to build and meet the feasibility requirements. Other extreme would be phase non-coherent transmission with duplicating every data in each AP and relying on single frequency network, however it will be inefficient. We need a smart way to find the balance in terms of complexity versus robustness and performance.

6.3 Towards a common architecture

In this section we present our recent results on key technical components, as a first step towards understanding how to develop a common scalable and frequency-agile architecture.

6.3.1 Analog centralized beamforming

The type of D-MIMO system architecture and functional split that can be used depends very much on the overall system bandwidth. High system bandwidths (several GHz) are only available on very high frequency bands while lower system bandwidths (e.g. 100 MHz or less) are available on sub-6 GHz bands. Therefore, on lower bands, where the bandwidth is limited it can be feasible to use an electrical based fronthaul technology such as Ethernet. Ethernet provides up to 10 Gbps rate and can also provide up to 100 W or electrical power using PoE 802.3bt Type 4. On lower frequency bands the digital processing requirements of each APU is also reasonable limited.

However, on sub-THz frequency bands the very wide system bandwidth prohibits the use of electrical cables for the fronthaul, and we must instead use optical fronthaul connections. It is also not feasible, at least withing the early 6G time-frame, to assume that the APUs will be capable of performing any meaningful digital processing on such high bandwidth signals. The APUs need to use low power to remain small enough for large volume installation and this is not compatible with extreme requirements on digital processing.

Therefore, one promising architecture for high frequency and high bandwidth D-MIMO systems is to utilize analog radio over fibre (ARoF) as depicted in Figure 6-6. To keep the APUs operating with low power usage (to reduce the heat dissipation and the resulting size and weight) the APU consists of nothing more than an optical add and drop multiplexor (OADM), a photo detector (PD), a directly modulated laser (DML), and some analog components related to TX and RX. Using wavelength division multiplexing (WDM) it is still possible to serialize the fronthaul and connect many APUs to the same physical fibre cable. All digital processing (e.g. precoding, channel estimation, etc) is performed in the CPU where the constraints on size and weight are more relaxed and a somewhat higher power consumption can be acceptable.

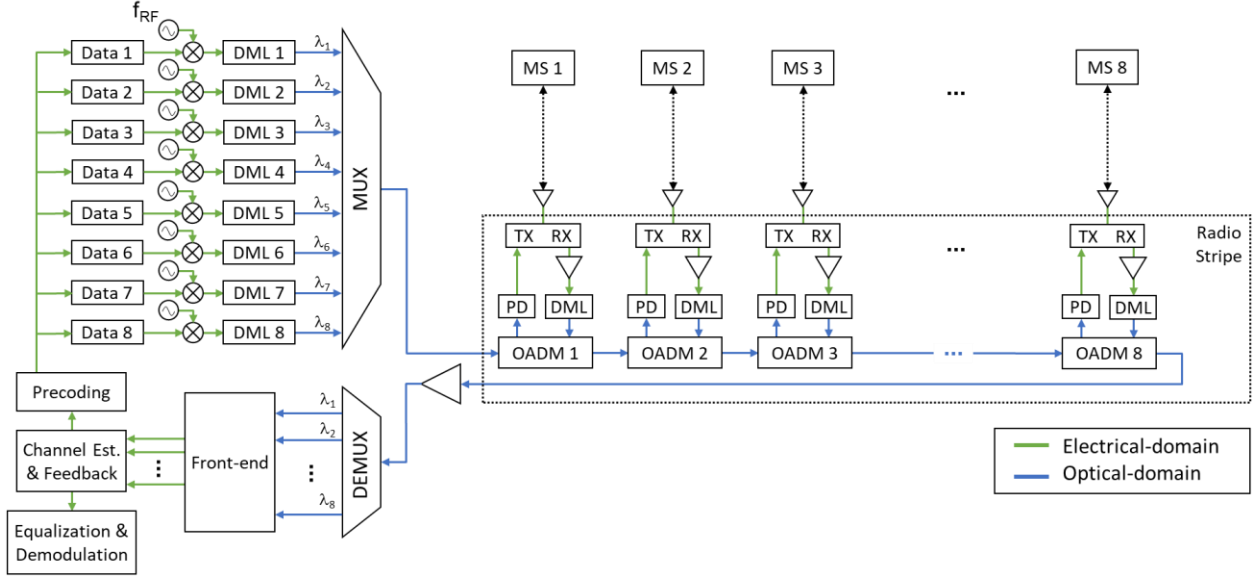


Figure 6-6: A wide bandwidth D-MIMO system can be implemented using ARoF and WDM.

6.3.2 Distributed digital beamforming

6.3.2.1 Beamforming Computations and Weight Distribution

This section presents reciprocity-based (UE-centric) Interference Aware Distributed Zero-Forcing (IADZF) method and compares with Centralized Zero-Forcing (CZF). Each distributed precoding done in clusters/subsets are interference-aware, i.e., consider minimizing the power interfering to other clusters.

Let N APs coherently serve K randomly distributed UEs in a UE-centric way as shown in Figure 6-1. For UE-centric AP clustering (a.k.a. subset), the method in [NTD+18] has been set by grouping the APs that provides sufficiently high SNR values with the best channel quality that contribute at least $\alpha\%$, e.g., 95%, of large-scale fading coefficients towards the k -th UE.

Centralized Zero Forcing (CZF): All APs form a single cluster, i.e., can transmit signals to any UE, and ZF is done in the central entity. Let the received signal be represented in terms of channel gain (\mathbf{H}) and precoding (\mathbf{W}) matrices as

$$\mathbf{y} = \mathbf{H}\mathbf{W}\mathbf{q} = [\mathbf{H}_1^H \quad \mathbf{H}_2^H \quad \dots \quad \mathbf{H}_K^H]^H \mathbf{W}\mathbf{q}, \quad (6-1)$$

where \mathbf{q} is the data symbol vector, $\mathbf{H}_k = [\mathbf{h}'_{k1} \quad \mathbf{h}'_{k1} \quad \dots \quad \mathbf{h}'_{kN}]$ is the channel gain matrix for the k -th UE with all serving APs. Then, the precoding matrix (\mathbf{W}) can be found by

$$\mathbf{W} = \min_{\mathbf{X}} \|\mathbf{H}\mathbf{X} - \mathbf{I}\| = \mathbf{H}^H [\mathbf{H}\mathbf{H}^H]^{-1} \cong \widehat{\mathbf{H}}^H [\widehat{\mathbf{H}}\widehat{\mathbf{H}}^H + \mathbf{\Gamma}]^{-1}, \quad (6-2)$$

where $\widehat{\mathbf{H}} = \mathbf{H} + \widetilde{\mathbf{H}}$ and $\mathbf{\Gamma} = \mathbf{E}\{\widetilde{\mathbf{H}}\widetilde{\mathbf{H}}^H\}$ is the error covariance matrix.

Distributed Zero Forcing (DZF): Multiple clusters are formed in a UE-centric way where APs in each cluster only serve the UE inside the given cluster. The precoding coefficients are calculated for each cluster separately. \mathbf{H}_i is the channel gain matrix between the N_i APs and K_i UEs in the i -th cluster (C_i), \mathbf{G}_i is the interference channel matrix between the APs inside C_i and UEs outside C_i , and \mathbf{W}_i is the precoding matrix for C_i . Then, $\widehat{\mathbf{W}}_i$ can be found with interference unaware Traditional Distributed Zero Forcing (TDZF) and Interference Aware Distributed Zero Forcing (IADZF) as following

$$TDZF: \quad \widehat{\mathbf{W}}_i = \min_{\mathbf{X}} \|\mathbf{H}_i\mathbf{X} - \mathbf{I}\| = \mathbf{H}_i^H [\mathbf{H}_i\mathbf{H}_i^H]^{-1}, \quad (6-3)$$

$$\text{IADZF: } \widehat{\mathbf{W}}_i = \min_{\mathbf{X}} \left\| \begin{bmatrix} \mathbf{H}_i \\ \mathbf{G}_i \end{bmatrix} \mathbf{X} - \begin{bmatrix} \mathbf{1} \\ \mathbf{0} \end{bmatrix} \right\| = [\mathbf{H}_i^H \mathbf{H}_i + \mathbf{\Lambda}_i]^{-1} \mathbf{H}_i^H, \quad (6-4)$$

where $\mathbf{\Lambda}_i = \mathbf{G}_i^H \mathbf{G}_i$ is the interference covariance matrix. In case of disjoint clusters, $\widehat{\mathbf{W}}_i$ for each cluster are independent, and combined precoding matrix (\mathbf{W}) throughout the network is the direct sum of each $\widehat{\mathbf{W}}_i$ where off-diagonal blocks are zero matrices. Common APs in different subsets creates dependency between separate $\widehat{\mathbf{W}}_i$, then \mathbf{W} is composed of K UE-specific precoding vectors, \mathbf{W}_k as

$$\mathbf{W} = [\mathbf{W}_1 \quad \mathbf{W}_2 \quad \cdots \quad \mathbf{W}_K] = [\mathbf{v}_1^H \quad \mathbf{v}_2^H \quad \cdots \quad \mathbf{v}_N^H]^H, \quad (6-5)$$

where the calculated $\widehat{\mathbf{W}}_k$ are the non-zero elements of \mathbf{W}_k . In order to ensure that none of the APs exceed maximum transmit power limit, combined precoding matrix need to be normalized as

$$\bar{\mathbf{W}} = \frac{\mathbf{W}}{\max_n \|\mathbf{v}_n\|}. \quad (6-6)$$

Performance Evaluation:

Performance has been evaluated in an indoor scenario with randomly distributed blockers, for different number of regularly deployed APs each with M antenna elements and K uniformly distributed single-antenna UEs. The configuration parameters used in the simulations are given in Table 6-1. Perfect channel estimation and lossless, high capacity fronthaul is assumed. RF imperfections, hardware impairments, phase noise, power amplifier nonlinearities are omitted from the scope of this work.

Table 6-1: Simulation Parameters

Parameter	Model Specification	
Frequency range (GHz)	28	100
Bandwidth (MHz)	200	5500
Maximum AP transmit power	13 dBm	
Number of subarrays	1	
Vertical/Horizontal antenna elements	4/8	8/16
Number of UEs	{20, 40}	
Propagation Model	3GPP InH [38.900]	
Area size	100 m x 100 m	
Number of blockers	1000	
Blocker size	Max: 2m x 3m, Min: 0.5m x 1m	
Duplexing	TDD with 50% downlink	
AP Noise Figure (dB)	7	10
Overhead ratio	1:3	

Figure 6-7 demonstrates that IADZF method applied over UE-centric clusters with $\alpha = 95\%$ clustering method, can achieve the performance of CZF method at which all APs serves each UE, for different deployment sizes on sub-THz band. Two methods converge in relatively dense deployments. Due to the higher path-loss and weaker signal penetration, SE decreases as frequency increases.

IADZF has been compared with interference unaware TDZF in Figure 6-8 for different cluster sizes, $N_k = 1$, $N_k = 4$, $\alpha = 95\%$ clustering approach, and $N_k = N$, i.e., all AP simultaneously transmit to all UEs, operating at 28 GHz. It has been shown that larger subsets using IADZF method, brings more precoding gain and increases the SE. However, if distributed precoders are interference unaware, increased subset size degrades the performance.

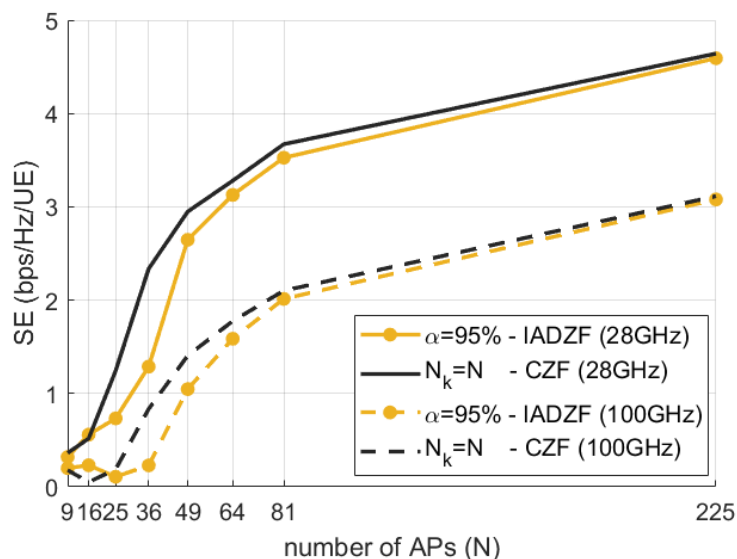


Figure 6-7: SE performance comparison of IADZF and CZF for different cluster sizes for 20 UEs operating at 28 and 100 GHz.

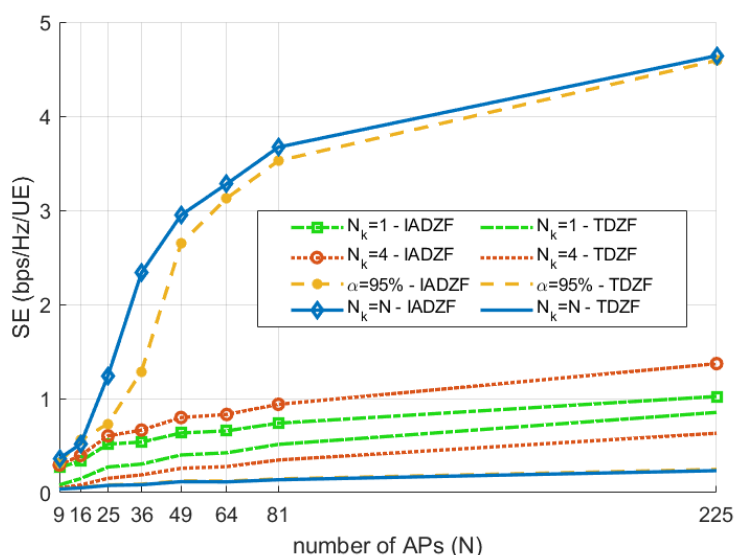


Figure 6-8: SE Performance comparison of IADZF and interference unaware TDZF for different cluster sizes for 20 UEs operating at 28 GHz.

Cumulative distribution functions (CDFs) of signal to interference and noise ratio (SINR) values of 20 UEs served by 49 APs for different serving cluster sizes, e.g., $N_k = 1$, $N_k = 4$, $\alpha = 95\%$ clustering approach, and $N_k = 49$ is shown in Figure 6-9. It has been shown that more APs involved in coherent transmission brings higher degree of diversity, hence better interference cancellation and performance. Effect of the operating frequency is negligible for small size of serving AP subsets. Nonetheless, as frequency increases, APs close to the UE become dominant while distant APs do not contribute much which decreases the received signal strength, eventually the SINR. Small clusters can still provide good enough SE performance on the average, and particularly can utilize the high bandwidth at high frequency bands. Another highlight is that more APs can enable the cell-edge UEs, e.g., %5 of the UEs, having positive SINR.

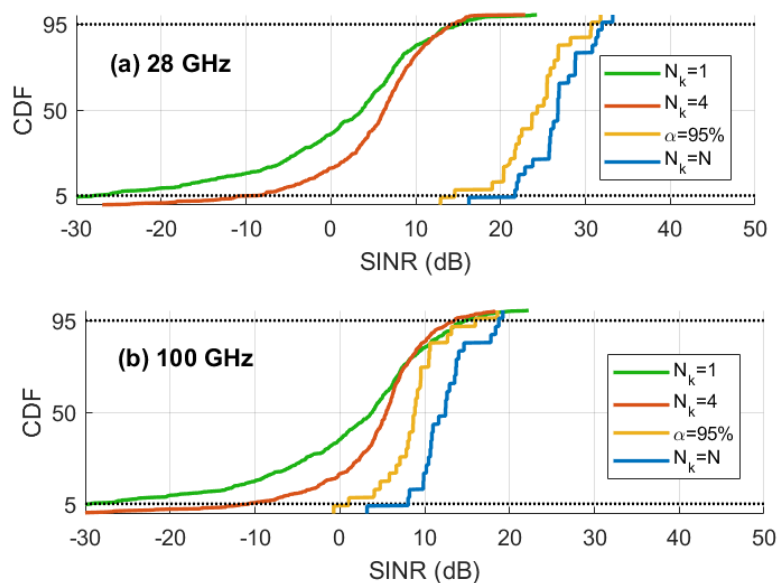


Figure 6-9: SINR performance for IADZF for $N = 49$ APs and $K = 20$ UEs evaluated at (a) 28 GHz and (b) 100 GHz.

Figure 6-10 demonstrates the average SE performance over 40 UEs w.r.t. different antenna distributions, e.g., $N = 64 \times M$ antennas are distributed over $L = \{1, 4, 16, 64\}$ locations. It has been shown that semi-distributed ($L = 4$) or fully distributed ($L = 64$) deployments perform similar for single cluster case, i.e., Herein, there is a trade-off between implementation and deployment complexities. One cluster including all APs in the network, can still achieve high SE values by collocating the antennas ($L = 1$), but it has higher implementation complexity. Many but smaller subsets ($N_k = \{1, 4\}$) are easier to implement joint processing, however, more scattered deployment is necessary for good enough performance.

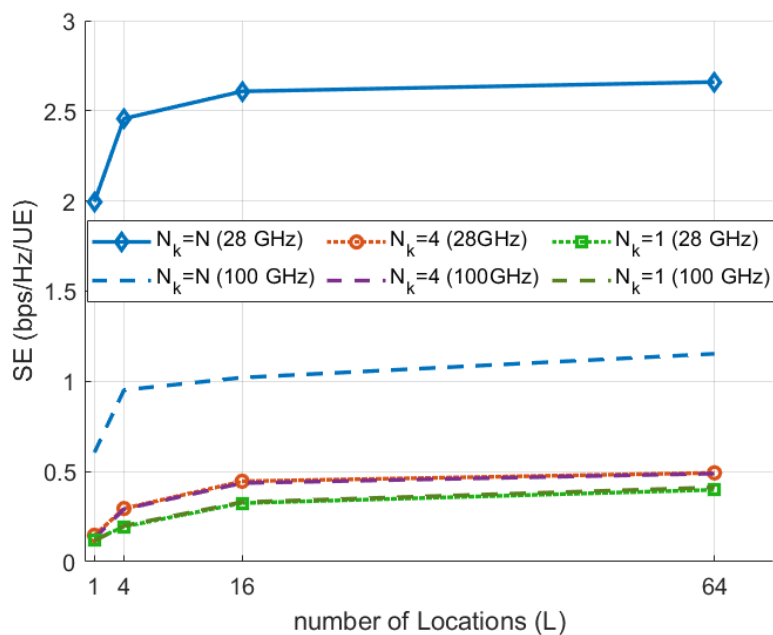


Figure 6-10: Performance comparison for collocated ($L = 1$), partially ($L = \{4, 16\}$) and fully distributed ($L = 64$) deployments for different operating frequencies for $N_k = \{1, 4, 64\}$.

6.3.2.2 Hybrid Precoding in Cooperative Millimeter Wave Networks

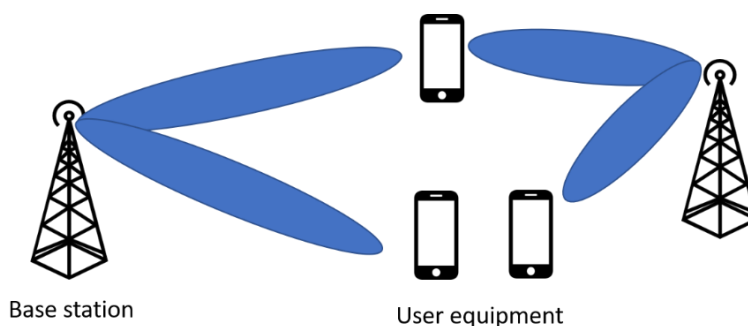


Figure 6-11: A mmW network where BSs jointly transmit to the users with beamforming.

Here we investigate BS coordination schemes in mmW networks that allow multiple streams to be transmitted jointly from multiple BSs, taking hardware and channel characteristics into account. Users are being served using spatial multi-flow and implements successive interference cancellation to decode the data streams sequentially.

As shown in Figure 6-11, we consider a downlink multi-cell and multi-user mmWave network with M multi-antenna BSs and K single antenna users. We assume the hybrid precoding architecture is used at the BSs, as it is shown to achieve high spectral efficiency with reduced hardware power consumption compared to that of the fully digital precoding (FDP), due to the reduced number of RF chains [AGZ17]. The number of antennas at BS is denoted by N_m and the number of RF chains L_m . Depending on the number of phase shifters (PSs), the fully connected hybrid precoding architecture (FHP) requires each RF chain connected to all antennas and the partially connected hybrid precoding architecture (PHP) connects each RF chain to a subset of the antennas [GDH16]. In addition, we assume that the sum power consumption of all BSs is divided into the hardware power consumption, including the PSs and

the digital-to-analog converters (DACs), and the RF transmit power. The hardware power consumption is given by

$$P_m^{\text{hw}} = [N_m^{\text{PS}} P_{\text{PS}} + L_m (P_{\text{DAC}} + P_{\text{RF}})] / (1 - \Delta_m), \quad (6-7)$$

where Δ_m is a power loss factor which accounts for the extra power dissipated at various non-transmission related parts such as power supply loss and active cooling. Also, P_{PS} , P_{DAC} and P_{RF} denote the power consumption of the PSs, DACs, and RF chains, respectively, and N_m^{PS} is the number of PSs. The number of PSs needed by each architecture is given by the FDP: $N_m^{\text{PS}}=0$, $L_m=N_m$, the FHP: $N_m^{\text{PS}}=L_m N_m$, and the PHP: $N_m^{\text{PS}}=N_m$. We further assume that if a BS is associated with no users, it can enter a silence mode in which the hardware consumption is reduced.

Our objective is to minimize the sum power consumption such that the per-user minimum spectral efficiency, the per-BS maximum power constraint and the hybrid precoding constraint are guaranteed. We propose a sub-optimal algorithm by decoupling the optimization problem into an analog precoding problem, which only depends on the channel information, and a digital precoding problem that minimizes the sum power consumption by solving a semi-definite program. The proposed hybrid precoding algorithm jointly associates users to the BSs, finds the optimal BS silence strategy with minimum power, and enables us to jointly serve a user by multiple BSs. For the detailed system model and algorithm, cf. [FMS21].

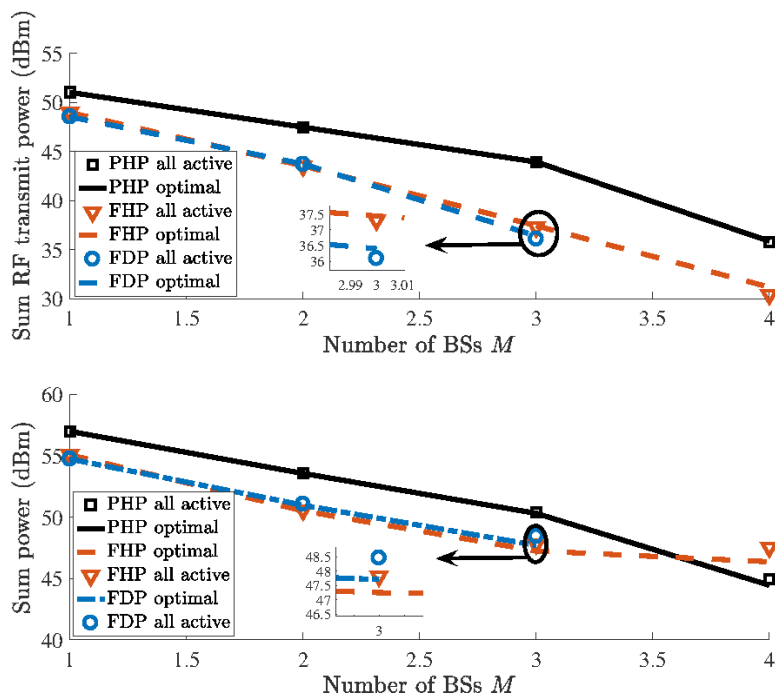


Figure 6-12 (a) Sum RF transmit power and (b) sum power consumption versus the number of BSs. For each architecture, simulation results based on all BSs being active are compared to the optimal case when the silent mode is enabled. Network parameters: number of antennas $N_m = 64$, number of users $K = 4$, number of RF chains $L_m = 4$ per BS, PS power consumption $P_{\text{PS}} = 40\text{mW}$, DAC power consumption $P_{\text{DAC}} = 200\text{mW}$, RF chain power consumption $P_{\text{RF}} = 40\text{mW}$, $\Delta_m=0.15$ and target spectral efficiency $\tau_k = 4$ bit/s/Hz per user.

In Figure 6-12 (a), the result shows that network densification and cooperative transmissions lead to a better chance for a user to be served by BSs with good channel conditions, thus, requiring less RF transmit power to achieve a target spectral efficiency. In Figure 6-12 (b), for $M > 4$, the PHP starts to consume less sum power than the FHP, since the hardware power increase has less effect on the sum power consumption than that of the FHP. Also, Figure 6-12 shows that the power consumption difference between the optimal case and the sub-optimal case is small. It is worth noting that the total power consumption depends on the power consumption of the PSs, RF chains and the DACs, and the

power scaling in the silence mode. Setting a low value for the hardware power consumption will give advantages to the all-active case and, thus, reducing the difference between the case of all-active and the case of the optimal silence mode. Our parameters setting is based on the carrier frequency at 28 GHz. When higher frequencies are considered, the available transmit power will be further limited. Thus, the proportion of the hardware power will most likely increase, and the advantage of silence mode may be more prominent.

6.3.3 Integrated access and backhauling

6.3.3.1 Coordinated mesh based IAB

A challenge with D-MIMO is how the backhaul/fronthaul can be solved efficiently. If bandwidth is not the primary constraint as for example in early deployment and at THz frequencies, integrated access and backhaul can be an efficient approach to maintain flexibility and have efficient deployment. In this section, we investigate a concept how efficient AP selection combined with access and backhaul scheduling can be performed in a TDD system, where backhaul/fronthaul share resources. The simplest system setup is illustrated in Figure 6-13.

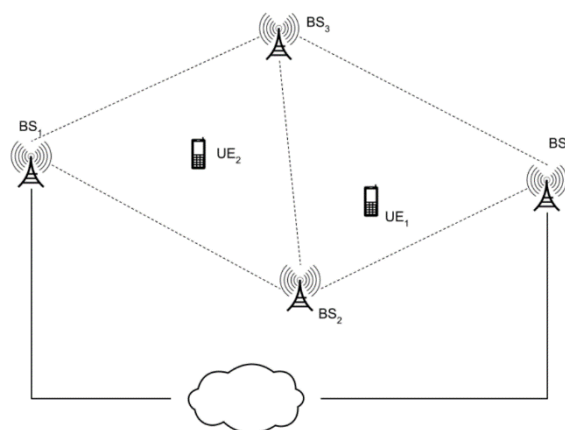


Figure 6-13 Basic network to illustrate scheduling and routing problem

In Figure 6-13, BS1 and BS4 have direct links to the core network, while BS2 and BS3 use in-band backhauling. In the network, the following constraints apply to all BSs and UEs:

- UEs can see at least one BS.
- Both BS1 and BS4 can be associated with BS2 or BS3, but they cannot see each other. Besides, BS2 and BS3 can communicate with each other.
- All BSs work in the TDD manner, i.e., either in TX or RX phase in each time slot.
- One UE is served by only one BS in RX mode in each time slot, i.e. Antenna/AP selection is used as the most primitive form of D-MIMO.
- One BS allows multiple access links in one time slot using different frequency resources. Note that this will increase cost of link when scheduled and routed.

In a more general form, all BSs together form a backhaul/fronthaul mesh. Note at this point, no assumption is made on the traffic to be routed to the core, i.e. the function split between BS and core. Up to this point, this is abstracted in a cost-metric, which can be changed depending on beamforming capability, channel model, deployment.

The overall problem to be solved is:

- Which AP should a UE connect to?
- In which time-slot should it be scheduled?
- Which route should the traffic be routed through fronthaul/backhaul mesh?

Given a cost-metric (for example, number of hops to core and throughput), the problem can be divided into time-slot allocation and shortest-path optimization. Time-slot allocation is illustrated in Figure 6-14 which shows how BSs and UEs are grouped as part of optimization process.

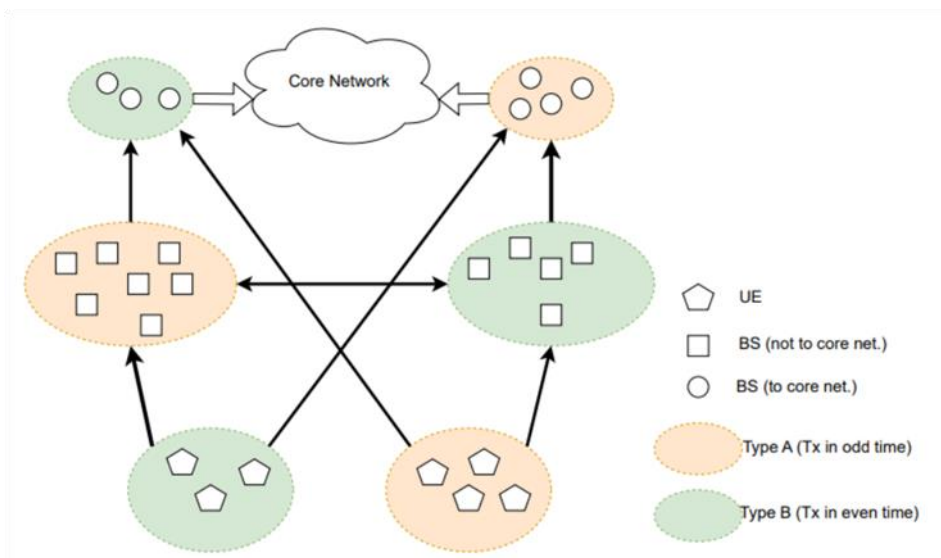


Figure 6-14: UE and BS/AP grouping in odd and even time-slots, prior to routing optimization.

For a given grouping of nodes (odd and even time-slots), the second problem to be solved is between which nodes traffic should be sent. From which UE to which AP, and if an AP needs to transport traffic to the core, which backhaul/fronthaul links should be used.

Both problems need to be solved jointly and exhaustive search becomes already prohibitively complex for small networks. Thus, a greedy algorithm was developed, which has a complexity that is linear in the number of UEs.

Initial example results: In Figure 6-15, a random network with weighted links, consisting of 50 UEs and 10 BSs is illustrated. Link weights are determined by path-loss only. The vertices in red, blue, and green denote UE, ordinary BS and BS with core access, respectively. The arrows on edges indicate network flow along a path from UE to the core network. A and B indicate the time-slots assigned to the nodes.

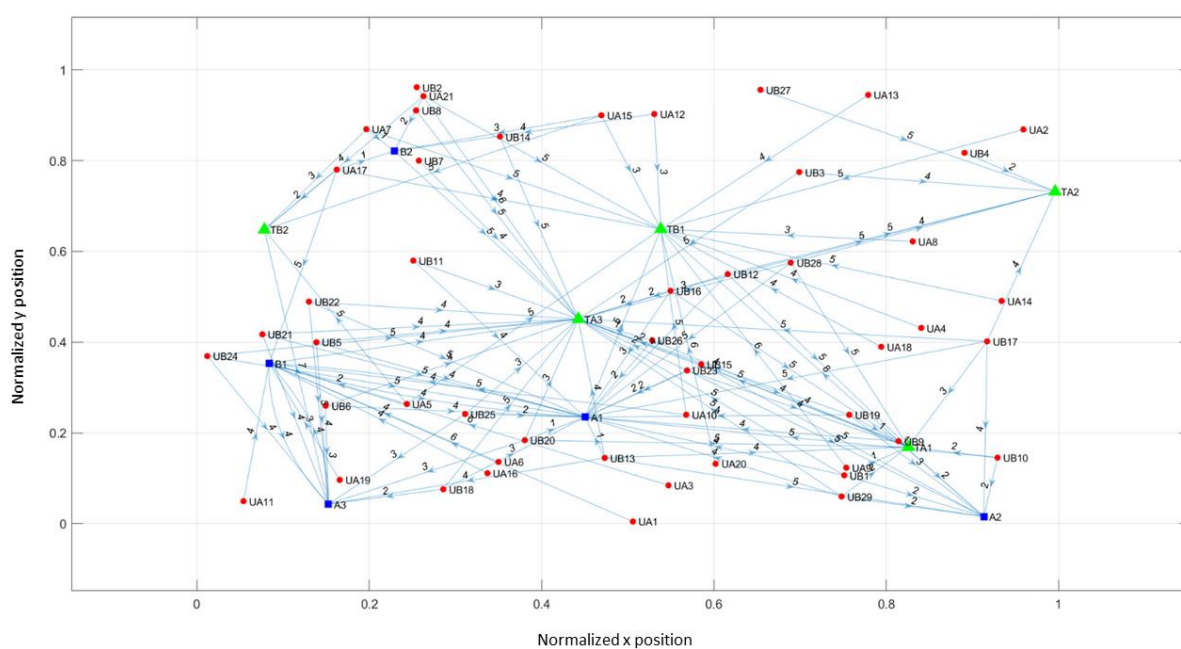


Figure 6-15: Network of 50 UEs and 10 BS/APs

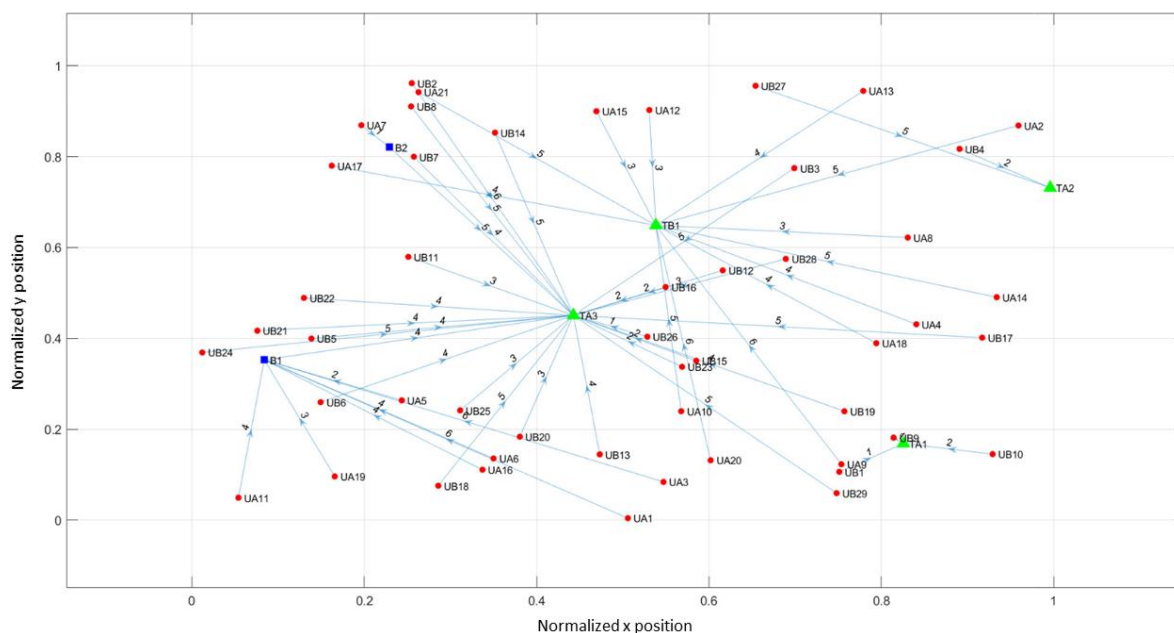


Figure 6-16: Assigned network after cost-optimization (number of hops for all links)

The work presented above focused on developing a joint scheduling and routing optimization algorithm for integrated access and backhaul (IAB) mesh networks, that can be used on larger networks which can readily be applied to upper mmW and sub-THZ specific deployments.

6.3.3.2 IAB Coverage analysis

As discussed earlier, wireless backhaul/fronthaul is a crucial enabler for successful deployment of distributed large MIMO systems. A cell-free network will probably underlie a traditional cellular network and is likely to use APs with large distributed antenna arrays. The potential offered by IAB techniques can be very helpful in this regard by alleviating the fronthaul problem and by reducing the deployment cost in massive base station densification scenarios compared to the fiber deployment which requires a noteworthy initial investment for trenching/installation.

Motivated by the presence of very wide bandwidths at mmW carrier frequencies and above, IAB networks allow the operator to use part of the spectrum resources for wireless backhauling [TMM+19]. In 3GPP NR, IAB network configurations allow to provide flexible low-cost wireless backhaul using 3GPP NR technology in international mobile telecommunication (IMT) bands and provide not only backhaul, but also the cellular services in the same node. This will be a complement to existing microwave point-to-point backhauling in suburban and urban areas.

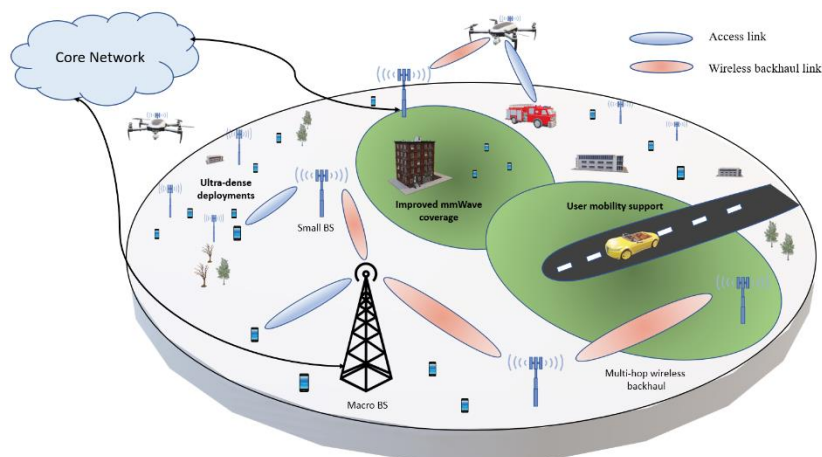


Figure 6-17: Illustration of IAB.

An outdoor two tier heterogeneous IAB network, where a few (potentially, fibre-connected) APs, i.e. macro base stations (MBSs) and small base stations (SBSs), provide other APs as well as the mobile devices inside their cell area with wireless backhaul and access connections, respectively, is illustrated in Figure 6-17.

6.3.3.2.1 Integrated Access and Backhaul vs Fiber

In this section, we discuss the IAB network performance and evaluate its performance in comparison with those achieved by hybrid IAB/fiber-connected networks using an FHPPP (finite homogeneous Poisson point process)-based stochastic geometry model, e.g., [SAD18], [AMH18], i.e., a PPP with a constant density, with random distributions of the IAB nodes as well as the user equipment's (UEs) inside a finite region. The details of the evaluation can be found in [MMF+20].

Table 6-2: Simulation parameters

Parameter	Value
Carrier frequency	28 GHz
Bandwidth	1 GHz
Path loss exponents	[LoS, NLoS] = (2, 3)
Main lobe antenna gains	[MBS, SBS, UE] = (24, 24, 0) dBi
Side lobe antenna gains	[MBS, SBS, UE] = (-2, -2, 0) dBi
Antenna powers	[MBS, SBS, UE] = (40, 24, 0) dBm

In Figure 6-18, we study the service coverage probability of the IAB networks with those obtained by the scenarios having a fraction of fibre-connected SBSs, as well as the cases without SBSs (Refer to Table 7-1 for main simulation parameters). Figure 6-18 (On the left), compares the performance of IAB and fibre-connected networks, in terms of service coverage probability, i.e., the probability of the event that the minimum target rate requirements of the UEs are satisfied. Then, Figure 6-17 (On the right) shows the network service coverage rate as a function of the fraction of fibre-connected SBSs and characterizes the system performance with the cases without SBSs.

This is motivated by the fact that, in practice, some of the SBSs may have easy access to fibre. Here, we assume the fibre-connected SBSs to be randomly distributed in the considered network area. It is observed that for a wide range of parameter settings, the IAB network has the ability to provide effectively the same levels of network service coverage probability as that of fibre-backhauled network with relatively small increase in the number of deployed IAB nodes from Figure 6-18.

Such a small increment in the number of IAB nodes, leads to several advantages:

- Increased network flexibility: In contrast to fibre-backhauled networks, where the APs can be installed only in the places with fibre connection, the IAB nodes can be installed in different places if they have an acceptable connection with their parent nodes. This increases the network flexibility and the possibility for topology optimization remarkably.
- Reduction in network cost: An SBS is much lower in cost than laying fibre [OF16, Table 7]. Also, different evaluations reveal that, for dense urban/suburban areas, even in the presence of dark fibre, the IAB network deployment reduces the total cost of ownership.
- Reduction of time-to-market: Due to the required regulatory permissions, digging and construction time, laying fibre typically takes a long time. In such cases, IAB can help to install new base stations/radio sites quickly.

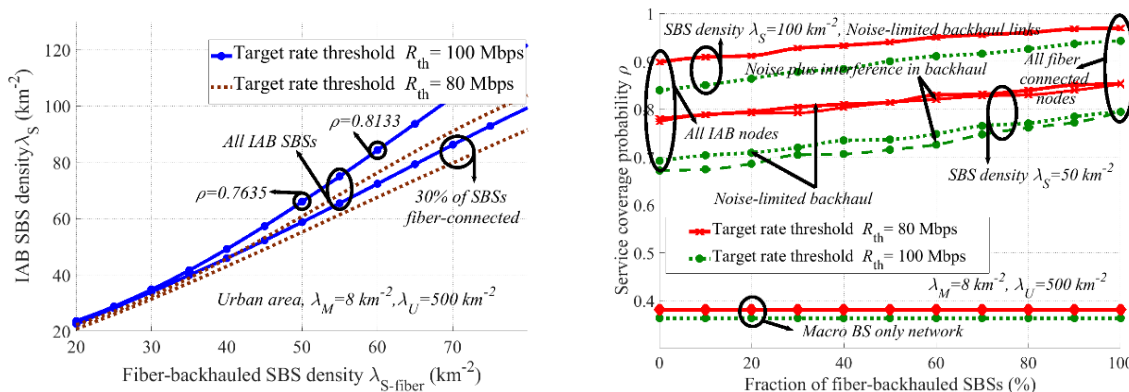


Figure 6-18: (left) fibre-backhauled networks. (right) Service coverage probability as a function of percentage of fibre-backhauled SBSs.

6.3.3.2.2 Genetic algorithm-based topology optimization for IAB

Due to the increase of network size in dense areas, which is the main point of interest in IAB networks, finding solutions for optimal network topology/routing is important. Since such optimization problem is very complex, an exhaustive search over all possible deployment options quickly becomes infeasible. This motivates a potentially suboptimal machine learning approach, which gives effective (sub)optimal solutions with reasonably satisfactory implementation complexity. Particularly, we propose a genetic algorithm (GA) based scheme to optimize the base station locations and non-IAB backhaul link placement. The details of the proposed scheme can be found in [MMM+21].

Unlike the non-IAB backhaul-connected networks, IAB networks may be prone to environmental effects, especially due to the blockage in dense urban environments and the tree foliage in sub-urban environments. It should also be noted that although IABs' main point of interest is dense urban areas, it has the capability to be deployed in suburban areas as well.

In Figure 6-19 we evaluate the effect of the blockage in urban areas and tree foliage on the network performance of an IAB network in suburban areas with random deployment and GA-optimized non-IAB backhaul link distribution. Here, the results are presented for different rate requirements of the UEs for the access links with path loss exponents 3, 4 for LOS, NLoS propagations and main lobe antenna gains of 18, 18, 0 dBm for main base station (MBS), SBS and UEs, respectively. Particularly, Figure 6-19 (left) shows the service coverage probability considering the Poisson point process (PPP)-based germ-grain blocking model while in Figure 6-19 (right) presents the results for the average hop distance of 450 m which corresponds to SBSs density of 8 km⁻² in a suburban area.

Based on Figure 6-19, the following conclusions can be derived:

- The GA-algorithm based optimized network deployment shows considerable resilience to blockage and tree foliage, compared to the unoptimized random network.
- The service coverage probability in suburban area with a random IAB network deployment is considerably affected by the tree foliage loss. This is especially witnessed when the tree density

is increased. However, with the introduction of GA algorithm-based optimization on selecting the appropriate non-IAB backhaul link distribution, we observe a resilience to the tree foliage.

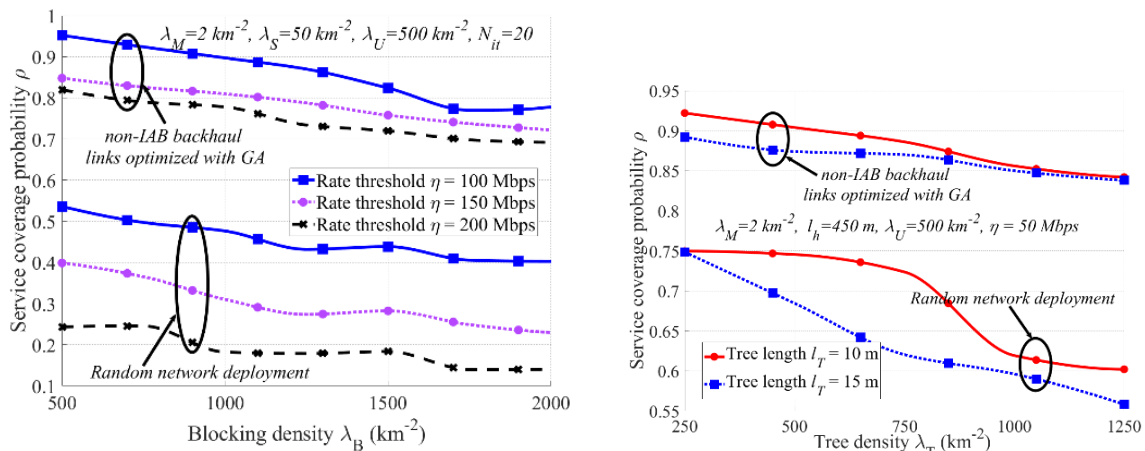


Figure 6-19: (left) Service coverage probability of the IAB network as a function of the blocking density with MBS, SBS and UE transmit powers $P_m, P_s, P_u = (40, 24, 0)$ dBm. (right) Service coverage probability of the IAB network as a function of tree density with $P_m, P_s, P_u = (40, 33, 0)$ dBm.

In general, IAB robustness is hard to predict in the presence of tree foliage due to the influence of characteristics of the trees/vegetation on the link quality. Particularly, the link quality may vary due to the number of wet trees, snow on the trees, leaf percentage in different seasonal changes and wind. However, we conclude that proper network planning can reduce the adverse effects on IAB, even though it is prone to medium/highly densified tree foliage in suburban areas. Moreover, mmW IAB in areas with low/moderate amounts of tree foliage is expected to perform well.

6.4 Conclusions

In this chapter we introduced challenges and opportunities with D-MIMO and its potential role in 6G. We elaborated on the different challenges at lower and upper mmW/THz bands, calling for a scalable approach from digital to analog approaches. We also emphasized the need for efficient backhaul fronthaul solutions by integrating fibre and in-band wireless solutions. Since densification is the key enabler to meet coverage and reliability targets at the higher frequency bands and there seems to be sufficient spectrum available, low-cost solutions are more important than spectral efficiency (at least in the early roll-out phases) calling for decentralized solutions, whereas in the lower mmW bands the need for higher spectral efficiency calls for digital less distributed approaches. To this end we highlighted some of our ongoing research results on analog centralized beamforming; digital distributed and centralized beamforming; and integrated access and backhauling.

7 Understanding the above-100 GHz wave-material interaction and wave propagation through measurements

7.1 Wave-material interaction analysis

The use of upper mmW frequencies involves the use of highly directional antennas with a substantial risk of blocking the link between the transmitter and the receiver, and therefore the use of reflected and scattered paths to maintain communication. It is then essential to have a good understanding of the transmission and reflection losses at sub-THz frequencies of common building materials, and also to be able to compare those losses with the corresponding values at lower frequencies.

Related references already available in the literature could be classified into three categories. Some publications analyze the channel at pointed frequencies, for example 28 GHz, 73 GHz, 140 GHz as in [XKJ+19], where the authors identify transmission and reflection attenuations and compare them in frequency. Other references offer continuous analysis but are limited to 100 GHz as in the study reported in [KMH19]. Finally, the last group of references is generally based on spectroscopic techniques and offers continuous analysis from 100 GHz up to a few THz. For example, reference [PJW+07] analyzes transmission coefficients up to 1 THz but starts at 100 GHz and does not allow a comparison with the frequencies currently used by wireless communication systems. At the standardized level, the International Telecommunications Union (ITU) has specified material characteristics up to 100 GHz [ITU-R2040-1].

Therefore, this section aims to extend the current existing knowledge on material characterization by providing continuous measurements between 2 and 170 GHz of transmission losses for different materials composing an indoor environment. The results will provide a better understanding of the interactions of the electromagnetic wave with different materials over a wide range of frequencies currently in use or potentially usable for future communication systems such as 6G.

The measurements were carried out using vector network analysers (VNAs) based measurement system, equipped with frequency extenders for frequencies above 50 GHz. Two VNAs were used to continuously cover the frequency band 2 GHz – 170 GHz. As the measured frequency band is significantly wide, the measurements were done in sub-bands with adaptable equipment for each band. Six sub-bands listed in Table 6-1 were defined respecting the operating frequencies of either the antennas for frequencies below 50 GHz, or the frequency extenders for frequencies above 50 GHz. This system allows free space measurements of transmission and reflection coefficients at normal incidence, a general schematic of the measurement set up that includes VNA, antennas and frequency extenders is shown in Figure 7-1.

Table 7-1: Frequency bands and associated equipment

Frequency band	VNA	Frequency extenders	Waveguide or Connector	Antenna	Gain
2 GHz - 12 GHz	Rohde & Schwarz ZVA-40	No	SMA	Dual ridge horns SH800	6 - 15 dBi
12 GHz - 30 GHz				Dual ridge horns SH2000	6 - 15 dBi
30 GHz - 50 GHz	Keysight PNA-67			Flann Microwave horns 23240-25	25 dBi
50 GHz - 75 GHz	Rohde & Schwarz ZVA-40	OML V15VNA2	WR15	Flann Microwave horns 25240-20	20 dBi
75 GHz - 110 GHz		OML V10VNA2	WR10	Flann Microwave horns 27240-20	20 dBi

110 GHz - 170 GHz		VDI E8257DV06	WR6.5	Millitech horns SGH-06	25 dBi
-------------------	--	------------------	-------	------------------------	--------

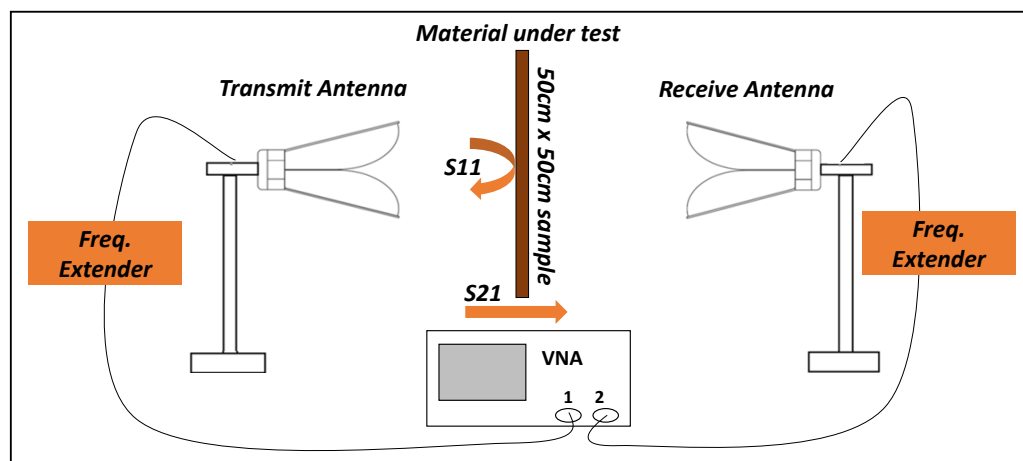


Figure 7-1: Measurement set up

In this section, the focus will be only on transmission measurements. The holding system for antennas and frequency extenders is shown in Figure 7-2. One of the antennas is connected to a moving rail on the X axis and the second antenna is attached to a Y-Z rail. After aligning the two antennas, the distance between them is fixed at about 1 m. A specific material holder was manufactured to insert material samples of dimensions 1.50 m x 1.50 m and variable thickness between the two antennas while minimizing the potential diffractions generated by the sample edges.

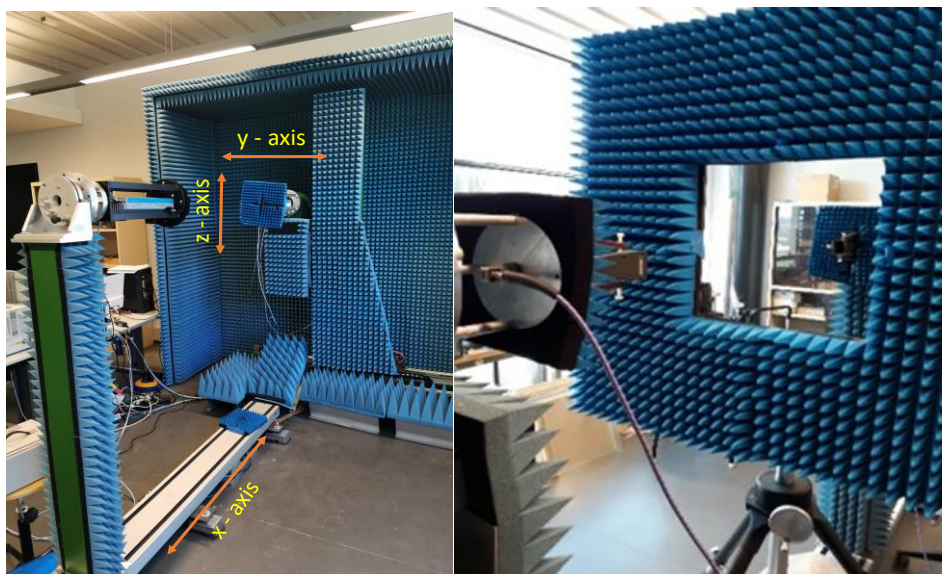


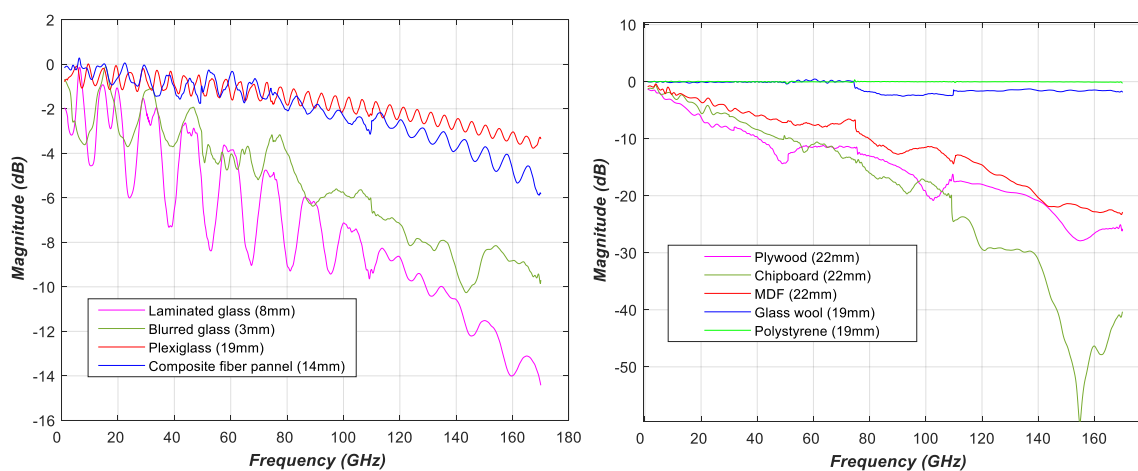
Figure 7-2: Measurement and positioning system

The analysed materials are typical materials of the indoor environment, such as glass, plexiglass, wood and its derivatives, plasterboard, concrete, sound, and thermal insulation. Table 7-2 shows the set of measured materials and their thickness. For each frequency band, the measurement process consisted of the following measurement steps: first, the designated measurement equipment was installed and the VNA was configured. Then, a free space measurement serving as a reference measurement was carried out. Finally, the material holder was inserted between the two antennas, the materials were measured, and their raw data were collected. When all the materials were measured, a new frequency band was selected, and the previously described process was applied again.

Table 7-2: Measured material samples and their thickness

Material	Thickness [mm]
Laminated Glass	8
Blurred Glass	3
Plexiglass	19
Composite fibre panel	14
Plywood	22
Chipboard	22
Medium density fibreboard (MDF)	22
Plasterboard BA13	13
Plasterboard BA18	18
Plasterboard Duotech19	19
Mortar (Cement + sand)	22
Glass wool	19
polystyrene	19

The post-processing method consists of three stages. First, the raw material measurements and the reference measurement are filtered by the procedure called "Time-Gating". This involves applying a temporal filter to eliminate from the raw measurement, the noise and the far multipaths that are not resulting from an interaction between the EM wave and the material under test. Second, the raw material response is normalized by that of free space to extract the intrinsic material response from the raw measurement, and thus correct for effects of the measurement equipment. Finally, the six bands are joined together, and the results are presented in what follows.

**Figure 7-3: Transmission losses of some measured materials**

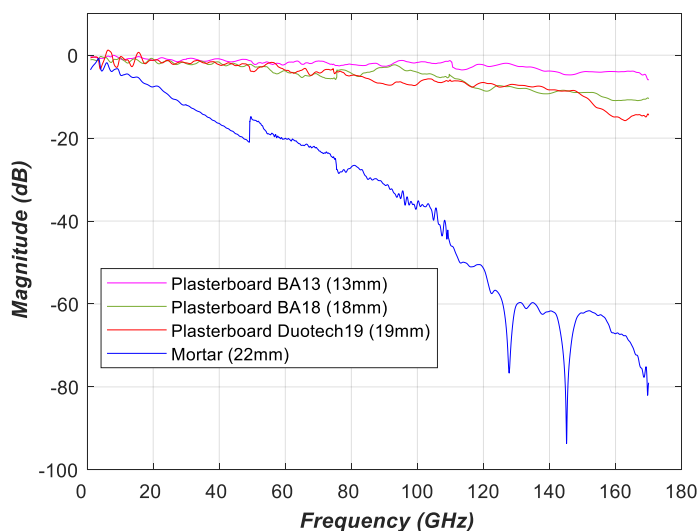


Figure 7-4: Transmission losses of some measured materials

The transmission coefficient results of different materials are presented in Figure 7-3 and Figure 7-4. As expected, and modelled by the dielectric materials theory, transmission losses increase with frequency but not in a regular manner for all materials. Regular oscillations are observed for glass and plexiglass which are due to interference between the direct path and the internal multi-reflections. Irregular oscillations are observed, more accentuated at frequencies above 100 GHz for materials such as wood, glass wool or plasterboard, which could be explained by the inhomogeneity of the materials. This inhomogeneity could also explain the discontinuities at the border frequencies between frequency bands because the samples were not positioned in a strictly identical manner for the different frequency bands. Finally, at frequencies above 100 GHz, strong frequency selectivities appear, the physical cause of which is not clearly established.

The results of reflection losses are currently in process. They will give a further understanding to this first analysis and allow it to be deepened by evaluating the linear losses of each material.

7.2 Multipath Channel Measurements

This section summarizes indoor and outdoor channel sounding and data post-processing methods at 140 GHz band, performed in the greater Helsinki region, Finland. Channel sounding is our basis to know “typical channels” and hence developing a channel model in the future.

7.2.1 Channel Sounder Architecture

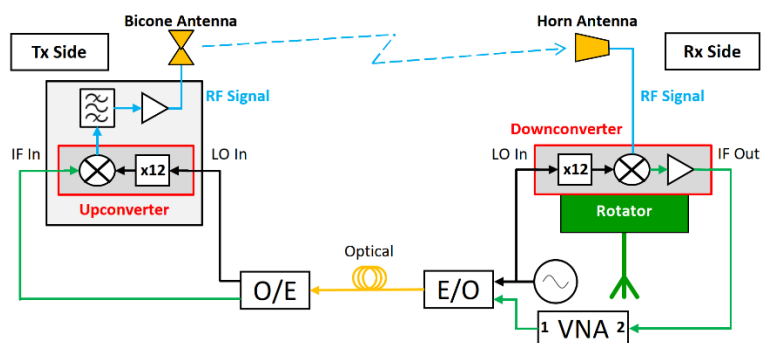


Figure 7-5: Channel sounder for D-band (110 to 170 GHz).

Aalto's D-band channel sounder applies swept-frequency method using a VNA which can obtain the channel response with high temporal resolution and high dynamic range. The number of points for the VNA sweep measurements and the IF bandwidth number were set to 10,001, and 2 KHz, respectively. The IF signals from and to the VNA are translated to RF through the upconverter on the Tx side and downconverter on the Rx side as shown in Figure 7-5. The LO signal needed for this frequency translation is supplied by a signal generator situated on the RX side. A Radio-over-fibre (RoF) system which consists of Optical-to-Electrical (O/E) and Electrical-to-Optical (E/O) converters, and a military-grade optical fibre cable with two single-mode fibres, is employed to distribute the IF signal and LO signal to allow channel measurements with large TX-RX separation distance. Vertically polarized antennas are installed on the TX and RX. A 0 dBi bicone antenna with 360° azimuth HPBW and 45° elevation HPBW is on the TX side and a 19 dBi horn antenna with 10° azimuth HPBW and 40° elevation HPBW is on the RX side. The angular information of the channel on the RX side is obtained by rotating the horn antenna with 5° or 10° steps over azimuth; no elevation scanning was made. Furthermore, the sounder transmits at output RF of 140 – 144 GHz and effective isotropic radiated power (EIRP) of 30 dBm. The observed noise floor is around –128 dBm and assuming an SNR requirement of 10 dB, the measurable path loss of this channel sounder is 148 dB.

7.2.2 Measurement Steps

During measurement campaigns, the RX side of the channel sounder is usually placed in a single location while the TX side being lightweight and mounted on a mobile tripod is moved to different locations. The sounder components are warmed-up first by turning them on for at least two hours before performing any measurements to minimize any channel impulse response (CIR) gain and delay fluctuations which would otherwise contribute uncertainties to the measured response of the channel. Before proceeding to the over-the-air measurements, a back-to-back (B2B) measurement is first performed by connecting the RF port of the frequency upconverter to that of the downconverter with a 30 dB waveguide attenuator with known response \tilde{H}_{att} ; 50 frequency sweeps of data are collected during this B2B configuration, and their average is applied later to the channel measurements data to de-embed the effects of the sounder components. Then, the TX and RX antennas are installed and set at the same height to simplify the processing and analysis of measured paths. The system is automated such that it sweeps the whole RF range while the RX antenna is fixed to a particular direction, then the rotator pivots by one step on the azimuth and sweep the frequency again. These steps are repeated until the whole specified azimuth range are scanned. Note that in all the measurements performed, only the azimuth is scanned while the elevation is held constant. After scanning the whole azimuth range, the TX antenna is moved to a different location. A pair of TX and RX locations is referred here as a link.

7.2.3 Uncertainties

It was found that physical disturbance on the optical fibre cable during frequency sweep can lead to gain and delay fluctuations of the detected paths from the measured channel impulse response [MMK21]. An extensive characterization of the measured channel impulse response under varying conditions of the optical fibre cable was performed for a B2B configuration. The gain and delay fluctuations of the strongest path of the B2B channel are summarized in Table 7.2.3-2. Approximately the same amount of fluctuations should be expected even for other paths than strongest one in the measurements. Hence, to minimize such fluctuations, the optical fibre cable was made sure to be undisturbed during measurements. Meanwhile, when the cable is left static or when we change the position of the cable, which occur when we move the TX side to another location, measurement uncertainties are found to be insignificant.

Table 7-3: Measurement Uncertainties [MMK21]

Condition of the fibre cable	CIR Gain Fluctuation (dB)	CIR Delay Fluctuation (ns)
Static	0.4	0.0
Changing Positions	1.0	0.0
Continuously Disturbed	6.2	0.4

7.2.4 Data Post-Processing

7.2.4.1 Back-to-back Calibration

The data of interest directly obtained from the VNA after a frequency sweep is the forward transmission scattering parameter S_{21} , which is typically assumed to be equal to the transfer function \tilde{H}_{21} of the radio channel. When doing channel measurements, the VNA measures not only the response of the channel \tilde{H} , but also the response of the channel sounder components \tilde{H}_{cs} such as the cables, RoF and the frequency converters, i.e. $\tilde{H}_{21} = \tilde{H} \cdot \tilde{H}_{cs}$. The B2B calibration must be performed to remove the contribution of \tilde{H}_{cs} from the measured transfer function as described in Section 7.2.2. The B2B measurement then gives us $\tilde{H}_{b2b} = \tilde{H}_{att} \cdot \tilde{H}_{cs}$. Therefore, the channel transfer function without the effects of the channel sounder can be calculated as

$$\tilde{H} = \frac{\tilde{H}_{21}}{\tilde{H}_{cs}} = \tilde{H}_{21} \cdot \frac{\tilde{H}_{att}}{\tilde{H}_{b2b}}. \quad (7-1)$$

7.2.4.2 Path Detection

According to [KSJ+16], the angular-dependent channel transfer functions $\tilde{\mathbf{H}} \in \mathbb{C}^{N_f \times N_t}$ from the channel sounding are obtained for each TX-RX links; N_f and N_t denote the number of frequency bins and azimuth pointing directions of the RX horn antenna, respectively; $\mathbf{H}(l, m)$ denotes the (l, m) -th entry of the matrix \mathbf{H} , $1 \leq l \leq N_f$ and $1 \leq m \leq N_t$.

Matrices of angular-dependent channel impulse responses \mathbf{H} are derived by the inverse fast Fourier transform of each column of $\tilde{\mathbf{H}}$ with a rectangular window. The power angular-delay profile \mathbf{P}_{PADP} is derived as $\mathbf{P}_{PADP} = \mathbf{H} \odot (\mathbf{H})^*$, where \cdot^* and \odot denote conjugate operation and element-wise multiplication, respectively. A noise threshold P_{th} is defined for later analyses as

$$P_{th} = \frac{P_{offset}}{(l_1 - l_0 + 1)N_t} \sum_{l=l_0}^{l_1} \sum_{m=1}^{N_t} \mathbf{P}_{PADP}(l, m), \quad (7-2)$$

where l_0 and l_1 define the range of delay where only noise presents; P_{offset} is offset of the power relative to the estimated noise level to derive the noise threshold. Higher P_{offset} leads to more conservative detection of the signal over the noise level. Power angular spectrum of the channel PAS is defined by a marginal integral of the de-noised PADP $\hat{\mathbf{P}}_{PADP}$ over the delay domain as

$$PAS(m) = \frac{1}{N_f} \sum_{l=1}^{N_f} \hat{\mathbf{P}}_{PADP}(l, m), \quad (7-3)$$

where $\hat{\mathbf{P}}_{PADP}$ is made by padding zeros to all the (l, m) -th entries fulfilling $\mathbf{P}_{PADP}(l, m) < P_{th}$. The power delay profile (PDP) can also be derived from the PADP by taking the marginal integral over the azimuth angle as

$$PDP(l) = \frac{1}{N_t} \sum_{m=1}^{N_t} \hat{\mathbf{P}}_{PADP}(l, m). \quad (7-4)$$

Propagation paths are detected as local peaks of the PADP. The peaks can be identified directly using the PADP, but can also be detected sequentially for the ease of implementation; that is to detect local

maxima first on the PDP and then look for the greater maximum at the specified delay bins using the PADP. Since many local maxima are just noise especially at the large delay, only meaningful peaks that satisfy $P_n > P_{th}$ are considered valid in the subsequent analysis. The local maxima are further subject to finer peak search across the grid defined by the delay and azimuth angular bins. The fine search is made through interpolation of the neighbouring delay and angular bins using a peak-normalized gain pattern of the sinc function and the RX horn antenna, respectively, so that the estimated peak gives the best representation of $\mathbf{P}_{PADP}(l, m)$ locally around the peak. We particularly consider the delay and angular bins giving the local maximum and their immediate neighbours as the bins for the fine search.

The estimated peaks after the fine local search represents the propagation paths denoted by $\{\phi_n, \tau_n, P_n\}_{n=1}^{N_p}$, where ϕ_n , τ_n and P_n are azimuth angle on the RX side, propagation delay, power of the n -th path, $1 \leq n \leq N_p$, N_p is the number of paths. The path powers consist of the gain during wave propagation and that of the TX and RX antennas. Denoting the combined maximum TX-RX antenna gains as G_{ant} , the gain during wave propagation is given by $\hat{P}_n = \frac{P_n}{G_{ant}(\phi_n)}$. A set of parameters

$$\mathcal{P} = \{\phi_n, \tau_n, \hat{P}_n\}_{n=1}^{N_p}, \quad (7-5)$$

will be published after the Hexa-X project concludes for links of some measurement sites introduced in the next subsection.

7.2.5 Indoor Channel Sounding and Initial Observations

This subsection describes an indoor environment where 140 GHz channel sounding was performed. Observations on the measured PADP are given as initial understanding of wave propagation in the environment.

7.2.5.1 Entrance Hall Measurements

Channel measurements at 140 GHz were previously performed in an airport and in a shopping mall [SKJ+21]. Here, we selected a new indoor site that has many more small objects, i.e., the entrance hall of the Electrical Engineering building of Aalto University in Maarintie 8, Espoo, Finland as shown in Figure 7-6. Most of the areas have high ceilings and some have single floor ceilings. The sides are a combination of cement and metallic walls, and glass walls with metallic frames as a partition to office spaces. There are also metallic cylindrical columns, staircases, lockers, glass partitions, chairs and tables in the area. The measurements were performed during night or holidays so that there were no moving objects during the measurements. The measurements in this venue were performed twice with the first one on December 2020 and the second one on May 2021. The antenna locations for the December and May measurements are shown in Figure 7-7 and Figure 7-8, respectively. There were 11 links measured for the first measurement campaign, of which two are LOS and nine are NLOS links. Meanwhile, more links were considered in the second measurement campaign which has 56 links, of which 12 are LOS and 56 are NLOS links. In addition, angular steps of 10° and 5° were applied in the first campaign and second campaign, respectively. The TX and RX antennas were set to 1.85m. The paths data derived from the first entrance hall measurements were utilized to analyse the small-scale fading and evaluate the capacity of an omni-directional THz wireless channels [EAM+21].



Figure 7-6: Entrance hall surroundings.



Figure 7-7: Entrance hall (December 2020) antenna locations.



Figure 7-8: Entrance hall (May 2021) antenna locations.

7.2.5.2 Observations on Power Angular Delay Profiles

An exemplary PADD of an LOS link from Tx25-Rx1 link in the second measurement is plotted in Figure 7-9. Note that peaks are highlighted with square markers with colours representing their path gains. As expected, the path with highest gain and shortest delay is found at 160° azimuth angle, corresponding

to the direction of Tx25 antenna location seen from the RX antenna. Since the TX-RX distance between the antennas is short (10.4 m) and they are in a tight space with a lot of nearby objects, there are paths arriving from almost all azimuth directions. The PADP for an exemplary NLOS link (Tx7-Rx1) is shown in Figure 7-10. Although Tx7 is well behind a wall, strong paths, that are likely due to single-bounce reflections on the nearby elevator door, are still found. Visual inspection of other PADPs reveals that signal reflections occur on the walls, metallic cylindrical columns, glass partitions, metallic lockers, and staircase covered with metallic frames.

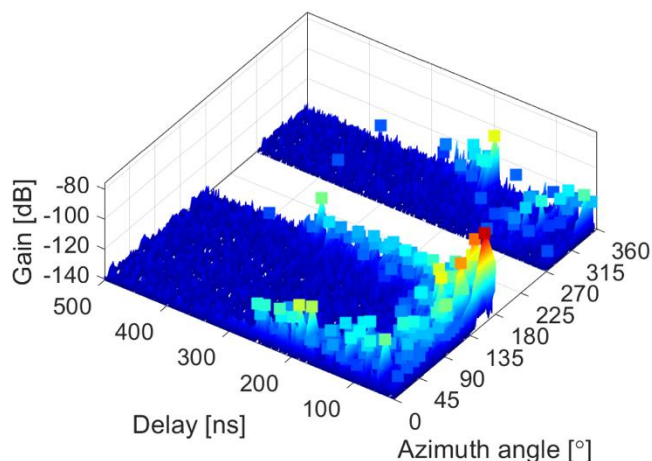


Figure 7-9: Power Angular Delay Profile of an LOS Tx25-Rx1 link in the second entrance hall measurements.

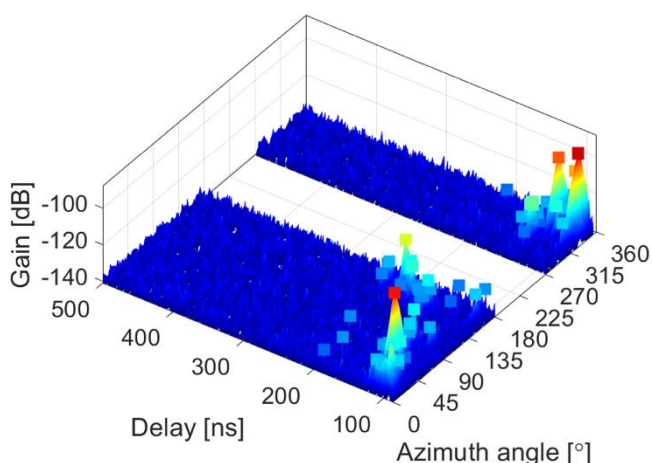


Figure 7-10: Power Angular Delay Profile of an NLOS Tx7-Rx1 link in the second entrance hall measurements.

7.2.6 Outdoor Measurements

7.2.6.1 Campus Measurements

The first outdoor measurement was conducted in the vicinity of one of the Electrical Engineering buildings of Aalto University in Maarintie 8, Espoo, Finland. The surroundings of this venue are shown in Figure 7-11. The outside walls of the buildings in the area are mainly made up of bricks and have glass windows and doors with metallic frames. There are also few large metallic structures installed on the walls. Metallic posts, trees and parking space with cars moving from time to time can also be found in the area. As seen on the map shown in Figure 7-12, large structures are usually found only on one side of the antenna locations, while the other side is almost an open space. Also, the environment is almost static as there were few and occasional passers-by. Two RX antenna locations each having 20

corresponding TX antenna locations were considered as depicted in Figure 7-12 and Figure 7-13, respectively. Each RX location has 16 LOS links represented by green pins and 4 NLOS links represented by yellow pins. The angular step of the RX horn antenna scanning over azimuth was set to 5° and both antenna heights to 1.85 m.



Figure 7-11: Campus surroundings.



Figure 7-12: Campus antenna locations for Rx1 links.



Figure 7-13: Campus antenna locations for Rx2 links.

7.2.6.2 Observations of Power Angular Delay Profiles Obtained in the Campus Measurements

Figure 7-14 shows the PADP of an LOS link (Tx18-Rx1) in the campus measurements. An LOS around 0° azimuth angle as expected is found. Aside from this LOS path, there are also significant paths due to single bounce reflection on the building, one is at 35° azimuth and the other is at 180° . Another interesting PADP is from LOS Tx5-Rx1 link plotted in Figure 7-15. Two groups of strong paths at 90° azimuth can be observed in which one of them is the LOS while the other with the higher delay corresponds to a single bounce reflection on a large metallic sand container at the back of Tx5 shown in Figure 7-16. The only outage link in this measurement campaign is the longest Tx19-Rx1 link while the rest of links have LOS path or have single bounce reflection on the outside wall of the buildings.

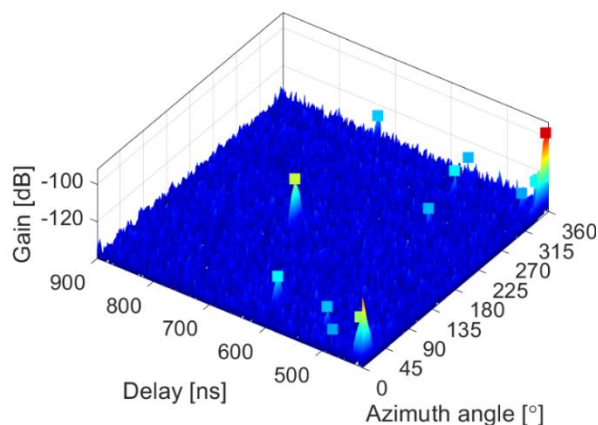


Figure 7-14: Power Angular Delay Profile of LOS Tx18-Rx1 link in the campus measurements.

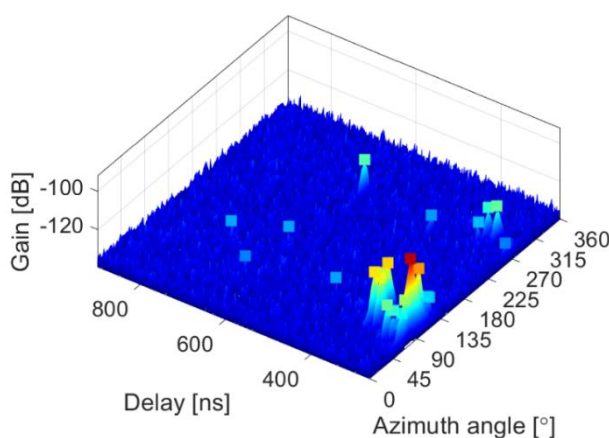


Figure 7-15: Power Angular Delay Profile of LOS Tx5-Rx1 link in the campus measurements.



Figure 7-16: Metallic structure in the campus environment.

7.2.6.3 Residential Measurements

Another outdoor measurement campaign was performed in a sub-urban environment along Leppävaarankatu, Espoo, Finland. The street is mostly surrounded by residential buildings with some commercial buildings. The surroundings of this residential area are shown in Figure 7-17. Metallic street posts and trees are also in the area. Unlike the campus environment, this environment is busier with people frequently walking around, and cars driving around and parking between the sidewalk and the street. The measurements covered one RX antenna location and 55 antenna TX locations as shown in Figure 7-18. There are 13 LOS links indicated by green pins and 42 NLOS links indicated by yellow pins. Most of these TX antenna locations are randomly scattered in the area. Some of them are placed along a straight line with narrow spacing near a building corner from an illuminated region to shadow region of the RX antenna. There are two sets of these corner measurements with the first one from Tx3 to Tx10 and the second one from Tx29 to Tx37. The angular step of the RX horn antenna scanning over azimuth was set to 5 degrees and both antenna heights to 1.85 m.



Figure 7-17: Residential surroundings.



Figure 7-18: Residential antenna locations.

7.2.6.4 Observations of Power Angular Delay Profiles Obtained in the Campus Measurements

An exemplary PADP for residential measurements is shown in Figure 7-19. In addition to the strongest LOS path, a strong single bounce reflection on the building near the RX antenna occurs in this link at 100° azimuth. Weak paths are also found in other azimuth directions. Another PADP is shown in Figure 7-20. It is an NLOS link (Tx7-Rx1) in which the Tx antenna is completely blocked by the corner of a building. It can be noticed that a strong path is found at 240° azimuth due to a single bounce reflection on a building. The links that are found to be outage are Tx15-, Tx17-, Tx38-, Tx40-, Tx43- and Tx50-Rx1.

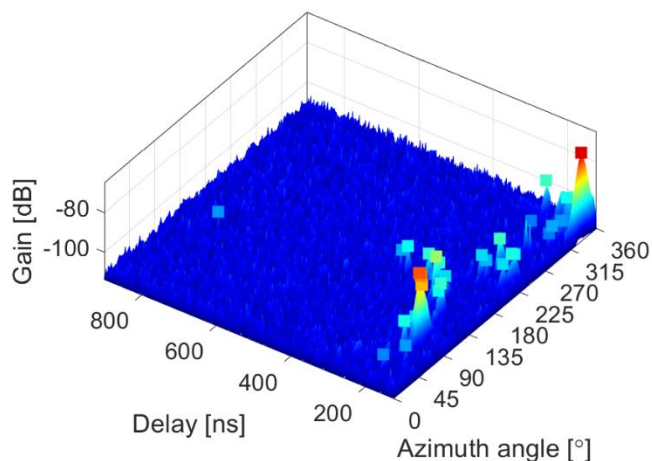


Figure 7-19: Power Angular Delay Profile of Tx19-Rx1 link in the residential measurements.

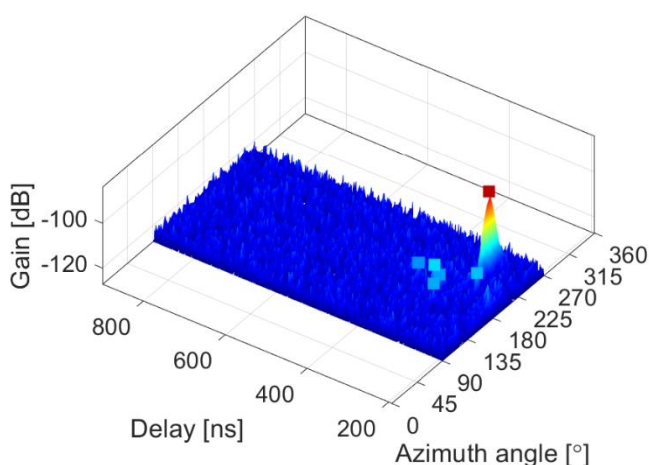


Figure 7-20: Power Angular Delay Profile of Tx7-Rx1 link in the residential measurements.

7.2.6.5 City Center Measurements

The last outdoor measurement campaign was performed in an urban environment in the city center along Aleksanterinkatu, Helsinki, Finland. This environment was also the venue of a previous measurement campaign which analysed the multipath cluster parameters of 15 GHz and 28 GHz small-cell backhaul links [SKJ16]. The street is surrounded by commercial buildings, forming a street canyon. The surroundings of this commercial area is shown in Figure 7-21. The street is primarily intended for pedestrians, blocking vehicular traffic except for trams. There are rare metallic signposts found on the street. The location has heavy loads of pedestrians and has some vehicles that park on the sidewalks occasionally. The total number of measured links is 40 and among those links 19 TX locations are LOS and 21 TX locations are NLOS to the RX location as illustrated in Figure 7-22. Most of these TX antenna locations are again randomly scattered in the area except for closely spaced TX locations for corner measurements to observe transition of wave propagation from lit to shadowed regions of the RX antenna, as indicated in the same figure. The angular step was set to 5° and both the TX and RX antenna heights was set to 2.00. Higher antenna height was selected for this environment to reduce uncertainties due to blockage of people and especially of cars and vans parking on the sidewalk.



Figure 7-21: City center surroundings.

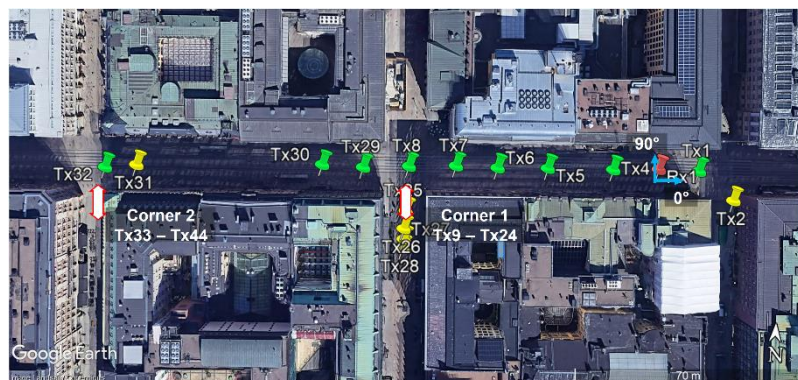


Figure 7-22: City center antenna locations

7.2.6.6 Observations of Power Angular Delay Profiles Obtained in the City Center Measurements

The PADP of the farthest LOS link (Tx32-Rx1) in the city center measurements is plotted in Figure 7-23. There is an LOS component at 180° and a single-bounce component at 200° which is again due to the reflection on a building on the bottom side of the map. Meanwhile, the PADP of an NLOS link (Tx39-Rx1) is shown in Figure 7-24 in which a path is still found even the link is heavily obstructed by a building corner. Only the Tx41-Rx1 link is outage among the measured links.

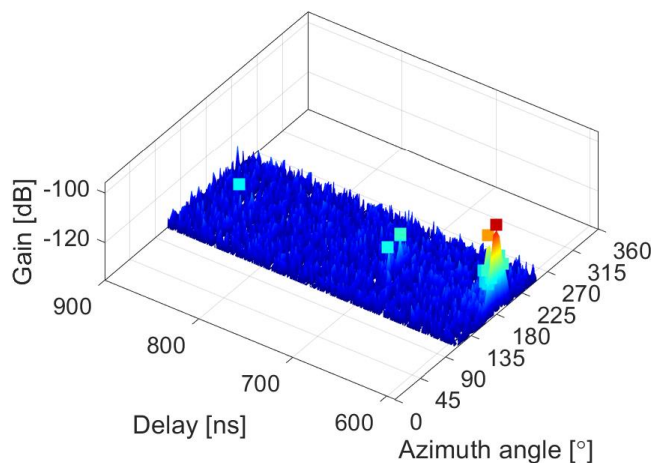


Figure 7-23: Power Angular Delay Profile of Tx32-Rx1 link in the city center measurements

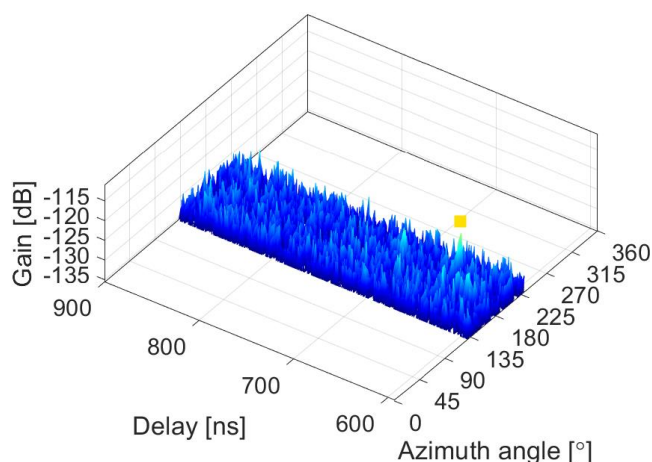


Figure 7-24: Power Angular Delay Profile of Tx39-Rx1 link in the city center measurements

7.3 Measurement-based analysis of 140 GHz multipath channels

7.3.1 The number of independent beams

Practical questions rise when conducting research for enabling communications at upper mmW radio frequencies. One of them, relevant for antenna, RF circuit, algorithm, and system researchers, is how many beams does upper mmW propagation channel support. In other words, how many significant beam directions with respect to the beam gain dynamics and expected correlation a propagation channel can support using a practical beam shape. Insight to the question is provided in [KGH+21] by defining methods to approximate the number of independent beams and by introducing resulting empirical beam number distributions that are based on the methods applied to the D-band measurement data described in Section 7.2. The evaluation is performed by using estimated PADPs of propagation channels and embedding a beam pattern to angularly filter them. The intention is to determine how many approximately independent beams of the given shape can be allocated on the PADP of each measurement location.

7.3.1.1 Methods for evaluating the beam number

The starting point is de-noised measurement data providing powers, delays, and azimuth angles of discrete multipaths in different environments and for different links (TX/RX locations). The PADP of a measured propagation channel as defined in Section 7.2.4.2 can be written as

$$P(\Omega, \tau) = \sum_{l=1}^L P_l \delta(\Omega - \Omega_l) \delta(\tau - \tau_l), \quad (7-6)$$

where L is the number of paths, $\delta(\cdot)$ is the delta function, and P_l , Ω_l , and τ_l are the gain, angle, and propagation delay of the l th path, respectively. Examples of PADPs are shown in Figure 7-14 and Figure 7-15. Any representative beam shape can be selected for the methods. For the results shown in this evaluation, a simple synthetic pattern defined in 3GPP specification [38.901] is selected. The beam of 10° HPBW and 30 dB peak to minimum gain ratio is illustrated in Figure 7-25. Three methods are briefly described in the following. A more detailed description can be found in [KGH+21].

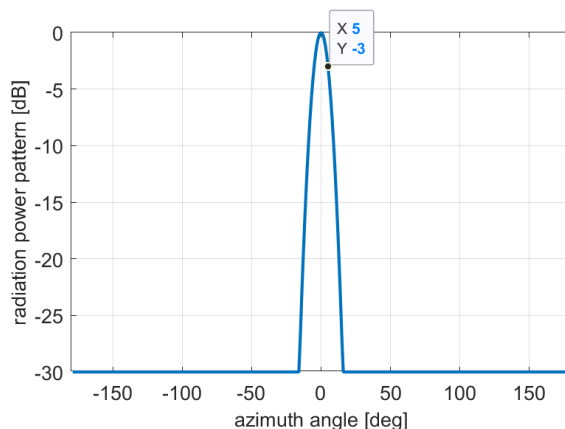


Figure 7-25: 3GPP beam shape with 10° HPBW used in beam number evaluation (half power, i.e., -3 dB point is at 5°).

Method 1: Number of local maxima

The first method counts the number of local maxima of the PAS observable by steering the selected beam pattern over all azimuth angles. This continuous PAS is obtained by taking convolution of the measured discrete PAS defined in eq. (7-2) and denoted here $P(\Omega)$, and the beam pattern $G(\Omega)$. The resulting continuous PAS corresponds to channel gain with the beam steered to directions α and is defined as

$$B(\alpha) = \int P(\Omega)G(\alpha - \Omega) d\Omega = \sum_{l=1}^L P_l G(\alpha - \Omega_l). \quad (7-7)$$

The first method selects all local maxima of $B(\alpha)$, $\alpha \in [0, 2\pi]$ that fall within a dynamic range counted from the global maximum of $B(\alpha)$. The dynamic range can be chosen, e.g., 10 or 20 dB, depending on the considered SNR requirements and related aspects of the envisaged system.

An example discrete PAS from an airport measurement is shown in Figure 7-26. This figure illustrates the continuous PAS defined in (7-7) and the corresponding selected beam directions using different methods, where the selections of method 1 are denoted by yellow triangles. In this case, the dynamic range was selected as 10 dB and in total three peaks, corresponding to three independent beam directions, were found.

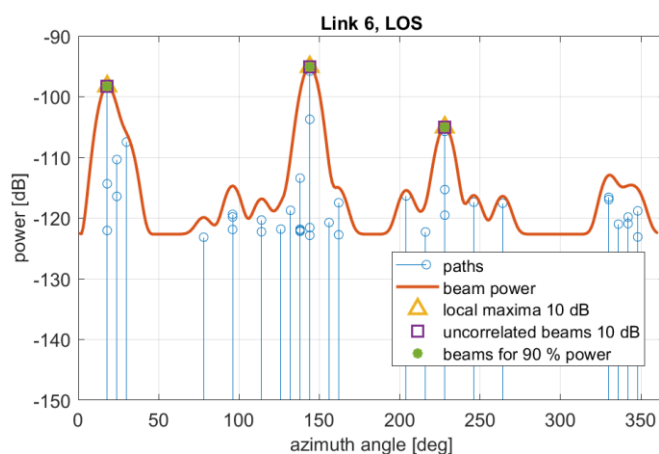


Figure 7-26: Measured path powers, the beam power and the independent beam directions found by using different methods in an example link. [KGH+21].

Method 2: Number of uncorrelated beams

The second method uses also the delay domain information of PADPs. For that purpose, each measured PADP defined in (7-6) is extended to a complex impulse response by introducing a random phase term for each path $l = 1, \dots, L$. The beam steering introduced in (7-7) is performed for the artificial impulse response and resulting continuous beam steered impulse response to direction α at propagation delay τ is

$$h(\alpha, \tau) = \sum_{l=1}^L \sqrt{P_l G(\alpha - \Omega_l)} e^{j\psi_l} \delta(\tau - \tau_l), \quad (7-8)$$

where ψ_l is the random phase term, uniformly distributed in $[0, 2\pi]$, of path l . The assumption of independent random phases across multipaths is reasonable, since the wavelength is very short and even a small displacement changes phases substantially. Next, impulse responses $h(\alpha, \tau)$ are Fourier transformed to frequency responses $H(\alpha, f)$ for discrete frequency points determined by the chosen centre frequency and bandwidth. The last intermediate parameter to be determined is the correlation coefficient of beam steered frequency responses in beam steering angles α_1 and α_2 . It is

$$R(\alpha_1, \alpha_2) = \frac{|\int H(\alpha_1, f) \overline{H(\alpha_2, f)} df|}{\sqrt{\int |H(\alpha_1, f)|^2 df \int |H(\alpha_2, f)|^2 df}} \quad (7-9)$$

where $\overline{(\)}$ denotes the complex conjugate operator.

The algorithm of Method 2 finds first the global maximum of $B(\alpha)$ and selects its argument as α_1 . Then all directions α , whose correlation $R(\alpha_1, \alpha)$ with the selected α_1 is higher than a threshold value, are discarded. Next the global maximum is found among the remaining set of directions and the previous step is repeated. This is done until no directions α are left. The set of independent beam directions is composed by the found maxima that are within a target dynamic range, similarly as in Method 1.

This method uses information of both propagation delays and angles. If there are numerous paths grouped in an angular sector, Method 2 finds beam directions also outside of the local maxima of $B(\alpha)$. An example of this condition is shown in Figure 7-27.

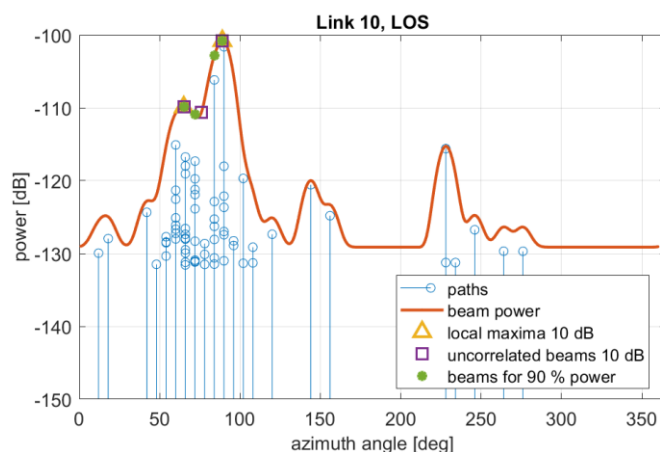


Figure 7-27: Measured path powers, the beam power and the independent beam directions found by using different methods in an example link. [KGH+21].

Method 3: The minimum number of beams for X% power

In the third method, the principle is to find beam directions such that a certain percentage, e.g. 90 %, of the available channel gain is gathered by the corresponding beams. Again, the first selected direction is in the global maximum of $B(\alpha)$. The magnitude of $G(\alpha - \Omega)$ is reduced from components of the discrete PAS $P(\Omega)$ and new beam steered PAS $B(\alpha)$ is determined. This procedure is repeated until the target percentage of available channel gain is captured by the sum of beam gains onto selected beam directions.

This method provides substantially different beam numbers in the cases of angularly highly dispersed propagation channel. An example of such condition is shown in Figure 7-28.

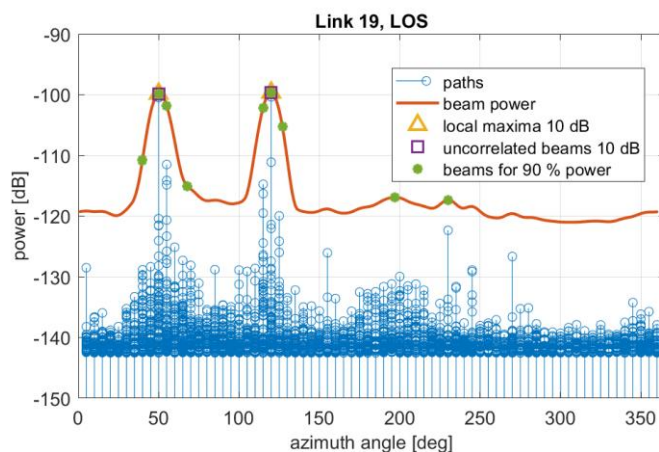


Figure 7-28: Measured path powers, the beam power and found independent beam directions using different methods in an example link. [KGH+21].

7.3.1.2 Resulting beam counts

Measured PAPDs of 55 indoor locations, measured at D-band by Aalto university, are analyzed with the three methods. Two dynamic ranges, 10 and 20 dB, are used both in Methods 1 and 2. The percentage in Method 3 is set to 90%. Resulting number of independent beams on all 55 cases are shown in Figure 7-29 (a). The 55 TX/RX locations represent both LOS and obstructed LOS (OLOS) conditions. OLOS cases are denoted by blue circles in the figure. Empirical cumulative distribution functions (CDF) are extracted from beam number occurrences shown in Figure 7-29 (a). These CDF curves are plotted in Figure 7-29 (b). From the results, one can approximate that the considered propagation channels support only one beam in 11–42% of cases. Two beams are supported in 23–29% and three beams in 13–23% of cases. Four or more beams can be allocated in 14–40%, depending on the selected evaluation method.

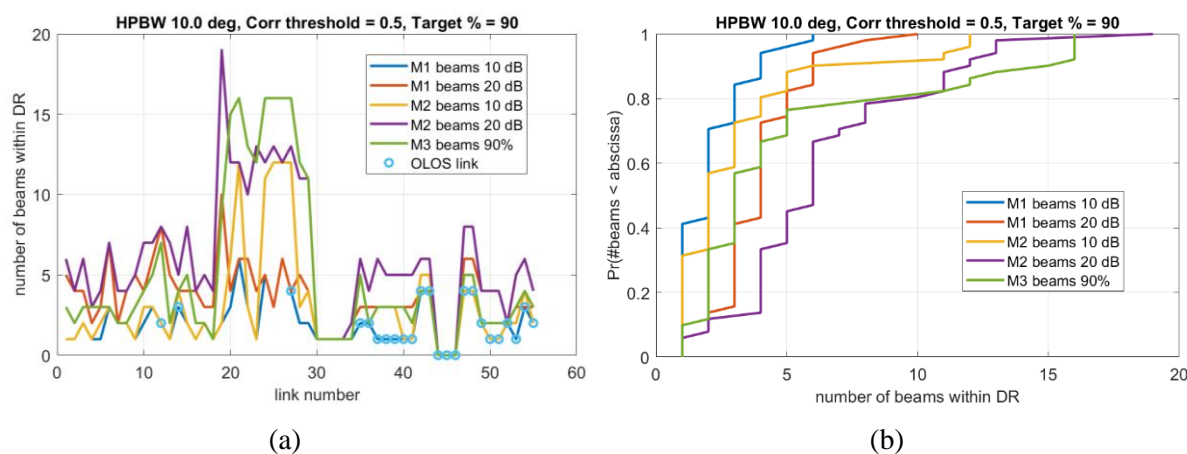


Figure 7-29: (a) Number of beams in 55 independent links as determined using three methods and two dynamic range values. (b) Cumulative distribution functions of beam numbers in 55 links using three methods and two dynamic range values. [KGH+21].

7.3.2 Wave scatterer identification

Among possible analyses of the measured channels, here we report results from wave scatterer identification by fusing the measured propagation path data on the map of the environment. There are several benefits in identifying scatterers, e.g., 1) giving insights into wave propagation mechanisms of

140 GHz channels, 2) providing bases for geometry-based modelling of wave propagation channels, among others.

7.3.2.1 Measurement-Based Ray Tracer

The measurements discussed in Section 7.2 provide angular information only on one side of the link hence we call them as single-directional propagation measurements. Figure 7-30 illustrates the single-directional measurements in which the only object in the channel is a flat smooth wall on the side. The omnidirectional antenna on the TX side, directive antenna on the RX side, and the scatterer center are located at \mathbf{r}_k^{Tx} , \mathbf{r}_k^{Rx} , and $\mathbf{r}_{k,n}^{\text{S}}$, respectively, for link k and path n . Furthermore, path n of link k is detected at the rotator angle of $\Omega_{k,n}^{\text{Rx}}$ on the RX side and has propagation delay of $\tau_{k,n}$. This measured angle comprises of azimuth $\phi_{k,n}^{\text{Tx}}$ and zenith $\theta_{k,n}^{\text{Rx}}$ angles. In our setup, the RX directive antenna is fixed at zenith equal to 90° and is only swept across different azimuth directions. Thus, in the case of our measurements, $\Omega_{k,n}^{\text{Rx}} = (\phi_{k,n}^{\text{Rx}}, 90^\circ)$.

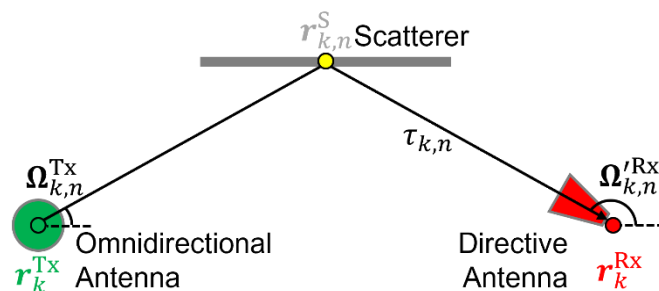


Figure 7-30: Single-directional propagation measurements

This set of known and measured information alone is not sufficient to generate a double-directional model of the channel and the location of the scatterers which are essential in describing the channel more accurately. The double-directional model consists of angular information both on the TX side and RX side which denote them here as angle-of-departure (AoD) $\Omega_{k,n}^{\text{Tx}} = (\phi_{k,n}^{\text{Tx}}, \theta_{k,n}^{\text{Tx}})$ and angle-of-arrival (AoA) $\Omega_{k,n}^{\text{Rx}} = (\phi_{k,n}^{\text{Rx}}, \theta_{k,n}^{\text{Rx}})$, respectively. The complete double-directional information of the paths could have been obtained by sweeping the RX horn antenna over the zenith angles and by also sweeping the angles on the TX side using a directional antenna. However, applying such method will dramatically increase the measurement time needed.

Alternatively, a measurement-based ray tracer (MBRT) [JKJ+09] is implemented here to estimate the double-directional information of the channel as illustrated in Figure 7-31. The MBRT requires additional input called point cloud data \mathbf{C} which are detailed geometrical database of the environment and contains the coordinates and normals of each point. The point cloud data of the entrance hall environment is shown in Figure 7-32. The idea is to launch optical rays from the RX antenna location in the point cloud to the measured AoA $\Omega_{k,n}^{\text{Rx}}$ of paths, with its length corresponding to the measured propagation delay $\tau_{k,n}$ so that its path undergoes various propagation mechanisms dictated by the point cloud data. The endpoint of this ray-traced path is denoted here by $\mathbf{r}_{k,n}^{\text{RT}}$ which we want to be as close as possible to the actual TX location \mathbf{r}_k^{Tx} . To take into account the ambiguity in the AoA due to some half-power beamwidth (HPBW) of the RX antenna, rays are also launched on the azimuth and zenith adjacent to $\Omega_{k,n}^{\text{Rx}}$. In addition, the first Fresnel ellipsoid formed by the source point of the ray, i.e., RX location, and the image point of the TX location is used to identify the potential interaction points in the point cloud that generate the reflected rays. When multiple points are found in the first Fresnel ellipsoid, we consider all of them as the source of specular reflections, ending up with *multiple* path trajectories for a single path estimate from measurements. From the input data \mathbf{r}_k^{Tx} , \mathbf{r}_k^{Rx} , \mathbf{C} , $\Omega_{k,n}^{\text{Rx}}$ and $\tau_{k,n}$, we can estimate $\mathbf{r}_{k,n}^{\text{S}}$, $\Omega_{k,n}^{\text{Tx}}$ and $\Omega_{k,n}^{\text{Rx}}$. Naturally, the accuracy of these estimates depends on the accuracy of the input data. Also, the MBRT is presently limited to specular reflections of only up to two bounces.

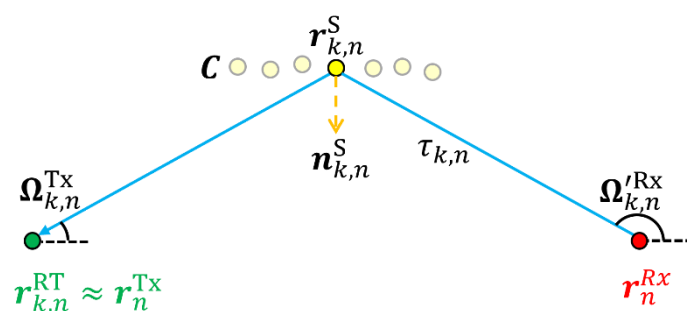


Figure 7-31: Measurement-based ray tracer.

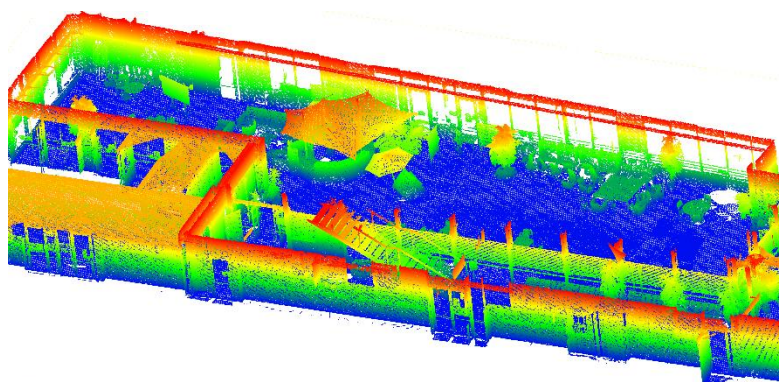


Figure 7-32: Entrance Hall point cloud data.

7.3.2.2 Most Probable Ray-Traced Path

For each measured angle $\Omega_{k,n}^{Rx}$, it is expected that we obtain multiple output estimates due to the uncertainties of input data and to the path trajectory estimation method based on the point cloud. In the MBRT, we choose the most likely path trajectory and to reduce the implication of the uncertainty on output path parameter estimates by setting several thresholds. One of them is a distance error threshold R at the end point of the trajectory, i.e., the distance error $\delta_R = \|\mathbf{r}_{k,n}^{RT} - \mathbf{r}_k^{Tx}\| \leq R$, similarly to the ordinal implementation of ray-launching simulations of wave propagation. Some exemplary results of AoD estimates using the MBRT for Tx14-Rx2 link ($k = 38$) and path $n = 11$ are shown in Figure 7-33. There are more than one AoD estimates for the single measured path. The most plausible path estimate can simply be the one with the lowest distance error, δ_R . However, a large cluster of estimates, which does not necessarily contain the estimate with lowest δ_R , may be a stronger indication that the path actually occurred in that cluster and not in the single and isolated estimate with lowest δ_R . To take this into account, the following *clustered* approach of paths are applied.

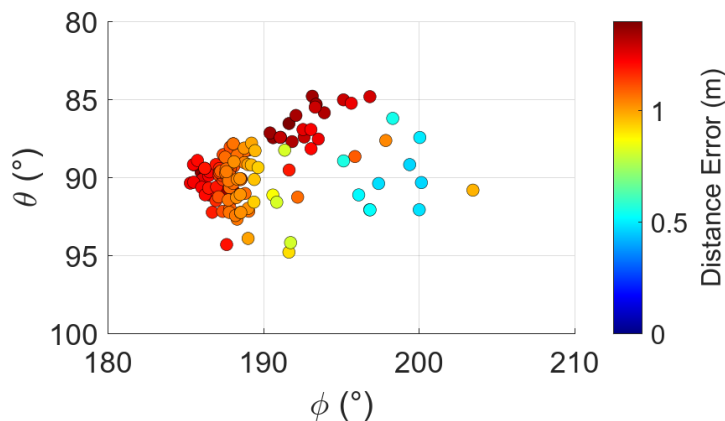


Figure 7-33: AoD estimates for Tx14-Rx2 link ($k = 38$) and path $n = 11$.

The AoD, AoA, and scatterer estimates are jointly clustered using Density-based spatial clustering of applications with noise (DBSCAN). The function is available in MATLAB; weights are assigned to each estimate using a piece-wise linear function plotted in Figure 7-34. The general idea is to assign higher weights to estimates with lower distance error. We set the w of the first interval $0 \leq \delta_R \leq 0.7$ to have small slope so that almost equal weights are assigned to estimates that may have distance error due to uncertainties in antenna locations and measured rotator angles. Beyond this interval, the weight decreases at a faster rate.

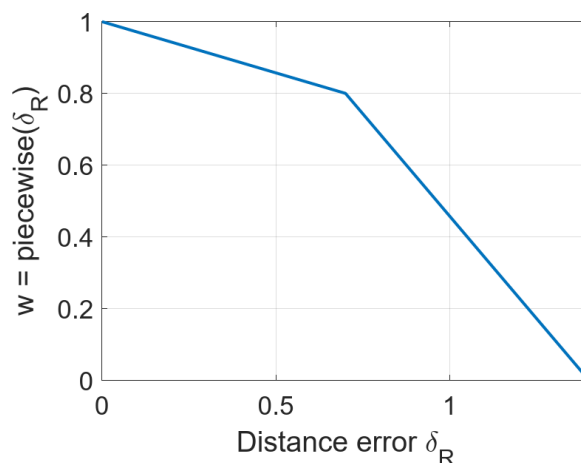


Figure 7-34: Linear piecewise function as weighting to derive the cost function in DBSCAN clustering.

The cluster with the highest total weights is selected as the most probable cluster. The single value estimate is obtained by getting the weighted mean of AoD, AoA, and scatterer coordinates in the selected cluster; the spread of the cluster around the mean represents *uncertainty* of the path estimates originated from those of input data as well as our method of relating the measured path estimates with the geometry of the environment.

7.3.2.3 Scatterer Identification Results

An illustrative MBRT result using the measured path estimates from the entrance hall is presented here. A center frequency of 142 GHz is assumed in the ray-tracing simulation. To shorten the simulation time, instead of applying the full HPBW mentioned in Section 7.2, a reduced radiation pattern with azimuth HPBW and elevation HPBW of 8° and 30° , respectively, is applied in the MBRT. Rays are launched from the RX location to the measured AoA $\Omega_{k,n}^{RX}$ and to its adjacent directions for every $\Delta\phi = 1^\circ$ and $\Delta\theta = 3^\circ$ until the reduced radiation pattern is covered. This setting results in 63 rays launched for every measured path. For Tx14-Rx2 link ($k = 38$) of the second entrance hall measurements that has 12 measured paths, $12 \times 63 = 756$ total rays were launched with the simulation runtime of 6.5 hours. The distance error threshold is set to $R = 1.4$ m. Eight out of 12 of the measured paths in Tx14-Rx2 link are successfully traced from the RX to Tx locations by the MBRT.

The scatterers found in one of the measured paths of Tx14-Rx2 link of the second entrance hall measurements is plotted in Figure 7-35. It can be seen that this path is most likely a single bounce reflection on a cylindrical column.

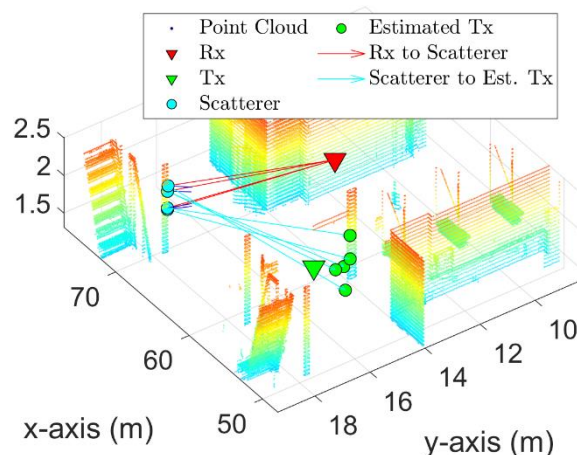


Figure 7-35: Scatterers identified for path 1 of Tx14-Rx2 link of the second entrance hall measurements.

The AoD and AoA estimates of all the traced paths by the MBRT in Tx14-Rx2 link are shown in Figure 7-36 (a) and (b), respectively. The plots show both the estimates with the lowest distance error, and the weighted mean of the selected cluster for each path. The 1 standard deviation (1σ), which measures the uncertainty of the estimates, is the weighted standard deviation using the piecewise linear function shown in Figure 7-34. On the plots, the 1σ range is so small for all paths that it is not visible. It can be noticed that there are instances that the estimates using the two selection criteria do not overlap. As expected, since the TX and RX antennas are at the same height, the AoA and AoD estimates generally lie around $\theta = 90^\circ$.



Figure 7-36: (a) Angle-of-departure estimates and (b) Angle-of-arrival estimates for Tx14-Rx2 link of the second entrance hall measurements.

The MBRT was applied to all the links in the second entrance hall measurements. It was found that some of the paths were not successfully traced from the RX to TX locations by the ray-tracer. This can be attributed to the uncertainty of input data, e.g., the point cloud missing translucent objects, the limited number of bounces considered and missing propagation mechanisms in the ray-tracer such as diffraction. Hence, as a future work, the MBRT will be improved by increasing the number of specular reflection bounces and by implementing other propagation mechanisms such as diffuse scattering and diffraction. In addition, translucent objects do not appear in the point cloud data and hence the MBRT presently assumes that signals completely penetrate those objects. It is possible that large flat glass walls reflect 140 GHz radio signals and hence produce paths with meaningful power. Thus, running the MBRT after adding them into the point cloud will also be an important study in the future.

8 Proof-of-concepts for communications

As outlined in this deliverable, the transition to higher carrier frequencies and larger bandwidth offers opportunities in terms of high data-rates, low latency, etc. but also poses challenges in terms of hardware-constraints and transceiver architectures. To emphasize that the concepts developed in this work-package in Sections 4-6 are of practical relevance, different types of demonstrations are planned. All demonstrations are based on a high-level communication block diagram as illustrated below:

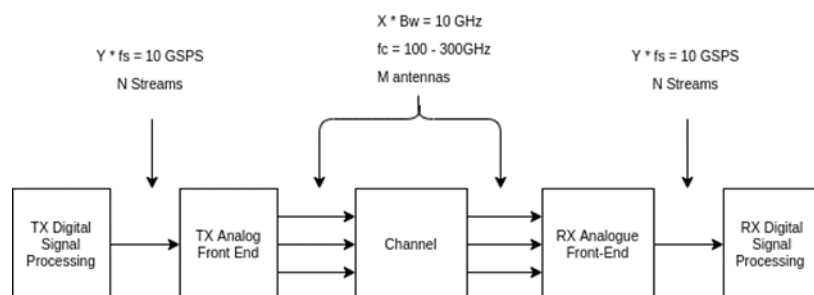


Figure 8-1: Basic system partitioning, where N is the number of digital Tx streams, Y is the number of parallel DA/AD channels, M is the number of Tx and Rx antenna elements and X is the number of parallel RF channels used.

Each demonstration activity replaces a component or components of the simulation-based investigation with a real-world hardware implementation to enable hardware in between analyses. For example, the analogue transceiver and the radio channel in the simulator are replaced with real hardware, but the algorithms are still executed in the simulator.

8.1.1 Digital Architecture and Waveforms

Demonstration purpose: Digital-architecture scalability and key algorithms

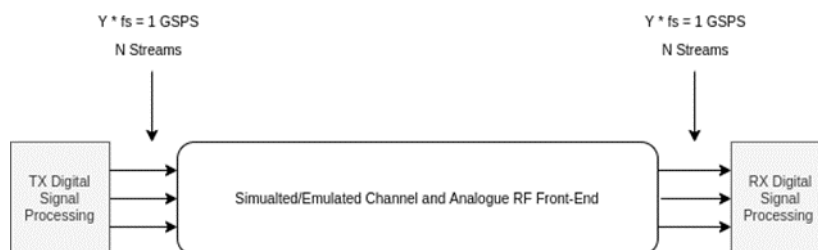


Figure 8-2: Digital architecture demonstration, implementing selected base-band algorithms in real-time, while the analogue system components are simulated.

This setup will be used to demonstrate digital implementation for new waveforms and algorithms. One of the key components of the demonstration is parallelization of system components and data (e.g. frequency multiplexing). The channel and the high frequency RF components in this demonstration setup are emulated.

8.1.2 High-bandwidth communication at upper mmW using different waveforms:

Demonstration purpose: Effect of hardware impairments on different waveforms.

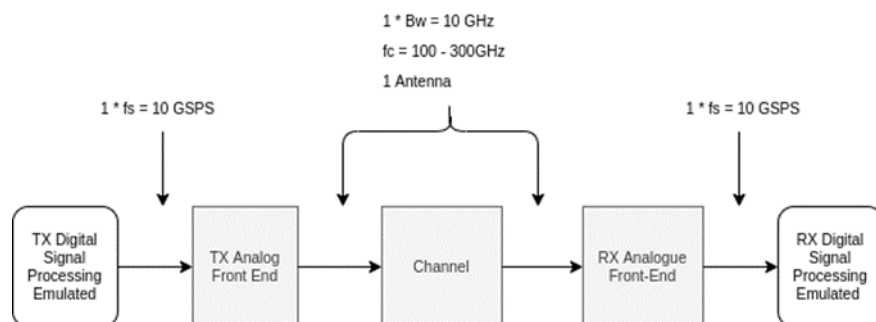


Figure 8-3: Demonstration setup for demonstration of high bandwidth communication. IQ samples are generated and analysed offline, but real RF hardware and an over the air channel is used during the transmission.

This demonstrator setup demonstrates high bandwidth communication signal at high mmW frequencies. The setup is based on commercial measurement equipment, where the Tx is implemented with an arbitrary waveform generator (ARB) and an upconverter and the Rx is implemented with a downconverter and a high frequency sampling oscilloscope. The transmitted signal data and waveform are generated offline in the form of IQ samples which are conveyed to ARB for digital waveform generation. The up- and down conversions are performed with frequency extenders that can support wide band modulated signals. The received signal analysis is performed offline after the received signal has been sampled to memory. Directive antennas which are connected to the frequency extenders are used to transmit and receive signals from OTA radio channel. Additional radio frequency amplifier may be used with the Tx extender to improve the OTA range during the demonstration.

Demonstration activities with this setup are highly inter-connected and -dependent on the signal simulator development presented in Section 3 and the waveform development described in section 4.

8.1.3 Common hardware for communication, localization, and sensing

Demonstration purpose: Combined and shared setup for multi-static sensing and communication.

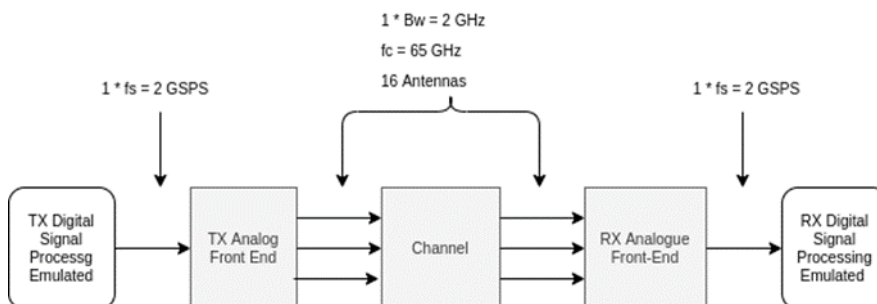


Figure 8-4: Demonstration setup for joint localization, sensing and communication.

This setup is based on FPGA based digital baseband boards, that can transmit, and sample received IQ data that is processed offline. In contrast to the previous setup of Section 8.1.2, the demonstrated signal bandwidth is lower and the carrier frequency supported is 65 GHz. However, the setup supports analogue beamforming at both Tx and Rx, which is a fundamental aspect in localization and sensing for demonstration.

Conclusions

The 6G radio system will significantly enhance the data rates compared with 5G systems, and new modelling challenges at RF system, signal waveform and circuit levels will be encountered. Each of these aspects needs to be carefully studied that simulation and measurement results between different modelling levels can be appropriately taken into account. Non-idealities and -linearities of RF circuits require simple models for link level analysis while more complex models are needed for the waveform studies. We have proposed three level modelling approach based on signal power levels, nonidealities abstracted to the effective channel model for digital link performance analysis and RF non-idealities modelled with behavioural models from sample to sample simulations. We have presented first RF high level models for RF system level blocks which have been used for first RF performance evaluations.

The results presented in the document indicate that radios to support 100 Gbps can be implemented with current technologies. The current consumption of ADCs for 100 Gbps data rate has been studied, and it is estimated, that total ADCs power consumption of currently available industrial ADCs is 40 W, and such power consumption can be barely tolerated in the 6G base stations. If the same ADCs could be implemented with the best academic converters, then the power consumption could be in range of 40 mW. It should be noted that academic and industrial converters have significant differences in, e.g., clocking circuits, output driving capability and electrical interfaces, and thus direct comparison is difficult. We have shown in the report that different phase noise models can give the same EVM performance with different but noise spectral properties.

We have multiple technological challenges to be solved for 6G radios and as an example, integration level of upper mmW frequency radios and noise figure performances of the LNAs with several RFIC processes have been studied. CMOS and SiGe BiCMOS offer the best opportunity to meet the stringent integration requirement necessary for array antenna system. Unfortunately, their noise performances degrade significantly as operational frequency increases since beyond 100 GHz. The best noise figures approach 10 dB at 200 GHz range and at 300 GHz frequency NFs are in range of 18-20 dB.

On the other hand, GaAs and InP devices deliver decent noise performance in the whole mmW range, maintaining a best NF level close to 8 dB even at 300 GHz. However, their integration capabilities are relatively limited and is considered to be unsuitable for antennas in package systems at the upper mmW bands. Based on our NF analysis, CMOS and SiGe are the optimal candidates in terms of integration and Rx noise figure below 170 GHz frequencies. For frequencies above 170 GHz, there is no single technology that meet both requirements, thus, intelligent heterogeneous combination of the technologies can become necessary.

It is demonstrated that the 6G waveforms need to be robust to RF impairments. Preliminary results show that DFTS-OFDM and SC-FDE possess better robustness towards phase noise and PA nonlinearities compared with legacy OFDM, which in turn results in a better link budget – also important in 6G context given expected diminishing of PA output power capabilities. Also it is demonstrated that the complexity of an iterative receiver for DFTS-OFDM, bringing performance improvements over non-iterative receiver structures, can be expected to have reasonable complexity. Finally, the ZXm waveform, attractive due to its very low demands on ADC resolution and hence conducive to lowered power consumption, is demonstrated to be sensitive to uncompensated phase noise; however, a more relevant result is a performance analysis including phase noise compensation, which is left for future work.

We have provided a general overview on beamforming and presented a signal model under ideal assumptions for the study of limitations and challenges of different architectures. In particular, beamforming design is highly influenced by the channel characteristics and the hardware constraints, not only because of the RF impairments but also the complexity of signal processing. For instance, hybrid beamforming with multiple signal chains can be beneficial for multipath channel. By means of theoretical analysis, we show that increasing the data rate with larger bandwidth and relaxing the link budget requirements is more practical than focusing on increasing the link budget by increasing the antenna array size. However, increasing the bandwidth comes at the cost of violating the conventional

narrowband assumption. The wideband is translated to non-flat frequency response of the antenna array, leading to a frequency selective channel even under LoS scenario. However, to cope with wideband signals, it is foreseen to use parallel multiband streams in order to achieve the required data rate. On the contrary, increasing the array size results in narrow beams, which is challenging for beam alignment and tracking. In the future work, we will instigate more on the beamforming design, considering mainly the trade-off between the array size, and the bandwidth. In addition, further work to be done in beam management, which requires more understanding of the channel characteristics

Challenges and opportunities with D-MIMO and its potential role in 6G were introduced, and the different challenges at lower and upper mmW/THz bands were highlighted. This calls for a scalable approach from digital to analog approaches. We also emphasized the need for efficient backhaul fronthaul solutions by integrating fibre and in-band wireless solutions. Densification is the key enabler to meet coverage and reliability targets at the higher frequency bands and there seems to be sufficient spectrum available. Thus, low-cost solutions are more important than spectral efficiency, at least in the early roll-out phases. In the lower mmW bands the need for higher spectral efficiency calls for digital less distributed approaches.

Radio wave and material interaction measurements from 2 GHz to 170 GHz have showed that the transmission losses of EM waves through materials in our living space have increasing trend. Due to internal multi-reflections and the inhomogeneity of the materials, there are regular and irregular oscillations around the trend. Further studies of the oscillations and material parameters are on-going.

Spatio-temporal channel sounding in realistic cellular sites at 140 GHz revealed that communication signals can be delivered from the transmit and receive sides through multiple paths, indicating possibilities of link diversity and multiplexing through pencil beam antennas at both link ends. One to four independent signal paths can be found at indoor sites, while the number of paths at outdoors is smaller than indoors according to the initial analyses of outdoor measurements. Thorough analyses of the number of paths along with their difference to below-100 GHz cases are on-going.

Based on all observation highlighted in this report, new technological advances are needed when first 6G radios are in the ramp-up phase with a reasonable size, current consumption, and affordable cost.

References

- [36.803] 3GPP TR 36.803, “Study on new radio access technology: Radio Frequency (RF) and co-existence Aspects (Release 14)”, September 2017
- [36.888] 3GPP TR 36.888, “Study on provision of low-cost Machine-Type Communications (MTC) User Equipments (UEs) based on LTE (Release 12)”, June 2013.
- [37.340] 3GPP, “TS 37.340: NR; Multi-connectivity”, Overall description (Release 15), 2018.
- [38.101 - 2] 3GPP TS 38.101 – 2, “User Equipment (UE) Radio Transmission and Reception; Part 2: Range 2 Standalone (Release 16)”
- [38.104] 3GPP; “Technical Specification Group Radio Access Network; NR; Base Station (BS) radio transmission and reception,” Rel. 17, V17.3.0, Sept. 2021.
- [38.211] 3GPP TR 38.211, “NR; Physical channels and modulation”, Release 16
- [38.212] 3GPP TS 38.212, “NR; multiplexing and channel coding (release 15),” 2018.
- [38.214] 3GPP TS 38.214, “Physical Layer Procedures for Data (Release 15)”
- [38.802] 3GPP TR 38.802, “Study on New Radio Access Technology Physical Layer Aspects (Release 14)”, September 2017
- [38.808] 3GPP TR 38.808, “Technical Specification Group Radio Access Network; Study on supporting NR from 52.6 GHz to 71 GHz”, Release 17
- [38.900] 3GPP, “TR 38.900: Study on channel model for frequency spectrum above 6 GHz,” Jun. 2016.
- [38.901] 3GPP TR 38.901, “Study on channel model for frequencies from 0.5 to 100 GHz,” 3GPP, Tech. Rep. V14.1.1, July 2017.
- [3GPPR4-040367] The 3rd Generation Partnership Project (3GPP), TDoc R4-040367, TSG RAN WG4 31, “Comparison of PAR and cubic metric for power derating, Tech. Doc.,” 2004.
- [3GPPR4-165901] 3GPP, RAN4 Tdoc, “Further elaboration on PA models for NR”
- [3GPPR4-1610279] 3GPP, RAN4 Tdoc, “On mm-wave ACLR for 45 and 70 GHz”
- [5Gc] “5G channel models up to 100 GHz”
[http://www.5gworkshops.com/5G_Channel_Model_for_bands_up_to100_GHz\(2015-12-6\).pdf](http://www.5gworkshops.com/5G_Channel_Model_for_bands_up_to100_GHz(2015-12-6).pdf)
- [AAS86] J. B. Anderson, T. Aulin, and C.-E. Sundberg, Digital Phase Modulation. NY: Plenum Press, 1986
- [ABC+14] Andrews, J. G., Buzzi, S., Choi, W., Hanly, S. V., Lozano, A., Soong, A.C. K., and Zhang, J. C. (2014). What will 5G be? IEEE J. Sel. Areas Commun., 32(6):1065–1082.
- [AGZ17] W. B. Abbas, F. Gomez-Cuba, and M. Zorzi, “Millimeter wave receiver efficiency: A comprehensive comparison of beamforming schemes with low resolution ADCs,” IEEE Trans. Wireless Commun., vol. 16, no. 12, pp. 8131–8146, Dec. 2017.

- [ALR01] A. N. D'Andrea, V. Littici, and R. Reggiannini, "Nonlinear predistortion of OFDM signals over frequency-selective fading channels," *IEEE TCOM*, vol. 49, pp. 837-43, May 2001.
- [AMG+14] Ahmed Alkhateeb, Jianhua Mo, Nuria Gonzalez-Prelcic, and Robert W. Heath. MIMMO precoding and combining solutions for millimeter-wave systems. *IEEE Communications Magazine*, 52(12):122–131, 2014.
- [AMH18] S. M. Azimi-Abarghouyi, B. Makki, M. Haenggi, M. Nasiri-Kenari, and T. Svensson, "Coverage analysis of finite cellular networks: A stochastic geometry approach," in *Proc. Iran Workshop Commun. Inf. Theory (IWCIT)*, Tehran, Iran, Apr. 2018, pp. 1–5.
- [Arm02] J. Armstrong, "Peak-to-average power reduction for OFDM by repeated clipping and frequency domain filtering," *IEE Electron. Lett.*, vol. 38, pp. 246-247, Feb. 2002.
- [BCF19] R. Bomfin, M. Chafii, and G. Fettweis, "Low-Complexity Iterative Receiver for Orthogonal Chirp Division Multiplexing," in *IEEE WCNC workshops*, (Marrakech, Morocco), Apr. 2019.
- [BDZ+19] Buzzi, S., D'Andrea, C., Zappone, A., and D'Elia, C. (2019). User-centric 5G cellular networks: Resource allocation and comparison with the cell-free massive MIMO approach. *IEEE Trans. Wireless Commun.*, pages 1–1.
- [BJ20] L. Belostotski and S. Jagtap, "Low-noise amplifier (LNA) performance survey," *Univ. of Calgary, Canada*, Jan. 2020. [Online] Available: <https://www.ucalgary.ca/lbelosto>
- [BHS18] Björnson, E., Hoydis, J., and Sanguinetti, L., "Massive MIMO has unlimited capacity," *IEEE Trans. Wireless Commun.*, 17(1): 574–590, 2018.
- [BNC+21] R. Bomfin, A. Nimr, M. Chafii, and G. Fettweis, "A Robust and Low-Complexity Walsh-Hadamard Modulation for Doubly-Dispersive Channels," *IEEE Commun. Lett.*, vol. 25, no. 3, pp. 897–901, 2021.
- [BZM+18] R. Bomfin, D. Zhang, M. Matthé and G. Fettweis, "A Theoretical Framework for Optimizing Multicarrier Systems Under Time and/or Frequency-Selective Channels," in *IEEE Communications Letters*, vol. 22, no. 11, pp. 2394-2397, Nov. 2018.
- [BWM+21] Björnson, E., Wymeersch, H., Matthiesen, B., Popovski, P., Sanguinetti, L., & de Carvalho, E., "Reconfigurable intelligent surfaces: A signal processing perspective with wireless applications," 2021, arXiv preprint arXiv:2102.00742.
- [DCJ+95] Douillard, C. and Jezequel, M., Berrou, C., Picart, A., and Didier, P., "Iterative correction of intersymbol interference: turbo-equalization", *European Transactions on Telecommunications*, 1995.
- [DJ99] J. A. Davis and J. Jedwab, "Peak-to-mean power control in OFDM, Golay complementary sequences," *IEEE Trans. Inf. Theory*, vol. 45, pp. 2397-2417, Nov. 1999.
- [EAM+21] E. N. Papatiriou, A. -A. A. Boulogeorgos, M. Francis De Guzman, K. Haneda and A. Alexiou, "A New Look to THz Wireless Links: Fading Modeling and Capacity Assessment," 2021 *IEEE 32nd Annual International Symposium on Personal, Indoor and Mobile Radio Communications (PIMRC)*, 2021, pp. 1-5.
- [FDB+19] G. Fettweis, M. Dörpinghaus, S. Bender, L. Landau, P. Neuhaus and M. Schlüter, "Zero Crossing Modulation for Communication with Temporally

- Oversampled 1-Bit Quantization," 2019 53rd Asilomar Conference on Signals, Systems, and Computers, 2019, pp. 207-214, doi: 0.1109/IEEECONF44664.2019.9048794.
- [FKH08] T. Frank, A. Klein, and T. Haustein, "A survey on the envelope fluctuations of DFT precoded OFDMA," in Proc. International Conference on Communications ICC, Beijing, China, May 2008.
- [FKV06] Foschini, G.J ; Karakayali, K ; Valenzuela, R.A; "Coordinating multiple antenna cellular networks to achieve enormous spectral efficiency", IEEE Proceedings Communications, 2006.
- [FMI99] M. P. C. Fossorier, M. Mihaljevic and H. Imai, "Reduced complexity iterative decoding of low-density parity check codes based on belief propagation," in IEEE Transactions on Communications, vol. 47, no. 5, pp. 673-680, May 1999.
- [FMS21] C. Fang, B. Makki, J. Li and T. Svensson, "Hybrid Precoding in Cooperative Millimeter Wave Networks," IEEE Trans. Wireless Commun., vol. 20, no. 8, pp. 5373-5388, Aug. 2021
- [GDH16] X. Gao, L. Dai, S. Han, C. L. I, and R. W. Heath, "Energy-Efficient Hybrid Analog and Digital Precoding for MmWave MIMO Systems with Large Antenna Arrays," IEEE J. Sel. Areas Commun., vol. 34, no. 4, pp. 998-1009, Apr. 2016.
- [GHH+10] Gesbert, D., Hanly, S., Huang, H., Shamai (Shitz), S., Simeone, O., and Yu, W. (2010). Multi-cell MIMO cooperative networks: A new look at interference. IEEE J. Sel. Areas Commun., 28(9):1380–1408.
- [GPS+20] G. Wikström et al., "Ever-present intelligent communication", Ericsson White Paper, Nov 2020, Online: <https://www.ericsson.com/en/reports-and-papers/white-papers/a-research-outlook-towards-6g>.
- [HA+21] Y. Heng, J. G. Andrews, J. Mo, V. Va, A. Ali, B. L. Ng, and J. C. Zhang, "Six Key Challenges for Beam Management in 5.5G and 6G Systems", IEEE Communication Magazine, July 2021
- [HEX21-D12] Hexa-X project deliverable D1.2 Expanded 6G vision, use cases and societal values, Eds. M. Hoffmann, M. Uusitalo, M.-H. Hamon, B. Richerzhagen, G. D’Aria, A. Gati and D. Lopez, Apr. 2021.
- [HEX21-D21] Hexa-X project deliverable D2.1 Towards Tbps Communications in 6G: Use Cases and Gap Analysis, Eds. K. Roth, N. Michailow, A. Pärssinen and H. Halbauer, Jun. 2021.
- [HSE+18] Ibrahim A. Hemadeh, Katla Satyanarayana, Mohammed El-Hajjar, and Lajos Hanzo. Millimeter-Wave Communications: Physical Channel Models, Design Considerations, Antenna Constructions, and Link-Budget. IEEE Communications Surveys Tutorials, 20(2):870–913, 2018.
- [HJW+13] X. Hong, Y. Jie, C.-X. Wang, J. Shi, and X. Ge, "Energy-spectral efficiency trade-off in virtual MIMO cellular systems," IEEE J. Sel. Areas Commun., vol. 31, no. 10, pp. 2128–2140, Oct. 2013.
- [HW21] H. Halbauer, T. Wild, "Towards Power Efficient 6G Sub-THz Transmission," Joint EuCNC & 6G Summit, June 8-11 2021, Porto, Portugal
- [IB05] P. Ioannides and C.A. Balanis. Uniform circular and rectangular arrays for adaptive beamforming applications. IEEE Antennas and Wireless Propagation Letters, 4:351–354, 2005.

- [IBN+19] Interdonato, G., Björnson, E., Ngo, H. Q., Frenger, P., and Larsson, E. G., "Ubiquitous cell-free massive MIMO Communications," *EURASIP J. Wireless Commun. and Networking*, 2019(1):197–209, 2019a.
- [Imm90] K. A. S. Immink, "Runlength-limited sequences," in *Proceedings of the IEEE*, vol. 78, no. 11, pp. 1745-1759, Nov. 1990, doi: 10.1109/5.63306.
- [JKJ+09] J. Poutanen, K. Haneda, J. Salmi, V.-M. Kolmonen, A. Richter, P. Almers, and P. Vainikainen, "Development of measurement-based ray tracer for multi-link double directional propagation parameters," *2009 3rd European Conference on Antennas and Propagation*, 2009, pp. 2622-2626.
- [JMZ+14] Jungnickel, V., Manolakis, K., Zirwas, W., Panzner, B., Braun, V., Lossow, M., Sternad, M., Apelfröjd, R., and Svensson, T., "The role of small cells, coordinated multipoint, and massive MIMO in 5G," *IEEE Commun. Mag.*, 52(5):44–51, 2014.
- [JA04] A. D. S. Jayalath and C. R. N. Athaudage, "On the PAR reduction of OFDM signals using multiple signal representation," *IEEE Commun. Lett.*, vol. 8, pp. 425-427, July 2004.
- [KJ04] B. S. Krongold and D. L. Jones, "An active-set approach for OFDM PAR reduction via tone reservations," *IEEE Trans. Signal Process.*, vol. 52, pp. 495-509, Feb. 2004.
- [KMH19] A. Karttunen, M. Mökkönen and K. Haneda, "Investigation of 5G Radio Frequency Signal Losses of Glazing Structures," in *All Eyes on Smarter Glass Performance Day 2019*, Tampere, Finland, June 2019.
- [KNS16] K. Kim, J. No and D. Shin, "On the Properties of Cubic Metric for OFDM Signals," in *IEEE Signal Processing Letters*, vol. 23, no. 1, pp. 80-83, Jan. 2016, doi: 10.1109/LSP.2015.2502261.
- [KGH+21] P. Kyösti, M. F. De Guzman, K. Haneda, N. Tervo and A. Pärssinen, "How many beams does sub-THz channel support," in *IEEE Antennas and Wireless Propagation Letters*, October 2021.
- [LDF18] L. T. Landau, M. Dörpinghaus, and G. P. Fettweis, "1-bit quantization and oversampling at the receiver: Sequence-based communication," *EURASIP J Wirel. Comm.*, vol. 2018, no. 1, p. 83, 2018.
- [KSJ+16] K. Haneda, S. L. H. Nguyen, J. Järveläinen and J. Putkonen, "Estimating the omni-directional pathloss from directional channel sounding," *2016 10th European Conference on Antennas and Propagation (EuCAP)*, 2016, pp. 1-5.
- [LJT+19] M. E. Leinonen, M. Jokinen, N. Tervo, O. Kursu and A. Pärssinen, "System EVM Characterization and Coverage Area Estimation of 5G Directive mmW Links," in *IEEE Trans. on Microw. Theory and Techn.*, vol. 67, no. 12, pp. 5282-5295, Dec. 2019
- [LTJ+19] M. E. Leinonen, N. Tervo, M. Jokinen, O. Kursu and A. Pärssinen, "5G mm-Wave Link Range Estimation Based on Over-the-Air Measured System EVM Performance," *2019 IEEE MTT-S Intern. Microw. Symp.*, 2019, pp. 476-479
- [LSC+12] Lee, D., Seo, H., Clerckx, B., Hardouin, E., Mazzarese, D., Nagata, S., and Sayana, K., "Coordinated multipoint transmission and reception in LTE-advanced: Deployment scenarios and operational challenges," *IEEE Commun. Mag.*, 50(2):148–155, 2012.

- [MA01] P. Moqvist, T. Aulin, "Multiuser SCCPM with iterative decoding," *Electronics Letters*, vol.37, no.19, pp.1174,1176, 13 Sep 2001.
- [Mar10] Marzetta, T. L., "Noncooperative cellular wireless with unlimited numbers of base station antennas," *IEEE Trans. Wireless Commun.*, 9(11):3590–3600, 2010.
- [MM95] U. Mengali, M. Morelli, "Decomposition of M-ary CPM signals into PAM waveforms," *IEEE Transactions on Information Theory*, vol. 41, no. 5, pp. 1265–1275, Sept. 1995.
- [MMF+20] C. Madapatha, B. Makki, C. Fang, O. Teyeb, E. Dahlman, M. S. Alouini, T. Svensson, "On Integrated Access and Backhaul Networks: Current Status and Potentials," in *IEEE Open Journal of the Communications Society*, vol. 1, pp. 1374-1389, 2020, doi: 10.1109/OJCOMS.2020.3022529.
- [MMK21] M. F. De Guzman, M. Hassan and K. Haneda, "Uncertainty of Millimeter-Wave Channel Sounder due to Integration of Frequency Converters," 2021 17th International Symposium on Wireless Communication Systems (ISWCS), 2021, pp. 1-6.
- [MMM+21] C. Madapatha, B. Makki, A. Muhammad, E. Dahlman, M. -S. Alouini and T. Svensson, "On Topology Optimization and Routing in Integrated Access and Backhaul Networks: A Genetic Algorithm-Based Approach," in *IEEE Open Journal of the Communications Society*, vol. 2, pp. 2273-2291, 2021, doi: 10.1109/OJCOMS.2021.3114669.
- [MZF18] M. Matthé, D. Zhang and G. Fettweis, "Low-Complexity Iterative MMSE-PIC Detection for MIMO-GFDM," in *IEEE Transactions on Communications*, vol. 66, no. 4, pp. 1467-1480, April 2018.
- [Mur21] B. Murmann, "ADC Performance Survey 1997-2020," [Online]. Available: <http://web.stanford.edu/~murmann/adcsurvey.html>. Accessed May 7, 2021.
- [NAM+17] Nayebi, E., Ashikhmin, A., Marzetta, T. L., Yang, H., and Rao, B. D., "Precoding and power optimization in cell-free massive MIMO systems," *IEEE Trans. Wireless Commun.*, 16(7):4445–4459, 2017.
- [NAY+17] Ngo, H. Q., Ashikhmin, A., Yang, H., Larsson, E. G., and Marzetta, T. L., "Cell-free massive MIMO versus small cells," *IEEE Trans. Wireless Commun.*, 16(3):1834–1850, 2017.
- [NDF19] P. Neuhaus, M. Dörpinghaus and G. Fettweis, "Oversampled 1-Bit Quantized Wideband Systems: Is it Better to Spend Samples in Time or in Space?," 2019 IEEE 20th International Workshop on Signal Processing Advances in Wireless Communications (SPAWC), 2019, pp. 1-5, doi: 10.1109/SPAWC.2019.8815543.
- [NDH+20a] P. Neuhaus et al., "Sub-THz Wideband System Employing 1-bit Quantization and Temporal Oversampling," *ICC 2020 - 2020 IEEE International Conference on Communications (ICC)*, 2020, pp. 1-7, doi: 10.1109/ICC40277.2020.9148753.
- [NDH+20b] P. Neuhaus, M. Dörpinghaus, H. Halbauer, V. Braun and G. Fettweis, "On the Spectral Efficiency of Oversampled 1-Bit Quantized Systems for Wideband LOS Channels," 2020 IEEE 31st Annual International Symposium on Personal, Indoor and Mobile Radio Communications, 2020, pp. 1-6, doi: 10.1109/PIMRC48278.2020.9217277.

- [NHJ+21] S. L. H. Nguyen, K. Haneda, J. Järveläinen, A. Karttunen, and J. Putkonen, "Large-scale parameters of spatio-temporal short-range indoor backhaul channels at 140 GHz," in Proc. 2021 IEEE 93rd Veh. Tech. Conf. (VTC2021-Spring), Helsinki, Finland, 2021.
- [NJK+18] S. L. H. Nguyen, J. Järveläinen, A. Karttunen, K. Haneda, and J. Putkonen "Comparing radio propagation channels between 28 and 140 GHz bands in a shopping mall," in Proc. 12th European Conf. Ant. Prop. (EuCAP 2018), (London, UK), pp. 1–5, 2018.
- [NML+21] P. Neuhaus, D. M. V. Melo, L. T. N. Landau, R. C. de Lamare, and G. Fettweis, "Zero-crossing modulations for a multi-user MIMO downlink with 1-bit temporal oversampling ADCs," in Proc. European Signal Proc. Conf. (EUSIPCO), Virtual Conference (Dublin, Ireland), Aug. 2021.
- [NP00] R. van Nee, R. Prasad, "OFDM for Wireless Multimedia Communications", 1st ed. Artech House, 2000.
- [NTD+18] Ngo, H. Q., Tran, L., Duong, T. Q., Matthaiou, M., and Larsson, E. G., "On the total energy efficiency of cell-free massive MIMO," IEEE Trans. Green Commun. and Netw., 2(1):25–39, 2018.
- [OF16] E. J. Oughton and Z. Frias, "Exploring the Cost, Coverage and Rollout Implications of 5G in Britain," Cambridge, U.K.: Centre Risk Stud., 2016.
- [OS13] A. V. Oppenheim and R. W. Schaffer, Discrete-Time Signal Processing, Pearson Education Ltd., 3rd Ed., London, UK, p. 1056, 2013.
- [PBH+21] E. N. Papatotiriou, A.-A. A. Boulogeorgos, K. Haneda, M. F. de Guzman, and A. Alexiou, "An experimentally validated fading model for thz wireless systems," Scientific Reports, vol. 11, p. 18717, Sep 2021.
- [PCS+19] S. Pellerano, Steven Callender, Woorim Shin, Yanjie Wang, et al., "A Scalable 71-to-76GHz 64-Element Phased-Array Transceiver Module with 2x2 Direct-Conversion IC in 22nm FinFET CMOS Technology," 2019 IEEE International Solid- State Circuits Conference - (ISSCC), 2019, pp. 174-176, doi: 10.1109/ISSCC.2019.8662496.
- [PLT21] A. Pärssinen, M. E. Leinonen and N. Tervo, "Experiences and future challenges in prototyping RF systems and their components from 5G towards 6G, " presentation in Workshop titled as "Platforms, testbeds, and trials - The next step for 5G and future wireless networks, " in IEEE Intern. Microw. Symp., 20-25 June 2021, Atlanta, USA.
- [PRN+03] Arogyaswami Paulraj, Arogyaswami Paulraj Rohit, Rohit Nabar, and Dhananjay Gore. Introduction to space-time wireless communications. Cambridge university press, 2003.
- [RKL+20] K. Rikkinen, P. Kyosti, M. E. Leinonen, M. Berg and A. Parssinen, "THz RadioCommunication: Link Budget Analysis toward 6G," in IEEE Communications Magazine, vol. 58, no. 11, pp. 22-27, November 2020.
- [RS00] D. Raphaeli and A. Saguy, "Linear equalizers for turbo equalization: A new optimization criterion for determining the equalizer taps", in Proc. Int. Symp. Turbo Codes Related Topics, 2000.
- [RVH95] P. Robertson, E. Villebrun and P. Hoeher, "A comparison of optimal and sub-optimal MAP decoding algorithms operating in the log domain," Proceedings IEEE International Conference on Communications ICC '95, 1995

- [RLG+20] P. Rodríguez-Vázquez, M. E. Leinonen, J. Grzyb, N. Tervo, A. Parssinen and U. R. Pfeiffer, "Signal-processing Challenges in Leveraging 100 Gb/s Wireless THz," 2020 2nd 6G Wireless Summit (6G SUMMIT), 2020, pp. 1-5.
- [SAD18] C. Saha, M. Afshang, and H. S. Dhillon, "Integrated mmWave access and backhaul in 5G: Bandwidth partitioning and downlink analysis," in Proc. IEEE Int. Conf. Commun. (ICC), May 2018, pp. 1–6.
- [SDG+09] D. Schreurs, M. O'Droma, A. A. Goacher, M. Gadringer et. al., "Power Amplifier Behavioral Modeling," Cambridge University Press, p. 263, 2009.
- [SDF21] M. Schlüter, M. Dörpinghaus and G. P. Fettweis, "Joint Phase and Timing Estimation with 1-bit Quantization and Oversampling," in IEEE Transactions on Communications, doi: 10.1109/TCOMM.2021.3113946.
- [SE10] T. Svensson, T. Eriksson, "On Power Amplifier Efficiency with Modulated Signals," Vehicular Technology Conference (VTC 2010-Spring), 2010 IEEE 71st, vol., no., pp.1,5, 16-19 May 2010.
- [SFE+09] T. Svensson, T. Frank, T. Eriksson, D. Aronsson, M. Sternad, and A. Klein, "Block interleaved frequency division multiple access for power efficiency, robustness, flexibility and scalability," EURASIP J. Wireless Commun., Special Issue 3GPP LTE and LTE Advanced, Nov. 2009.
- [SFS11] C. Studer, S. Fateh, and D. Seethaler, "ASIC implementation of soft-input soft-output MIMO detection using MMSE parallel interference cancellation," IEEE J. Solid-State Circuits, vol. 46, no. 7, pp. 1754–1765, Jul. 2011.
- [SH+19] S. Shahramian et. al., "A Fully Integrated 384-Element, 16-Tile, W-Band Phased Array With Self-Alignment and Self-Test", IEEE Journal of Solid-State Circuits, Vol. 54, No. 9, Sept. 2019
- [SKJ16] S. L. H. Nguyen, K. Haneda and J. Putkonen, "Dual-Band Multipath Cluster Analysis of Small-Cell Backhaul Channels in an Urban Street Environment," 2016 IEEE Globecom Workshops (GC Wkshps), 2016, pp. 1-6.
- [SKJ+21] S. L. H. Nguyen, K. Haneda, J. Järveläinen, A. Karttunen and J. Putkonen, "Large-Scale Parameters of Spatio-Temporal Short-Range Indoor Backhaul Channels at 140 GHz," 2021 IEEE 93rd Vehicular Technology Conference (VTC2021-Spring), 2021, pp. 1-6.
- [SS03] T. Svensson and A. Svensson, "Constrained envelope continuous phase modulation," IEEE Vehicular Tech. Conf. VTC03-Spring, vol. 4, Jeju, Korea, April 2003, pp. 2623–2627.
- [SS09] T. Svensson and A. Svensson, "Design and Performance of Constrained Envelope Continuous Phase Modulation", Waveform Diversity & Design Conference, Orlando, Florida, Feb. 2009.
- [Sve02] T. Svensson, "Spectrally Efficient Continuous Phase Modulation". Gothenburg, Chalmers, University of Technology. Ph.D. thesis, Technical report 435, Dec. 2002. Online: <https://research.chalmers.se/en/publication/?id=455>.
- [Tre02] H. van Trees, "Optimum Array Processing", John Wiley and Sons, New York, 2002
- [TAP+08] S. Thompson, A. Ahmed, J. Proakis, J. Zeidler, and M. Geile, "Constant envelope OFDM," IEEE Trans. Commun., vol. 56, pp. 1300-1312, Aug. 2008.

- [TKS02] M. Tuchler, R. Koetter and A. C. Singer, "Turbo equalization: principles and new results," in *IEEE Transactions on Communications*, vol. 50, no. 5, pp. 754-767, May 2002.
- [TL19] Thomas H. Lee, "The Design of CMOS Radio-Frequency Integrated Circuits", Cambridge University Press, 1998, page 287.
- [TMM+19] O. Teyeb, A. Muhammad, G. Mildh, E. Dahlman, F. Barac, and B. Makki, "Integrated Access Backhauled Networks," in *Proc. IEEE Veh. Technol. Conf. (VTC-Fall)*, Sept. 2019.
- [TS02] J. Tan and G. Stüber, "Constant envelope multi-carrier modulation," *IEEE MILCOM*, Oct. 2002.
- [TS11] M. Tüchler and A. C. Singer, "Turbo Equalization: An Overview," in *IEEE Transactions on Information Theory*, vol. 57, no. 2, pp. 920-952, Feb. 2011.
- [TTP17] T. Tuovinen, N. Tervo and A. Pärssinen, "Analyzing 5G RF System Performance and Relation to Link Budget for Directive MIMO," in *IEEE Trans. on Ant. and Prop.*, vol. 65, no. 12, pp. 6636-6645, Dec. 2017
- [WHM+21] Hua Wang, Tzu-Yuan Huang, Naga Sasikanth Mannem, Jeongseok Lee, Edgar Garay, David Munzer, Edward Liu, Yuqi Liu, Bryan Lin, Mohamed Eleraky, Sensen Li, Fei Wang, Amr S. Ahmed, Christopher Snyder, Sanghoon Lee, Huy Thong Nguyen, and Michael Edward Duffy Smith, "Power Amplifiers Performance Survey 2000-Present," [Online]. Available: https://gems.ece.gatech.edu/PA_survey.html
- [WPS11] M. Wylie-Green, E. Perrins, and T. Svensson, "Introduction to CPM-SCFDMA: A novel multiple-access power-efficient transmission scheme," *IEEE Transactions on Communications*, vol. 59, no. 7, pp. 1904–1915, July 2011.
- [XKJ+19] Y. Xing, O. Kanhere, S. Ju and a. T. S. Rappaport, "Indoor Wireless Channel Properties at Millimeter Wave and Sub-Terahertz Frequencies," in *IEEE Global Communications Conference (GLOBECOM)*, Hawaii, USA, 2019.
- [XWX+19] Y. Xu, W. Wang, Z. Xu and X. Gao, "AVX-512 Based Software Decoding for 5G LDPC Codes," *2019 IEEE International Workshop on Signal Processing Systems (SiPS)*, 2019, pp. 54-59
- [YCC14] L. Yeh, Y. Chen and H. Chuang, "A novel ultra-compact and low-insertion-loss 77 GHz CMOS on-chip bandpass filter with adjustable transmission zeros," *2014 44th European Microwave Conference*, 2014, pp. 1056-1059, doi: 10.1109/EuMC.2014.6986620.
- [ZBM+20] J. Zhang, E. Björnson, M. Matthaiou, D. W. K. Ng, H. Yang and D. J. Love, "Prospective Multiple Antenna Technologies for Beyond 5G," in *IEEE Journal on Selected Areas in Communications*, vol. 38, no. 8, pp. 1637-1660, Aug. 2020.
- [ZCL+19] Zhang, J., Chen, S., Lin, Y., Zheng, J., Ai, B., and Hanzo, L., "Cell-free massive MIMO: A new next-generation paradigm," *IEEE Access*, 7:99878–99888, 2019.
- [ZHL+18] T. Zemen, M. Hofer, D. Löschenbrand and C. Pacher, "Iterative Detection for Orthogonal Precoding in Doubly Selective Channels," in *2018 IEEE 29th Annual International Symposium on Personal, Indoor and Mobile Radio Communications (PIMRC)*, 2018.
- [ZNS+21] S. Zeitz, P. Neuhaus, M. Schlüter, M. Dörpinghaus and G. Fettweis, "Soft-Output Equalizers for Systems Employing 1-Bit Quantization and Temporal

- Oversampling," 2021 IEEE Wireless Communications and Networking Conference (WCNC), 2021, pp. 1-6.
- [VBPG15] Roberto Vallauri, Giorgio Bertin, Bruno Piovano, and Paolo Gianola. Electromagnetic field zones around an antenna for human exposure assessment: Evaluation of the human exposure to EMFs. *IEEE Antennas and Propagation Magazine*, 57(5):53–63, 2015.
- [WLwP+09] Junyi Wang, Zhou Lan, Chang woo Pyo, T. Baykas, Chin sean Sum, M.A. Rahman, Jing Gao, R. Funada, F. Kojima, H. Harada, and S. Kato. Beam codebook-based beamforming protocol for multi-Gbps millimeter-wave WPAN systems. *IEEE Journal on Selected Areas in Communications*, 27(8):1390–1399, 2009.
- [Zat98] M Zatman. How narrow is narrowband? *IEE Proceedings-Radar, Sonar and Navigation*, 145(2):85–91, 1998.

Annex A

Section 6.3.2.1 Beamforming Computations and Weight Distribution

System Model:

Let N APs equipped with M antennas connected to CPUs through high-capacity fronthaul links, where CPUs are also coordinated by another central entity via high-capacity backhaul links. Multiple APs coherently serve K randomly distributed single-antenna UEs in a UE-centric way as shown in Figure 6-1. The following variables are defined for $n = 1, \dots, N$ APs, $j, k = 1, \dots, K$ UEs. Let for q_k be the data symbol to be transmitted to the k -th UE, where $E\{q_k q_j\} = \delta_{jk}$ where $\delta_{jk} = 1$ for $j = k$, $\delta_{jk} = 0$ otherwise. $\mathbf{h}_{kn} \in \mathbb{C}^{1 \times M}$ represent the complex-valued channel coefficients between the n -th AP and the k -th UE, then, the transmitted data signal from the n -th AP to all the UEs can be written as $\mathbf{x}_n = \sum_{k=1}^K \boldsymbol{\omega}_{kn} q_k$, where $\boldsymbol{\omega}_{kn} \in \mathbb{C}^{M \times 1}$ is the precoding vector.

Received Signal and SINR:

Precoding weights are adjusted considering each AP has a peak transmission power limit which is denoted by P_n for n -th AP. Single frequency network transmission is assumed network-wide, and the zero mean circularly symmetric additive white Gaussian noise with variance α_η^2 is given by η_k . Then, the received signal for k -th UE is formulated as a function of precoding weights as follows:

$$y_k(\boldsymbol{\omega}) = \sum_{n=1}^{N_k} \sqrt{P_n} \mathbf{h}_{kn} \boldsymbol{\omega}_{kn} q_k + \sum_{j=1, j \neq k}^{N_k} \sum_{n=1}^{N_j} \sqrt{P_n} \mathbf{h}_{jn} \boldsymbol{\omega}_{jn} q_j + \eta_k, \forall k, \quad (8-1)$$

where first term is the intended signal received from the APs in the dedicated serving AP subset, and the other terms represent the interference and noise term, respectively. Then the SINR (γ) is given as

$$\gamma_k(\boldsymbol{\omega}) = \frac{|\sum_{n=1}^{N_k} \sqrt{P_n} \mathbf{h}_{kn} \boldsymbol{\omega}_{kn}|^2}{\sum_{j=1, j \neq k}^{N_k} |\sum_{n=1}^{N_j} \sqrt{P_n} \mathbf{h}_{jn} \boldsymbol{\omega}_{jn}|^2 + \alpha_\eta^2}, \forall k, \quad (8-2)$$

and eventually the downlink Spectral Efficiency (SE, ζ) per-UE is found as

$$\zeta(\boldsymbol{\omega}) = \frac{1}{K} \sum_{k=1}^K \log_2[1 + \gamma_k(\boldsymbol{\omega})]. \quad (8-3)$$